Technische Universität München
TUM School of Engineering and Design

Spontaneous Damage Behavior of Wet Multi-Plate Clutches under Transient Slip Conditions

Thomas W. Schneider

Vollständiger Abdruck der von der TUM School of Engineering and Design der Technischen Universität München zur Erlangung eines

Doktors der Ingenieurwissenschaften (Dr.-Ing.)

genehmigten Dissertation.

Vorsitz: Prof. Dr.-Ing. Markus Zimmermann

Prüfende der Dissertation:

1. Prof. Dr.-Ing. Karsten Stahl
2. Prof. Dr.-Ing. Wolfram Volk
3. Prof. Dr.-Ing. Max Marian

Die Dissertation wurde am 01.07.2024 bei der Technischen Universität München eingereicht und durch die TUM School of Engineering and Design am 20.12.2024 angenommen.

Vorwort

Die vorliegende Dissertation entstand während meiner Tätigkeit als wissenschaftlicher Mitarbeiter am Lehrstuhl für Maschinenelemente, Forschungsstelle für Zahnräder und Getriebesysteme (FZG) der Technischen Universität München. Sie basiert auf den Ergebnissen zweier Forschungsprojekte der Forschungsvereinigung Antriebstechnik e.V. (FVA).

Mein besonderer Dank gilt all jenen, die mich sowohl beruflich als auch privat auf diesem Weg unterstützt haben. Besonders danken möchte ich …

… Prof. Dr.-Ing. Karsten Stahl, meinem Doktorvater, für die hervorragende Betreuung, das mir entgegengebrachte Vertrauen sowie das inspirierende und vielseitige Arbeitsumfeld an der FZG. Sein Fachwissen und die vielfältigen Möglichkeiten zur persönlichen und fachlichen Weiterentwicklung haben wesentlich zum Gelingen dieser Arbeit beigetragen.

… Prof. Dr.-Ing. Wolfram Volk und Prof. Dr.-Ing. Max Marian für die Übernahme des Korreferats sowie den wertvollen fachlichen Austausch.

… Prof. Dr.-Ing. Markus Zimmermann für die freundliche Übernahme des Prüfungsvorsitzes.

… meinem Abteilungsleiter Dr.-Ing. Hermann Pflaum, dessen umfangreiche Erfahrung, Expertise und konstruktive Diskussionen entscheidend für den Erfolg dieser Arbeit waren. Sein Engagement bei der Korrektur sowie die bereichernden Gespräche, auch nach seiner aktiven Zeit, waren von unschätzbarem Wert.

... meiner geschätzten Kollegin, Teamleiterin und späteren Abteilungsleiterin Dr.-Ing. Katharina Völkel, für die kontinuierliche Unterstützung.

… allen FZG-Mitarbeitenden in Verwaltung, E-Labor, Labor und Werkstatt. Namentlich erwähnen möchte ich Kornelia Güth und Andrea Hünlein für die unermüdliche Bewältigung organisatorischer Belange. Reiner Duschek, Ralf Kiepfer, Klaus Winkler, Markus Pflügler, Thomas Rath, Harald Mayr für ihre tatkräftige Unterstützung bei der Fertigung von Prüfstandskomponenten. Besonderer Dank geht an Richard Brandoni für die Unterstützung am Prüfstand, die bereichernden privaten Gespräche und die wertvolle Zusammenarbeit im Prüffeld. Marco Breidinger, Inge Brodschelm und Wilma Leykamm für die Durchführung von REM-Analysen und metallographischen Untersuchungen.

... den Mitgliedern des projektbegleitenden Ausschusses „Schaltbare Kupplungen und Bremsen“, die die Forschungsprojekte durch ihre fachliche Begleitung und Unterstützung ermöglicht haben.

… meinen studentischen Hilfskräften, Bacheloranden, Semestranden und Masteranden für die umfassende und zuverlässige Mitarbeit. Insbesondere danke ich Andreas Zilkens und Gonzalo Schuster Tapia für ihren unermüdlichen Einsatz, ihr beeindruckendes Fachwissen und ihr handwerkliches Geschick.

… Patrick D. Fischer, durch den ich über meine Semesterarbeit den Weg an die FZG fand und der mich durchgängig unterstützt, gefördert und zu meiner Promotion ermutigt hat.

… meinen Abteilungskollegen Korbinian Stadler, Marco Mileti, Daniel Grötsch, Patrick Strobl, Lukas Pointner-Gabriel, Johannes Wirkner, Aaron Zang, Andreas Lenhart für die kollegiale Zusammenarbeit, den Zusammenhalt und die gemeinsamen Aktivitäten auch außerhalb des Lehrstuhls.

… allen weiteren Assistenten und Mitarbeitenden des Lehrstuhls für die besondere, freundschaftliche Atmosphäre und die daraus resultierenden beruflichen sowie privaten Erlebnisse. Besonders Bernd Morhard, Lorenz Constien, Philipp Schnetzer, Dr.-Ing. Michael Hein, Christoph Leonhardt, Daniel Schweigert, Dr.-Ing. Dominik Kratzer, Benedikt Siewerin, Stefan Reitschuster, André Sitzmann, Michael Geitner möchte ich hier hervorheben.

… meinen Kollegen aus dem Leitungskreis Dr.-Ing. Thomas Tobie, Dr.-Ing. Michael Otto, Dr.-Ing. Josef Pellkofer und Dr.-Ing. Thomas Lohner für ihre stetige Unterstützung.

… meinen Bürokollegen Philipp Roth und Stefan Sendlbeck für die angenehme Zusammenarbeit, die inspirierenden Gespräche und die gegenseitige Unterstützung, die stets für Motivation gesorgt hat.

… meinen Studienkollegen Maximilian Gruber, Christoph Hartmann, Enzo Maier, Marc Hirschka, Manuel Biedermann und Philipp Yoldasis, die die gemeinsame Studienzeit zu einem unvergesslichen Lebensabschnitt gemacht haben.

… .. meiner Tante Ingrid und meinem Onkel Wolfgang, deren unermüdliche Unterstützung und Ermutigung mich stets begleitet und inspiriert haben.

… meinen Eltern Hans und Marianne, die mir durch ihre beständige Unterstützung in allen Lebenslagen meinen beruflichen Werdegang ermöglicht haben, sowie meinen Schwestern Franziska und Alexandra, die für eine wundervolle Familie sorgen. Fleiß und Durchhaltevermögen waren stets meine Begleiter – Werte, die ich meinen Eltern verdanke.

Der größte Dank gilt meiner Frau Elena. Mit Ihr an meiner Seite hatte ich nie Zweifel, dass wir gemeinsam alles erreichen können. Ihr Verständnis für frühe Morgen und späte Abende, Ihre Energie, Begeisterungsfähigkeit und die Fähigkeit, diese auf andere zu übertragen, sind bewundernswert.

Meine größte Motivation und Energie ziehe ich aus meiner Familie, insbesondere meinen Kindern Elias, Hannah und Clara. Ihnen widme ich diese Arbeit.

Poxdorf, 22.02.2024 Thomas Schneider

Abstract

In this dissertation, the spontaneous damage behavior of wet multi-plate clutches under transient slip conditions is investigated, a critical factor for the efficiency, safety, and comfort of modern automotive drivetrains. Wet multi-plate clutches are widely used in limited slip differentials and torque vectoring systems with the goal of improving the lateral dynamics of the vehicle. The scope of the study is to investigate the failure mechanisms of these clutches using three types of friction linings (paper, carbon composite, and woven carbon) and different steel plate thicknesses. A testing and evaluation methodology, grounded in the current state of the art, is proposed and validated through preliminary tests to identify different failure mechanisms.

The study identifies varied failure mechanisms: buckling of steel plates in systems with paper and carbon composite linings, and delamination of friction lining in assemblies with woven carbon linings. A key result is the identification of a critical temperature range that indicates upcoming failure in different systems, regardless of the different failure mechanisms and the friction linings used.

Both two- and three-dimensional finite element models have been developed to further understand the thermo-mechanical behavior of the clutches during operation. The results underscore the significant influence of design parameters, such as the thickness of the steel and lining plates and the thermal properties of the materials, on the thermal behavior of the clutch. The research recommends a symmetrical and uniform design of clutch components to increase resistance to deformation, such as buckling, and to reduce thermal stresses.

In addition, predictive models derived from simulation data and using machine learning algorithms have been developed to predict potential damage states and thereby aid in damage prevention. Among these, the back-propagation neural network model stands out for its accuracy in predicting temperature increases and critical conditions. For applications requiring real-time predictions, a decision-tree-based model is recommended because of its practicality and because it significantly outperforms other algorithms in prediction speed.

The contributions of this dissertation are manifold, providing profound insights into the damage mechanisms of wet multi-plate clutches and critical knowledge for the refinement of clutch design. Furthermore, the development of effective predictive maintenance strategies based on these findings promises to prevent spontaneous damage and increase the reliability of vehicle powertrains.

Contents

Nomenclature

Sign	Unit	Description
Latin symbols		
A	m^2	Apparent contact area
$A_{FE\text{-}Model}$	m^2	Contact area in the FE-Model
A_{Flank}	m^2	Tooth flank area
A_{rat}	–	Area ratio of the FE-Model to the real part
$A_{\vartheta Rf}$	K·s	Temperature-time integral, damage characteristic value according to Hensel [Hen14]
c_{cp}	J/kg·K	Specific heat capacity carrier plate
c_i	J/kg·K	Specific heat capacity of solid *i*
c_{fl}	J/kg·K	Specific heat capacity friction lining
c_{sp}	J/kg·K	Specific heat capacity steel plate
D	N/m^2	Elastic matrix
d_b	mm	Diameter of drill hole of the steel plate
d_{cp}	mm	Thickness carrier plate
d_{fl}	mm	Thickness friction lining
$d_{i,fl}$	mm	Inner diameter friction lining
d_m	mm	Mean frictional diameter
$d_{o,fl}$	mm	Outer diameter friction lining
$d_{i,sp}$	mm	Inner diameter steel plate
$d_{o,sp}$	mm	Outer diameter steel plate
d_{sp}	mm	Thickness steel plate
d_t	mm	Thermocouple diameter
E	N/m^2	Young’s modulus
E_{fl}	N/m^2	Young’s modulus friction lining
F_a	N	Axial force
h_c	$W/m^2{\cdot}K$	Thermal contact conductance
J	kgm^2	Mass inertia
L	m	Stretched length
L_0	m	Initial length
ΔL	m	Length change
N	–	Number of slip phases
n	min^{-1}	Speed

Sign	Unit	Description
Δn	min^{-1}	Differential speed
Δn_{max}	min^{-1}	Max. differential speed
p	–	Probability
p	$\mathrm{N/mm^2}$	Surface pressure
q	$\mathrm{J/mm^2}$	Friction work
$\dot{q}$	$\mathrm{W/mm^2}$	Friction power
$\dot{q}_{\mathrm{max}}$	$\mathrm{W/mm^2}$	Max. friction power
$\dot{q}$	$\mathrm{W/mm^2}$	Heat flux density
$\dot{Q}$	W	Heat flow rate
r	m	Radius
r_{m}	mm	Mean frictional radius
T	Nm	Torque
T	K	Temperature field
ΔT	K	Temperature difference
T_0	K	Initial temperature
T_{cp}	K	Temperature field carrier plate
t_{cp}	mm	Thickness carrier plate
$T_{\mathrm{cp,fl}}$	K	Temperature field carrier plate in contact with the friction lining
T_{f}	Nm	Friction torque
T_{fl}	K	Temperature field friction lining
t_{fl}	mm	Thickness friction lining
$T_{\mathrm{fl,cp}}$	K	Temperature field friction lining in contact with the carrier
$T_{\mathrm{fl,sp}}$	K	Temperature field friction lining in contact with the steel plate
T_i	K	Temperature field of solid body *i*
T_{max}		Maximal temperature
T_{oil}	°C	Oil temperature
T_{sp}	K	Temperature field steel plate
t_{sp}	mm	Thickness steel plate
$T_{\mathrm{sp,fl}}$	K	Temperature field steel plate in contact with the friction lining
t	s	Time
$U_{n,\mathrm{rel}}$	%	Relative measurement uncertainty slip speed
$U_{T,\mathrm{rel}}$	%	Relative measurement uncertainty steel plate temperature
$U_{\mu,\mathrm{rel}}$	%	Relative measurement uncertainty coefficient of friction
v	m/s	Sliding speed
v_{rel}	m/s	Relative sliding speed
$\dot{v}_{\mathrm{oil}}$	$\mathrm{mm^3/mm^2/s}$	Specific oil flow rate
z	–	Number of friction interfaces

Sign	Unit	Description
z	m	Axial coordinate
Greek symbols		
δ	–	Proportionality coefficient
ε	%	Total strain
ε_T	%	Thermal strain
ε_E	%	Mechanical strain
θ	°	Angular coordinate
λ_{cp}	W/m·K	Thermal conductivity carrier plate
λ_{fl}	W/m·K	Thermal conductivity friction lining
λ_i	W/m·K	Thermal conductivity of solid *i*
λ_{sp}	W/m·K	Thermal conductivity steel plate
μ	–	Coefficient of friction
μ_{top}	–	Characteristic coefficient of friction value
ρ	kg/m³	Density
ρ_{cp}	kg/m³	Density carrier plate
ρ_{fl}	kg/m³	Density friction lining
ρ_{sp}	kg/m³	Density steel plate
ρ_i	kg/m³	Density of solid *i*
σ	N/m²	Stress
ω_{rel}	rad/s	Relative angular velocity

Indices

a	Axial	max	Maximum
cp	Carrier plate	min	Minimum
f	Friction	o	Outer
fl	Friction lining	ref	Reference
fp	Friction plate	sp	Steel plate
i	Inner	t	Thermocouple
m	Mean		

Glossary

2D	Two-dimensional	GfT	Gesellschaft fuer Tribologie e.V.
3D	Three-dimensional	GP	Gaussian Process
AI	Artificial intelligence	GUM	Guide to the Expression of Uncertainty in Measurement

ATF	Automatic transmission fluid	HV	Vickers hardness
BSE	Backscattered electron	ISO	International Organization for Standardization
BPNN	Backpropagation Neural Networks	KLP	Kupplungs-Lebensdauer-Pruefstand
CFD	Computational fluid dynamics	MAPE	Mean Absolute Percentage Error
CoF	Coefficient of friction	MSE	Mean Squared Error
CFRC	Carbon fiber reinforced carbon	NVH	Noise Vibration Harshness
CFRP	Carbon fiber reinforced plastic	OAT	One-at-a-time
CV	Cross validation	PR	Polynomial Regression
DIN	Deutsches Institut fuer Normung	RMSE	Root Mean Squared Error
DOF	Degree of Freedom	SAE	Society of Automotive Engineers
DT	Decision Tree	SE	Secondary electron
EDX	Energy Dispersive X-ray Spectroscopy	SEM	Scanning electron microscopy
e.V.	Eingetragener Verein	SP1	Steel plate 1
FEM	Finite element method	SP2	Steel plate 2
FDM	Finite difference method	SP3	Steel plate 3
FP1	Friction plate 1	SVR	Support Vector Regression
FP2	Friction plate 2	TEI	Thermoelastic instability
FP3	Friction plate 3	TST	Tribological surface transformation
FS1	Friction system 1	TTS	Tribological transformation of surface
FS2	Friction system 2	VDI	Verein Deutscher Ingenieure
FS3	Friction system 3		

1 Introduction

Wet multi-plate clutches are important components for the functioning, safety, and comfort of modern automotive powertrains. In heavy and sporty vehicles, the number of new registrations is steadily increasing [Kor21, Kor22]. These vehicles often use wet multi-plate clutches in limited-slip differentials and torque vectoring systems to improve lateral dynamics through transient slip operation. Over the past few decades, growing torque demands in both internal combustion and electric vehicles have led to improved transmission performance [Ifd22]. Consequently, wet multi-plate clutches are expected to transmit more power in a comparable package space, without compromising service life, loss behavior, or shifting comfort. However, the demand for higher power density is in competition with the need for high operational reliability.

Vehicle transmission applications are almost always safety-critical because a failure of the clutch can render the vehicle undrivable. Spontaneous damage is a concerning issue, as it can lead to clutch failure with just one shift and is unpredictable [Str17]. The design of multi-plate clutches is complicated by the diverse physical and tribological properties of various types of friction materials, as well as their resulting damage patterns. Consequently, clutches are often over-dimensioned to mitigate the risk of spontaneous damage during operation.

Existing test methods for evaluating the tendency of wet multi-plate clutches towards spontaneous damage typically focus on individual operating points and mechanical load variables [Str17]. However, various studies [And90, Sch20a, Sni06, Su06b, Yu19a] demonstrate that the thermal behavior of wet multi-plate clutches significantly affects their spontaneous damage behavior. An optimized clutch design aims to reduce thermal damage, necessitating investigations into variations in steel and friction plate geometrical parameters and material selection, particularly for the friction lining. Performing experimental investigations on component test rigs, as well as microstructure, topography, and SEM analyses, is essential for this objective. Given that a comprehensive measurement and analytical description of the thermal behavior of wet multi-plate clutches are nearly unattainable, the use of simulation with finite element models becomes indispensable for understanding tribological and thermomechanical processes. Such simulation models enable extensive parameter studies and sensitivity analyses.

In addition to avoiding high friction interface temperatures and associated damage through appropriate layout and adapted clutch design, critical system states can be mitigated during operation. In industrial and automotive transmissions, the thermal behavior of clutches is calculated in real-time to prevent such states [Gro21a]. In other disciplines, data-based predictions are increasingly complementing online calculation tools [Lia18, Mad19]. However, the critical limiting temperatures for spontaneous damage occurrence are currently unknown for these calculation tools or prediction models. As a result, current systems either fail to prevent spontaneous damage, or they operate below their maximum performance capabilities due to overly conservative limits.

Despite optimized clutch design and prediction models designed to avert overload cases, damage can still occur during operation. For this reason, condition monitoring gains increasing importance in modern drive systems, replacing traditional reactive or preventive maintenance with condition-based maintenance. This change is motivated by the high costs and time required for removing friction elements, which often lead to transmission write-offs [Sto23]. To ensure reliable condition monitoring of wet multi-plate clutches, a comprehensive

understanding of the system's tribological behavior after overload or spontaneous damage is crucial.

2 State of the Art

The following section presents the fundamentals that are used for achieving the research objectives in this thesis. The modes of operation and properties of wet multi-plate clutches are explained. Furthermore, the damage behavior, design recommendations, and thermomechanical simulation models are discussed in detail.

2.1 Wet Multi-Plate Clutches

The first mention of a multi-plate clutch design consisting of friction and steel plates is presented by Weston [Wes68] in 1868. In this work, Weston introduces a variety of designs (see Figure 2.1) of brakes and clutches, which are specifically intended for hoist and windlass applications. Nowadays, multi-plate clutches find use in many drive technology applications and fulfill a variety of functions. Examples include torque vectoring systems and differential locks in modern vehicles. In industrial systems, these clutches serve, among other uses, to engage ancillary units and to act as slipping clutches designed to protect against overloads and vibrations.

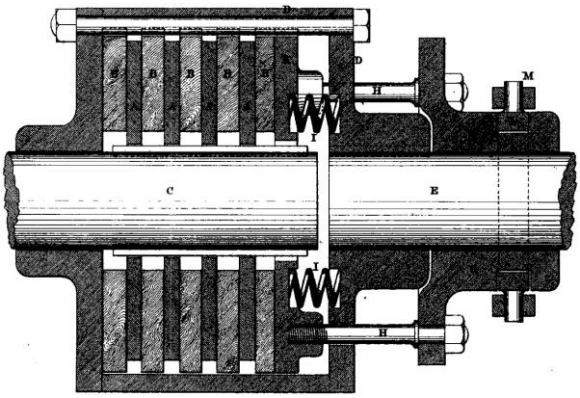

Figure 2.1: Design of a friction clutch [Wes68].

2.1.1 Design

Wet multi-plate clutches are classified as shiftable externally actuated friction clutches and brakes and adhere to VDI standard 2241 [VDI82]. The main clutch components include the outer and inner carrier, outer and inner plates, friction linings, end plates, and pressure plate [VDI82]. The inner and outer plates are arranged in an alternating pattern. These plates are non-rotatably connected to their corresponding drivers, allowing them to move in the axial direction. In the non-shifted state, the two shafts generally exhibit different speeds. Actuating the clutch synchronizes the shafts when under load. The torque is determined by the friction between the inner and outer plates, which are pressed against each other by an applied axial force. By arranging several inner and outer plates in series, the axial force is simultaneously applied across multiple friction interfaces, enabling an increase in the friction torque. Wet multi-plate clutches are oil-cooled and generally exhibit a higher power density than dry clutches [Voe20a]. A distinction can be made between immersion in oil, oil bypass, splash oil, and oil supply from inside through the shaft [VDI82].

A comprehensive overview of the type and function of friction clutches and friction brakes is presented by Niemann [Nie83]. More detailed descriptions of the design and operating principles of wet multi-plate clutches and brakes can be found in company publications by Hoerbiger [Hoe01] and Ortlinghaus [Ort04].

2.1.2 System Requirements

The requirements for wet multi-plate clutches, especially for their friction linings, primarily depend on various operating conditions. Naunheimer et al. [Nau19], Rao [Rao11], and Voelkel [Voe20a] summarize these requirements. Desired properties include smooth shifting behavior, i.e., a consistent coefficient of friction curve over the sliding speed, as well as a drop in the

coefficient of friction toward static friction, which affects the controllability of the clutch. Moreover, shudder must be avoided in order to ensure favorable NVH behavior. A long service life is just as crucial as a high torque transmission capacity, indicated by a high coefficient of friction. Factors that influence the service life include low wear, high mechanical strength, and high thermal load capacity. Additional criteria encompass consistent friction properties throughout the service life of both the oil and lining, as well as insensitivity to metallic abrasion, particles and water in the oil, and minimal no-load losses.

2.1.3 Operating Modes

Depending on the application, wet multi-plate clutches are operated in different sliding speed ranges. These application-specific differences must be considered when performing experiments used to characterize clutch damage and friction behavior.

The load shift mode (see Figure 2.2) is used to characterize friction and damage behavior at sliding speeds exceeding 0.03 m/s. In this case, the clutch is first accelerated to the maximum differential speed Δn_{max} in the disengaged position. The clutch is then closed, and a defined axial force F_a is applied. The acting frictional torque synchronizes the outer and inner plates. [Mei15]

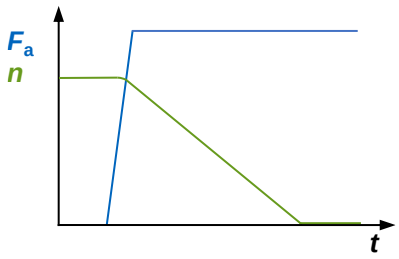

Figure 2.2: Load shift (based on Meingassner [Mei15]).

A constant axial force F_a is applied to the clutch pack in the steady slip mode (see Figure 2.3). A differential speed Δn is then set, and the clutch is operated constantly at this slip speed for a defined period of time. Finally, the speed is reduced to a standstill, and the clutch is disengaged. [Mei15]

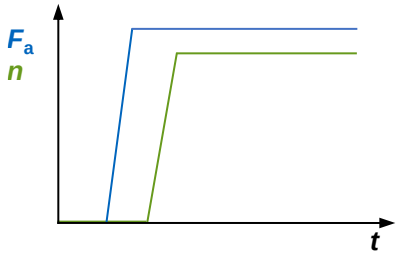

Figure 2.3: Steady slip (based on Meingassner [Mei15]).

In the transient slip mode (see Figure 2.4), the clutch is actuated at a constant axial force F_a in the same way as in steady slip mode. The clutch is then repeatedly accelerated to the differential speed Δn, and the differential speed Δn is then reduced back to zero. [Mei15, Voe20a]

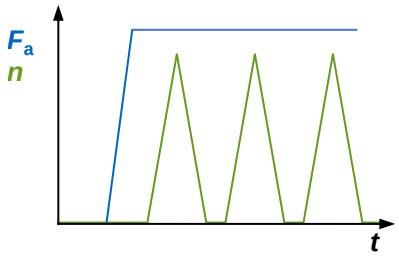

Figure 2.4: Transient slip (based on Meingassner [Mei15]).

In the case of micro-slip, the actuated clutch is loaded with a constant torque to investigate the frictional behavior and to determine the coefficient of static friction (see Figure 2.5). The micro slip operating mode is present if relative rotation occurs between the inner and outer carriers. If no relative rotation occurs, then the clutch is being operated in static friction mode. [Mei16]

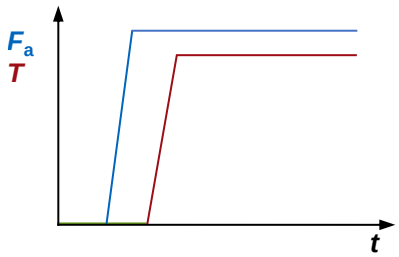

Figure 2.5: Micro slip (based on Meingassner [Mei16]).

2.1.4 Friction Material Pairings

Various friction pairings, which influence shifting, damage, and wear behavior [Bac10, Hen14, Jon13], are used for wet clutches, depending on the application requirements. Typical

requirements for the friction pairing include low material and manufacturing costs, low wear, durability, a high dynamic and static coefficient of friction, favorable noise behavior, low no-load losses, oil compatibility, temperature resistance, and safety against overload [VDI84, Hua19, Mar07, Nau19, Nie83, Win85]. A friction partner made of steel is generally chosen due to its ability to meet the above requirements [Win85]. These steel plates are manufactured in series production by punching from the coil and machining with geometrically undefined cutting edges [Hoe01, Voe20a]. Punching burrs can be removed, and specific surface properties (e.g., roughness) can be adjusted [Fis73, Voe20a, Yes92]. The typical steel plate materials are heat-treatable steels (e.g., C60) [Hoe01, Ost01] that can be post-treated by means of various hardening and coating processes (e.g., quenching and tempering [VDI84, Hoe01, Lef13, Ort04, Pfl98, Win85], nitriding [VDI84, Pfl98, Sit07], nitrocarburizing [Sit07], phosphating [Hoe01, Pfl98]). Both wear resistance and seizure resistance are improved thereby. The typical second friction partners include sintered bronze-based friction linings, paper-based friction linings, and carbon friction linings applied to a supporting steel plate [Fei08, Nau19, Voe20a]. Friction materials such as molybdenum for high pressures [Hoe01, Ort04] and ceramics for temperature resistance [Ber13, Czé09, Hoe01, Nie83] are used in particular applications. A second friction partner made of steel, sintered iron, or gray cast iron [VDI84, Gro18, Hoe01, Nie83, Ost01] is chosen when electromagnetic properties are required.

The macroscopic and microscopic design of the friction interfaces significantly influence friction behavior, thermal load capacity, torque increase during shifting, and drag torque [Hoe01, Pfl98]. Therefore, friction plates are provided with macroscopic grooves in the form of radial grooves, spiral grooves, wafer grooves, and parallel or sunburst grooves, enabling sufficient cooling of the closed clutch through oil flow [Gro18, Pfl98, Sit07]. These grooves facilitate rapid oil displacement from the friction contact when the clutch is actuated. As a result, load-bearing hydrodynamic effects are avoided [Voe20a]. At the microscopic level, friction plates possess high surface roughness and porosity. This leads to improved cooling, and load-bearing hydrodynamic lubrication films are thereby also avoided [Dev04, Mat93, Mat97a, Pfl98, Sit07].

Bronze-Based Sinter Friction Lining:

Bronze-based sinter friction linings (hereinafter referred to simply as sinter friction linings) contain about 60 % to 75 % copper [Mae05, Win85, Yev22] and less than 10 % of each element such as lead, tin, iron, aluminum, SiO_2, Fe, graphite, Sn, Mn, MoS_2, and zinc [Kwa14, Mae05, Nau19, Win85]. During the manufacturing of sinter friction linings, the sintered friction lining and a binding agent in powder form are sprinkled directly onto the supporting steel plate and then sintered in a continuous furnace [Bac10]. This process ensures a strong bond between the carrier plate and the friction lining. A uniformly compacted friction interface exhibiting plane parallelism is achieved through pressing. In addition, pressing can be employed to introduce various groove patterns without the use of machining methods and to affect the sinter density and porosity [Hoe01]. Sinter friction linings are characterized by high thermal conductivity [Mae05, Mar09, Ort04, Rod60, Voe18, Yev22], high bearable contact pressure [Hoe01, Ort04], and good durability [Hoe01, Ort04, Yev22]. Given these properties and the relative disadvantages in terms of comfort compared to paper-based and carbon friction systems [Mae05, Voe20a], sinter friction systems are commonly utilized in industrial gearboxes and commercial vehicles [Nau19, Voe20a]. Ankur [Ank21] and Kwabena [Kwa14] demonstrate that material properties can be optimized during manufacturing through compaction pressure, sintering temperature, and sintering time. The influence of different fibers on the mechanical and tribological properties of a semi-metallic copper friction material

is investigated by Ho et al. [Ho05]. Copper and brass fibers significantly enhance the strength of the friction material. According to Guha Keshav et al. [Guh21], strength and hardness can also be improved by the addition of steel fibers and fly ash. Celebi Efe et al. [Cel12] study the mechanical properties of copper enhanced by SiC particles in the matrix. Their results show that composite hardness increases with the number of particles and particle size.

Paper Friction Lining:

Paper friction linings are classified as organic friction linings [Ing10c]. The name refers to the manufacturing process, which is similar to that of paper production [Ing10c]. The individual components of the lining (fibers, fillers, and chemicals) are first dissolved in water, dried, impregnated with a resin as a binder, and cured [Ing10c]. Typical fibers of interest include cellulose fibers [Chi01, Hoe01, Ito98, Mae05], synthetic fibers [Hoe01, Ito98], aramid fibers [Ing10c, Kea97, Win85], basalt fibers [Ing10c], glass fibers [Sit07, Win85], and cotton fibers [Gao02a, Kea97, Mae05, Win85]. Given the comparatively high thermal stability for an organic resin material of > 300 °C [Kea97], the mechanical strength, and the chemical stability against a wide range of solvents, a phenolic resin [Hoe01, Ing10c, Ito98, Kit94, Nau19, Win85, Yag15], a modified phenolic resin [Ing10c], or a cresylphenolic resin [Ing10c, Win85] is usually used for preparing the composite [Sit07]. The elastic and porous paper friction lining resulting from the fiber braiding is finally applied to a mechanically stabilizing carrier plate [Sit07]. Paper friction linings are characterized by a high load limit, good friction behavior (i.e., high dynamic coefficients of friction and good friction characteristics), and thus no friction oscillations [Voe20a, Wag93]. Clutches with paper friction linings offer favorable clutch comfort characteristics and are widely used in the automotive sector [Voe20a]. A variety of fillers, such as diatomaceous earth [Ing10c, Ito98], clay [Ing10c], silicone particles [Ing10c], cashew dust [Ing10c], barite [Ing10c, Win85], calcium carbonate [Ing10c], graphite [Ito98, Kea97, Nak97, Sit07, Wag93, Win85], SiO_2 [Acu16a, Sit07], Al_2O_3 [Acu16a, Kea97, Sit07, Win85], FeS [Sit07], ZrSiO, copper particles [Acu16a, Sit07], mineral wool [Sit07], and activated carbon [Ito98], are used to improve friction stability, coefficient of friction, and curing of the lining. The negative aspects of paper friction linings include their low-pressure stability [Bru91] and high wear [Fei15, Ran04, Wag93].

Carbon Friction Lining:

Carbon friction linings are also classified as organic friction linings and are composed of a matrix material, one or more fiber materials, and, in some cases, fillers and friction modifiers [Awa05, Foe15, Sat06]. Carbon fibers are used as reinforcement due to their remarkable properties, such as self-lubrication, chemical inertness, high strength, high Young's modulus, and excellent thermal stability [Che20, Kea97, Omr15, Wan18, Wu20]. The carbon fibers for such linings are usually based on polyacrylonitrile, whereas pitch fibers and rayon fibers are niche products [Hua09, Ran04, Sto21, Sto23]. Besides carbon fibers, additional fiber types are added to non-woven carbon friction linings in order to reduce cost and improve friction properties. Aramid fibers [Ler19, Sto23, Wen16c], basalt fibers [Izi91], cellulose fibers [Nic95], glass fibers [Nar93] and acrylic fibers [Cro93, Eva90] are mentioned in the literature. Polymer materials are used as matrix materials that have an excellent strength-to-weight ratio and outstanding tribological properties [Wu20]. Typical engineering examples include thermoplastics such as polyamide [Kuk99, Kum16], polybutylene terephthalate [Lin18], polycarbonate [Lee01, Mer05, Zha18b], and polyetheretherketone [Bij15, Guo17]. These materials are primarily semi-crystalline polymers with a low glass transition temperature [Wu20]. Phenolic [Ahm19, Fei12] and epoxy [Lee06, Sur10, Zho09] are usually chosen as

thermoset matrix materials. Given its high mechanical strength, hardness, and good chemical resistance, epoxy is the most commonly used matrix material in applications [Wu20]. The carbon friction linings currently available on the market can be divided into woven and non-woven categories based on their design principle [Acu16a, Aug12, Bac13, Jon13, Ran04, Sto23]. Non-woven friction linings include paper-based friction linings reinforced with carbon fibers and particles (known as composite carbon) [Old06, Ran04, Wen16b] and two-ply carbon friction lining [Gro21b, Jon13, Ran04, Sto21]. Woven friction linings are divided into woven carbon fiber reinforced plastic (CFRP) [Fei12, Liu12, Su06a, Yan22] and woven carbon fiber reinforced carbon (CFRC) [Gib89, Kal16, Nag14, Sto21, Zha09c], based on the matrix.

Composite carbon friction linings are manufactured using a process similar to that of paper friction linings. Specifically, they are made from a single-layer resin matrix with fillers and non-directional fiber reinforcements [Acu16a, Foe15, Sto23]. The properties of composite carbon friction linings closely resemble those of paper friction linings. They typically offer good frictional behavior regarding shifting comfort, but their compressive stability is limited [Acu16a]. Foege et al. [Foe15] and Kearsey [Kea97] provide further details on the manufacturing process of composite carbon friction linings.

Dual-layer friction linings consist of a base layer and a friction layer. The base layer is typically an aramid fiber-reinforced thermosetting resin, with the aramid fibers being dispersed in the resin in an undirected manner [Acu16a, Ran04]. The friction layer comprises finely dispersed carbon particles of small size (about 20 ... 100 µm), which are bonded to the resin during the curing of the base layer [Acu16a]. The advantages of dual-layer friction pads lie in their cost and friction level stability, although they exhibit poorer wear behavior and compression stability compared to other carbon friction linings [Ran04].

Woven friction linings consist of fiber fabrics impregnated with resin and are typically composed of polyacrylonitrile fibers [Jon13, Kum22]. The impregnation rate of the resin exerts a decisive influence on the stability and porosity of the lining and must strike a compromise between both objectives [Acu16a, Wen16b, Wu20, Zha05]. Depending on the matrix, a distinction is made between carbon fiber reinforced plastic (CFRP) and carbon fiber reinforced carbon (CFRC). Carbon, when serving as a matrix material, can enhance the friction lining's temperature resistance [Foe15, Gib89, Gro21b, Ran04] and thermal conductivity [Che20, Kea97].

In general, carbon friction linings merge the advantages of paper and sinter friction systems, boasting excellent wear behavior, temperature resistance, friction behavior, noise behavior, and pressure stability [Ahm19, Awa05, Fei12, Fei15, Gib89, Luo16a, Old06, Ran04, Voe20a]. Their only drawback, when compared to other friction lining variants, lies in cost [Kea97, Ran04, Voe20a]. Given these performance characteristics, one typically uses carbon friction linings in aerospace, motorsports, commercial vehicles, and automotive applications [Acu16a, Awa05, Gib89, Iva09, Nag14]. To further refine frictional properties [Wan19a, Wan15, Zha05], wear resistance [Su06a, Wan19a, Zha05], and adhesion properties between fibers and matrix [Su06a, Wan19a, Zha05], various chemical pretreatments are conducted on the fibers, and fillers as well as nanoparticles are incorporated into the matrix material. The typical fillers for carbon friction linings comprise nano-$CaCO_3$ [Su06a], nano-SiO_2 [Su06a], nano-TiO_2 [Su06a], carbon nanotube [Ala17, Ues16, Wan19a, Wan15], nano-ZnO [Zha05], nano-SiC [Zha05], POLYFLUO® 150 wax [Zha05], and boron nitride nanoplates [Ues16]. In order to improve the adhesion with the matrix material, the fibers can be pretreated with nitric acid or aqueous hydrogen peroxide [Nak17, Pit97, Wan19a].

2.1.5 Friction Characteristics and Model Conceptions of Boundary Layers

The friction behavior plays an essential role in the safe operation and shifting comfort of a wet clutch. Due to the importance of friction characteristics for clutch performance, this section explains the basic concepts, model conceptions of boundary layers, and various influencing factors.

The German Society for Tribology (Gesellschaft fuer Tribologie e.V. (GfT)) [GFT02] defines friction as an interaction between material areas of bodies that are in contact and counteract a relative movement. The bodies consist of substances that can be solid, liquid, or gaseous [GFT02]. According to Fleischer [Fle72], friction is the loss of mechanical energy at the start, during, and at the conclusion of a relative motion between material areas in contact. Thus, friction is invariably related to motion, including static friction. Although there is no macroscopic change in the position of the bodies in the case of static friction, microscopically, a distance is traversed in the adhesive interface due to material expansion [Bar01]. Depending on the state of motion, friction can be divided into static, dynamic, and starting friction [GFT02]. Depending on the affiliation of the material areas engaged in the friction process, external and internal friction can be present [GFT02, Bar01]. External friction occurs when the areas of material in contact are parts of different bodies, whereas internal friction occurs when the materials in contact belong to the same body [GFT02, Fle72].

Furthermore, multiple friction states can be distinguished, depending on the aggregate state of the substances involved [GFT02, Dec18, Wit21]. Solid friction is the friction between or within areas of material with solid-state properties [Czi20, Wit21]. Thus, solid friction can occur as external friction caused by adhesion between different regions of matter, and internal friction caused by deformation within a matter region [Bar10a]. If material areas in contact are covered by a solid boundary layer (e.g., an oxide layer), this is referred to as boundary layer friction. If, however, the boundary film is very thin (e.g., an adsorption layer), this is termed boundary friction [Bar10a]. Hydrodynamic friction is the internal friction in a material region exhibiting liquid properties, and gas friction is the internal friction in a material region exhibiting gas properties [Czi20]. Mixed friction describes any mixed form of the friction states mentioned above [Bar10a], but most commonly refers to the simultaneous presence of solid and hydrodynamic friction [GFT02, Nie19, Wit21]. In the case of friction clutches, Pflaum [Pfl88] assigns typical friction coefficient values to various friction states, including boundary friction, mixed friction, and hydrodynamic friction. Furthermore, Pflaum [Pfl88] and Winkler [Win08] show that hydrodynamic load components do not significantly impact the frictional behavior of clutches, and that primarily boundary friction prevails. Stribeck [Str02] investigates the frictional behavior of hydrodynamic plain bearings and presents a suitable representation of the various frictional states of a lubricated tribological system, as a function of macro- and microgeometry, lubricant, and operating conditions (see Figure 2.6). According to Stribeck [Str02], the coefficient of friction can be plotted against the rotational speed, sliding speed, or a parameter variation of the viscosity, the sliding speed, and the load. The load and viscosity must remain constant in a representation using sliding speed or rotational speed. The condition of hydrodynamic friction, occurring at high sliding speeds, is sought-after mainly in plain bearings due to low friction losses and low-wear operation. As the sliding velocity decreases, a transition from hydrodynamic to mixed friction occurs. With a further reduction in sliding speed, a friction minimum is reached in the mixed friction area. This friction minimum exists in the area of mixed friction because, in the case of initial solid body contacts, the external load is still largely supported by the hydrodynamic load-bearing force. Boundary friction remains minimal in this

case. Given the decrease in hydrodynamic friction at a decreasing sliding velocity, the sum of the fluid and boundary friction acts to further reduce system friction. Boundary friction dominates mixed friction on the left side of the minimum. Since the highest coefficients of friction are realized in this area, it represents the desired friction condition for friction clutches [Acu16a, Pfl88, Win08]. Typically, the maximum coefficient of friction is obtained at a sliding speed of zero. [Bar01, Bar10a, Czi20, Str02, Wit21]

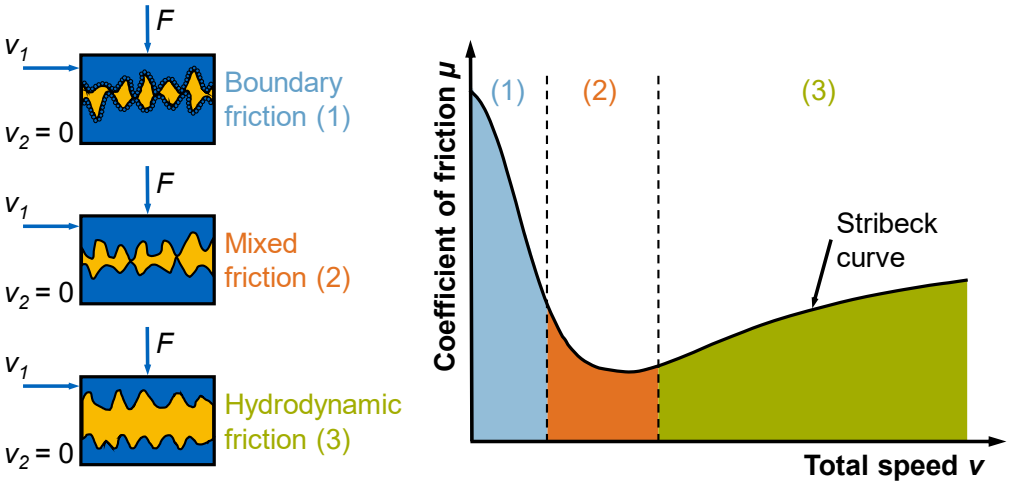

Figure 2.6: Friction conditions of a hydrodynamically lubricated radial plain bearing inspired by Wittel et al. [Wit21] based on the model of Stribeck [Str02].

In the case of solid friction, the friction and wear behavior is significantly determined by the structure and properties of the formed boundary layers [Bar10a]. In addition to the term “boundary layer”, terms such as “tribological layers” [Ina00] or “tribomutation” [Keh98, Keh99] are also mentioned in the literature. The interaction of the lubricant and the ambient medium with the surfaces of the contact partners significantly alters the zones close to the contact surfaces [Loh16]. A model of the boundary layer structure of synchronizers is presented by Winkler [Win08] (see Figure 2.7) and is extended by Tomic [Tom09]. According to Voelkel [Voe20a], this model can be applied universally to the application of wet multi-plate clutches and is also described by other researchers, such as Eguchi et al. [Egu01], Layher [Lay11], and Ingram et al. [Ing10b]. The boundary layer is divided into an outer and an inner boundary layer. In the case of metals, the inner boundary layer consists of a manufacturing-related or tribologically induced deformation or strengthening zone and may have an element composition and concentration different from that of the base material [Bar01]. The outer boundary layer typically has a composition different from the base material and may consist of oxide layers, adsorption layers, and impurities [Czi20]. In the case of lubricated contact, the formation of tribologically favorable boundary layers can be promoted by layer-forming additives added to the base oil [Bar10a, Loh16]. The effect of these additives is rooted in interaction processes with the surfaces. In this process, adsorption layers and reaction layers can form as a result of the reaction of the additives or their components with the solid surface [Bar01, Bar94, Bar10b]. Meyer [Mey84] categorizes additives into groups that modify the physical properties of lubricating oils (e.g., viscosity index improvers), the chemical properties of lubricating oils (e.g., antioxidants), and the properties of contact surfaces (e.g., extreme pressure additives). The effectiveness of the additive depends on the reaction’s activation energy, surface temperature, additive concentration, base lubricant, and the chemical- physical properties of the solid [Bar01, Bar94, Win08]. In experimental studies of automatic transmission fluids, Farfán-Cabrera et al. [Far15] highlight the need for additives

such as anti-wear agents, antioxidants, detergent dispersants, and friction modifiers for use in clutches. In particular, the need for detergents or dispersants used to avoid glazing the friction material of clutches is elaborated upon.

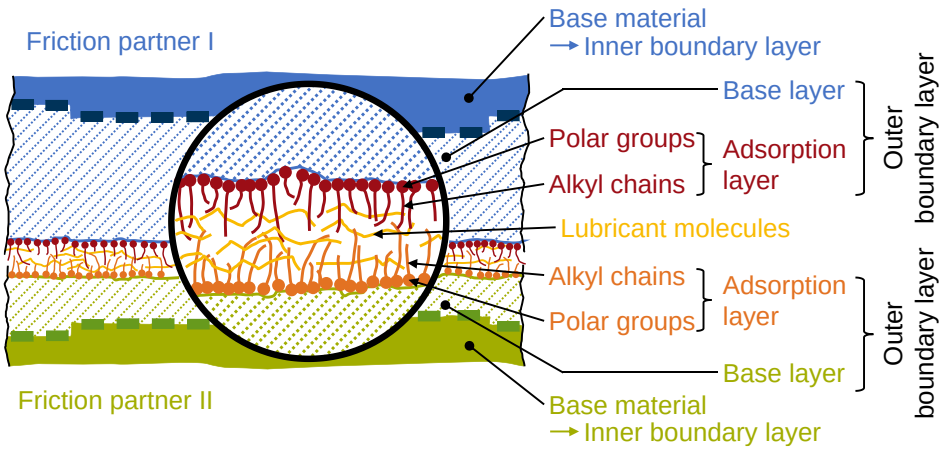

Figure 2.7: Boundary layer of a friction-loaded contact (based on Winkler [Win08]).

Ingram et al. [Ing10a] investigate the effect of a range of additive solutions on friction as a function of sliding speed. Succinimide dispersant and sulfonate detergent additives cause an increase in friction above that of the base oil at medium to high sliding speeds. Over-based and neutral detergents exhibit almost identical friction curves. These results indicate that a calcium carbonate film is deposited on the steel friction surface when an over-based detergent is present. However, this outcome does not influence friction since the alkyl group of the sulfonate controls it. Friction increases with sliding speed when using long-chain surfactant additives such as fatty acids and amines, as well as commercially available organic friction modifiers. A number of ATF base oils comprising various friction modifiers, e.g., a fatty amide friction modifier and calcium detergent combination, are studied by Zhao et al. [Zha12]. The results of the post-test surface analysis are linked to the friction performance in order to investigate the friction-modifying mechanisms of the additives. The fatty amide in the formulations is essential for anti-shudder performance because it provides low friction at low speeds. The results of surface analysis (XPS, ToF-SIMS and ATR FT-IR) show that the friction modifiers significantly affect the tribofilm composition.

2.2 Damage Mechanisms

Wet multi-plate clutches are subjected to high loads, which can be divided into mechanical (e.g., pressure, sliding speed) and thermal (e.g., surface temperature, cooling behavior) loads. These loads not only influence the frictional behavior but also alter and damage the friction system. Various damage mechanisms are known for wet multi-plate clutches. These damage mechanisms can be subdivided into spontaneous damage and long-term modifications, according to their temporal characteristics. Whereas long-term modifications occur due to a continuous change in the friction system over several shifting operations, up to tens of thousands, spontaneous damage occurs within just a few individual shifting operations.

2.2.1 Long-Term Damage Mechanisms

Long-term damage to sinter friction systems is discussed in the literature, including wear, changes in friction behavior, and clogging of the friction lining [Gon15, Nym06, Wim05, Xia20, Zho19]. Determining the causes of such phenomena is the subject of numerous research projects. Wimmer [Wim05] investigates the damage behavior of sinter friction materials in load collectives. The coefficient of friction level of sintered metallic linings depends on the friction

work and the peak temperature at the friction interface. Increasing loads lead to a smoothing of the friction lining and to decreasing coefficient of friction. Yao et al. [Yao07] investigate the properties of the worn surface of Cu-based powder metallurgical brake materials after machining under operating conditions. The worn surface is divided into three zones, depending on the degree of destruction of the friction film: a heavy wear zone, a light wear zone, and another light wear zone. Grain wear and fatigue wear are the main mechanisms of severe wear. Abrasion is the primary mechanism of the mild wear zone, where the friction film regenerates. The light wear zone results from the regeneration of the friction film on the mild wear zone. Gong et al. [Gon15] investigate Cu-based wet friction clutch wear behavior using a ring-on-ring test. A wear diagram for Cu-based friction material under oil lubrication conditions is proposed and linear equations are developed to mark the transition boundaries between different wear regimes. The predominant wear mechanisms of the copper-based friction material in the ultra-mild wear range include plastic deformation and microplowing. Abrasive wear occurs in mild wear, and delamination and abrasive wear are involved in severe wear. Fatigue and oil wedge aggravate the delamination wear of friction material in heavy wear conditions. Zhou et al. [Zho19] establish friction and wear maps of copper matrix composites, demonstrating that the friction materials exhibit a stable high coefficient of friction and low wear rates at an iron volume content of between 10 % and 15 %. According to the wear mechanism map, adhesion is the primary wear mechanism for low iron content (≤ 5 vol.-%) and low brake energy density. At the same iron content, severe plastic deformation is observed at a high brake energy density (> 38 J/mm^2). Plow wear is observed at moderate brake energy density (8-30 J/mm^2). Oxidation-delamination wear is the main wear mechanism at moderate iron content (5-15 vol.-%) and high brake energy density (> 25 J/mm^2). At high iron content levels (≥ 15 vol.-%), delamination is identified as the predominant wear mechanism, especially when the braking energy density exceeds 30 J/mm^2. Xiong et al. [Xio07] used an experimental approach to study how Fe and SiO_2 components affect the friction and wear characteristics of Cu-based materials. However, the Fe and SiO_2 effects on the abrasion properties are very complex. Moderate iron content reduces wear, especially wear at high speeds. SiO_2 effectively improves the frictional resistance at high speeds and increases the wear loss at low speeds. The wear mechanism of Cu-based brake pads is investigated by Xiao et al. [Xia20]. Oxidation, delamination, and spallation are the dominant wear mechanisms. The results demonstrate that a ~2 µm thick nanostructured tribolayer of CuO and Fe_2O_3 is formed on the worn surface due to plastic deformation, mechanical mixing, oxidation, and sintering. Due to its oxide-based composition and high hardness, the tribolayer enables a much higher coefficient of friction and wear resistance than the original surface. Debris settles in the pores, causing the friction interface temperature to rise further. The influence of changes in the topography of the sintered friction material on the frictional characteristics of wet clutches is investigated by Nyman et al. [Nym06] using an experimental method. Characterizing the topography makes it possible to predict the remaining service life of a sintered friction material in a wet clutch. Hensel [Hen14] proposes a characteristic value for the description of the thermal load of clutches for load shifting, which allows a correlation of the damage with the thermal load. It is demonstrated that various damage mechanisms exist, depending on temperature level and cooling. Yu et al. [Yu19b] compare the wear mechanisms of copper and paper-based friction materials and determine that the wear depth increases dramatically with increasing ambient temperature. Both the coefficient of friction and the wear depth of the Cu-based friction material are much larger than those of the paper-based friction material. The variation of the wear mechanism causes the failure of Cu-based friction material. Given a gradual deterioration of

working conditions, abrasive wear, furrow wear, adhesive wear, and peel wear occur successively in Cu-based friction material. In addition, the failure of paper-based friction lining is associated with the wear of the fibers and the softening and decomposition of the resin, resulting in a much smoother surface.

According to the literature, adhesive wear and thermal degradation are the main causes of long-term modification in paper friction systems [Gao02a, Nym06, Omp13, Omp15]. Adhesive wear occurs when a friction material slides against the mating surface, thus forming abrasive particles due to the removal of the weakest surfaces by the mechanism of plastic deformation [Omp15]. Thermal degradation occurs when the temperature at the interface is relatively high, as a result of which the carbonization process of the cellulose fiber and resin content in the friction material occurs [Omp15]. The two damage mechanisms change the surface topography [Gao02b, Nym06, Omp13], resulting in an increase in the actual contact area [Gao02a, Ing10c, Kim05, Omp13], and the mechanical and physical properties change [Chi01, Mae03, Mat95, Omp13]. Ompusunggu et al. [Omp10] demonstrate that these two phenomena influence the shear strength of the friction lining. Maeda and Murakami [Mae03] link the shear strength reduction to fiber carbonization and the influence of additives (detergent and dispersant components). Chiba [Chi01] confirms the influence of the lubricant, but considers the shear strength reduction to be the result of pore growth. As the size of the pores increases, the resin bonds between the fibers are weakened. Ost et al. [Ost01] investigate the friction and wear behavior of paper-based wet clutches in both SAE #II [Aut12a] and pin-on-disk tests, analyzing the influences of material parameters and operating conditions on the coefficient of friction and wear rate. However, the pin-on-disk tests cannot accurately reflect friction material wear because they cannot reproduce the same thermal conditions as the SAE #II tests. Although this limits the validity of the data obtained using the pin-on-disk test in terms of the influence of contact pressure on wear rate, it can be concluded that the wear rate of the friction material increases with the increasing hardness of the separator plate. Lingesten et al. [Lin12] describe a two-stage wear rate phenomenon using a specialized test rig equipped with multiple sensors, which enable the continuous measurement of temperature, gearbox torque, speed, and friction lining wear rate. The test results demonstrate a two-stage wear phenomenon with a clear transition from an initial low wear rate to a much higher rate after a certain number of engagement cycles at a high power input (see Figure 2.8). Yang et al. [Yan98, Yan97] perform thermogravimetric analysis in a study used to quantify the change in a cellulose weight ratio in a friction material during use. The strong influence of thermal effects on weight and friction material properties is demonstrated. Based on this finding, the authors propose a useful degradation model for characterizing material behavior as a function of the use cycle. Its applicability, however, faces difficulties in explaining the two-stage wear behavior suggested by Lingesten et al. [Lin12]. Calcut et al. [Cal04] and Sarkar et al. [Sar04] develop an empirical degradation model to predict the service life of an automatic transmission fluid (ATF). The flexible service life model enables either predictive or real-time end-of-life calculations under various

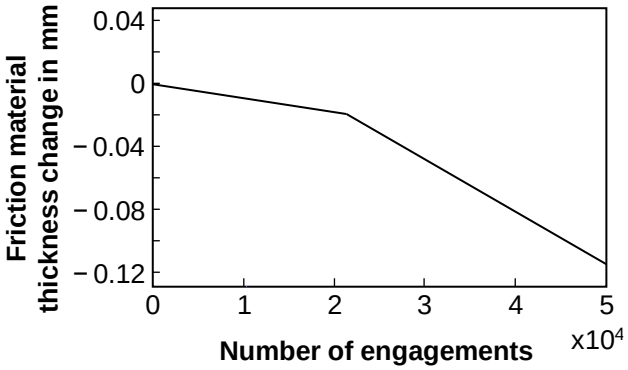

Figure 2.8: Schematic representation of the two-stage wear model based on Lingesten et al. [Lin12].

transmission design strategies and customer driver behavior, as reflected in operating temperatures, shift characteristics, fluid volume, and fluid distribution throughout the transmission. A methodology for the classification of friction linings in friction clutches is presented by Graswald [Gra07]. After a preliminary selection, potentially suitable friction linings are analyzed in detail using a statistically planned experimental program. The calculation model for the service life of the friction linings obtained simultaneously with this analysis can be used for service life prediction, and therefore for designing friction clutches. The service life under collective loading can be estimated with the aid of a damage accumulation hypothesis, with the fundamental criterion being wear. Research on the damage of organic friction linings by Maeda and Murakami [Mae03] shows a high level of correlation between the clogging of porosity and the decrease of the coefficient of friction at high sliding speeds. Visually, this phenomenon is manifested by a smooth and shiny surface, indicating that the friction material loses its porosity due to the deposition of debris particles. Based on the experimental results, it is thought that improving the high-temperature detergency of ATFs can inhibit the blocking of wet friction material pores, thereby extending the material service life. Damage to the friction material of wet clutches caused by deposits of lubricant degradation products on the friction material surface is described as glazed by Newcomb et al. [New06]. According to Blau [Bla05] and AbuBakar [Abu08], this phenomenon is also observed in dry-running brakes. In the latter case, the glazed surface in the friction material is formed by dirt debris bound by decomposed organic compounds. The term “glazing” should thus describe a smooth and shiny film on the friction material surface formed by dirt particles bound to decomposed organic compounds, which may result from a combination of adhesive wear and thermal degradation of the friction material or/and the deposition of ATF degradation products [Omp15]. Vernersson et al. [Ver12] observe a temperature dependency of the wear rate of organic friction linings in their experiments. According to these experiments, the wear rate increases significantly above 500 °C surface temperature, whereas it increases only very slightly before this level. Hensel [Hen14] conducts comprehensive research on long-term damage behavior under load shifting with organic friction systems. The development of a life test methodology enables the identification of performance limits under short-term loading and the assessment of long-term damage under sustained and cumulative loading. Research by Hensel [Hen14] demonstrates that, with regard to organic paper friction linings, in addition to the peak friction surface temperature, the temperature-time collective at the friction interface, e.g., rapid or slow cooling, influences the damage behavior and also the coefficient of friction characteristics. Osanai [Osa90] establishes a relationship between deterioration of the friction characteristics, carbonization of the friction lining, and thermal stress. Increasing peak friction surface temperature increases damage to the friction lining, resulting in less favorable friction behavior. Cho et al. [Cho18] experiment on the wear properties of two different types of paper-based wet friction materials, one with and one without carbon fibers, using a pin-on-reciprocating plate tribotester. The wear properties are quantified based on Archard’s [Arc56] wear law by comparing confocal microscope images of paper-based friction materials before and after the tests. Higher wear rates are observed with increasing normal force and sliding velocity. It is also found that the wear rate of the paper-based friction material without carbon fibers is lower than that with carbon fibers, by a factor of 1.3 – 2.7. In addition, the carbon fibers are broken into pieces of smaller lengths by the sliding contact, which may contribute to the wear progress. The carbon fibers can also cause significant abrasive wear on the counter surface.

Typical long-term changes in carbon friction systems include clogging of the friction lining with oil-cracking products and wear particles, abrasive wear, adhesive wear, fiber breakage, and

matrix degradation [Acu16a, Ran04, Sto23, Su06b]. Rank and Kearsey [Ran04] perform a life test with three different carbon friction linings. All of the friction linings investigated exhibit low wear rates and high coefficient of friction. In addition, the lubricant influence on the coefficient of friction is considered to be low, which is also confirmed by Stockinger [Sto23]. Acuner [Acu16a] demonstrates smoothing of the surface via experimental tests due to clogging of the coating pores over the test period. The load parameters and the thermal stability of the lubricant and its additives influence the strength of the clogging. EDX analyses detect sodium, sulfur, phosphorus, and zinc in low-reference oil and show increased calcium, sulfur, and phosphorus deposits in high-reference oil. These elements are typically used in additive components of the lubricant. In contrast to research performed by Weber and Poll [Web15], the deposits are more chemically resistant. Not even the cleaning procedure before the SEM measurements is able to remove them [Acu16a]. Acuner [Acu16a] demonstrates, based on experiments with model fluids in the component test rig and subsequent SEM/EDX analyses, that the detergent additive (over-based calcium sulfonate) is significantly responsible for the formation of deposits, and that the dispersant additive (succinimide) tends to inhibit deposits. It cannot be clarified whether the detergent decomposes due to high temperatures and accumulates in the friction lining or binds other cracked oil constituents and adheres with them in the friction lining. Fei et al. [Fei12] investigate the effect of phenolic resin on friction and wear behavior using four carbon fabric-reinforced phenolic resin composites produced by impregnation friction materials. The carbon fabric/phenolic resin composites have excellent wear resistance and do not damage the steel plate. Based on the study, the optimum phenolic resin content of carbon fabric/phenolic resin composites is 25 % by weight, considering the coefficient of friction, friction stability, and wear resistance. Decomposition and micro-decomposition of the resin are the primary wear mechanisms for the sample with resin content above 25 wt%. Micro-cutting, fracturing, and removing carbon fibers, together with the formation of tiny debris on the surface, seem to be the predominant wear mechanism for the low resin-content friction materials. The results by Su et al. [Su06a], Wang [Wan10], and Wag et al. [Wan15] are thereby confirmed in addition to observing fiber breakage and carbon fibers tearing out of the matrix. Su et al. [Su06a] also demonstrate an increased temperature dependence of the wear rate for carbon friction linings since, at temperatures above 240 °C, the adhesive resin is degraded or decomposed and loses its ability to bind the carbon fibers. Wu et al. [Wu20] investigate polycarbonate and epoxy resin-based composites reinforced with staple fiber fabric and different amounts of impregnating resin. The primary factor influencing the specific wear rate is the degree of resin impregnation. The partially impregnated composites have a lower specific wear rate than fully impregnated composites. Finally, the main wear mechanisms identified for poly-carbonate-based composites are abrasive, adhesive, and fatigue wear. Conditions for the above wear mechanisms include matrix wear, plastic flow, resin drag fracture, resin crush deformation, plow fracture, fiber/matrix debonding, and fiber breakage. Regarding epoxy-based composites, the main wear mechanisms are abrasive wear and fatigue wear. Mainly micro-cutting fracture, plowing fracture, fiber/matrix debonding, fiber breakage, and crushing fracture are observed thereby. Wenbin et al. [Wen16b] compare three carbon friction linings partially filled with carbon fiber powders to improve the weak interfacial bonding between carbon fabric and phenolic matrix. The damage to the friction linings is analyzed and compared with the aid of SEM images. The main wear mechanisms are matrix cracking and fiber breakage caused by bending the fibers. Fiber breakage caused by abrasion debris is also observed. Lehua et al. [Leh18] investigate the effect of MoS_2 on carbon fabric composite wear and friction behavior under wet load shifting

conditions. SEM images are used to demonstrate the damage forms of fiber breakage, fiber cracking, and fiber-matrix debonding in the case of friction lining and pitting on the mating friction surface. The wear mechanism starts with the loading of the fibers by the vertical pressure and friction force of the counterpart during the friction phase. The fibers tear and detach due to high shear stress. At the same time, the high temperature caused by the friction significantly reduces the strength of the material, resulting in the flaking of the resin matrix and the reduction of wear resistance, known as adhesive wear. Strongly adherent fibers are gradually worn down and thinned out by wear until they finally break. The detached resin matrix and fiber breakage act as a third body and cause the onset of abrasive wear. The MoS_2 filled into the composites produces corrosive substances through a tribochemical reaction during friction, which leads to pitting on the mating surface. Wenbin [Wen15] investigates the mechanical and tribological properties of carbon fabric/phenolic composites with different weave filament counts. Both composites exhibit similar wear behavior, starting with adhesive wear at the beginning of the test and abrasive wear in the late phase. Wear abrasion (including resin abrasion, fiber abrasion, and metal abrasion) occurs first. The resulting abrasion then begins to plow through the contact surface, and bending, breaking, and tearing of fibers occur. As a result, the tearing of the fibers and the deposition of debris lead to the appearance of cavities in some places. At the same time, the steel counter friction plate smooths out during the process of the test. SEM images show that fiber-matrix debonding and cavity formation dominate for the composite with a lower weave filament count. Severe fiber bending and excessive fiber breakage are observed in the composite having a large number of weave filaments. Changes in the frictional behavior and wear mechanisms of carbon fiber composites under oil-lubricated conditions during load shifting throughout their service life are systematically studied by Fei et al. [Fei16]. The combination of adhesive wear, abrasive wear, and thermal degradation is considered to be the primary wear mechanism under oil-lubricated conditions throughout the service life. Different wear characteristics are described in parallel and perpendicular directions of the surface. The fibers aligned in the parallel direction undergo continuous polishing, leading to instances of fiber breakage and fragmentation. In the perpendicular direction, the fibers undergo polishing and cutting.

2.2.2 Spontaneous Damage

Spontaneous damage occurs within a few shifts and can be attributed to high mechanical and thermal loads [Sch19]. According to Strebel [Str17] and Schneider et al. [Sch19], spontaneous damage can be subdivided, depending on the friction material pairing. Hot spots and hot bands have been demonstrated for organic friction linings with metallic counter friction plates. The typical damage form for metal-on-steel friction pairs is adhesive wear and seizure (see Figure 2.9), which is often referred to as sinter carryover in the literature [Pfl98].

Snima [Sni06] discusses the performance limits on wet multi-plate clutches for sintered metal friction linings under continuous slip loads. Adhesive wear occurs at surface temperatures above 250 °C, associated with sinter carryover. The existing boundary layers produced by lubricant additives and the friction materials are removed during this process. Atomic bonds (micro-welds) form, especially at the plastically deformed micro-contacts between the steel plates and sintered linings. This process is attributed to the oil film breakdown and thermal and mechanical overload. The temperatures achieved in the experiments usually range between about 230 °C and 250 °C, thus reducing the proportion of hydrodynamic friction and the kinematic viscosity of the cooling oil. A temperature flash occurs as a result of the momentary local solid contact with coupled surface welds. The welds are immediately torn open in the

process, flecking the steel plate and leading to coefficient of friction peaks over time. Pfleger [Pfl98] systematically describes the damage form of sinter carryover for wet multi-plate clutches in load-shifting applications and divides them into three classes. Depending on the coefficient of friction increases caused by the seizure of the friction material and the steel plate, a distinction is made between light, medium, and heavy sinter carryover. Accordingly, light sinter carryover requires coefficient of friction peaks of up to 15 %, whereas heavy sinter carryover is characterized by an excess coefficient of friction of at least 30 %. Medium sinter carryover moves between the two levels. In addition, the area affected by the sinter carryover can be included in the evaluation. The sinter carryover caused by the thermal overload also clogs the pores of the friction plate, thus confirming the results of Duminy [Dum79]. Duminy [Dum79] investigates the damage behavior of wet multi-plate clutches during load shifting using the friction pair of steel and sintered bronze. The damage patterns for spontaneous damage include wear, clogging of the lining pores, cracking the lubricant, sinter carryover, and buckling of the steel plate. The failure criterion is the buckling of the steel plates (inversion of more than 0.1 mm). Schneider et al. [Sch19] initially distinguish between the damage patterns of discoloration of the steel plate and sinter carryover in the case of load shifting of metallic friction systems (see Figure 2.9). These damage patterns are further divided into the categories of large-scale and localized damage. A coefficient of friction increase of at least 20 % is specified as a failure criterion. With the aid of thermal simulations, Schneider et al. [Sch20a] show that the calculated maximum temperatures lie between 200 °C and 250 °C when recognizable sinter carryover occurs. In further studies, Schneider et al. [Sch20b] investigate the frictional behavior of pre-damaged multi-plate clutches during load shifting. For this purpose, three clutches are pre-damaged at different intensities so that spontaneous damage (local discoloration, sinter carryover) occurs. All of the pre-damaged clutches pass the endurance test, and the local discoloration and sinter carryover are no longer visible after the endurance test. In addition, there is a correlation between the intensity of the pre-damage and the coefficient of friction at the beginning of a shifting process. It is evident that the greater the pre-damage, the lower the coefficient of friction at the beginning of a cycle.

Figure 2.9: Local discoloration and sinter carryover on the steel plate for sinter friction systems [Sch20a].

Regarding friction systems with organic friction linings, Strebel [Str17] and Schneider et al. [Sch19] distinguish between locally limited, circular to elliptical, black discolorations, also called hot spots (see Figure 2.10). They also describe large areas of black discoloration, known in the literature as hot bands [Gra12]. Moreover, they make a distinction between hot spots with an increase in thickness less than or equal to 0.05 mm and those with an increase greater than 0.05 mm, using this distinction as a failure criterion. Schneider et al. [Sch21c] also perform endurance tests for organic friction elements with pre-damaged clutches (slight discoloration, severe local discoloration, and local thickening). It is demonstrated that several thousand shifts can still be performed using severely damaged plates. In contrast to local thickening, local discolorations become no longer visible after the test. A deterioration of friction behavior is observed. Distinctions for paper friction systems in load shifting, similar to those made by Schneider et al. [Sch19], are also made by Graf and Ostermayer [Gra12], Mann et

al. [Man21], and Panier et al. [Pan04b], who distinguish between hot spots and hot bands. In this context, hot bands refer to an inhomogeneous temperature distribution in the radial direction, and hot spots refer to a strongly distorted temperature field in the circumferential direction. Hot spots are, in particular, the maxima of the temperature field and can be identified as single dark discolorations.

Figure 2.10: Local discoloration and local thickening on the steel plate for paper friction systems [Sch20a].

Pfleger [Pfl98] classifies hot spots according to the size of the individual hot spots as well as the affected area of the steel plates. Also considered is whether any plastic deformation of the steel plate is associated with the hot spot damage. Wimmer [Wim05] adopts Pfleger's [Pfl98] classification, showing that depressions are present on the steel plates affected by hot spots due to local material removal at previously highly loaded areas. As the specific friction work increases, the average depth of the depressions increases. The friction behavior deteriorates significantly when hot spots are formed. Anderson and Knapp [And90] provide a qualitative description of various types of hot spots based on research regarding friction systems of automotive applications. Local hot spots are described which exhibit elliptical to circular damage. These local hot spots are divided into critical and non-critical local hot spots. Only cosmetic interface changes are detected on the surfaces of the non-critical local hot spots, e.g., brown to blue discolorations, and temperatures of up to 300 °C are reached. There is no structural transformation in the steel plates. Critical hot spots are characterized by plastic deformation, cracks on the surface, and residual martensite. The resulting martensite increases the volume of the steel plate. Based on the microstructural transformation, it is determined that a temperature of at least 750 °C is required for the development of critical hot spots. Schneider et al. [Sch20a] use thermal experiments to identify the maximum temperature at which hot spots occur. It should be noted, however, that local effects cannot be taken into account with their simulation model, which is why a relatively wide temperature scatter band (480 °C – 710 °C) results for the organic friction systems. Haemmerl [Hae95] further measures depressions of up to 12 µm in the centers of hot spots, which are described as yellow-brown and partly blue areas. However, Haemmerl does not describe structural transformations. Hensel [Hen14b] observes black discolorations (hot spots) and local increases in thickness at random areas on the steel plates in organic friction systems. Microstructural examinations show that grain refinement has taken place in these areas. Kasem et al. [Kas11] also demonstrate by means of metallurgical experiments that, due to the temperature effect, grain refinements and microstructural transformations accompany hot spots at the corresponding areas. Moreover, plastic deformations of the surface are observed in areas affected by hot spots. These plastic deformations are explained as melting of the steel material due to high temperatures and high mechanical loads. In addition to the microstructure measurements, infrared camera measurements of brake disks made by Kasem et al. [Kas11] exhibit locally excessive temperatures close to the austenitizing temperature at the points where hot spots form. The plastic deformation of the steel surface observed by Kasem et al. [Kas11] during friction processes is described by Eleoed et al. [Ele99] as "tribological transformation of surface – TTS" and by Antoni et al. [Ant12] as "tribological surface transformation – TST". Like Kasem et al. [Kas11], Panier et al. [Pan04b] perform thermal

measurements using a high-speed infrared camera on TGV disk brakes in order to better classify and explain thermal gradients on the disk surface. First, hot bands form, then thermal gradients develop on hot bands before macroscopic hot spots finally appear. Panier et al. [Pan04b] differentiate with respect to the individual damage classes (asperity, gradients on hot bands, hot bands, macroscopic hot spots, and regional hot spots), depending on the parameters of size and thermal level. Mann et al. [Man21] also perform infrared thermography measurements and confirm the observations made by Kasem et al. [Kas11] and Panier et al. [Pan04b] regarding the formation and development of hot spots and hot bands. In their measurements, hot spots concentrate radially on two hot bands characterized by different diameters. Hirano et al. [Hir07] contribute to the state of the art with their division of hot spots into the categories of cosmetic and heavy. Cosmetic hot spots refer to mere discolorations on the friction surface, while severe hot spots are caused by plastic deformation of the steel plate. The transformation of the pearlitic or ferritic microstructure of separator plates into martensitic microstructure in hot spot areas is described, which is also confirmed by Abbasi et al. [Abb14]. Yang et al. [Yan13] observe cracking in the inner and edge regions of the hot spots. Crack growth occurs through the propagation of individual cracks and the connection of multiple cracks. Li et al. [Li14] investigate crack propagation behavior under various braking conditions and find that high braking energy can accelerate crack propagation.

Barber [Bar67] analyzes the formation of hot spots and attributes them to thermal deformation of the friction interfaces, although the description of the heat generation phenomenon is uncertain. Barber [Bar69] later explains that the formation mechanism of hot spots is thermoelastic instability (TEI). According to the explanation of TEI, uneven load or pressure distributions in the frictional contact, for which fine irregularities in the microstructure of the friction partners are the cause, lead to locally excessive heat input and therefore increased temperatures. Due to the thermal expansion of a friction partner, the local pressure increases even more. Hence, TEI represents a self-reinforcing instability that continues to increase unless it is damped externally (e.g., by wear). An initial local deviation from the nominal surface pressure can become self-reinforcing and lead to instability. This outcome depends on whether thermal expansion or wear becomes the dominant mechanism. According to Barber [Bar69], TEI is mainly a function of sliding velocity and contact pressure. However, TEI can be partially avoided by choosing suitable friction partners that have smaller coefficients of thermal expansion, or by having a ratio of thermal conductivities closer to one. Building on these results, Dow and Burton [Dow72] formulate a two-dimensional analytical description of the TEI problem based on the heat conduction equation. They derive a stability limit for the formation of TEI in frictional contact for a simplified model geometry with two semi-infinite planes and while neglecting wear. They assume that there is an initial temperature non-uniformity and that the system becomes unstable as soon as a critical value for the sliding velocity is exceeded. According to TEI theory, a critical temperature level is exceeded during the process, leading to the formation of hot spots. The original pin-disk model is extended by Dow and Burton [Dow73] to include wear, which has a damping effect on thermoelastic instability. The wear particles improve the temperature level by absorbing the heat and thus stabilize the system. Burton et al. [Bur73] further develop this model to take into account the influences of material properties, coefficient of friction, and sliding velocity. The analysis considers the stability limit behavior, both when the friction materials are identical and when one friction partner, such as glass, acts as a perfect insulator. The value of the critical sliding velocity decreases with increasing differences in the conductivity of the friction materials. Similar to research by Dow and Burton [Dow72], Lebeck [Leb76] investigates the instability of two rings

in rotating, sliding contact. An analytical model is developed to describe TEI, including both the operating point (i.e., contact pressure and sliding velocity) and the waviness of the friction interfaces. It is demonstrated that contact conductance, ring stiffness, thermal coefficient of expansion, sliding speed, friction, thermal conductivity, and geometry are essential parameters with respect to stability. Lee and Barber [Lee93] extend the friction-excited thermoelastic instability analysis made by Dow and Burton [Dow73] to the case of a finite-thickness layer sliding between two half-planes. This extension aims to evaluate the influence of finite disk thickness on the stability behavior of an automotive disk brake. The results reveal a specific wavelength that is preferred for instability within a layered geometry. This contrasts with the behavior observed when two half-spaces slide against each other. In that scenario, the critical velocity decreases steadily as the wavelength increases. Using material properties and dimensions consistent with automotive practice, the layer model predicts critical velocities based on those observed in experiments. As a result, this model is much more accurate than the two-half-space model, which overestimates the critical velocities by an order of magnitude. However, the relevant experiments are performed at a constant axial force, meaning that the influence of pressure is not considered. Decuzzi et al. [Dec01] propose a two-dimensional analytical model used to predict the critical sliding velocity in multi-plate clutches and brakes. It is shown that the model of Lee and Barber [Lee93], which considers infinitely thick plates, significantly overestimates the critical speed for practical machine elements, with a critical speed difference of about 80 %. The study also demonstrates that the critical speed depends on the steel and friction plate thickness ratio. Jang and Khonsari [Jan02] develop a comprehensive model for analyzing the occurrence of thermoelastic instability in a wet clutch with paper friction lining. Porosity, deformability, the thickness of the friction material, and the thickness of the steel plate are considered. The lower limit of the critical speed is strongly influenced by Young's modulus and the thickness of the friction material. In contrast, the results indicate that the influence of Young's modulus and the thickness of the steel plate on the lower limit of the critical speed is relatively small. The model is extended by Jang and Khonsari [Jan03] to include surface roughness, hydrodynamic pressure, and viscous shear dissipation within the lubricating film. The model reveals that independent dimensionless parameters govern the critical speed, and that their interaction determines the susceptibility of a system to TEI. Of particular interest are the thickness of the conducting member and its surface roughness, the influence of the lubricant viscosity and film thickness, and the physical properties of the contacting bodies. The model demonstrates that the number of surface disturbances is directly related to the number of hot spots. A comparison with independent experimental results reveals a satisfactory prediction of the number of hot spots. These results are confirmed by Zhao et al. [Zha15], who use theoretical research to show that material properties, e.g., thermal conductivity and elasticity, and structural properties, e.g., the thickness of the friction lining, have a significant influence on the stability of the system. Abbasi et al. [Abb14] prove by way of theoretical and experimental investigations using a pin-on-disk test rig with a cast-iron friction lining that the points of highest temperature on the friction interface correlate with the points of highest surface pressure. In the friction system used, the wear rate increases with increasing temperature. As a result, the location of the highest temperature changes continuously, due to the increased wear at hot spots because excess pressure is reduced. Zagrodzki and Truncone [Zag90] confirm by way of theoretical and experimental research that, even at the transient sliding velocities occurring in many typical automotive or heavy machinery applications, unstable behavior is caused by a variation of the pressure distribution. Pressure differences are typically caused by geometry deviations,

material inhomogeneities, or uneven force application. Deviations from the nominal geometry are critical, especially in the case of the steel plate, since this disturbance is stationary in the coordinate system of the subsequent damage. Deviations in the friction plate change their position continuously due to the differential speed relative to the steel plate. Operating at above-critical speeds can result in severe hot spots from even a single momentary intervention.

Audebert et al. [Aud98] demonstrate by way of a numerical algorithm that clutch disks subjected to axisymmetric temperature variations can develop residual in-plane bending moments large enough to cause buckling during unloading. In this case, axisymmetric buckling (coning) occurs when the residual stress at the outer radius is tensile, and a non-axisymmetric "potato chip" mode occurs when it is compressive. An axisymmetric residual stress field thereby causes the non-axisymmetric shape. Buckling in single-sided disks is researched theoretically and experimentally by Cenbo et al. [Cen15]. Temperatures are measured using thermocouples at four different radii in the axial center of the clutch, and tests are performed under low and high lubrication regimes. It is shown that buckling of the plates occurs when the radial temperature difference becomes large enough, and the in-plane bending moment exceeds a critical value. Yu et al. [Yu20] discuss the potential damage caused by disk buckling, noting that disk deformation causes not only large temperature differences but also significant frictional torque between the contact and non-contact regions, which in turn exacerbates deformation. In simulation studies, Cui et al. [Cui15] demonstrate that three types of saucer-shaped deformation and one type of wave-shaped deformation occur, based on the transient thermal deformation model of the friction clutch. The boundary conditions of the disks and the thermal conductivity of the materials significantly influence the deformation pattern. Li et al. [Li17b] demonstrate that, depending on the steel plate thickness, buckling is caused either by radial thermal stresses or by circumferential thermal stresses. In their study, circumferential thermal stresses are dominant at steel plate thicknesses below 1.8 mm, and radial thermal stresses are dominant at thicknesses above 1.8 mm.

2.3 Influences of Engineering Parameters on the Load Carrying Capacity

The explanations in the previous chapter clarify that many different types of damage and damage mechanisms exist for wet clutches, influenced by a multitude of factors. The literature provides numerous design recommendations for damage prevention and performance improvement, which are discussed in the following section.

The current state of the art contains contradictory statements regarding the load parameters that can be tolerated without damage. The more theoretical studies mostly derive a sliding velocity limit for spontaneous damage [Al-02, Dow73, Dow72, Gra14, Jan02, Lee93, Li08, Ost13, Zag90, Zag09, Zha13]. However, this assumption is contradicted by Panier et al. [Pan04], among others. Their experiments state that hot spots can only develop when the load reaches a certain level, even if the relative speed reaches a certain value. Moreover, the research by Xiong et

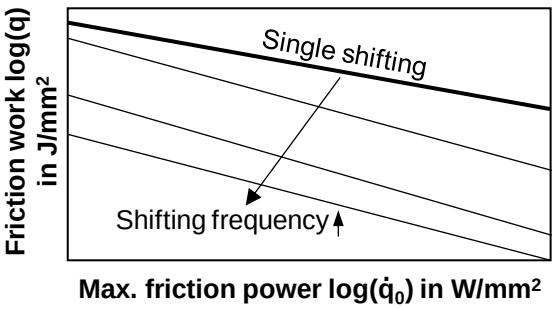

Figure 2.11: Permissible friction work as a function of friction power and shifting frequency inspired by Strebel [Str17] based on the investigations of Duminy [Dum79].

al. [Xio14] shows that the rotation of speed influences the number of hot spots, but not whether hot spots are formed at all. In addition, the number of hot spots decreases linearly when the contact pressure increases from 0.2 MPa to 2.6 MPa. When the contact pressure is low, the deformation remains in a hot band mode that eventually transitions to individual hot spots. Duminy and Federn [Dum77] explain that the performance limit of sintered metal friction clutches, defined by the allowable amount of shifting work, increases when the shifting frequency, friction surface pressure, and relative speed are reduced. Several diagrams are proposed for the design of sintered metallic disk clutches. Figure 2.11, for example, presents the performance limit overview for the parameters of area-related friction power, shifting frequency, and area-related shifting work. Based on the limiting case of a single layer, less friction work can be tolerated at an increasing shifting frequency for the same peak friction power. In addition, a nomogram is proposed which can be used to determine the permissible area-related friction work per shifting process, and the slipping time of the friction pairing as a function of the parameters friction surface pressure, initial relative velocity, coefficient of friction, and shifting frequency. The influence of the cooling oil quantity is achieved via correction factors. Findings by Duminy and Federn [Dum77] are also summarized in VDI Guideline 2241 Part 1 [VDI82] and Part 2 [VDI84]. Based on the results of Duminy and Federn [Dum77], many experimental studies have described the friction working limit as a function of the maximum friction power (see Figure 2.12) and operating frequency for the damage-free operation of wet multi-plate clutches operating under load shifting conditions [Dum77, Gro21b, Hae95, Sch21b, Sch19, Sch22d, Str17].

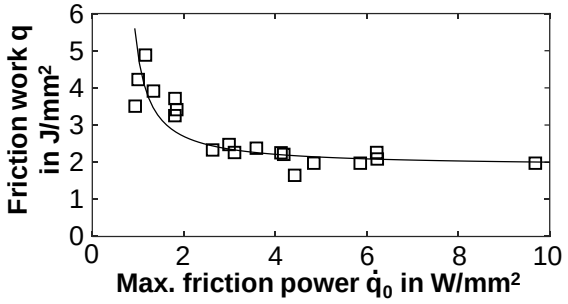

Figure 2.12: Permissible friction work as a function of max. friction power based on Schneider et al. [Sch19].

In addition to load limits in terms of sliding speed, frictional power, and frictional work, recommendations for temperature limits are proposed specifically to prevent damage. To avoid excessive friction disk wear, Yu et al. [Yu19a] suggest that the appropriate surface temperature should be maintained at 100 °C – 175 °C. Failure of the plates is reported at a surface temperature above 250 °C. Su et al. [Su06b] demonstrate by way of experimental studies of carbon fabric composites filled with nano-Al_2O_3 and nano-Si_3N_4 particles that wear rates of the composites increase significantly at elevated temperatures above 180 °C, a result which can be attributed to the degradation and decomposition of the resin adhesive. In contrast, Hensel [Hen14] does not propose a peak temperature as a characteristic value for characterizing the damage limit of wet multi-plate clutches. A characteristic value $A_{\vartheta Rf}$ is defined which enables correlation of the damage with the thermal load. Using $A_{\vartheta Rf}$, it can be shown that there are different damage mechanisms depending on the temperature level and the residence time at the temperature level. The characteristic value considers the thermal load, and not a single event throughout use. Anderson and Knapp [And90] describe focal hot spots associated with microstructural transformation and martensite formation, for which surface temperatures over 750 °C are required in the systems considered. Brown to blue discolorations on brake drums are indicated as non-critical focal hot spots. No microstructural transformation takes place. The required temperatures are significantly lower (200 °C – 300 °C) than in critical hot spots. To avoid sinter carryover, Snima [Sni06]

recommends cooling the friction linings well by recooling the cooling oil. Wu [Wu18] confirms this recommendation through simulations and demonstrates that an increased cooling oil flow rate increases the cooling capacity, thus leading to lower friction surface temperatures, which can reduce the damage tendency. Schneider et al. [Sch21b] also describe a statistically significant effect of oil flow rate on damage occurrence in paper friction systems under load shifting.

In addition to load parameters and external cooling, there also exists a variety of design parameters on the steel or friction plates to increase load-carrying capacity in terms of damage. For example, Li et al. [Li17a] investigate groove design influence on wet multi-plate clutch wear behavior. The waffle groove exhibits the highest wear rate compared to the radial and spiral grooves. Furthermore, it is shown that the grooves have a negative effect on wear for short shifting times (0.2 s), and friction linings without grooves are recommended. For long shifting times (3 s), the wear properties of the friction material are significantly improved by grooves compared to groove-free friction material. Schneider et al. [Sch21b, Sch22b] research the influence of grooves on spontaneous damage behavior during load shifting in paper and sinter friction systems. The experiments discover no statistically significant difference between the grooves investigated. Dow [Dow78] proposes design changes, e.g., special coatings or sacrificial parts. The sacrificial parts are intended to induce a desired wear that dampens the TEI. Studies performed by Xiong et al. [Xio14] also show that the wavelength of hot spots increases when the Young's modulus of the steel increases. In contrasting terms, it is evident that, when the Young's modulus decreases, the number of hot spots increases, until there is no single hot spot, but a hot band. Fieldhouse [Fie11] suggests a uniform mass distribution for the steel plates in order to ensure that the heat distribution is homogeneous, while Yu et al. [Yu19a] suggest increasing the number of teeth in each plate so as to improve the resistance to mechanical buckling. Several studies [Cen15, Cui15, Li17b, Wan22, Yu20] suggest that the thickness of the steel plate should be increased in order to prevent buckling. Li et al. [Li17b] further conclude that the critical thickness determines whether the circumferential or radial thermal stress dominates during thermal buckling, while Wang et al. [Wan22] clearly demonstrate in their simulative studies that doubling the steel plate thickness can increase the buckling strength by up to 398.4 %. On the other hand, the simulation results by Zagrodzki and Truncone [Zag03] indicate that reducing the thickness of the steel disk can significantly improve thermoelastic stability. At the same time, it is pointed out that thinner steel plates are more susceptible to well-known permanent deformations (cone formation, distortion). Furthermore, the steel plates serve as heat sinks, and a reduction in their thickness increases the average clutch temperature for the same load. Regarding load shifting with paper and sinter friction systems, Schneider et al. [Sch21b, Sch22b] demonstrate a clear influence of the steel plate thickness on damage occurrence. The thicker the steel plates, the higher the loads necessary for damage to occur. Decuzzi et al. [Dec01] determine that friction partners with a thickness ratio of around 1 are particularly susceptible to hot spots. It is also discovered that the critical wave parameter increases slightly with a decreasing thickness ratio. Decuzzi et al. [Dec01] suggest either increasing the thickness of the friction lining or decreasing the thickness of the steel plate. In contrast to these research results, Scieszka and Zolnierz [Sci07a, Sci07b] present evidence that increasing the steel plate thickness leads to an increase in the critical velocity regarding the occurrence of thermoelastic instability. Jang and Khonsari [Jan02], in turn, make it clear that the influence of the thickness of the steel plate on the lower limit of the critical speed is relatively small with respect to the formation of hot spots. At the same time, both the Young's modulus and the thickness of the

friction material strongly influence the critical speed. Furthermore, Li et al. [Li17a] emphasize the positive influence of the thickness of the friction lining on the wear rate. Scieszka and Zolnierz [Sci07a, Sci07b] also show, by way of a finite element model, that lowering the Young's modulus increases the range of critical velocity for thermoelastic instability. Fieldhouse [Fie11] follows Barber [Bar69] in describing non-uniformities as being one of the causes of hot spots. Fieldhouse [Fie11] also suggests when using friction materials with low Young's modulus to account for the continuous thickness differences of the steel plate. This way, the pressure non-uniformity can be compensated. As a result, the thickness differences of the plates lead to lower pressure non-uniformities, a result which is also demonstrated in recent publications by Zhao et al. [Zha18a], and Sabri et al. [Sab21a]. In the case of buckling, Yang [Hui15] and Wang et al. [Wan22] show that the Young's modulus does not influence the load-bearing capacity, whereas Wang et al. [Wan22] report that the coefficient of thermal expansion has a considerable influence. Keeping the coefficient of thermal expansion as low as possible is suggested, and is also recommended by Barber [Bar69], Xiong et al. [Xio14], and Scieszka and Zolnierz [Sci07a, Sci07b] in the case of hot spots. While the coefficient of thermal expansion should be kept small to avoid spontaneous damage, studies in the literature [Kub98, Kum11, Zha01] report that the coefficient of thermal conductivity of the friction lining should be chosen to be large, and a ratio of the thermal conductivities of the two friction materials should be closer to 1 [Bar69]. The thermal conductivity of the friction material can be increased by incorporating carbon fiber into a composite material [Kea97, Luo16b]. Groetsch et al. [Gro21b] confirm these results by way of experiments using carbon fiber reinforced carbon (CFRC) friction linings, which contain a carbon matrix in addition to carbon fibers. The carbon friction linings investigated exhibit excellent resistance to spontaneous damage. For example, Kearsey [Kea97] and Lam et al. [Lam06] also report that carbon friction plates are less prone to hot spot formation than paper friction plates. At the same time, the increased thermal conductivity of the friction lining leads to an increase in the temperature level of the friction lining, thus leading to the need for increasing the heat resistance of the fibers and the matrix material. For example, Fei et al. [Fei16], Huang et al. [Hua09], and Su et al. [Su06b] report that, regarding the development of wet composite clutches, a polymer matrix having excellent heat resistance should be selected in order to avoid damage. In addition, Fei et al. [Fei16] recommend improving the interfacial adhesion between the carbon fabric and the phenolic matrix. In order to improve the interfacial adhesion between matrix and fiber material, Wan et al. [Wan19a] suggest, on the one hand, pretreating the fibers with nitric acid, while on the other hand, Zhang et al. [Zha09b] recommend coating the fibers with SiO_2. Furthermore, Shamra et al. [Sha11] demonstrate by means of pin-on-disk tests that cold remote nitrogen-oxygen plasma-treated carbon fabric has better wear resistance than untreated carbon fabric. Many contributions propose adding fillers to the composite in addition to pretreating the fibers in order to increase interfacial adhesion and wear resistance. For example, Su et al. [Su06a] propose the fillers nano-$CaCO_3$, nano-SiO_2, and nano-TiO_2; Zhang et al. [Zha05] propose the fillers PFW, nano-ZnO and nano-SiC; Qi et al. [Leh18] propose the fillers MoS_2 with 20 wt%; and Su et al. [Su06b] propose the fillers 5 %nano-Al_2O_3 and 8 %nano-Si_3N_4.

2.4 Test Procedures

The complex interactions in the frictional contact described so far, as well as the large number of partly unknown parameters influencing the system behavior of wet clutches, make an exact prediction of the damage and the frictional behavior almost impossible. Therefore, in order to

be able to draw reliable conclusions about the performance of friction clutches, experiments play a central role in the design process. This section first provides an overview of tribology test categories and then presents test procedures for load shifting and slip operation.

According to DIN 50322 [DIN86], measurement and test procedures for the friction and wear behavior of tribological systems can be divided into six basic categories: I machinery field tests, II machinery bench tests, III subsystems bench tests, IV components bench tests, V component model tests, and VI laboratory tests. In this context, a higher category corresponds to a more significant system simplification. Machinery field tests (category I tests) involve testing actual final products under experimental conditions, in which case the wide range of experimental operating conditions are often unable to be sufficiently characterized [Czi20]. Considerable effort is required to confirm the test results in repeated tests and to verify them statistically. As a result, full-scale field trials are usually costly [Czi20]. In categories II to IV tests, actual machines, tribosystems, or components are examined in precisely defined bench tests, and the test results can be related to the actual technical structures [Czi20]. Tests in categories V to VI are fundamentally oriented, and no real components are used, rather only specimen models (e.g., pin-on-disk) [Czi20]. Given the complex system behavior, the broad field of application, and the described basic categories for testing tribological systems, many test procedures exist for determining the damage and friction behavior of wet friction clutches.

Acuner et al. [Acu13] develop a coefficient of friction short test for paper friction linings of wet clutches. Variations in pressure and sliding speed are used to evaluate friction behavior. The mass moment of inertia is kept constant in each test series, so that a variation in the friction work and the maximum friction power accompanies the variation of pressure and sliding speed. Stockinger et al. [Sto17] extend the test methodology for carbon and sintered friction materials in wet clutches. The life test methodology developed by Hensel [Hen14] is used to identify the decisive influencing parameters regarding friction and damage behavior and to simultaneously characterize the stress ability related to these parameters. In addition, a characteristic value for the description of the thermal load ($A_{\vartheta Rf}$) is defined, enabling a correlation between damage and thermal load. With the aid of $A_{\vartheta Rf}$, it is possible to demonstrate that various damage mechanisms exist, as a function of temperature level and cooling. In addition, collective tests at two load levels are performed several times in a row and are used to investigate recovery effects during continuous operation. Pfleger [Pfl98] and Wimmer et al. [Wim05] investigate far more complex load collectives, varying sliding speed, pressure, specific friction work, and maximum specific friction power at different load levels. These load collectives are strung together as often as required, depending on the research objective (e.g., clutch failure). Haemmerl [Hae95] uses step tests with ten shifts per load step to investigate hot spots on wet multi-plate clutches. The mass inertia, axial force, and speed are varied during the step tests. A correlation is qualitatively reported between specific friction work and maximum specific friction power at damage onset. It is reported that, regarding brake circuits with high peak specific friction power and low specific friction work, there is no damage to the friction system, whereas hot spots are observed at lower maximum friction power levels in circuits with higher friction work. Similarly, step tests with ten load cycles per load step are used by Fairbank et al. [Fai01]. The speed is increased from load step to load step, and the mass moment of inertia is kept constant. However, the slipping time is kept constant by adjusting the axial force. In addition, Hirano et al. [Hir07] use a similar experimental procedure to investigate hot spot phenomena on wet multi-plate clutches by means of nine braking circuits per load step. The specific friction work and specific friction power are increased from load level to load level by

increasing the initial speed. The mass inertia and pressure remain constant during the individual step tests. Strebel [Str17] presents a test method for investigating the spontaneous damage behavior of sinter and paper friction systems for load shifting. The load on the multi-plate clutch is increased from load level to load level in a step test. At ten shifts per load level, the number of shifts is small enough to avoid long-term damage and large enough to achieve spontaneous damage. After each load level, the multi-plate clutch is able to be inspected for any damage, and the test parts are documented. The cycle time, i.e., the time between two successive shifts, is chosen to be 40 s, which is large enough to ensure that the clutch is cooled back to the lubricant temperature (80 °C by default) before each shift, which means that the steady-state temperature of the clutch has already been reached by the first shift. A run-in test is performed before the actual step test to compensate for manufacturing tolerances and inhomogeneities in the individual clutches. This test method is subsequently used by Schneider et al. [Sch21b, Sch19, Sch20b, Sch21c] in numerous experiments on paper and sinter friction systems and is also successfully applied by Groetsch et al. [Gro21b] as well as Schneider et al. [Sch22d] with regard to carbon friction systems.

The Society of Automotive Engineers (SAE) provides standardized test procedures for durability and friction tests of multi-plate clutches using the SAE #II multi-plate clutch test rig [Aut12a]. This rig is utilized to evaluate the friction characteristics of multi-plate clutches in automatic transmissions with automotive transmission fluids, and it is also capable of conducting durability tests on wet friction systems. The test procedures J2487 [Aut19b] and J2488 [Aut19c] describe a step test with 200 cycles per load level, based on a stepwise increase of the friction work at a constant output speed of 3 600 min^{-1} and 6 000 min^{-1}, respectively. At each load level, the moment of inertia must be increased while the lubricant temperature and the flow rate are kept constant over the entire running time. The specific purpose of the test procedures is to define a stepped power test used to evaluate wet friction system performance variation as a power level function. Test procedure J2489 [Aut12b] is developed to evaluate the performance variations of wet friction systems as a function of the number of cycles. Individual load levels from tests J2487 [Aut19b] and J2488 [Aut19c] are strung together as often as required to produce a continuous shift test at a constant load level. In addition, test procedure J2490 [Aut19a] is used to evaluate the variation of wet friction system performance as a function of speed, temperature, and pressure. This test procedure involves four 50-cycle break-in levels at 3 500 rpm with increasing steps of contact pressure, followed by 16 levels consisting of 25 dynamic engagements and one breakaway following the completion of the 25th dynamic cycle. The 16 levels are obtained by varying initial engagement speed, contact pressure, and oil sump temperature while the inertia is kept constant, at 0.701 $\mathrm{kg/m^2}$.

In addition to the test procedures presented thus far regarding load shifts, there are also a few experimental procedures for clutches under transient conditions. Szappanos et al. [Sza06] present the development of a friction screening test using a Full-Scale Low-Velocity Friction Apparatus (FS-LVFA) designed to investigate breakaways at low speeds, such as those encountered during the operation of limited slip differentials. The test consists of four phases (break-in, pre-durability performance evaluation, durability, and post-durability performance evaluation) and is used to investigate fundamental interactions between the friction material and the lubricant. Henley et al. [Hen10] further develop the proposed test procedure from Szappanos et al. [Sza06] by adding a statistical data analysis method to facilitate a comparison of the tested friction materials and lubricants. Schenkenberger et al. [Sch06] develop a μ-split

screening test using the SAE #2 friction test rig to provide faster and more accurate screening of candidate fluids. A complete test consists of 40 cycles of chatter, μ-split, and moan events. The chatter event comprises a speed sweep from 0 to 25 rpm over 4 s, a dwell at 25 rpm for 4 s, and a return to 0 rpm over 4 s (see Figure 2.13). To match field conditions, the chatter event is performed under constant load and in both the forward and reverse directions. In the μ-split event, a differential speed is built up when pressure is applied, and the predefined differential speed is maintained. The moan event is a discrete velocity event at 40 rpm. The load remains constant for the entire duration of the event, which lasts 30 s. The test compares and evaluates lubricants for use in limited slip differentials concerning friction behavior and NVH behavior. Whittcar et al. [Whi10] optimize the proposed test procedure by Schenkberger et al. [Sch06] in terms of equipment modifications, data analysis, and correlation to full-vehicle μ-split testing. Voelkel [Voe20a] develops a test method used to characterize the running-in behavior of slipping multi-plate clutches. In order to investigate the frictional behavior of slipping clutches in a manner as close as possible to the application, vehicle data from various test drives (race tracks, mountain passes, μ-split) are evaluated, and relevant load conditions are identified. Six application-related load levels of different specific stresses are derived based on identifying relevant differential speed lock-up torque combinations. A slip cycle in transient slip consisting of five slip phases and a connected cooling phase is used. In a slip phase, the clutch, which is subjected to axial force, is opened up in a triangular differential speed curve, and the differential speed is reduced again. Between the individual slip phases, the closed clutch is stationary for a duration of one second.

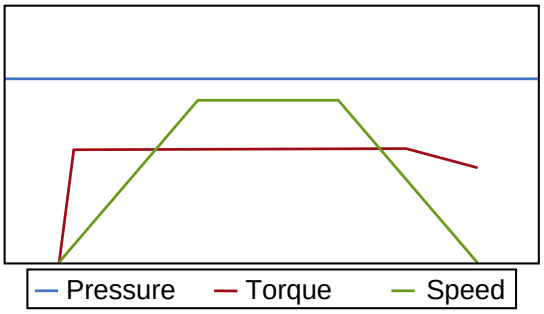

Figure 2.13: Sample of a chatter event based on Schenkenberger et al. [Sch06].

2.5 Numerical Analysis of the Thermomechanical Behavior

The presented state of the art clarifies that the thermal behavior is an important factor in the design of a multi-plate clutch. The previous sections show that the temperature at the friction interface determines the boundary layer structure and, therefore, the friction and damage behavior of the clutch. It is also shown that high temperatures can damage the lubricant. Therefore, a good understanding of the heat flow through these components is essential when optimizing their design.

The actuation of a clutch is a process in which kinetic energy is converted into thermal energy (see Figure 2.14). The parameters of speed, contact pressure, coefficient of friction, and thermophysical properties of the materials change during clutch actuation (see Section 2.1). In this process, frictional heating during braking causes thermoelastic deformation, changing the contact pressure distribution $p(x,y,t)$ and therefore the distribution of frictional heating $q(x,y,t)$ [Yi02]. The coupling between the mechanical and thermal problems is established by the energy balance relation $q(x,y,t) = \mu \cdot v \cdot p(x,y,t)$, where μ is the coefficient of friction and v is the sliding velocity [Yi02].

Experimental tests or theoretical calculations can determine the temperature distribution in the clutch components during actuation. Experimental tests are generally time-consuming and expensive, and are used to validate numerical solutions. Analytical calculations considering

friction heating systems require half-spaces or plane-parallel strips, so applying a finite domain is impossible. Obtaining an exact solution to the problem is extremely difficult due to the complex geometry of clutch components. [Yev10]

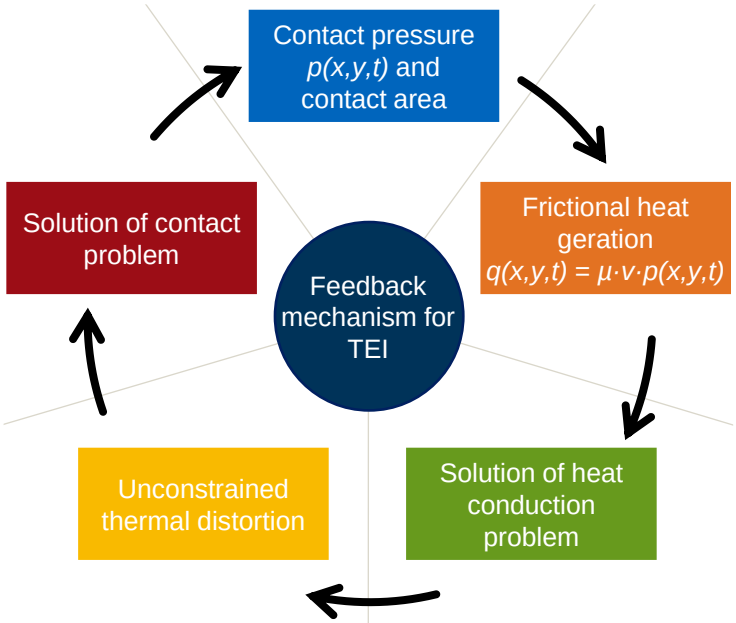

Figure 2.14: The feedback process for TEI based on Yi et al. [Yi02].

The foundational research behind modern thermal and thermomechanical clutch models dates back to the early 20th century. For instance, Geiger [Gei37] used a simple one-dimensional model to calculate clutch temperatures, taking into account heat conduction through the connecting components. Furthermore, Geiger [Gei37] observes that the converted energy and friction interface temperature are relevant to clutch damage. Hasselgruber [Has59] investigates the chronological history of the temperature of friction clutches during a single shifting process for the one-dimensional case. The analytical calculation formula for the temperature increase is developed by solving the differential equation using Laplace's singularity method. However, the model assumptions (semi-infinite bodies, one-dimensional heat conduction problem) limit the applicability to short shifting times, thick plates, a single shifting process, and a friction power curve described by a polynomial approach. Steinhilper [Ste62] extends the work of Hasselgruber [Has59] to large slipping times and calculates the axial temperature distribution of a multi-plate clutch using a superposition method. Steinhilper [Ste63a, Ste63b, Ste64] develops thermal networks in further work. The thermal networks are converted into electrical circuit diagrams to conduct experimental investigations. The accuracy of the computational results is confirmed by comparison with experiments. Steinhilper further notes that a one-dimensional thermal design approach is usually sufficient for practical purposes. Lauster and Staberoh [Lau73] consider the thermal behavior of wet multi-plate clutches during successive shifting cycles, in which case the heating of the clutch due to drag losses can also be considered. The end temperature of the respective preceding shift cycle forms the start temperature for the following shift. Unless the clutch cools back down to the lubricant temperature during the cooling phase, the maximum plate temperature will rise to a certain steady-state value. Haemmerl [Hae95] uses the finite difference method to calculate the temperature behavior in wet multi-plate clutches, and his work forms the basis for the FVA program KUPSIM, which is continuously evolved [Voe16, Woh09]. Using KUPSIM, thermal design and recalculation are possible for changing operating loads of clutches. The calculation models and the results are validated by comparison with test bench results, showing a high level of agreement. In addition, based on the finite difference method, Tatara and Payvar [Tat02] calculate the temperature distribution in wet multi-plate clutches during the friction, closed, and open cooling phases. Besides load shifting, continuous slip is also considered, whereby the largest fraction of frictional heat is dissipated through the lubricant. The heat transfer coefficients required for this purpose are calculated according to

Payvar [Pay91]. Regarding longer slippage times, Pacey and Turnquist [Pac90] report improved heat dissipation. Zagrodzki [Zag85] investigates the axisymmetric transient temperature and quasi-static thermal stress distributions in wet clutches. The finite difference method is used for calculating the temperature distribution, and the finite element method is used for calculating the thermal stresses. The contact pressure is uniformly distributed over the friction interfaces and is assumed to be independent of the thermoelastic deformations. The coefficient of friction is considered to be constant and independent of a radial coordinate, and the frictional heat equals the power density of the frictional forces. Temperature gradients and radial stress components occur due to differences in local velocities in the radial direction. It is evident that the maximum thermal stress reached is below the yield point of the material, and the damage behavior of the clutch cannot be predicted. The axial stress in the clutch is about 30 times higher than the circumferential and radial stresses. The circumferential and radial stress components at the friction surfaces are compressive stresses, and tensile stresses occur inside the disk. As a result of the superposition of axial and radial temperature gradients, compressive stresses are present at the outer diameter and tensile stresses at the inner diameter. The influence of the radial component of the temperature gradient on the values and distribution of thermal stresses is found to be dominant. The yield stress of the materials investigated does not surpass the equivalent Huber-Mises stress level. In further investigations, Zagrodzki [Zag90] performs a thermomechanical analysis of temperature and thermal stresses, including the non-uniform contact pressure distribution in a multi-plate clutch. The influence of wear is neglected, which, as mentioned, could weaken the thermoelastic instability phenomenon. A clutch with 10 friction interfaces, consisting of nine plates coated with friction material, hydraulic pistons, and an opposing plate, is analyzed. The distributions of normal pressures on the friction interfaces greatly influence the temperature gradients in the disks as well as the resulting thermal stresses. In most unfavorable situations, the stresses can exceed the yield point of the materials used. In the following, Zagrodzkiy and Truncone [Zag03] and Zagrodzki [Zag09] compare the quality of the results and the numerical computational effort of two- and three-dimensional finite element models. Due to the lower computational effort of two-dimensional models, they accept the less accurate results and report slightly underestimated maximum temperatures for two-dimensional models. As a result, only focal hot spots are considered in the simulations, and the associated critical velocities are determined as a function of the wavelengths of the modes considered. Using a two-dimensional finite difference model, Jen and Nemecek [Jen08] compare the calculated temperatures of a multi-plate clutch by way of experimental measurements. Differences are found in the circumferential direction. While the simulation determines uniform temperature distributions in the circumferential direction, differences are discovered in the measurements concerning the absolute temperatures and the time curves. Zhao et al. [Zha08] build an axisymmetric finite element model to analyze the thermomechanical behavior of multi-disk dry clutches and disk brakes. The transient changes in temperature and stress tensor components for a single engagement are analyzed. Explicitly different material properties are investigated, including carbon-carbon composites. In contrast, Rao et al. [Rao89] determine the temperature distributions during repeated braking cycles. Following Zagrodzki [Zag85], it is assumed that the total kinetic energy is converted into heat. The heat capacity of the friction lining is not considered, and it is assumed that the brake disk absorbs all of the heat energy. In addition, temperature-independent material properties are used, and the finite element model is validated through experimental tests. The brake disks are radially drilled and equipped with thermocouples for this purpose. Koetniyom et al. [Koe02] also investigate the

thermomechanical behavior of a disk brake during repeated braking operations. However, they use temperature-dependent material parameters obtained in specially performed experimental measurements. The heat energy is determined using the vehicle's kinetic energy, and both convection and radiation are taken into account in the analysis. The required heat transfer coefficient is taken from Grieve et al. [Gri98]. One section of the disk brake is analyzed in order to limit the numerical effort. Mackin et al. [Mac02] also investigate brake disks in experimental and theoretical studies, focusing on crack formation. The loads that can cause thermal cracks during operation are identified. Using FEM models, radial, circumferential, and equivalent Huber-Mises stresses are determined, and the number of cycles until brake disk failure is determined based on the Coffin-Manson model [Bue98]. It is demonstrated that compressive stresses prevail during braking, whereas tensile residual stresses prevail in the circumferential direction during cooling. In the hub area, the material yield strength is exceeded by the maximum equivalent stresses. In addition, the experimentally determined values are about 11 % lower than those determined using the FEM model. Wu et al. [Wu16] determine the thermal fatigue crack propagation during consecutive emergency braking for high-speed brake disks using FEM. In the first step, the thermophysical, mechanical, and fracture mechanics parameters for brake disks made of alloyed forged steel are determined experimentally at different temperatures. The calculation results are used to evaluate the fatigue life and safety margin while in service. The predicted peak temperature and calculated crack geometry agree well with the experimental data, and the thermal fatigue crack propagation is used to evaluate the safety level of the brake disk. Yi et al. [Yi02, Yi00] develop a finite element method to determine the critical sliding velocity for the thermoelastic instability of axially symmetric clutches and brakes. The critical sliding velocity is related to the number of hot spots. Temperature measurements on the brakes exhibit non-uniform distributions in the circumferential direction. The experiments also show that hot spots can be explicitly identified, especially at high sliding velocities. The theoretical predictions of the critical speed agree well with the experimental results. Graf and Ostermeyer [Gra12, Ost13] analyze disk brakes in relation to TEI using analytical, numerical, and experimental methods. Wear, heat generation, thermal expansion, and thermal conduction are taken into account in the analyses to investigate the formation of hot spots and hot bands. The location of the calculated hot band is identical to the location of maximum pressure and therefore dominates the effective friction radius. It is also shown that the critical velocity for hot band formation is lower than the one for hot spot formation.

In more recent work, three-dimensional simulations see increasing development and use for analysis, in addition to two-dimensional simulation models, due to improved numerical computing capacity. Xiong et al. [Xio14] investigate the formation of hot spots in multi-plate clutches using simulations. A three-dimensional finite element model of a multi-plate clutch is developed to simulate the hot spot generation process and illustrates the generation mechanism scenario. The formation process is divided into three phases. First, local heating occurs, which leads to local hot expansion, and the first hot spot forms on a steel plate. Then, due to thermal stresses, another hot spot forms alternately on the other side of the steel plate. The generation of more hot spots continues until a sinusoidal deformation with hot spots is achieved over the entire circumference of the steel plate. A series of simulations show that the wavelength of the hot spots increases almost linearly as the speed, pressure, coefficient of thermal expansion, and Young's modulus of the steel plate increase. Motivated by observations of macroscopic cracks on the friction interface of TGV high-speed trains, Dufre'noy and Weichert [Duf03] also investigate the formation of cracks in disk brakes. Using

FE simulations, a segment of 30° of the entire disk is analyzed with respect to influences on crack formation. The thermal results of the numerical calculations agree well with those from experimental thermographic measurements. The simulated residual stress values are verified by the hole drilling strain gage method. Lower values are obtained in the radial direction than in the circumferential direction, which is consistent with the calculations. The highest residual stress values are near the hot spot, as Dufre'noy and Weichert [Duf03] also determine numerically. Furthermore, Grzes et al. [Grz16] use pulsed infrared thermography to validate the finite element model of a railroad braking system. In addition, the simulated temperatures are validated using measured values of thermocouples from experimental tests. The validated finite element model is then used to compare and evaluate many different friction materials. Gao et al. [Gao07] investigate the thermomechanical behavior of brake disks using a three-dimensional FEM model. Variations in temperature and stress development are observed due to rotational motion, and a clear relationship between temperature development and the change in equivalent stress is demonstrated. The maximum values for temperature and stress are reached in about half of the braking time. The highest stress values are observed in the circumferential direction, followed by the radial direction. The maximum equivalent stress exceeds the yield strength of the disk material in the working zone. The temperature decreases after braking is completed, resulting in residual plastic strain. This temperature change results in the disk no longer being under compressive stress during braking, but under tensile stress after cooling. It is pointed out that macroscopic cracks may appear in the friction interface after several braking operations. A nonlinear three-dimensional FEM model of high-speed train brake disks with thermo-mechanical coupling is created in ANSYS by Zhang et al. [Zha09a]. A 90° segment of the brake disk is modeled for this purpose. The thermal field calculation shows that different temperature distributions exist along the circumferential and vertical directions of the brake disks. Given the results of the stress calculations, it is evident that compressive stresses cause the plastic deformations of the friction interfaces, and the yield strength compressive stress is exceeded at the surface of the disk. The surfaces and interior of the brake disks will also be subjected to periodic fatigue stresses, consisting of residual tensile and compressive stresses, which will cause cracking in the disk. During braking, compressive stresses are present on the contact interface of the brake disk and, after stopping, the sign of the stresses changes, and tensile stresses are present. On the other hand, Thilak et al. [Thi11] develop a three-dimensional 360° finite element model of a disk brake using ANSYS. This model is used to perform transient thermoelastic analyses during repeated brake applications. Temperature, deformation, and stress fields in the brake disk made of three composite materials and one cast iron for high thermal and mechanical loads are investigated. To calculate the thermoelastic behavior of the disk brakes, the coupled heat conduction and elasticity equations are solved with contact problems. A similar analysis is performed by Sowjanya and Suresh [Sow13], who use ANSYS to perform structural and thermal analysis of the disk brake using three materials (stainless steel, cast iron, carbon-carbon composite). It is assumed that the materials used are homogeneous and isotropic. Stainless steel offers better braking performance than other materials from a deformation point of view, but cast iron performs better with respect to loading. To investigate the thermal behavior of multi-disk friction pairs in hydro viscous drives, a three-dimensional transient temperature model is developed for the numerical simulation by Cui et al. [Cui14]. Grooved and non-grooved friction disks are compared with respect to pressure distribution and temperature behavior. However, it is demonstrated that the non-grooved areas tend to deform, and the friction linings are more likely to be deformed. Bao et al. [Bao16] build a three-dimensional finite element model of a

clutch. Typical pressure disturbances in friction disks along the circumferential direction, which can be caused by the failure of return springs, are determined by means of static calculations with finite elements. A thermal analysis is performed in the second step. The finite element method is used to determine the critical speed and temperature field of friction disks when thermoelastic instability failure occurs under pressure disturbances. Sabri et al. [Sab21a] develop a full three-dimensional model of a dry friction clutch system (single disk) using the finite element method to estimate the distribution of contact pressure between the contact elements of the clutch system under different operating conditions. The main result is that the contact pressure decreases with a decrease in Young's modulus of the friction lining, while the deformations increase. The results show that the structural stiffness of the friction lining increases the tendency of the friction system to operate in the stability zone. The influence of the material parameters on the contact pressure distribution in a multi-shear piston coupling is also investigated by Liu et al. [Liu21]. A finite element model and a thermodynamic numerical model are built for this purpose and validated using experimental pressure measurements. Similar to Sabri et al. [Sab21a], it is shown that increasing the Young's modulus and Poisson's ratio of the mating plate can effectively improve contact pressure uniformity. Yu et al. [Yu19c] analyze the contact pressure distributions on the friction interfaces when an outer circlip axially supports a multi-plate clutch using a finite element model. The calculation results show that the outer circlip leads to an inhomogeneous distribution of the contact pressure in both the radial and the axial directions. The radial contact pressure significantly affects the temperature fields on the friction interfaces, which bench tests can effectively verify. Both the simulation and the experimental results show that the outer circlip is identified as one of the main reasons for the increase in radial temperature difference. A three-dimensional finite element model and a thermodynamic numerical model of a multi-plate clutch with eight friction interfaces are developed by Liu et al. [Liu21] to investigate the influence of the material parameters on the contact pressure distribution. An experiment on the static pressure of the clutch verifies the accuracy of the numerical model. The pressure distribution index is proposed to evaluate the pressure differences of individual friction pairs. Wenbin et al. [Wen16a] present a thermal model of a clutch with carbon friction lining considering heat flow, convective heat transfer, and heat conduction. This model is solved using finite element analysis and validated by way of experimental data. The main focus of the research is the influence of the specific heat capacity and the thermal conductivity of the materials in order to reduce the temperature in the clutch and to avoid failure of the friction material. Through several contributions, the research group around Abdullah and Schlattmann builds two-dimensional [Abd13a, Abd14a, Abd18a, Abd12a, Abd13b, Abd14b, Abd18b, Abd12b] and three-dimensional [Sab19, Sab21a, Sab21b] finite element models of brakes, single-disk clutches, and multi-disk clutches with ANSYS and validates each with analytical methods. Using these models, sensitivity studies for contact pressure and penetration are performed by use of penalty and augmented Lagrange contact algorithms [Abd13a, Abd13c]. The importance of the contact stiffness (FKN value) between the contact surfaces of the friction coupling elements is highlighted. In addition to the FEM settings, the influences of geometry parameters (ratio of the inner to the outer radius of the friction surface [Abd12b], the thickness of the steel plate [Abd14d], the thickness of the friction lining [Abd18a, Sab19, Sab21b], grooves [Abd14c]), load parameters [Abd14a, Abd12a, Abd13b, Abd18b, Abd14d, Jab21] (differential speed, pressure), boundary conditions [Abd14b] (fixing of the clutch) and material parameters (Young's modulus [Sab21a], thermal conductivity [Abd14a]) are investigated.

In addition to understanding the thermomechanical behavior of brakes and clutches in greater detail and predicting thermoelastic instability, several contributions to the literature take a closer look at the damage mechanism of buckling by means of the finite element method. Wang et al. [Wan19b] analyze the temperature field distributions of friction pairs and the location of the maximum temperature. For this purpose, numerical simulations are set up for the three-dimensional equations regarding unsteady heat conduction with boundary value problems. The numerical problem is solved using the finite difference method. This research serves as a prerequisite for investigating the thermal buckling behavior. Based on Rayleigh-Ritz plate theory [Lie93] and Timoshenko's beam theory [Tim12], which assume that a curved beam buckles laterally when the in-plane bending moment exceeds the critical value, Ma [Ma04] derives the governing equations for studying the thermal buckling of annular disks. The finite element method is used to study the problem of thermal buckling, taking into account the geometrical and material parameters of the separated plate. Huizhou [Hui15] investigates the thermal buckling of brake and clutch disks using finite element analysis. Observations show that buckling appears when the temperature distribution is uniform at the circumference but non-uniform at the radius. Thermal buckling occurs when the temperature gradient exceeds a critical value, and therefore, is unlikely to occur at the beginning of the engagement process. Bagheri et al. [Bag17] focus on the nonaxisymmetric buckling behavior of isotropic homogeneous annular plates subjected simultaneously to the effect of a constant temperature increase and a constant angular velocity. Solving a plane stress formula determines the plate deformations and stresses before buckling (neglecting rotations and lateral deflection). The numerical results show that rotation can increase the critical temperature for annular disks having clamped outer rims. Zhao et al. [Zha16] use finite element analysis to investigate the stability limits of thermal buckling in automotive clutches. They demonstrate that the radial variation of temperature significantly affects the critical buckling temperature and the predominant buckling modes by the pattern of the radial temperature distribution. Whereas a linear or monotonic temperature pattern always leads to axisymmetric buckling modes, a temperature pattern with a temperature maximum in the center leads to non-axisymmetric potato chip modes. The associated critical temperature is typically much higher. The authors point out that thermoelastic instability can be induced at the beginning of the frictional engagement and can lead to banding modes and focal hot spots. Similar to Huizhou's [Hui15] studies, thermal buckling occurs only when the temperature gradient exceeds a critical value and therefore is unlikely to occur at the beginning of the intervention. In contrast, research by Li et al. [Li17b] demonstrates that the buckling shape is dependent on the steel plate thickness. Gong et al. [Gon18] investigate the thermal buckling characteristics of the pressure plate of a dry clutch under two typical thermal loads using the finite element method. They find that the temperature distribution along the thickness direction of the dry clutch pressure plate has no apparent influence on the critical temperature of thermal buckling and can, therefore, be neglected. The radial temperature distribution mainly induces thermal buckling. The boundary conditions of the pressure plate dominate the thermal buckling mode, and the thermal buckling of the pressure plate occurs more easily during the cooling phase than during the heating phase. Chen et al. [Che16] perform numerical analyses on the thermal buckling of automotive brakes and clutches using a reduced Fourier method. Commercial Abaqus software is used for model validation. The results demonstrate a certain wavenumber at which the buckling temperature reaches a minimum. In further studies, Chen et al. [Che19] demonstrate strong coupling between thermoelastic instability and thermal deformation in clutch disks. They calculate the critical buckling temperatures and the buckling deformation modes of the clutch

disk under specific temperature fields of the commercial finite element Abaqus software. The effects of several parameters, such as coefficient of friction, sliding velocity, and boundary conditions, are studied, and strong coupling between thermoelastic instability and thermal buckling is demonstrated. Moreover, the unstable temperature modes induced by thermoelastic instability can significantly change the temperature profiles for thermal buckling and, therefore, the critical buckling temperatures. Furthermore, it is determined with regard to the existence of focal hot spots that the minimum temperature for thermal buckling is characteristically much higher than the operating temperatures of clutches. The coupling between focal TEI hot spots and thermal buckling is, therefore, of less importance in real applications.

2.6 Conclusion of the State of the Art

This section examines the state of the art regarding the damage behavior of wet multi-plate clutches, operating modes, damage behavior, and thermomechanical simulation models of wet multi-plate clutches. In addition, experimental testing methods and influencing parameters on the load-carrying capacity of clutches are discussed. The following sections also summarize the most important findings from the current state of the art.

The following conclusions can be drawn concerning system requirements, operating modes, friction materials, and friction conditions:

- Wet multi-plate clutches are used in a wide range of automotive and industrial applications.
- Depending on the application, wet multi-plate clutches are operated in various ways and at a wide range of sliding speeds, resulting in different operating modes for experiments with the clutches.
- A variety of requirements are imposed on the clutch in terms of comfort, service life, and safety, depending on the application.
- One friction partner is typically made of steel.
- The second friction partner is applied to a steel carrier plate and is generally made of bronze-based sintered metal, paper, or, more recently, carbon. The mechanical properties, as well as the cost, can be optimized through the use of fillers and chemical pre-treatments.
- Bronze-based sinter friction systems are generally used in industrial systems due to their beneficial thermomechanical properties, whereas paper friction systems are preferred in automotive applications due to their comfort advantages. Carbon friction systems combine the advantages of bronze-based sintered and paper friction systems but are currently found only in high-performance applications due to cost disadvantages.
- Several parameters, including mechanical and thermal loads, friction material, base oil, and additives, influence the friction characteristics.
- Wet multi-plate clutches are operated in boundary friction regime.

The literature distinguishes between long-term changes and spontaneous damage, and the following conclusions can be drawn:

- Depending on the friction pairing, different long-term modifications exist, which are especially well-researched for load shifting with sinter and paper friction systems. Little research exists on long-term modifications in the context of non-steady slip operation and continuous slip operation.

- For sinter friction systems, typical modifications include smoothing of the lining and decreasing the coefficient of friction. Several published damage models and wear diagrams are available for predicting long-term behavior, some of which account for temperature effects on damage behavior.
- In the case of paper friction systems, typical long-term modifications include adhesive wear, thermal degradation of the friction material, and glazing. Damage models for predicting service life behavior usually incorporate thermal loads on the friction system.
- The typical long-term changes of carbon friction systems are well-researched, especially for synchronizers. These changes include abrasive wear of the steel friction surface, low wear rates of the lining, fiber breakage, and fiber departure from the matrix. Additionally, the influence of lubricant additives and thermal effects on the clogging of lining pores and the resulting drop in the coefficient of friction become apparent.
- Spontaneous damage can also vary depending on the friction pairing. Numerous research contributions specifically address sinter and paper friction systems in load shifting, while limited research exists on non-steady slip operation and continuous slip operation.
- Typical spontaneous damage for sinter friction systems includes local discoloration, buckling of the steel plates, adhesive wear, and sinter carryover with an increase in the coefficient of friction. Thermal limits, specifically for local discoloration and sinter carryover, are published.
- Local discoloration, microstructural changes, cracking, buckling of the steel plates, hot spots with local compression, and hot bands constitute the most common spontaneous damage found in paper friction systems. No thermal limits are available in the current state of the art for various damage classifications.
- To date, only two research contributions address spontaneous damage in carbon friction systems. These focus on load shifting and report on lining damage.

Based on the findings regarding parameters that influence the load-carrying capacity of clutches and spontaneous damage, the following conclusions can be drawn:

- The development of local spontaneous damage can be explained by the theory of thermoelastic instability.
- Thermal stresses can explain the formation of buckling of the plates in the radial direction.
- Many theoretical studies propose sliding velocity limits as an influencing variable for spontaneous load-induced damage, while experimental studies propose limit curves depending on specific friction power and specific friction work.
- Many research papers propose temperature limits or temperature integral limits for long-term modifications. Regarding spontaneous damage, only damage limits exist for bronze-based sinter friction systems in load shifting with regard to thermal load.
- Cooling, influenced by oil flow rate and groove design, plays a minor role in the load-carrying capacity related to spontaneous damage.
- The Young's modulus of the friction lining and the thickness of the friction lining have a positive influence on the thermoelastic instability, whereas the tendency to buckling is not affected.
- The recommendations regarding the thickness of the steel plate contradict each other in parts of the literature. A thin steel plate is suggested in order to avoid thermoelastic instability, while a thick steel plate is recommended as a temperature sink.

- Low thermal expansion and large thermal conduction coefficients are proposed for the materials used. In addition, the ratio between the thermal conductivity coefficients of the lining and the steel plate should be one.

The following content of the researched experimental test procedures are important with regard to the present work:

- Depending on the research objective, it is necessary to consider the simplification of the system under study when performing experiments.
- Specially adapted test rigs are essential for research, tailored to the mode of operation.
- Step tests constitute the standard approach for load shifting to determine performance limits related to spontaneous damage. Specific friction work and specific friction power are increased step-wise until damage occurs. Only a small number of shifts are performed at each load level.
- Test procedures for slipping clutches focus on typical loads that occur in locking differentials and concentrate on investigating the coefficient of friction. Test methods for determining damage limits for the unsteady slip mode of operation are not available in the literature.

The numerical analysis of the thermomechanical behavior of clutches has been the subject of research for a long time. The following conclusions can be drawn from the findings of the literature research:

- In industry, specialized numerical solution methods such as KUPSIM are preferred over generic commercial software solutions.
- Finite difference and finite element methods are employed to solve the numerical problems.
- Typically, axisymmetric two-dimensional simulation models are created. Recently, more and more publications also calculate a three-dimensional structure for the clutch.
- The research objectives in the literature include the determination of heat distribution, thermal stresses, mechanical stresses, crack development, critical speeds in relation to thermoelastic instability, and influence parameters (geometry, material parameters) on the thermal level. Load shifting in clutches and brakes is considered. Slip applications are not addressed through simulation in the literature.

3 Aim and Structure of the Thesis

3.1 Problem Statement and Motivation

The transient slip operation of wet multi-plate clutches is discussed only in general terms and is rarely addressed in textbooks on mechanical engineering and drive technology. For example, Naunheimer [Nau19] differentiates between the load shifting and continuous slip operating modes without mentioning transient slip operation. In scientific publications, on the other hand, research exists on the transient slip behavior of wet multi-plate clutches [Sch06, Voe20a]. However, these studies are limited to evaluating friction and running-in behavior. While comprehensive research on the behavior of wet multi-plate clutches in transient slip operation remains lacking, it is established that thermal and mechanical overloads significantly impact their susceptibility to spontaneous damage. Several aspects of transient slip operation in wet multi-plate clutches remain largely unexplored. These include the types of spontaneous damage that can occur, how material parameters and the geometric design of steel and friction plates affect damage behavior, and the impact of such damage on further clutch operation. Detailed guidelines, design recommendations, or temperature limits for avoiding spontaneous damage in transient slip operation are absent in the current state of the art. Especially in heavy and sporty vehicles — the registrations of which are continuously increasing [Kor21, Kor22] — wet multi-plate clutches are deployed in transient slip operation for applications such as limited-slip differentials and torque vectoring systems to improve lateral dynamics. Therefore, a pressing need exists for understanding damage behavior and for subsequent design recommendations.

3.2 Research Objectives

This work aims to investigate the spontaneous damage behavior of wet multi-plate clutches in the transient slip operating mode and to derive design recommendations. Specifically, the following objectives are pursued:

- **Development of a test procedure:** Based on the literature review, a test procedure is developed to investigate various operating points related to spontaneous damage. The selection of relevant operating conditions and validation of the test procedure are achieved through preliminary experimental investigations.
- **Identification of damage patterns and damage progression:** Damage patterns and progression for different friction systems in transient slip operation are identified.
- **Analysis of macro- and microgeometric modifications:** Depending on the damage patterns, macro- and microgeometric modifications to the multi-plate clutches are determined.
- **Analysis of microstructure and elemental composition:** Microstructural modifications and elemental compositions on the friction interfaces are analyzed concerning their damage patterns.
- **Evaluation of the friction and temperature behavior under high loads:** The friction and temperature behavior under high loads, as well as during subsequent shifts at the run-in level, is compared and evaluated.
- **Evaluation of the friction behavior in case of prior damage:** The friction and service-life behavior of clutches that were previously affected by spontaneous damage are investigated and evaluated.

- **Analysis of temperature and pressure behavior:** The temperature and pressure behavior during the shifting process in the axial, radial, and circumferential directions are analyzed. Additionally, the effects of significant material and geometric parameters on these behaviors are identified.
- **Identification of damage limits:** Critical temperature ranges for the occurrence of spontaneous damage are proposed for the investigated friction systems.
- **Derivation of a surrogate model to prevent damage:** Using the simulation data and machine learning algorithms, a prediction model for the temperatures occurring during the shifting process is proposed.
- **Deriving design recommendations:** Recommendations are derived for the application and design of wet multi-plate clutches in transient slip operation to prevent spontaneous damage.

By achieving these objectives, many unresolved questions can be answered concerning the investigation of the spontaneous damage behavior of wet multi-plate clutches in transient slip operation.

3.3 Thesis Structure

The solution path is based on the objectives of this thesis. To achieve these objectives, the current state of the art was first analyzed comprehensively, and conclusions are drawn to guide the solution path of this work. Due to the complex physical and chemical interactions at the friction interfaces, extensive test rig-based investigations are required to analyze the spontaneous damage behavior. Hence, a test method is developed based on the state of the art. Experimental investigations are conducted with three different lining variants and three steel plate variants, and their spontaneous damage behavior is evaluated comparatively. Operating conditions are varied, and the factors influencing the damage of the different systems are investigated. An evaluation methodology is developed based on known characteristic values to assess the damage behavior of different multi-plate clutches. Topography measurements, EDX and SEM analyses, and microstructure investigations are carried out to characterize the damage behavior. Additionally, clutches are intentionally pre-damaged with spontaneous damage of various intensities, and the influence of the pre-damage on the friction and service life behavior is analyzed by endurance tests.

According to the current state of the art, the differences in the spontaneous damage behavior of various friction and steel plates are attributed to the temperature and pressure distribution of different systems. Since it is difficult to measure and analytically describe the temperature and pressure distribution in the multi-plate clutch, simulations are necessary to understand the aforementioned thermomechanical processes. To achieve this, a two-dimensional thermomechanical model is developed for a multi-plate clutch. Additionally, three-dimensional thermomechanical simulations are performed to analyze influencing variables that cannot be represented in two-dimensional simulations, such as circumferential direction analyses. Verification and validation of the models are conducted based on experimental investigations previously performed. Critical influencing factors are identified through parameter variations with respect to loads, material characteristics, and geometric dimensions. The simulation data of the two-dimensional thermomechanical model are used to develop predictive models for the temperature behavior in the clutch using machine learning algorithms. In the subsequent discussion, the findings are interpreted as a whole, classified in the state of the art, and model

conceptions and design recommendations are derived. For better clarification, the thesis structure is shown graphically in Figure 3.1.

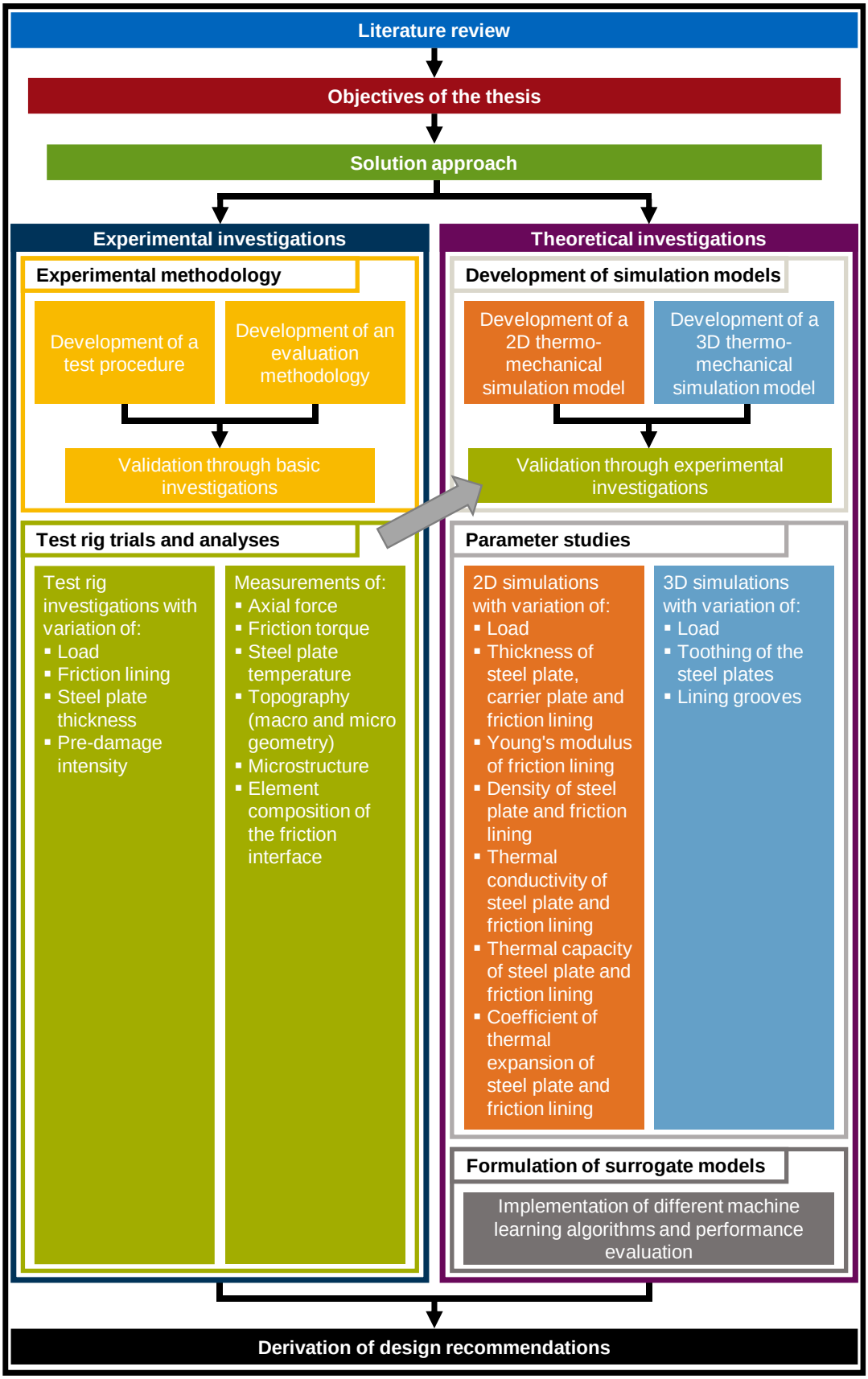

Figure 3.1: Visualization of the research methods applied, the correlations between the methods and the approach in this thesis.

4 Experimental Setup and Test Procedure

Experiments are carried out on the component test rig KLP-260 to investigate the spontaneous damage behavior of wet multi-plate clutches. The following sections explain the test equipment, test parts, test lubricant, experimental methodology, and evaluation methodology used in the study.

4.1 Test Rig, Measuring Equipment and Measuring Methods

4.1.1 Component Test Rig KLP-260

The experimental investigations are conducted on the component test rig KLP-260. The schematic structure is shown in Figure 4.1, and the relevant technical specifications are listed in Table 4.1. The KLP-260 test rig can operate in load shift, transient slip, and steady-state slip operating modes. A load cell connects the outer carrier to the test rig housing to measure the friction torque. The inner carrier is connected to the main shaft and can be driven by the main drive as well as the creep drive. If required, the inner carrier can be linked with the shiftable mass inertia J_2 as well as a manually adjustable inertia mass J_1. A hydraulic piston actuates the clutch with a displacement measuring system. The test clutch can be lubricated from the inside as well as from above with volume flow control and temperature control. In this way, it is ensured that the entire clutch assembly is well lubricated even at low speeds. In load-shifting mode, the speed-controlled main drive accelerates the main shaft, while an axial force is applied to the clutch plates by a force-regulated hydraulic cylinder through a thrust ring. In steady-state and transient slip operating modes, the clutch is subjected to a differential speed by the creep drive under defined axial force application. The electromagnetic clutch disconnects the main drive in this operating mode. [Mei15]

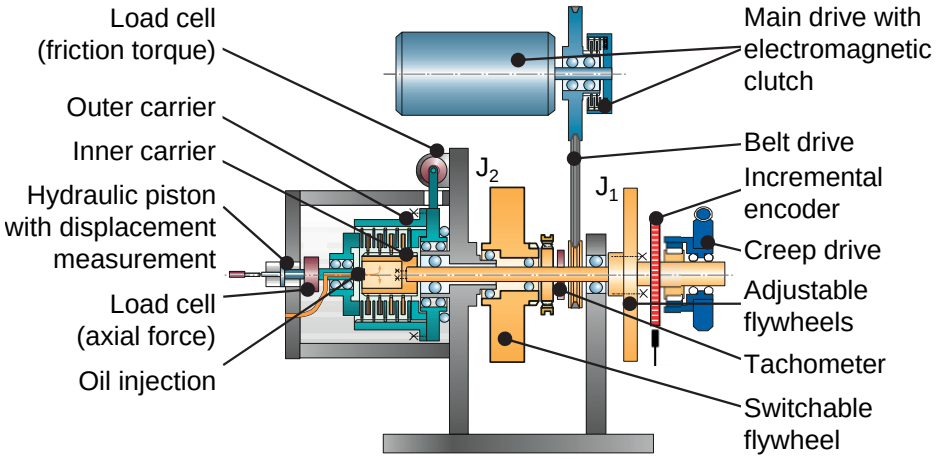

Figure 4.1: Schematic layout of the component test rig KLP-260 based on Meingassner [Mei15].

Max. friction torque in Nm	2 000
Max. axial force in N	20 000
Max. differential speed in min^{-1}	
• **Load shift mode**	7 000
• **Slip mode**	140
Mass moment of inertia in kgm^2	
• **J_1**	1.0
• **J_2**	0.1 … 0.75

Table 4.1: Technical data of the test rig KLP-260 [Mei15].

4.1.2 Macrogeometry Analyses

To determine macrostructural changes, three-dimensional topography measurements are conducted on plates with varying degrees of damage using the Infinite Focus G4 measuring device, as shown in Figure 4.2. The optical three-dimensional surface measuring device Infinite Focus G4 from Alicona is based on focus variation technology, also known as shape-from-focus. Focus variation is an area-based method to obtain an image with a full depth of focus and three-dimensional information of the object for optics with a shallow depth of focus. The height data necessary for a three-dimensional display is obtained by varying the focus position. The method can also be combined with active illumination to measure surfaces with poor structure, such as reflective surfaces. The system has various magnification objectives to measure objects at different resolutions. [Ali22]

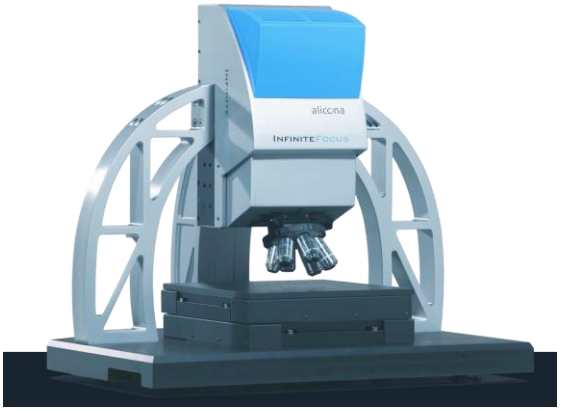

Figure 4.2: Measuring system Alicona Infinite Focus G4 [Ins22].

A 5x magnification objective is used for the measurements, which allows for a minimum measurable height of 0.41 µm and a measurement accuracy of 0.05 % at a step height of 1 mm. The chosen objective offers the optimal measurement time and accuracy balance for measuring steel and friction plate deformations.

4.1.3 Metallographic Analyses

Micrographs of individual steel plates are taken using standardized metallographic methods to qualitatively and quantitatively describe their microstructure. For this purpose, small samples are separated from the steel plates, which are embedded in synthetic resin for better handling. The samples are then ground and polished in several steps. Due to the high reflectivity of the surface, only the microstructural details whose reflectivity deviates extensively are detected on a polished surface. Generally, only non-metallic inclusions, cracks, and pores are examined in this condition of the sample. The polished surface is chemically etched with dilute acid (Nital 2 %, 3 s) to increase contrast, resulting in different reflectance conditions for the individual microstructural constituents. Analyses are performed on steel plates in new and used conditions. An Axio set from Carl Zeiss with various optics is used to create the micrographs. In addition, Vickers Hardness measurements in the low force range (HV1) according to DIN EN ISO 6507-1 [DIN18] are carried out using a fully automatic hardness tester Q60A from Qness. The measurements are performed on the inner, mean, and outer friction diameters. Type ARL infrared spectroscopy is applied for quantitative elemental analysis of the steel plates.

4.1.4 Microgeometry and Elemental Analyses

A scanning electron microscope (SEM) from CamScan is used to examine the sample surfaces. The SEM works by directing an electron beam onto the surface being studied within a vacuum chamber. As the electron beam interacts with the sample, different types of electrons are emitted from its surface. Detectors are utilized to record secondary electrons, backscattered electrons, and X-rays. To analyze the surface, the emitted secondary electrons

are observed. With the help of the backscattered electrons, material contrast is displayed. The emitted X-rays enable identification of the chemical elements. These X-rays are evaluated using energy-dispersive spectroscopy (EDX). The sample must undergo preparation before it can be examined with the SEM. Generally, samples need to be conductive to prevent charging under the electron beam. For non-conductive materials, conductivity is achieved by applying a thin layer of conductive platinum using a physical vapor deposition process. The measurements are conducted in each case on the mean friction diameter.

4.2 Test Parts and Lubricant

In the experimental tests, five selected friction systems are investigated. The use of series parts ensures a high application relevance of the results as well as a high manufacturing consistency. The test parts and lubricants are used in limited slip differentials.

The clutches under investigation consist of 10 friction interfaces with six outer and five inner plates. The assembly configuration of a clutch set is shown in Figure 4.3. The plates are marked for clear identification and are aligned with the corresponding markings on the carriers for reproducible assembly. The thermocouple (type K) for temperature measurement during the tests is mounted in the steel plate with the marking "C" in the center of the clutch assembly. A more detailed illustration for fixing the thermocouple can be found in Section 4.5.3.

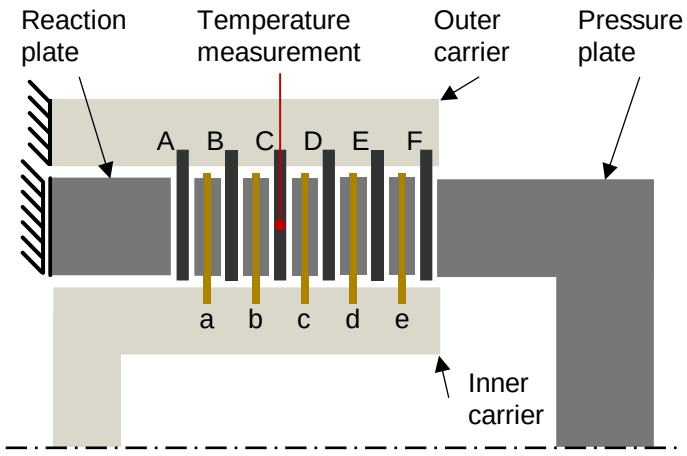

Figure 4.3: Schematic assembly of a clutch disk set with outer toothed steel plates and inner toothed friction lining disks in the component test rig KLP-260.

Figure 4.4 shows photographs of the investigated steel plate and their corresponding friction plates. The steel plates serve as outer plates, and the friction plates act as inner ones. Three different types of friction plates are being investigated. Friction plate FP1 features a paper friction lining, while friction plate FP2 has a carbon composite friction lining. Both friction plates possess the same segmented groove pattern. Friction plate FP3 has a woven carbon friction lining and differs from FP1 and FP2 in its groove pattern. All three friction plate variants are manufactured in one batch each.

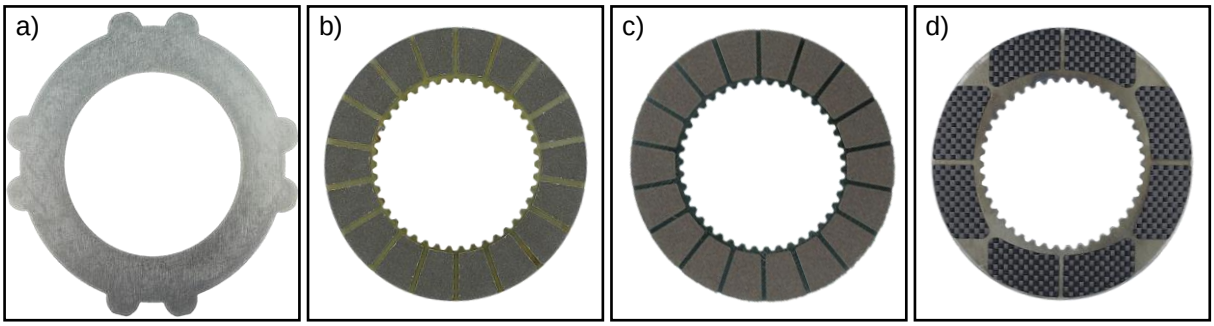

Figure 4.4: Photos of the test parts: a) steel plate, b) friction plate FP1 with paper friction lining, c) friction plate FP2 with carbon composite friction lining, d) friction plate FP3 with woven carbon friction lining.

The geometric dimensions of the friction plates are listed in Table 4.2.

	Symbol	FP1	FP2	FP3	Unit
Inner diameter friction lining	$d_{i,fl}$	68	68	70.5	mm
Outer diameter friction lining	$d_{a,fl}$	104	104	104	mm
Thickness friction lining	t_{fl}	0.39	0.39	0.27	mm
Thickness carrier plate	t_{cp}	0.8	0.8	0.8	mm

Table 4.2: Geometry data of the friction plate variants FP1, FP2, and FP3.

There are a total of three variants of steel plates. Steel plate SP1, also shown in Figure 4.4, serves as the reference. Steel plates SP2 and SP3 differ from steel plate SP1 by their thickness. Each variant of steel plates is produced in a single batch by one manufacturer. The geometrical sizes of the steel plates are listed in Table 4.3.

	Symbol	SP1	SP2	SP3	Unit
Inner diameter steel plate	$d_{i,sp}$	70	70	70	mm
Outer diameter steel plate	$d_{a,sp}$	105	105	105	mm
Thickness steel plate	t_{sp}	0.8	1.2	1.6	mm

Table 4.3: Geometry data of the steel plate variants SP1, SP2, and SP3.

Figure 4.5 shows the technical drawings of the steel plate SP1 and friction plate FS1.

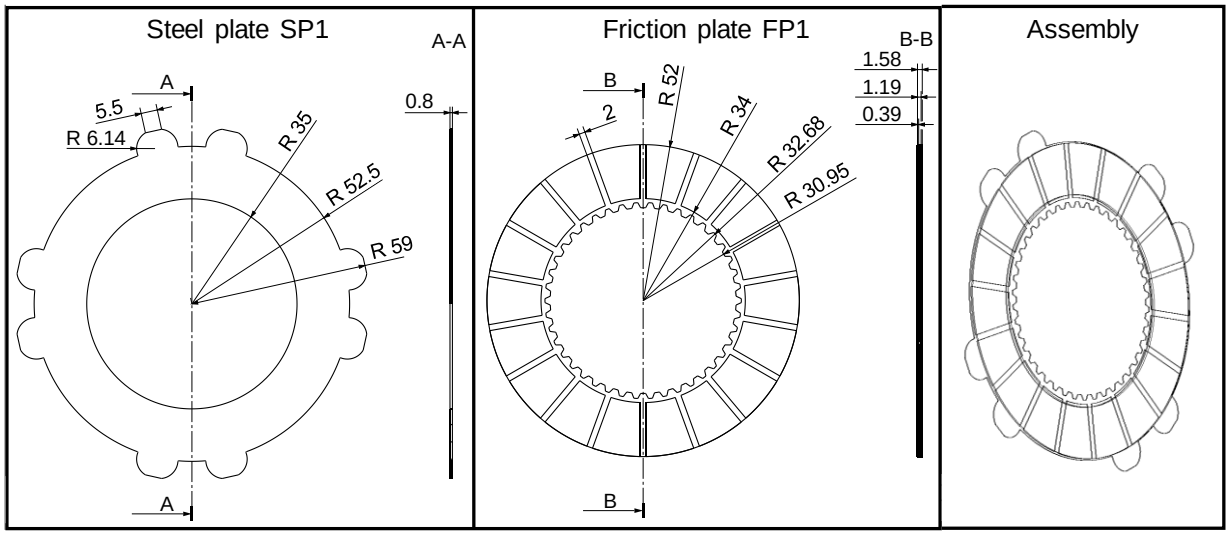

Figure 4.5: Technical drawings of the steel palte SP1 and friction plate FP1, and the assembly [Sch22c].

Twelve steel plates are analyzed by spark spectroscopy to determine their microstructural composition. In addition, Vickers Hardness measurements in the low force range (HV1) and microstructural examinations using micrograph analyses, as described in Section 4.1.3, are conducted. The results of the hardness measurements of the 12 steel plates are shown in Figure 4.6. The median hardness of the measured steel plates is 544.5 HV. Furthermore, Figure 4.6 displays three exemplary micrographs of the steel plates. The micrographs illustrate that the microstructure is martensitic. The chemical composition of the twelve steel plates measured can be seen in Figure 4.7.

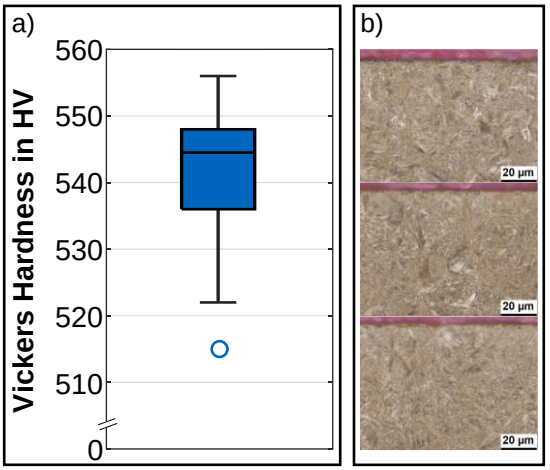

Figure 4.6: a) Measured Vickers Hardness of the steel plates, b) exemplary micrographs of the steel plates.

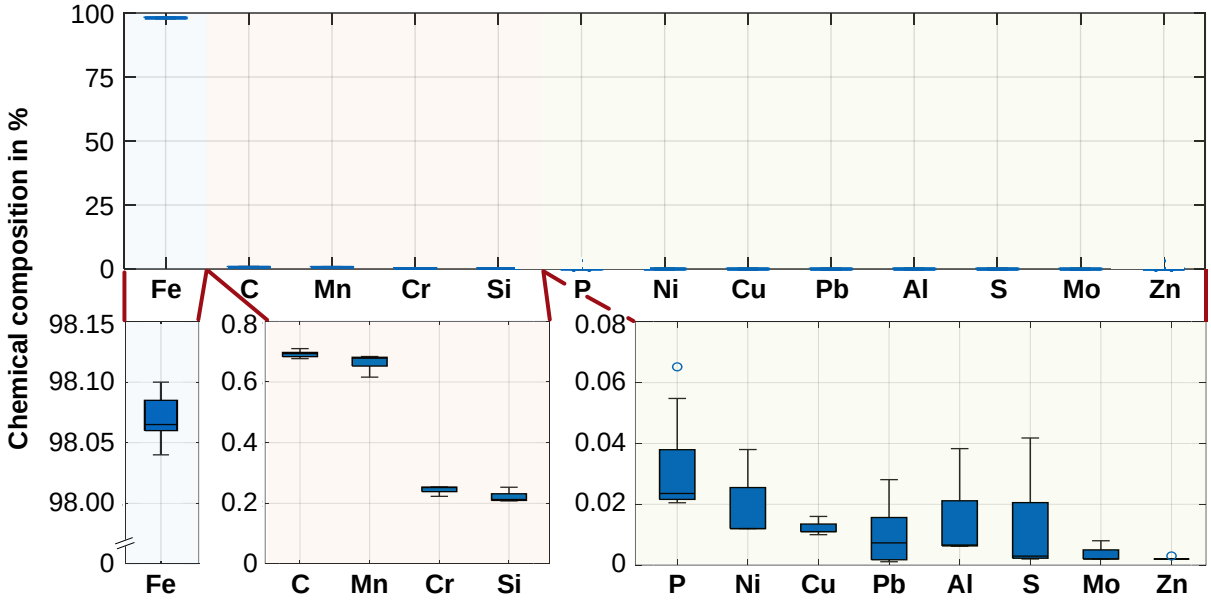

Figure 4.7: Chemical composition of 12 measured steel plates.

Different friction systems are set up from the various friction and steel plates (see Table 4.4). The friction systems FS1, FS2, and FS3 are formed from the reference steel plate SP1 and the friction plates FP1, FP2, and FP3. For the friction systems FS4 and FS5, the friction plate FP1 is used, and the steel plates are varied (SP2, SP3).

	FS1	FS2	FS3	FS4	FS5
Steel plate	SP1	SP1	SP1	SP2	SP3
Friction plate	FP1	FP2	FP3	FP1	FP1

Table 4.4: Assembly of the different friction systems formed from the various friction and steel plates.

The lubricant used for the experimental tests is a standard oil from the application of limited slip differentials and is made from synthetic oils and additives. The exact composition, as published by the manufacturer, is listed in Table A.1 in the appendix. In addition, an oil sample was analyzed by the company Oelcheck with regard to its element concentration (see Table 4.5) and its physical properties (see Table 4.6).

Element		Unit	Value
Calcium	Ca	mg/kg	2
Magnesium	Mg	mg/kg	1
Boron	B	mg/kg	231
Zinc	Zn	mg/kg	1
Phosphorus	P	mg/kg	2749
Barium	Ba	mg/kg	0
Molybdenum	Mo	mg/kg	1
Sulfur	S	Wt.%	2.64

Table 4.5: Element concentrations of the lubricant used.

Property	Unit	Value
Viscosity at 40 °C	mm^2/s	50.75
Viscosity at 100 °C	mm^2/s	9.17
Viscosity index	–	165

Table 4.6: Properties of the lubricant used.

4.3 Experimental Methodology

This section provides an overview of the procedure, conditions, and evaluation of the experiments. The same procedure and comparable conditions are considered for each experiment.

4.3.1 Run-In

Before the tests are carried out, all clutch assemblies undergo a run-in procedure. The characteristic of the run-in process is a nonlinear change in the coefficient of friction as a function of the number of shiftings [Voe20a]. According to Voelkel [Voe20a], a run-in is considered complete when the change in the coefficient of friction stabilizes into an approximately linear pattern (see Figure 4.8). In order to investigate the running-in behavior of slipping clutches as closely as possible to the application, Voelkel [Voe20a] describes a test methodology that serves as the basis for this work. A load collective consisting of six application-typical load levels with different contact pressure and differential speed is performed. Figure 4.9

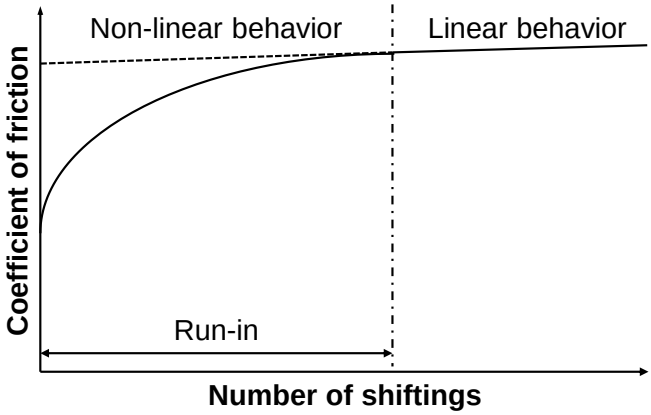

Figure 4.8: Exemplary coefficient of friction trend at the beginning of operation with identification of the phase of the run-in (based on Voelkel [Voe20b]).

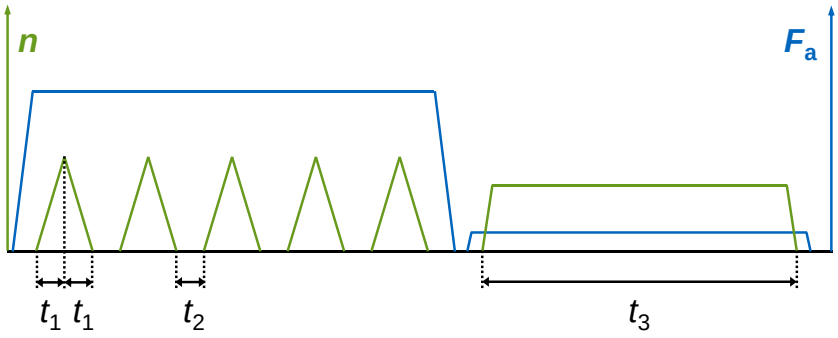

Figure 4.9: Schematic representation of a slip cycle (based on Voelkel [Voe20b]).

illustrates a slip cycle in transient slip, which includes five slip phases and a subsequent cooling phase, in a schematic format. In a slip phase, the clutch, subjected to an axial force, accelerates to a defined speed and then decelerates using a triangular differential speed curve (ramp t_1 = 1 s). Between the individual slip phases, the closed clutch remains stationary for a duration of t_2 = 1 s. In the cooling phase, the clutch is driven at a defined speed for a duration t_3 = 20 s to ensure complete cooling of all plates. The load collective of the run-in, consisting of six load levels, cycles a total of 200 times. Table 4.7 presents the various load levels, S1 through S6, of the load collective, along with their associated data. The load levels are cycled in the order S1-S4-S2-S5-S3-S6. [Voe20a]

Load level	Pressure in N/mm²	Differential speed in min⁻¹
S1	0.75	25
S2	1.50	25
S3	3.00	25
S4	0.75	50
S5	1.50	50
S6	3.00	50

Table 4.7: Data of the load levels of the run-in (based on Voelkel [Voe20b]).

4.3.2 Step Test

Based on the state of the art, step tests are applied to investigate spontaneous damage in this thesis. In step tests, one or more load parameters are usually increased stepwise during the test, enabling documentation of damage progression. The specific load of a multi-plate clutch (specific friction work, specific friction power) during transient slip operation is determined by the pressure, maximum differential speed, and load duration parameters, assuming a constant coefficient of friction. In this work, the goal is to investigate the largest possible parameter space. Therefore, all parameters are varied. The pressure and maximum differential speed vary between the different step tests, each employing its own test clutch. Within a step test, the load duration and the number of slip phases are increased (see Figure 4.10). A load level is defined by the number of slip phases N; i.e., load level 1 consists of one slip phase, load level 2 consists of two slip phases, and so forth. By increasing the number of slip phases from load level to load level, an increase in the specific friction work is achieved.

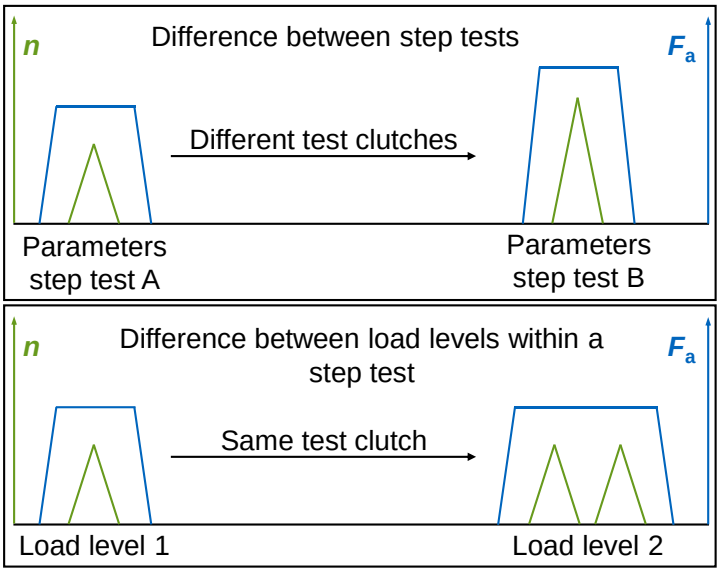

Figure 4.10: Schematic representation of the differences between step tests and the differences of load levels within a step test.

Before the start of each step test, the test rig is idled for one hour at an oil injection temperature of 80 °C. Thereby, a stationary mass temperature of the test parts is achieved and a stationary temperature distribution of the test rig mass is assumed. Afterward, the multi-plate clutch to be tested performs a load level consisting of ten repetitions of a slip cycle. The number of repetitions is based on Strebel's [Str16] research results for load shifting and is deliberately

chosen low to exclude long-term changes of the clutch. However, it is still high enough to detect possible random effects on spontaneous damage. Each slip cycle is followed by a cooling phase in which the plates cool down to the initial temperature of $T = 80$ °C. For this purpose, the signal of the thermocouple in steel plate “C” is used (see Figure 4.3). Each load level is followed by a reference load level with loads S5 (see Table 4.7) from the run-in. The slip cycle of the reference load level is run ten times and is used to evaluate the damage progress of the clutch pack (see Figure 4.11). After the completion of a load level, including reference cycles, the plates are cleaned, inspected for damage, and any damage is documented. After the visual inspection of the clutch, it is reinstalled in the test rig in accordance with Section 4.2. After that, the next higher load level is executed, and the procedure is repeated until the clutch failure occurs. The specific oil flow rate during the load levels is $\dot{v}_{oil} = 0.25\ mm^3/mm^2/s$. The oil flow is supplied from the inside (50 %) and the top (50 %). Due to the external lubrication, the clutch is lubricated even at low speeds.

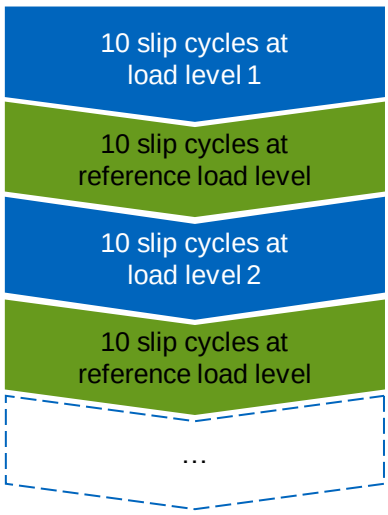

Figure 4.11: The procedure of a step test.

In addition to the spontaneous damage behavior in step tests, the influence of spontaneous damage on the friction behavior in endurance operation is investigated in experimental tests. In the first step, clutches undergo specific pre-damage in step tests following their run-in. In the second step, endurance tests are conducted using both these pre-damaged clutches and a non-pre-damaged reference clutch. The loads in the endurance tests correspond to the running-in conditions (see Table 4.7). The collective number is set at 1 000. The friction behavior of the pre-damaged clutches is then compared to that of the reference system and evaluated.

4.3.3 Evaluation Methodology

Particular emphasis is put on evaluating the friction behavior, in addition to topography measurements, visual examinations, temperature measurements, microstructure analyses, SEM, and EDX measurements. The friction behavior is described by characteristic coefficient of friction values and the progression of the coefficient of friction over the slip speed, also known as friction characteristic. Voelkel [Voe20a] uses the friction characteristic for the transient slip to define the characteristic value μ_{top}, which describes the coefficient of friction at maximum slip speed, and thus, characterizes the coefficient of friction level (see Figure 4.12).

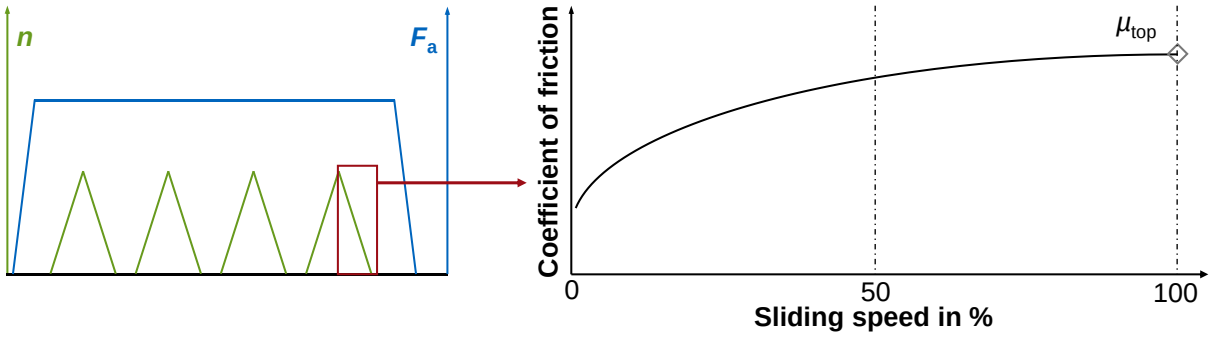

Figure 4.12: Exemplary friction characteristic for transient slip with coefficient of friction value μ_{top} (based on Voelkel [Voe20a]).

The friction properties are evaluated based on the last slip phase (see Figure 4.13). The coefficient of friction is plotted against the slip speed for the descending part of the slip phase. From this analysis, an objective description of the friction behavior is derived, using the coefficient of friction value μ_{top}. Further evaluation steps are then carried out. Bar charts with error bars are used to present the values of μ_{top} for each load level and each reference load level in the step tests. This enables the scatter of the coefficient of friction value μ_{top} within a load level to be evaluated, as well as any change in the coefficient of friction level across the individual load levels. In the case of the run-in and endurance tests, the coefficient of friction value μ_{top} is plotted against the number of cycles. This approach enables the evaluation of the development of the friction behavior over the entire test and the assessment of the reproducibility of several tests.

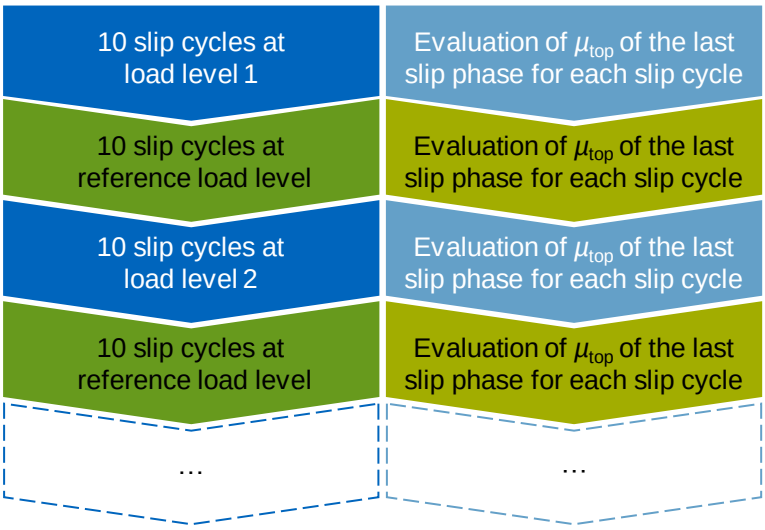

Figure 4.13: Procedure and evaluation of a step test.

4.4 Experimental Program

This section provides an overview of the experimental procedure and conditions. The same procedure and comparable conditions are applied to each experiment. The conditions of the basic investigations are presented first. The experimental program of the extended investigations is based on the results of the basic experiments, which are presented in Section 5.1.

4.4.1 Basic Investigations

Preliminary experiments are conducted to select the relevant operating conditions for the investigations of the damage behavior. In the initial step, the study aims to determine damage patterns in the case of failure for the friction systems FS1, FS2, and FS3. For this aim, the number of slip phases N is incrementally increased until failure occurs under constant load parameters. Additionally, the study addresses questions regarding the influence of the oil flow rate and the number of friction interfaces on temperature behavior by varying the loading parameters (pressure, max. differential speed). In the last step, the load ranges essential for conducting a meaningful analysis of damage behavior are determined. Table 4.8 shows the experimental test parameters of the different basic investigations.

	Damage patterns in case of failure	Influence of the oil volume flow on the thermal behavior	Influence of the number of friction interfaces on the thermal behavior	Influence of the load on the spontaneous damage behavior
Friction system	FS1 | FS2 | FS3	FS1	FS1	FS1 | FS2 | FS3
Pressure p in N/mm²	6.0	1.0 … 8.0	1.0 … 8.0	1.0 … 8.0
Max. differential speed Δn_{max} in min⁻¹	100	10 … 140	10 … 140	10 … 140
Oil volume flow $\dot{v}_{oil}$ in mm³/mm²/s	0.25	0.25 | 0.50 | 1.00	0.25	0.25
Number of friction interfaces z	10	10	6 | 10 | 14	10
Oil temperature T_{oil} in °C	80	80	80	80
Number of slip phases N	1 … 15	10	10	1 … 15

Table 4.8: Experimental test parameters of the basic investigations.

4.4.2 Extended Investigations

In the extended investigations, spontaneous damage behavior is examined in more detail. The results of the basic investigations inform the design of the extended investigations. This leads to an oil flow rate of 0.25 mm³/mm²/s and a number of friction interfaces of 10. The oil injection temperature is 80 °C. The mechanical loads are adapted to the friction system (FS1, FS2, FS3, FS4, FS5) to enable efficient and representative studies. Step tests are conducted in the extended experiments using the friction systems with the loads, as shown in Table 4.9, until failure. To analyze the damage behavior more precisely, topography measurements, optical assessments, temperature measurements, residual stress measurements, microstructure investigations, SEM and EDX measurements, as well as friction behavior investigations, are conducted with the clutches during the extended experiments. In the extended experiments, apart from the damage behavior alone, the influence of spontaneous damage intensity on the further clutch operation is also to be considered. For this purpose, individual clutch assemblies are pre-damaged, and an endurance test is run. This allows for a more detailed study of the friction behavior of pre-damaged clutches, compared to the non-pre-damaged reference system. The loads and the procedure in the endurance test correspond to those of the run-in (see Table 4.7) with a collective number of 1 000.

	FS1 | FS2 | FS3 | FS4 | FS5
Pressure p in N/mm²	4.0 … 8.0
Max. differential speed Δn_{max} in min⁻¹	50 … 140
Number of slip phases N	Until clutch failure

Table 4.9: Experimental test parameters of the extended tests

4.4.3 Test Overview

For better understanding, Figure 4.14 provides a schematic representation of the different types of tests, measurements, and analyses conducted in both the basic and extended investigations.

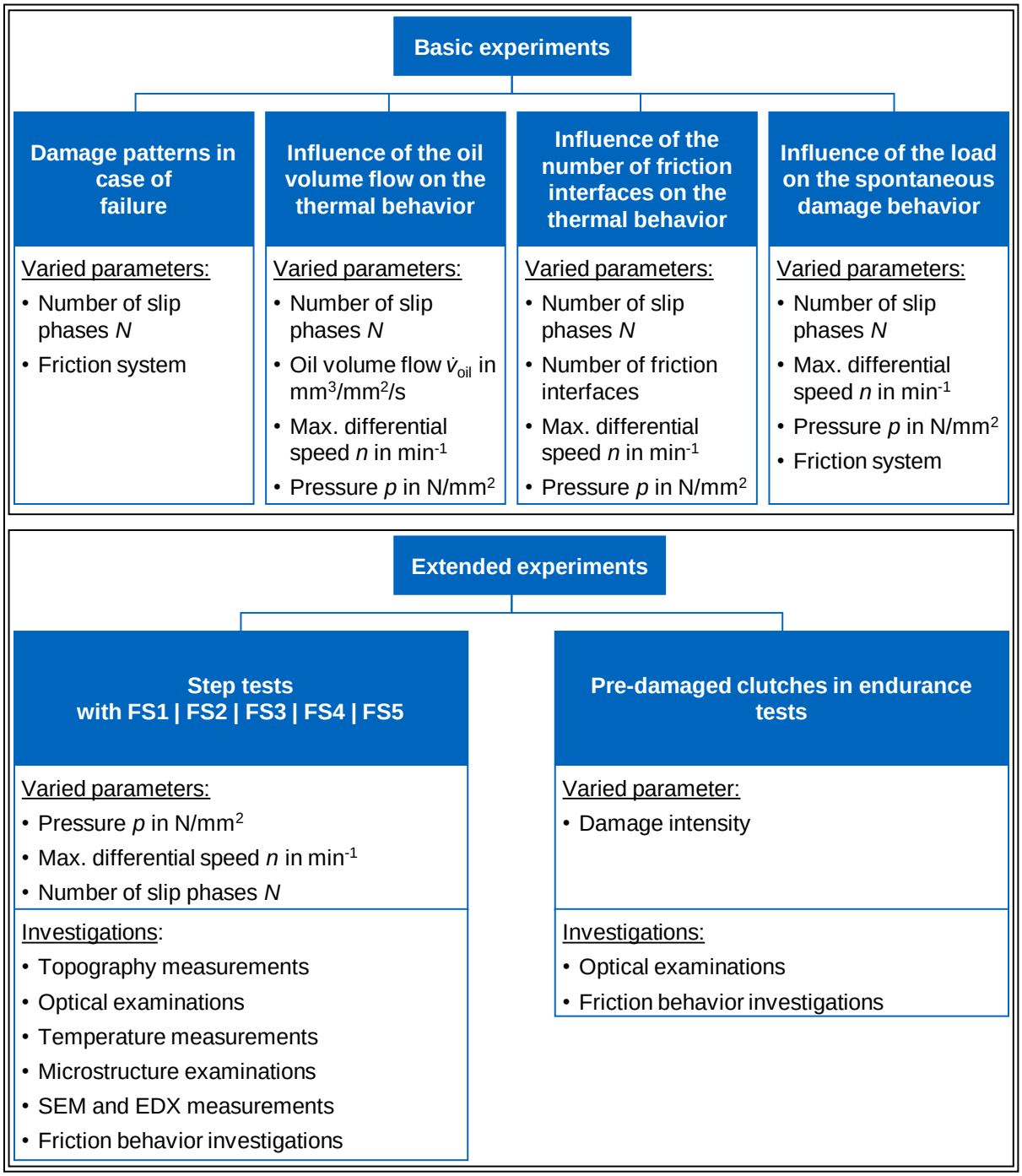

Figure 4.14: Schematic overview of the experimental program.

4.5 Measurement Accuracy

In the following section, an evaluation of measurement uncertainties of relatively measured parameters at the test rig KLP-260 is carried out according to the Guide to the Expression of Uncertainty in Measurement (GUM) from the Joint Committee for Guides in Metrology [Joi08]. Uncertainties for the coefficient of friction, the creep drive speed, and the steel plate

temperature are given because these parameters are included in the evaluation of the test results. Therefore, it is essential to understand the accuracy and deviations of the measurements in order to evaluate the gathered data properly. The analyses are based on the work of Baumgartner [Bau20], Schmid [Sch21a], and Willand [Wil21].

4.5.1 Determination of the Coefficient of Friction

The coefficient of friction is calculated using Equation (4.1), which combines the measured values of axial force F_a and friction torque T_f with the constant variables of number of friction interfaces z and mean frictional radius r_m. Both the axial force F_a and the friction torque T_f are measured by load cells. Both load cells are calibrated together with their amplifiers at the test rig. Variables that influence the measurement uncertainty for axial force F_a and friction torque T_f are:

$$\mu = \frac{T_f}{F_a \cdot z \cdot r_m} \qquad (4.1)$$

- Measurement uncertainty of the voltage signal of the transducer.
- Measurement uncertainty of the applied calibration force.
- Measurement uncertainty of the calibration factor.

Figure 4.15 shows the relative measurement uncertainty $U_{\mu,rel}$ of the coefficient of friction for temperatures of the load cells for axial force and friction torque of 70 °C in a three-dimensional plot. The results are projected into a two-dimensional plot to interpret the measurement uncertainty better. The coverage probability is p = 95.45 %. The relevant map range is depicted by drawing three characteristic curves as examples. Along these curves, the coefficient of friction μ assumes specific values ($\mu = 0.15$, $\mu = 0.10$, $\mu = 0.05$). Based on the axial forces measured in operation ($F_a > 10\,000$ N), a relative measurement uncertainty of $U_{\mu,rel} \approx 1.35$ % can be assumed accordingly.

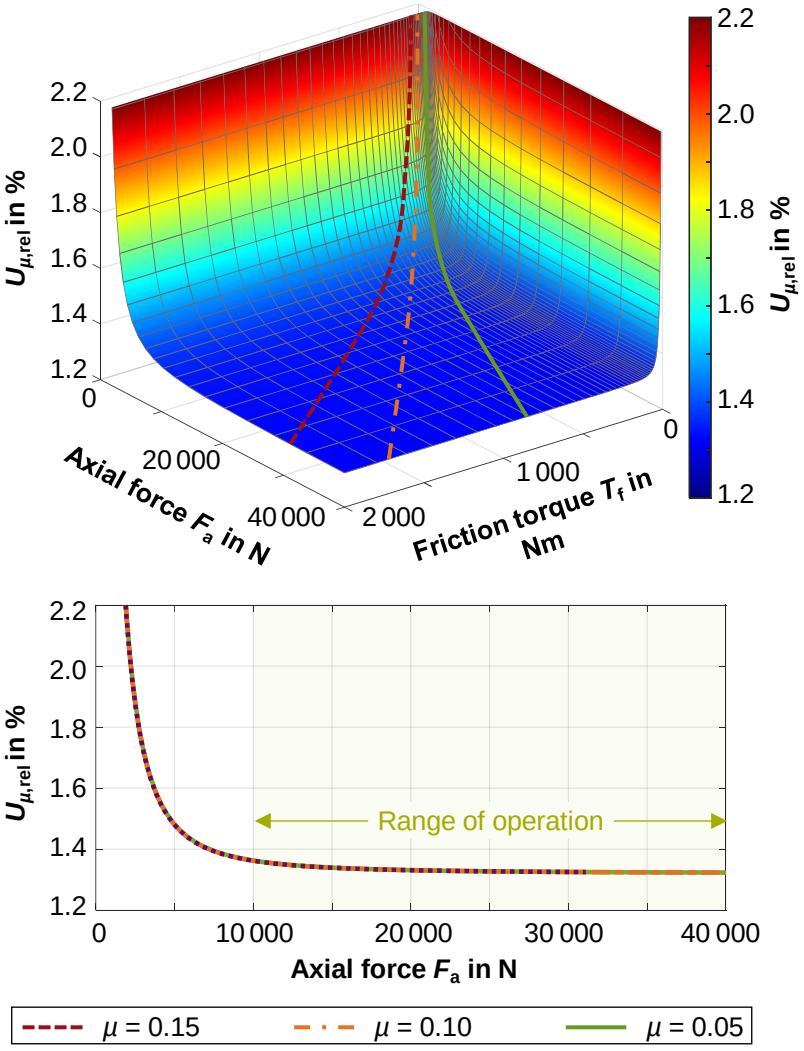

Figure 4.15: Relative measurement uncertainty $U_{\mu,rel}$ of the coefficient of friction μ in % at assumed sensor temperature of 70 °C.

4.5.2 Determination of the Sliding Speed

An incremental encoder is used to measure the slip speed. This encoder determines the angular velocity of the drive by photoelectric scanning. The variables that influence the measurement uncertainty of the slip speed at the creep drive include:

- Measurement uncertainty during speed measurement.
- Measurement uncertainty of the resolution at pulse converter.
- Measurement uncertainty of the voltage signal of the transducer.

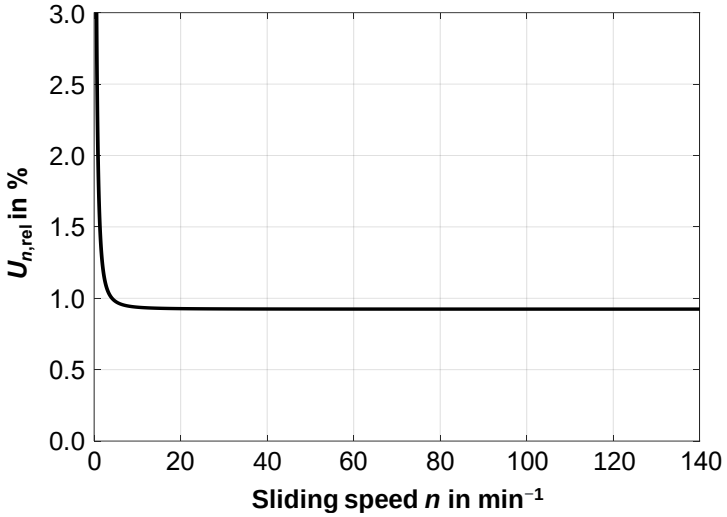

Figure 4.16: Relative measurement uncertainty $U_{n,rel}$ for slip speed in %.

Figure 4.16 shows the relative measurement uncertainty $U_{n,rel}$ for the slip speed with a coverage probability of p = 95.45 %. It indicates that for slip speeds $n > 10\,\text{min}^{-1}$, which are relevant for the scope of this work, the relative measurement uncertainty $U_{n,rel}$ is below 1.0 %.

4.5.3 Determination of the Steel Plate Temperature

A temperature sensor is fitted to a steel plate to measure the clutch's temperature during operation accurately (see Section 4.2). For this purpose, a hole is radially drilled in a steel plate into which the temperature sensor is inserted (see Figure 4.17). The drill hole has a diameter of $d_b = 0.3$ mm and is drilled radially up to the mean friction diameter of the steel plate. A type K thermocouple NiCr-Ni [The22] is used for temperature measurement. The sensor has an Inconel 600 outer sheath and a diameter $d_t = 0.25$ mm. The measuring range and the limit deviations for type K thermocouples are specified in DIN EN 60584 [DIN14]. Before the thermocouple is attached, thermal paste [Coo22] is inserted into the hole. For considering the relative measurement uncertainty of the thermocouple, the following parameters are taken into account:

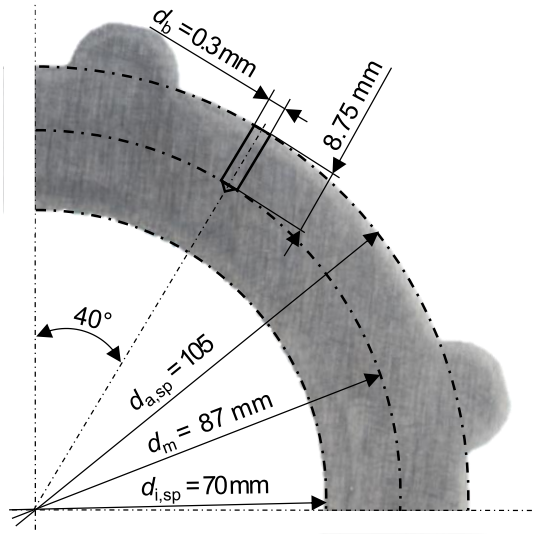

Figure 4.17: Position of the hole for the thermocouple and dimensions of the steel plate

- Measurement uncertainty of type K thermocouple according to DIN EN 60584-1 [DIN14] for $T < 1000$ °C.
- Measurement uncertainty of the voltage signal of the transducer.

The relative measurement uncertainty $U_{T,\mathrm{rel}}$ is shown in Figure 4.18, with a coverage probability of p = 95.45 %. For temperatures above 80 °C, it illustrates that the relative measurement uncertainty $U_{T,\mathrm{rel}}$ is below 3.0 %, and above 250 °C, it is below 1 %. To consider the response time of the thermocouple, the diameter of the thermocouple, the depth of the hole and the material values of Inconel 600 are taken into account. Assuming that 25 % of the sheath surface is in contact, the response time is 7 ms. A detailed calculation for the response time can be found at Willand [Wil21].

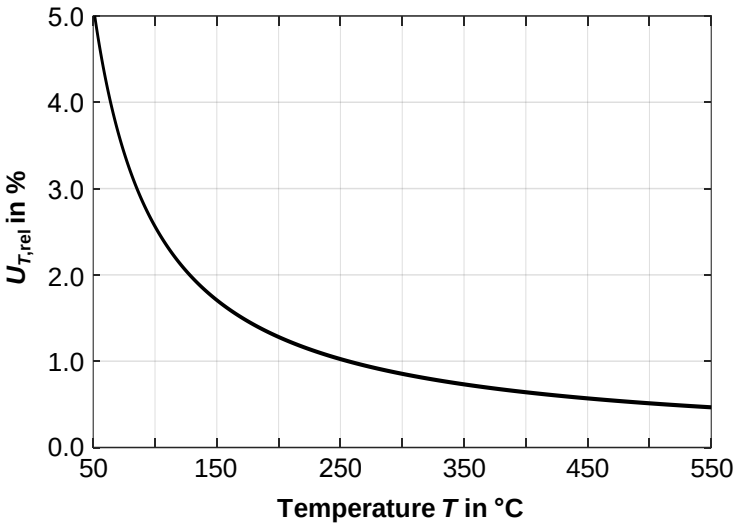

Figure 4.18: Relative measurement uncertainty $U_{T,\mathrm{rel}}$ for steel plate temperature in %.

5 Experimental Results on the Spontaneous Damage Behavior

This section presents the results of all the experimental work carried out as part of this thesis. In the first step, the results of the basic investigations on the test rig KLP-260 are presented, followed by the results of the extended investigations. The test procedure and evaluation of the test results documented in the following correspond to the test conditions and evaluation methods described in Section 4.

5.1 Results of Basic Investigations

The results of the basic investigations presented in the following section are primarily used to select relevant operating conditions for the extended investigations.

5.1.1 Damage Patterns in the Case of Failure

Initially, the cause of the failure of the friction system variants (FS1, FS2, FS3) is investigated. For this purpose, step tests, as described in Section 4.3.2, are carried out on the component test rig KLP-260 under the specified parameters:

$$p = 6.0\ \mathrm{N/mm^2},\ n = 100\ \mathrm{min^{-1}},\ T_{oil} = 80\ °\mathrm{C},\ \dot{v}_{oil} = 0.25\ \mathrm{mm^3/mm^2/s}$$

The clutch assemblies are removed after each load level, inspected for damage, and operated until system failure. Figure 5.1 shows the friction interfaces corresponding to the failure load level for the FS1 friction system. For the steel plates, discoloration of the friction interface can be seen on the outer friction areas of the clutch assembly (friction interfaces 1, 2, 3, 8, 9, and 10). Damage to the steel plates is more intense in the center of the clutch assembly (friction interfaces 4, 5, 6, and 7). In addition to severe discoloration, deformation in the form of buckling of the steel plates can also be observed. This deformation is up to 3 mm in the axial direction and leads to the fact that the system can no longer be operated. In the case of the friction material, the damage is discoloration of the friction linings and groove areas. The pictures show that the discoloration on the friction linings increases toward the center of the clutch assembly.

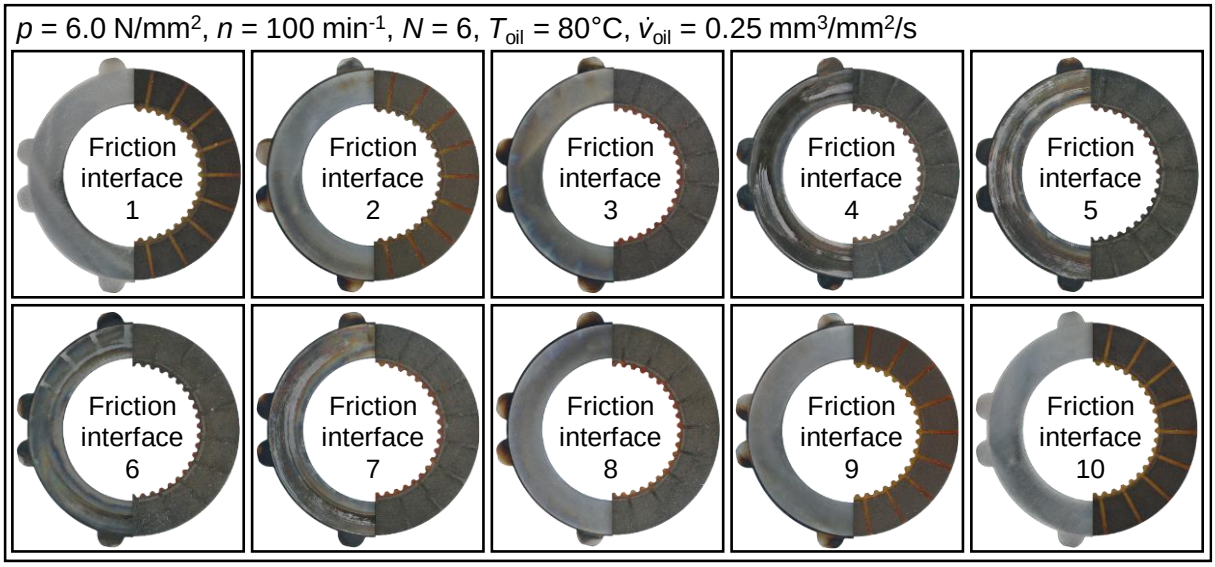

Figure 5.1: Damage patterns of friction system FS1.

Figure 5.2 shows the friction interfaces for the friction system FS2 after clutch failure. The cause of the failure of friction system FS2 is buckling of the steel plates in the center of the clutch assembly (friction interfaces 4, 5, 6, and 7). Further damage to the steel plates includes discoloration of the steel plates, which intensifies to the center of the clutch assembly. The

friction material also discolors strongly, except for interfaces 1 and 10. The friction material in contact with buckled steel plates (e.g., friction area 7) is abrasively worn on the outer diameter.

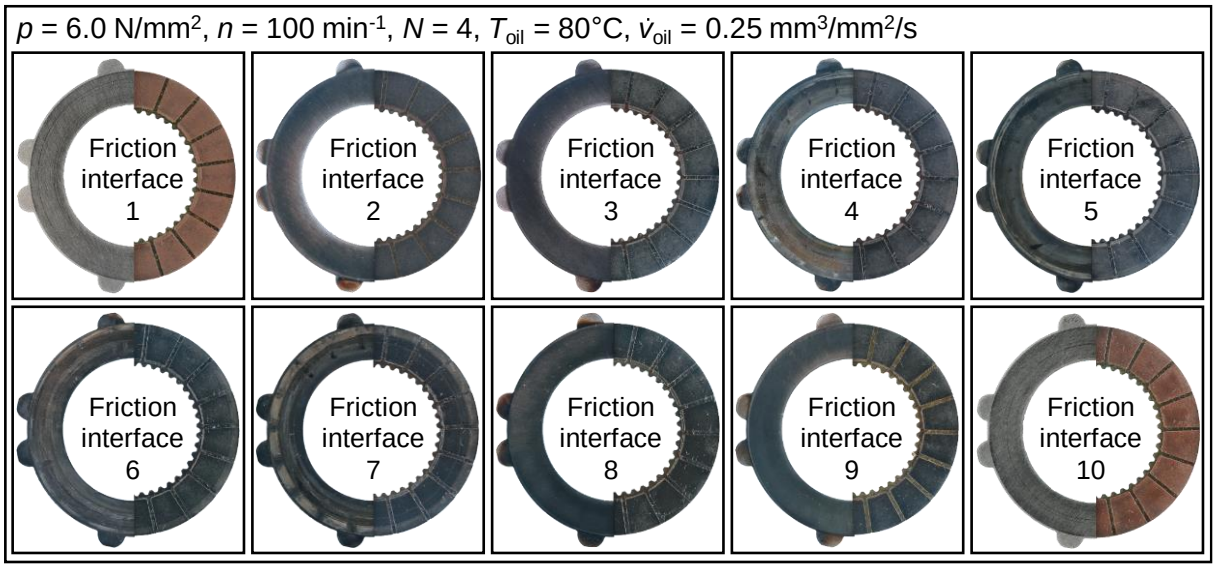

Figure 5.2: Damage patterns of friction system FS2.

For FS3, detachment of the friction lining leads to the failure of the system (see Figure 5.3). In the case of the friction plates in the middle of the clutch, the lining detaches completely (friction interfaces 3, 4, 5, 6, 7, and 8). The friction lining displaces from the carrier plate for the friction plates at the outer ends of the clutch. In contrast to friction systems FS1 and FS2, no buckling of the steel plates can be observed. Only a discoloration of the steel plates occurs, which is more noticeable in the center of the clutch assembly.

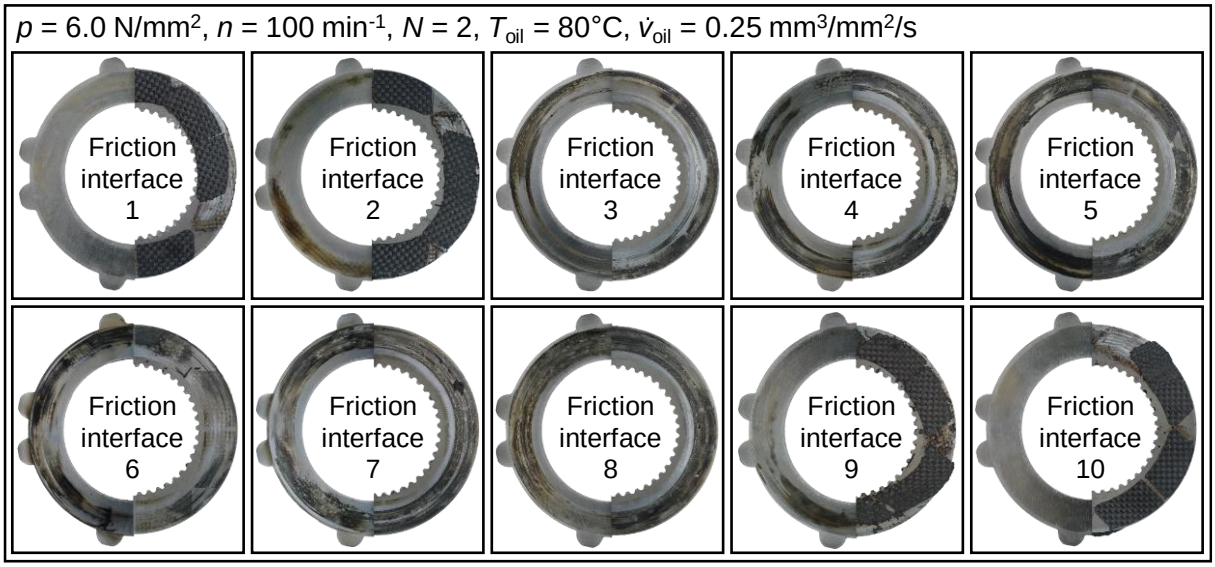

Figure 5.3: Damage patterns of friction system FS3.

5.1.2 Influence of the Oil Volume Flow on the Thermal Behavior

The increase in power density by cooling with oil is one of the core advantages of wet multi-plate clutches. During the friction phase, a considerable amount of heat is dissipated by convection of the cooling oil through the grooves. According to the state of the art, the amount of cooling oil flow significantly influences the clutch's thermal behavior. In order to determine the influence of the oil volume flow on the measured steel plate temperature, investigations

are carried out with the friction system FS1 on the component test rig KLP-260 with the following parameters:

$p = 1.0 \ldots 8.0$ N/mm², $n = 10 \ldots 140$ min^{-1}, $N = 10$, $T_{oil} = 80$ °C,
$\dot{v}_{oil} = \{0.25 \mid 0.50 \mid 1.00\}$ mm³/mm²/s, number of friction interfaces = 10

The left chart in Figure 5.4 shows a comparison of the measured temperatures in the steel plate C in the center of the clutch for oil flow rates $\dot{v}_{oil} = 0.50$ mm³/mm²/s and $\dot{v}_{oil} = 1.00$ mm³/mm²/s. Especially at high temperatures (> 250 °C), a clear difference between the two variants can be seen. For better data analysis, the temperature difference between the two series of measurements is plotted in the right chart in Figure 5.4. There is a difference in the measured steel plate temperature, and the absolute value of the temperature difference between the two measurement series increases with the measured steel plate temperature.

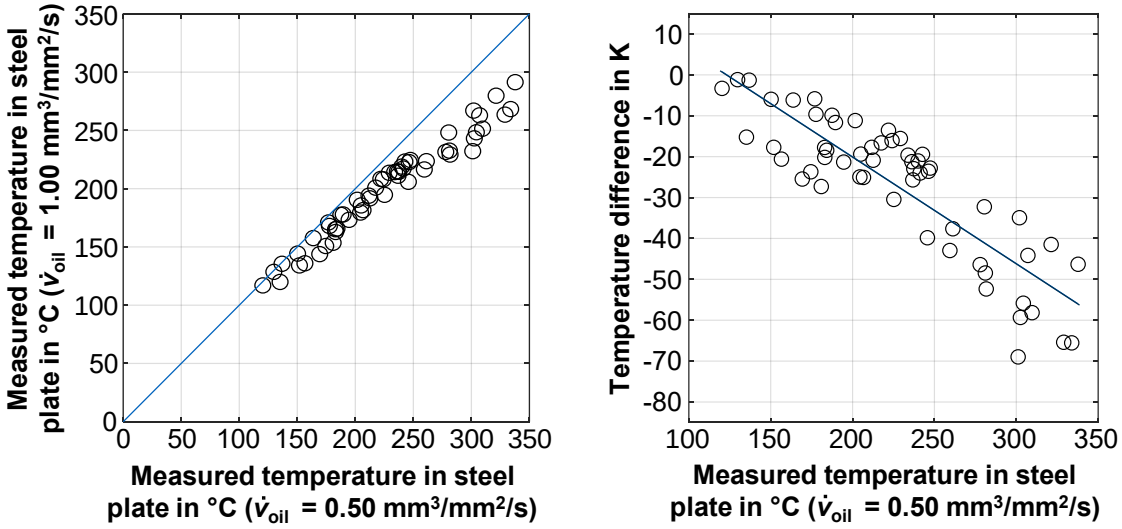

Figure 5.4: Measured steel plate temperatures for oil flow rate $\dot{v}_{oil} = 0.50$ mm³/mm²/s versus oil flow rate $\dot{v}_{oil} = 1.00$ mm³/mm²/s (left); temperature difference between the two series of measurements over the measured steel plate temperatures for oil flow rate $\dot{v}_{oil} = 0.50$ mm³/mm²/s (right).

To statistically validate the difference between the two variants, a t-test is performed, with the null hypothesis that the data (temperature difference) come from a normal distribution with mean 0. Since the p-value (p = 2.19e−16) is much smaller than the defined limit of 0.05, the null hypothesis can be rejected. A hypothesis test (ANOVA) is performed with respect to the regression line to investigate the stronger influence of oil flow at higher temperature levels on the temperature difference of the measured steel plate temperature. The null hypothesis states that the slope of the linear equation is equal to zero. The regression line is given by:

$$\Delta T = \beta_0 + \beta_1 \cdot T, \tag{5.1}$$

where ΔT is the temperature difference, T the measured temperature, and β_0 and β_1 are the regression coefficients. The null hypothesis can be rejected due to a probability value of p = 3.81e−34 (see Table A.2 in the appendix). Therefore, changing the oil flow rate from $\dot{v}_{oil} = 0.50$ mm³/mm²/s to $\dot{v}_{oil} = 1.00$ mm³/mm²/s has an effect on the temperature difference of the measured steel plate temperatures. The absolute value of the temperature difference between the two variants increases as the temperature level increases.

For oil flow rate $\dot{v}_{oil} = 0.25$ mm³/mm²/s and $\dot{v}_{oil} = 0.50$ mm³/mm²/s, the left diagram in Figure 5.5 compares the measured temperatures in the steel plate. The measuring points are more often located below the angle bisector. The influence becomes clearer in the right

diagram of Figure 5.5, which shows the temperature difference of the measuring points. As the measured steel plate temperature increases, the absolute value of the temperature difference of the measurement series also increases.

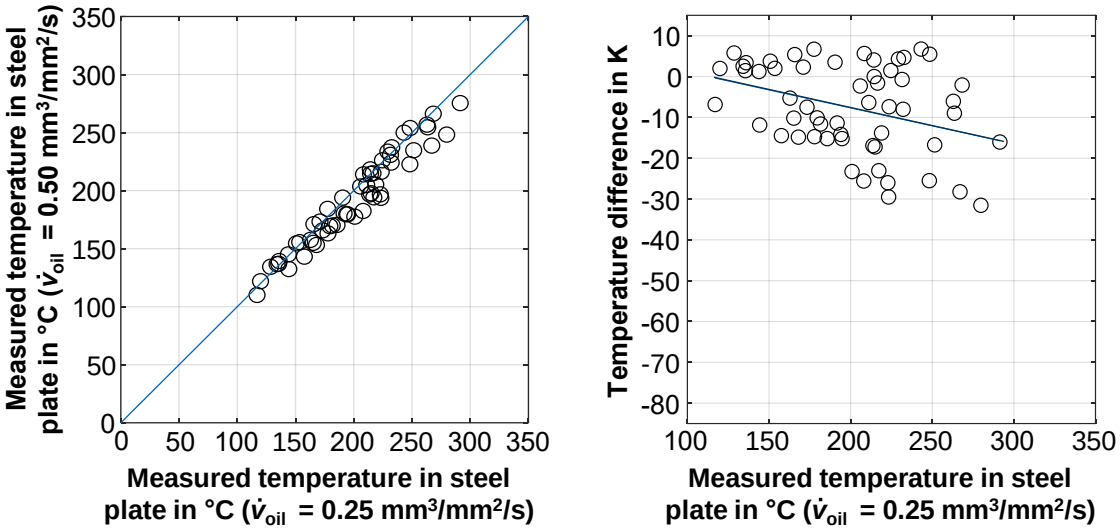

Figure 5.5: Measured steel plate temperatures for oil flow rate $\dot{v}_{oil} = 0.25$ mm³/mm²/s versus oil flow rate $\dot{v}_{oil} = 0.50$ mm³/mm²/s (left); temperature difference between the two series of measurements over the measured steel plate temperatures for oil flow rate $\dot{v}_{oil} = 0.25$ mm³/mm²/s (right).

In addition to the graphical representation, statistical tests (t-Test, ANOVA) are performed for validation. A t-test is used to examine whether the temperature differences between the two variants originate from a normal distribution with a mean value of 0. The probability value is p = 1.29e−16, and thus the null hypothesis can be rejected. The null hypothesis for the ANOVA states that the slope of the linear equation (see right plot in Figure 5.5) is equal to zero. The null hypothesis can be rejected due to a probability value of p = 4.92e−39 (see Table A.3 in the appendix). There is an effect of changing the oil flow rate from $\dot{v}_{oil} = 0.50$ mm³/mm²/s to $\dot{v}_{oil} = 0.25$ mm³/mm²/s on the temperature difference of the measured steel plate temperatures. The effect intensifies with increasing temperature levels.

In order to study the damage behavior, the test parameters are chosen with an oil flow rate of $\dot{v}_{oil} = 0.25$ mm³/mm²/s, as this rate has a significant and increasing effect on the temperature difference observed in the measured steel plate temperatures.

5.1.3 Influence of the Number of Friction Interfaces on the Thermal Behavior

The influence of the number of friction interfaces on the thermal behavior of the clutch is investigated similarly to the investigations in Section 5.1.2. The experiments are randomized in each test block, with three different numbers of friction interfaces (6, 10, and 14). The test parameters are as shown below:

$p = 1.0 \ldots 8.0$ N/mm², $n = 10 \ldots 140$ min^{-1}, $N = 10$, $T_{oil} = 80$ °C,
$\dot{v}_{oil} = 0.25$ mm³/mm²/s, number of friction interfaces = {6 | 10 | 14}

Temperature measurements are taken at the center of the clutch assembly in each case, as described in Section 4.2. In Figure 5.6, the left diagram compares the measured temperatures in the steel plate for the number of friction interfaces 6 and 10. A clear difference between the two sets of measurements can be observed, which increases at higher temperatures. The right diagram in Figure 5.6 shows the temperature difference between the two sets of measurements, making it easier to compare the data. The measured steel plate temperature

shows a difference between the two sets of measurements, and the absolute value of the temperature difference between the two measurement series increases with increasing temperature.

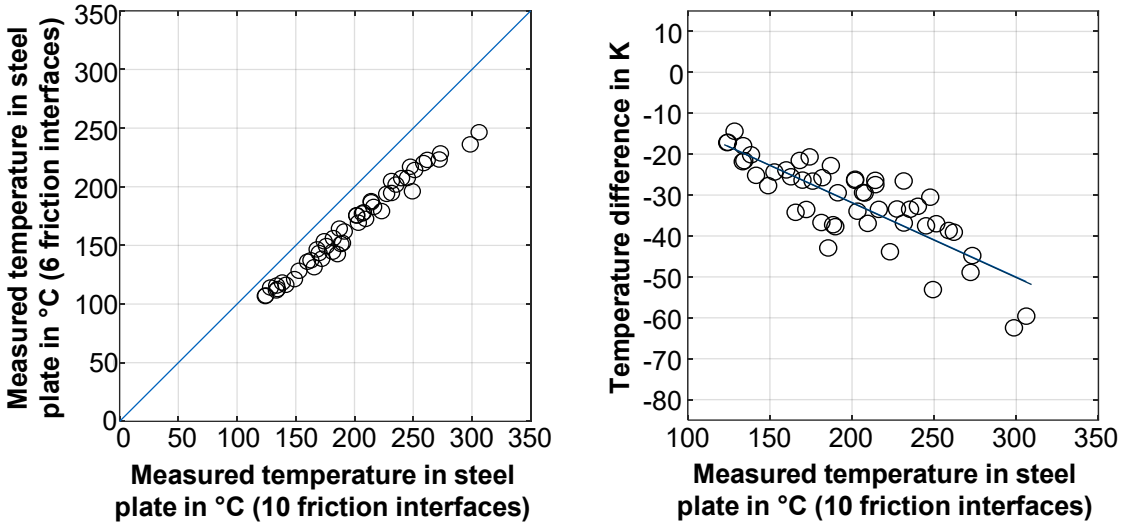

Figure 5.6: Measured steel plate temperatures for 10 versus 6 friction interfaces (left); temperature difference between the two series of measurements over the measured steel plate temperatures for 10 friction interfaces (right).

In the same way, as in Section 5.1.2, a t-test is performed for statistical validation with the null hypothesis that the data (temperature difference) originate from a normal distribution with mean 0. Since the p-value ($p = 1.15e{-}26$) is significantly smaller than the defined limit of 0.05, the null hypothesis can be rejected. Using ANOVA, the analysis investigates a correlation between the temperature level and the temperature difference. The null hypothesis for the ANOVA is that the slope of the linear equation (right plot in Figure 5.6) is zero. The null hypothesis can be rejected based on a probability value of $p = 3.26e{-}13$ (see Table A.4 in the appendix). Changing the number of friction interfaces from 6 to 10 has an effect on the temperature difference of the measured steel plate temperatures. The effect increases with increasing temperature levels.

The results of the experiments for 10 and 14 friction areas are shown in Figure 5.7.

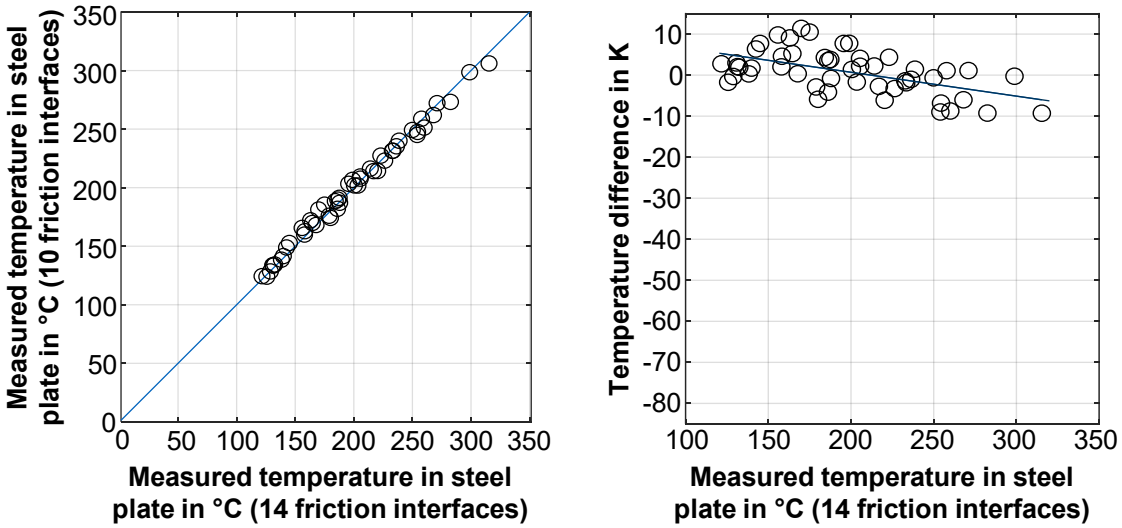

Figure 5.7: Measured steel plate temperatures for 14 versus 10 friction interfaces (left); temperature difference between the two series of measurements over the measured steel plate temperatures for14 friction interfaces (right).

Only a small difference is seen in the graphical representation. In the right diagram of Figure 5.7, it is evident that the temperature difference of the measuring points lies between −10 K and +10 K. A t-test is used to investigate whether the temperature differences of the two variants originate from a normal distribution with a mean value of 0. The probability value is p = 0.2839; thus, the null hypothesis cannot be rejected. Changing the number of friction interfaces from 10 to 14 has no statistically detectable effect on the temperature difference of the measured steel plate temperatures.

The test parameters are chosen with 10 friction interfaces to save resources, as the observed effect on the temperature difference is statistically significant, whereas increasing the number to 14 does not yield a significant difference.

5.1.4 Influence of the Loads on the Thermal Behavior

In this section, the load parameters for the systematic investigations are defined. An upper load limit (N = 2) and a lower load limit (N = 15) are defined to conduct investigations in the load range of spontaneous damage. It is known from the state of the art that the load limits concerning spontaneous damage can be described as a function of the specific friction power and the specific friction work. Step tests (see Section 4.3.2) with two slip phases $N = 2$ are conducted to determine the upper limit of the load parameters. Stepwise, the maximum specific friction power $\dot{q}_{max}$ is increased until system failure. For this purpose, the number of slip phases N remains constant in the step test. For the loading parameters at the lower limit of the investigation, step tests with fifteen slip phases ($N = 15$) are performed. The max. specific friction power $\dot{q}_{max}$ is again increased stepwise until failure. This procedure is carried out for the friction systems FS1, FS2, and FS3. Figure 5.8 shows two exemplary measurement diagrams for the friction system FS3.

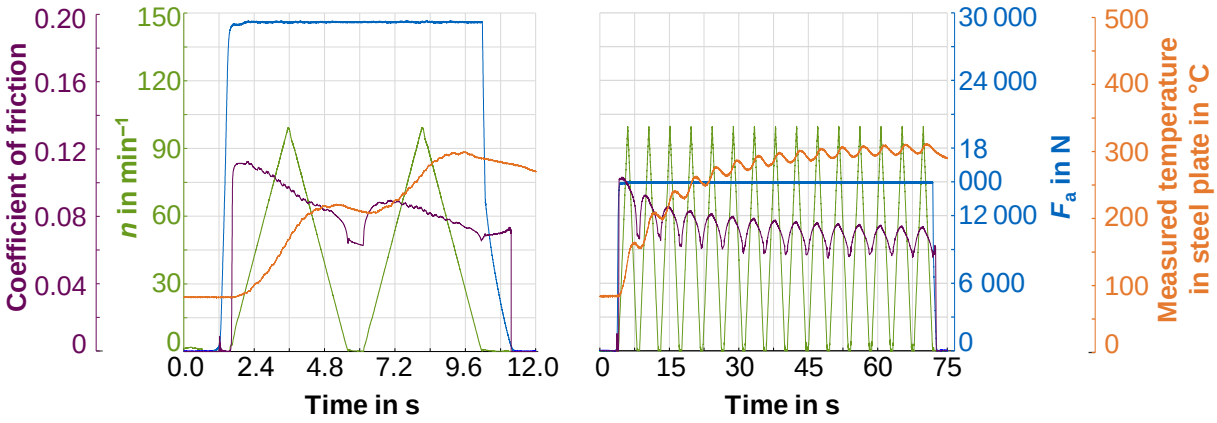

Figure 5.8: Exemplary measurement data for determining the lower (N = 2, left) and the upper (N = 15, right) load parameters for the extended investigations for friction system FS3.

With respect to the experiments, the max. specific friction power $\dot{q}_{max}$ that can be applied for the number of slip phases of $N = 2$ and $N = 15$ is determined so that failure does not occur. The values of the max. specific friction power $\dot{q}_{max}$ for the friction systems FS1, FS2, and FS3 are listed in Table 5.1.

	FS1, $N=2$	**FS1, $N=15$**	**FS2, $N=2$**	**FS1, $N=15$**	**FS3, $N=2$**	**FS1, $N=15$**
Max. specific friction power $\dot{q}_{max}$ in W/mm²	0.51	0.28	0.56	0.25	0.36	0.18

Table 5.1: Maximum friction power $\dot{q}_{max}$ that can be applied for the friction systems FS1, FS2, and FS3 for the number of slip phases of $N = 2$ and $N = 15$.

5.1.5 Preliminary Conclusion Regarding the Following Studies

The results of the basic investigations show that:

- The failure damage for friction systems FS1 and FS2 is buckling of the steel plates.
- The failure damage for friction system FS3 is the detachment of the friction lining.
- In the center of the clutch assembly, the damage is more extensive for all three friction systems than on the outer friction interfaces.
- The oil flow rate influences the thermal behavior of the clutch during the shifting process. As the oil flow rate increases, the measured temperature in the steel plates decreases.
- Changing the number of friction interfaces from 6 to 10 influences the thermal behavior of the clutch by decreasing the measured steel plate temperature.
- An influence of changing the number of friction interfaces from 10 to 14 on the measured steel plate temperature is not statistically verifiable.
- Upper and lower limit values for the max. specific friction power $\dot{q}_{max}$ can be found for the investigation of the spontaneous damage behavior.

5.2 Results of Extended Investigations

The conditions for the extended tests are selected in accordance with Section 4.3, taking into account the results of the basic tests from Section 5.1. In the first step, damage patterns and characteristics are identified. For this purpose, the damage patterns are studied macroscopically as well as microscopically using focus variation measurements, scanning electron microscope measurements, and microstructure examinations. In the second step, the friction and temperature behavior during the damage process is investigated. As a final step, the influence of spontaneous damage on further friction behavior is examined in the endurance tests. The experiments are carried out systematically on the component test rig KLP-260.

5.2.1 Damage Patterns Progression

Figure 5.9 shows an example of the damage behavior of three investigated friction systems during various step tests. The new condition, the condition after run-in, and the condition after the slip cycles $N = 1$, $N = 2$, $N = 3$, and $N = 4$ are shown. Based on the results of the preliminary tests, steel plates, and friction plates from the center of the clutch assembly are selected for representation. Also shown are the measured temperatures of the center steel plate at each load level. For better comparison, three tests are selected in which friction system failure occurs after four slip cycles. The loads are as described below:

- FS1: $p = 7.0\ \mathrm{N/mm^2}$, $n = 140\ \mathrm{min^{-1}}$, $T_{\mathrm{oil}} = 80\ °\mathrm{C}$, $\dot{v}_{\mathrm{oil}} = 0.25\ \mathrm{mm^3/mm^2/s}$
- FS2: $p = 6.0\ \mathrm{N/mm^2}$, $n = 140\ \mathrm{min^{-1}}$, $T_{\mathrm{oil}} = 80\ °\mathrm{C}$, $\dot{v}_{\mathrm{oil}} = 0.25\ \mathrm{mm^3/mm^2/s}$
- FS3: $p = 4.0\ \mathrm{N/mm^2}$, $n = 140\ \mathrm{min^{-1}}$, $T_{\mathrm{oil}} = 80\ °\mathrm{C}$, $\dot{v}_{\mathrm{oil}} = 0.25\ \mathrm{mm^3/mm^2/s}$

In the case of friction system FS1, a smoothing of the steel plate surface is observed after the run-in procedure. In the subsequent step test, the steel plate initially discolors at load level 3 ($N = 3$). At this load level, temperatures of 350 °C are measured in the steel plate. At load level 4, the system fails due to the buckling of the steel plates. The temperature measurements at this load level scatter strongly around the mean value of about 400 °C. The friction plates discolor during the step test in the area of the groove and the friction lining pads. In the failure load level, abrasive wear is observed in the area of the buckling of the steel plate.

Friction system FS2 also fails due to buckling of the steel plates. As initial damage, discoloration of the steel plates is observed at load level 2 ($N = 2$) at about 295 °C. With a further increase in the load parameters, the discoloration of the steel plate increases, and buckling occurs at load level 4 (about 500 °C). An increased scattering of the temperature measurement values is identified at this load level. After the run-in, a lightening of the friction lining is visible due to the absorption of the cooling oil. At higher loads and temperatures, the friction lining discolors to almost black. In the failure load level, abrasive wear is visible on the outer diameter.

Friction system FS3 fails due to detachment of the friction lining. No discoloration of the steel plates is observed in the load levels before failure. Likewise, no visual changes are visible on the friction plate. When the clutch fails, discoloration occurs on the steel and friction plates in addition to the detaching of the lining. Measurements of the steel plate temperature at failure are in the range of about 370 °C. In contrast to friction systems FS1 and FS2, no increased scatter is seen in the temperature measurement in the steel plate at the failure load level.

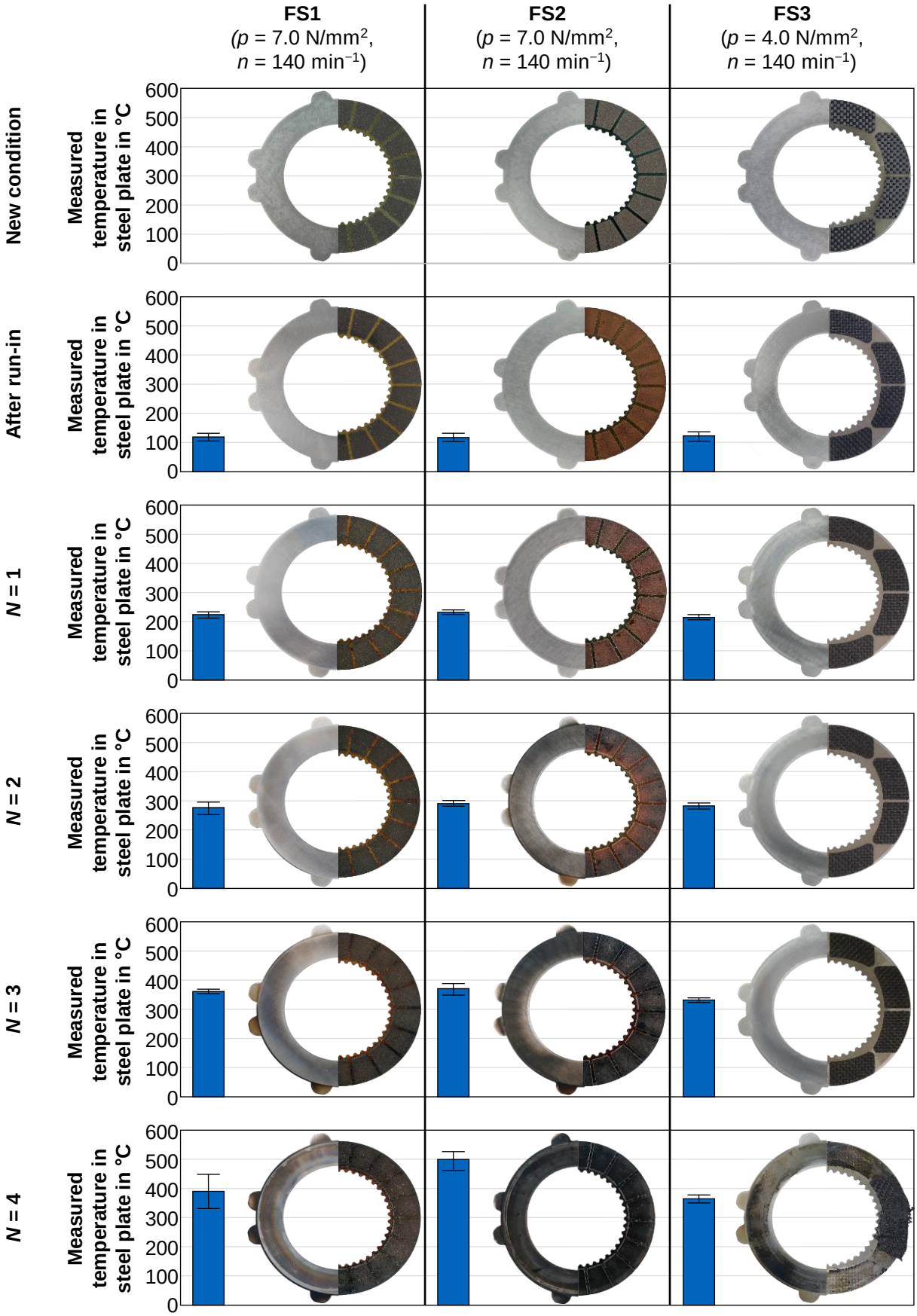

Figure 5.9: Damage pattern progression for friction systems FS1, FS2, and FS3.

5.2.2 Modification of the Macrogeometry

In this section, the macrogeometrical surface patterns are investigated as examples of different conditions of steel and friction plates. The results are obtained using the Alicona Infinite Focus G4 optical three-dimensional surface measuring device based on focus variation technology (see Section 4.1.2).

Figure 5.10 shows sections of steel plates in the states new condition, after run-in, and after failure. The loads for the individual states of the different friction systems (FS1, FS2, FS3) correspond to those given in Figure 5.9 In the right area of the figure, an adapted scale is shown for each condition. In the new condition, slight elevations (about 50 µm) can be observed in the area of the toothing. In the friction interface area, the surface macrogeometry is homogeneous. After run-in, the elevations in the area of the toothing increase slightly, while in the area of the friction interface, the surface macrogeometry remains homogeneous. After the failure of the plates, substantial buckling of the steel plates can be seen for the friction systems FS1 and FS2. The areas on the outer diameter increase compared to the inner diameter, and the surface contour changes occur in the radial direction. The height difference is about 2.4 mm. The change in the surface macrogeometry of the two plates of FS1 and FS2 is comparable. In contrast, no buckling of the steel plates is observed for the friction

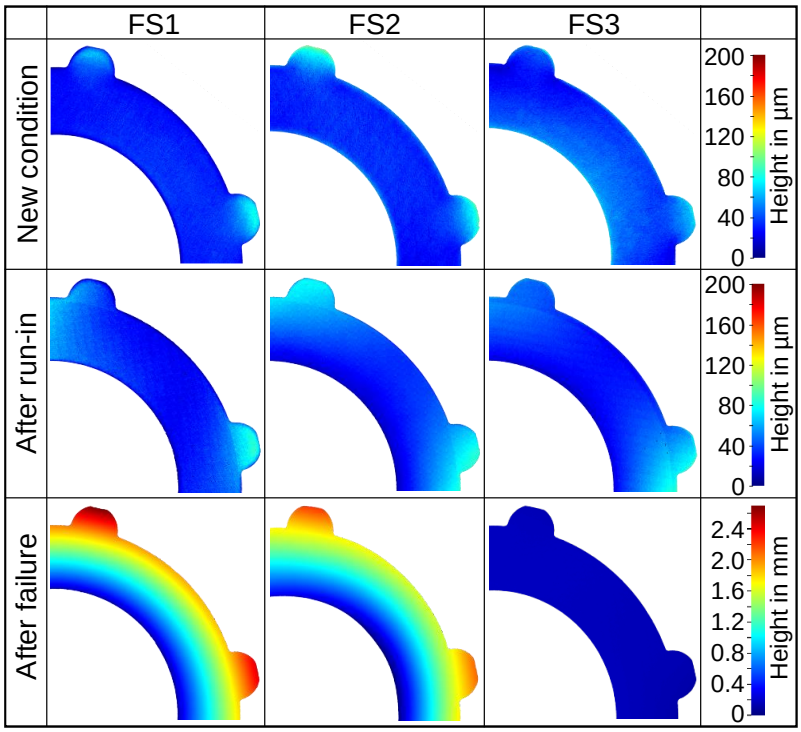

Figure 5.10: Macrogeometrical surface pattern of different steel plate conditions for the friction systems FS1, FS2, and FS3.

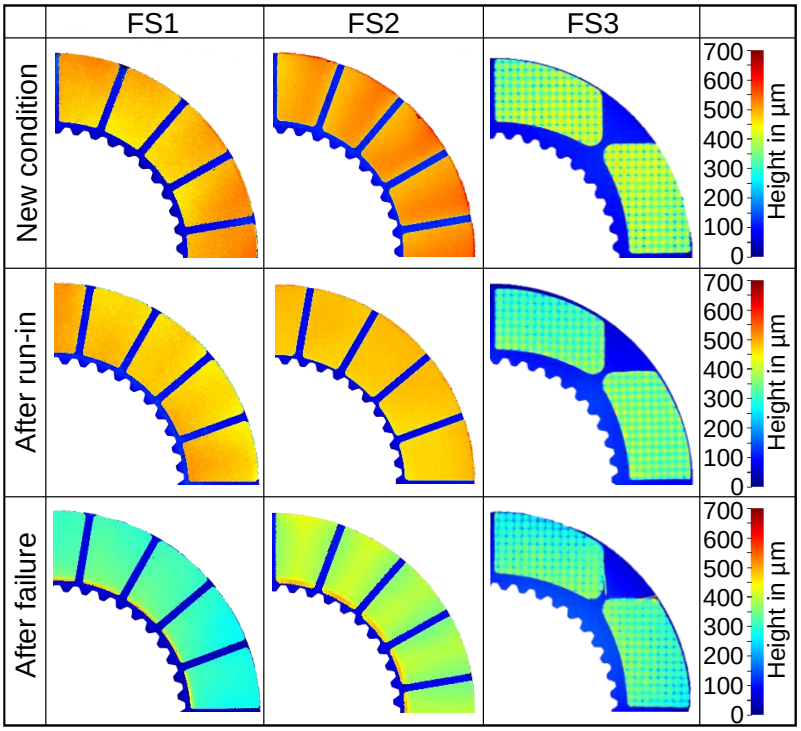

Figure 5.11: Macrogeometrical surface pattern of different friction plate conditions for the friction systems FS1, FS2, and FS3.

system FS3 after the failure of the clutch system. The surface macrogeometry is very homogeneous.

Figure 5.11 shows the macrogeometrical surface pattern for the friction plates in the states new condition, after run-in, and after failure. The loads assigned to the different friction systems (FS1, FS2, FS3) for each condition correspond to the values given in Figure 5.9. In new condition, the surfaces of the friction lining pads of the three friction plates are very homogeneous. After run-in, the friction linings are measured to be lower in height relative to the carrier plate, which serves as the reference height, compared to their height in the new condition. This modification can be explained by wear and compaction of the friction lining. The surface macrogeometry of the friction lining pads is very homogeneous for all three friction systems. The measurements after failure show that the thickness of the friction lining has further decreased. Elevations are visible on the inner diameter of the friction lining pads of friction systems FS1 and FS2. These areas are outside the friction interface, so there is no wear or compaction of the lining. In addition, a difference can be seen between the FS1 and FS2 friction linings. In the measurements of friction system FS3, it is noticeable that thinner thicknesses of the friction lining pad are measured after the run-in and after the failure. After failure, individual carbon fibers are torn out of the friction lining pad (see Figure 5.11).

5.2.3 Modification of the Microgeometry and the Elemental Composition

In addition to macrogeometrical investigations, the surfaces of selected friction plates and steel plates are analyzed using scanning electron microscopy (see Section 4.1.4). The analyses are presented using secondary electron (SE) and backscattered electron (BSE) imaging and EDX mappings. A total of nine elements are considered: carbon (C), oxygen (O), silicon (Si), phosphorus (P), sulfur (S), iron (Fe), calcium (Ca), chromium (Cr), and zinc (Zn). The results of these investigations for the FS1, FS2, and FS3 friction systems are presented below.

Friction system FS1:

Figure 5.12 shows BSE images of the friction lining FP1 of the friction system FS1 in the states new condition, after run-in, and after failure ($p = 6.0\,\mathrm{N/mm^2}$, $n = 120\,\mathrm{min^{-1}}$) at 25x and 150x magnification. After run-in, the images show an already incipient but not very pronounced smoothing of the friction lining. A clear surface smoothing can be seen on the failed friction plate, but also lining breakage. The difference in contrast in the BSE image shows that clogging of the lining porosity is mainly responsible for this. As described in Section 4.1.4, in BSE images, elements of lower atomic numbers appear dark, and elements of higher atomic numbers appear light. The dark regions represent fibers of the friction material, and the light areas denote lubricant residues [Acu16a]. EDX analysis can be used to identify the chemical elements of the friction lining surface. Figure 5.12 shows the results for carbon, phosphorus, sulfur, and iron. The remaining results are in the appendix (see Figure A.1 – Figure A.3). The mapping for carbon shows the structure of the paper fibers of the friction lining and correlate with the BSE images. In the failed condition, the smoothing is visible, and the fibers are barely visible. The porosity has decreased significantly. The EDX mappings for phosphorus and sulfur show more signals in the after failure state than in the new condition and after run-in states, confirming the increase in these elements. The signals are complementary to the signals of carbon. The iron mapping shows a structure similar to phosphorus in the after failure state. The intensity of the image signals is higher than in the after run-in and after failure states. In addition to the individual mappings, X-ray spectra are also prepared (see Figure A.1 – Figure A.3) in the appendix, confirming the mappings' results. The X-ray spectra

already show a slightly higher concentration of phosphorus, sulfur, and molybdenum relative to the new condition after the run-in. After failure, a further sharp increase in sulfur, phosphorus and molybdenum concentration is observed. In addition, higher iron content is measured.

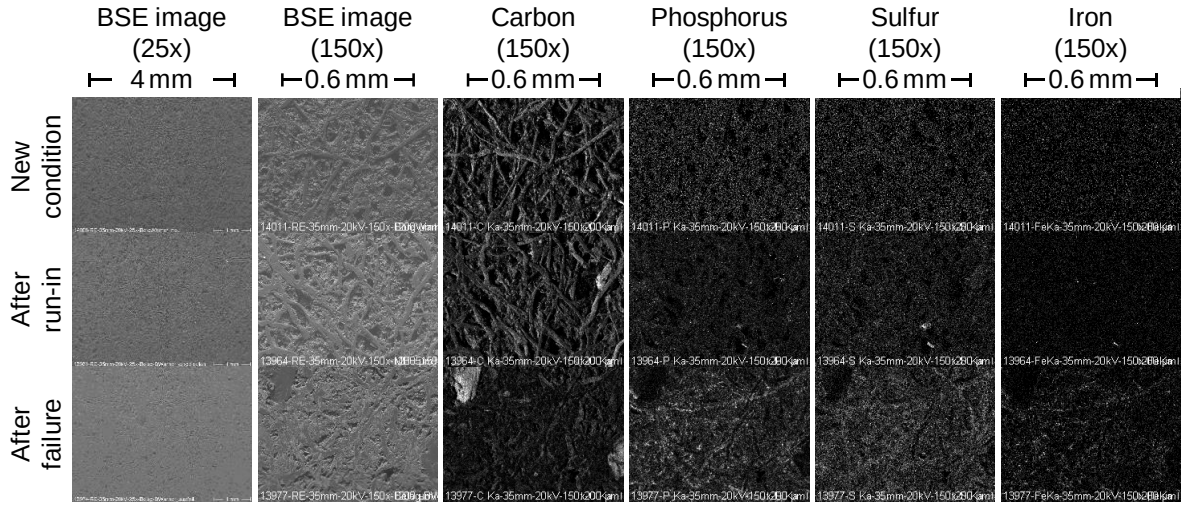

Figure 5.12: BSE images and EDX mappings for the elements carbon, phosphorus, sulfur, and iron of friction lining FP1 in the states new condition, after run-in, and after failure.

Figure 5.13 shows BSE images of the steel plate surfaces from step tests ($p = 6.0\,\mathrm{N/mm^2}$, $n = 120\,\mathrm{min^{-1}}$) with FP1 friction plates in the states new condition, after run-in, and after failure at 150x and 1 000x magnification. In both the new condition and after run-in states, scratches of varying depths are observed running in multiple directions. After run-in, some minor scratches appear to be partially smoothed. In the after failure state, smaller scratches are entirely smoothed, leaving only the deeper ones. EDX mappings help in determining the local distribution of the elements. In both the new condition and after run-in states, only widespread noise is visible for all elements. After failure, a higher number of X-ray quanta are registered. A pattern mirroring the BSE image is also observed for the elements carbon and sulfur. More signals are detected for carbon, phosphorus, and sulfur in the regions of the scratches than in the rest of the image.

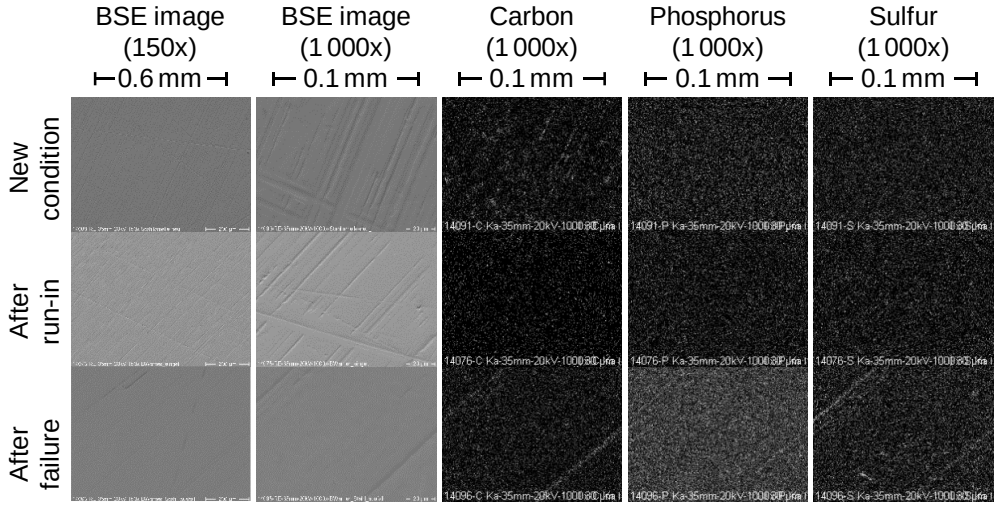

Figure 5.13: BSE images and EDX mappings for the elements carbon, phosphorus, and sulfur of steel plates for the friction system FS1 in the states new condition, after run-in, and after failure.

The X-ray spectra from the EDX analyses are shown in the appendix (see Figure A.4 – Figure A.6). The proportion of carbon is higher in the after failure state than in the

new condition and after run-in states. Similarly, the levels of phosphorus and oxygen are elevated in the after failure state compared to the new condition and after run-in states, in which they are present only in minimal amounts.

Friction system FS2:

Figure 5.14 presents BSE images of the friction lining FP2 of the friction system FS2 in the states new condition, after run-in, and after failure ($p = 6.0\,\mathrm{N/mm^2}$, $n = 140\,\mathrm{min^{-1}}$) at 25x and 150x magnification. In the BSE images, differences compared to the new condition are evident after run-in. There is an incipient smoothing of the friction lining on the carbon fibers that becomes visible. In the after failure state, the images reveal a clear smoothing of the surface and a clogging of the lining porosity. The smoothing of the friction lining is more pronounced than for the friction system FS1, both after run-in and after failure. The mappings for carbon depict the structure of the carbon fibers of the friction lining and correlate with the BSE images. While the structure is clearly visible in the new condition state and after run-in based on the image contrast, the contrast diminishes significantly in the after failure state. The carbon fibers become nearly invisible. The EDX mappings of phosphorus and sulfur indicate more signals in the after failure state than in the new condition and after run-in states. The iron mapping displays no additional signals after failure than in new condition and after run-in. The X-ray spectra (see Figure A.7 – Figure A.9) confirm these results. After run-in, a slight increase in the concentration of phosphorus and sulfur relative to the new condition can be observed. After failure, a sharp increase in the concentration of these two elements is seen, with the proportions of sulfur being more significant than those of phosphorus. The proportion of iron does not change significantly compared to the friction plates in the FS1 friction system.

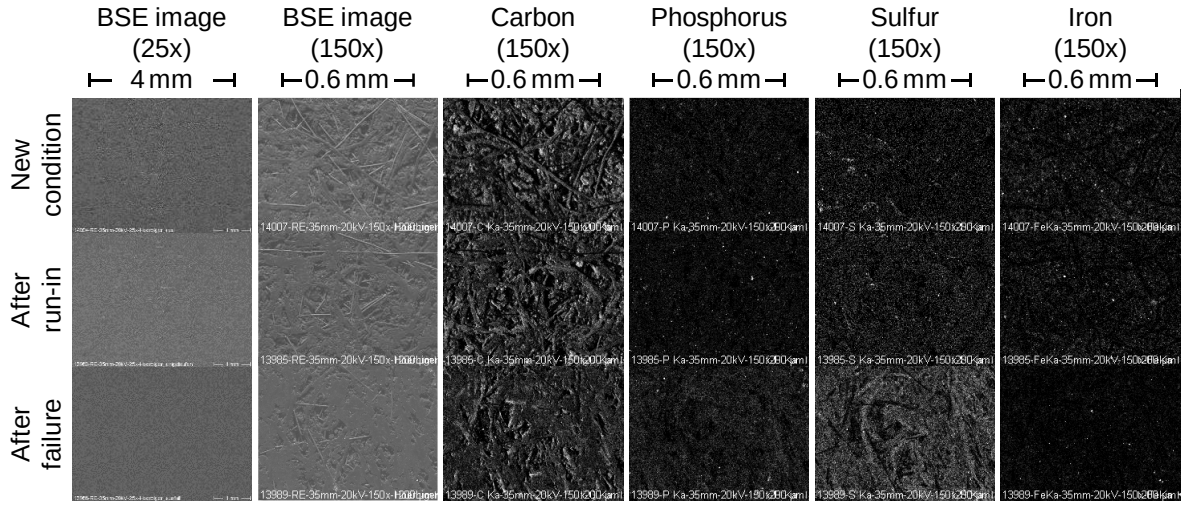

Figure 5.14: BSE images and EDX mappings for the elements carbon, phosphorus, sulfur, and iron of friction lining FP2 in the states new condition, after run-in, and after failure.

Figure 5.15 shows BSE images of the surface of steel plates from step tests ($p = 6.0\,\mathrm{N/mm^2}$, $n = 140\,\mathrm{min^{-1}}$) with FP2 friction plates in the states new condition, after run-in, and after failure at 150x and 1 000x magnification. In new condition, coarse and fine scratches can be seen on the steel surface. After run-in, only coarse scratches remain. In the after failure state, there are no significant changes in the surface topography compared to the after run-in state. The mapping of sulfur in the after failure state differs from the mappings of the new condition and after run-in states, with specific localized deposits of sulfur present. The carbon mappings show no differences between the states of the steel plate. The X-ray spectra from the EDX analyses, as shown in the appendix (see Figure A.10 – Figure A.12), confirm these results.

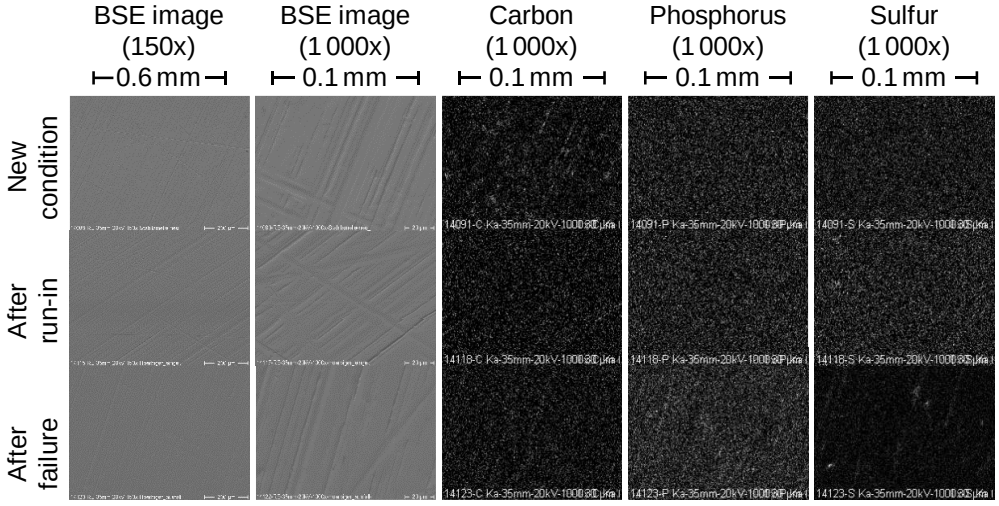

Figure 5.15: BSE images and EDX mappings for the elements carbon, phosphorus, and sulfur of steel plates for the friction system FS2 in the states new condition, after run-in, and after failure.

Friction system FS3:

Figure 5.16 shows BSE images of the friction lining FP3 of the friction system FS3 in the states new condition, after run-in, and after failure ($p = 4.0\,\mathrm{N/mm^2}$, $n = 140\,\mathrm{min^{-1}}$) at 25x and 150x magnification. In the images with 25x magnification, the woven structure of the friction lining can be clearly seen. After run-in, an island-shaped smoothing of the carbon friction lining can be seen, which is even more pronounced after failure. The BSE images with 150x magnifications show an apparent increase in the smoothings during the step test. The mappings for carbon display the structure of the carbon fibers of the friction lining and correlate with the BSE images. Compared to the new condition, the surface already appears slightly smoothed after the run-in. In the after failure state, the carbon fibers tend to show up weaker compared to the new condition and after run-in states. The EDX mappings of sulfur show more signals in the after run-in state than in the new condition state. After failure, a high amount of sulfur is detected on the friction interface. In the mappings of phosphorus, more X-ray quanta are registered after the run-in and after failure than in the new state. The iron mappings show point changes after run-in and after failure. The X-ray spectra shown in the appendix (see Figure A.13 – Figure A.15) confirm the results of the EDX mappings.

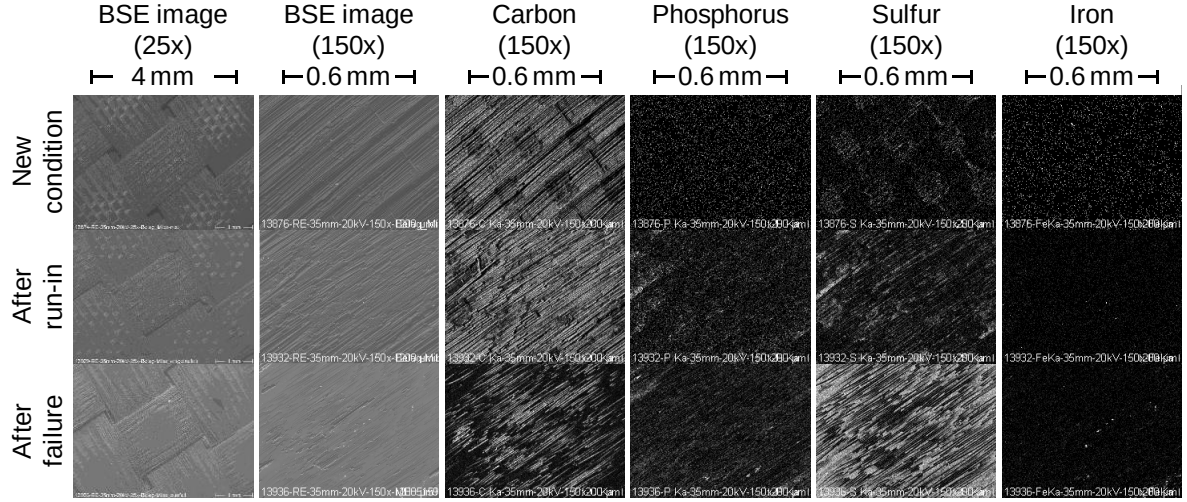

Figure 5.16: BSE images and EDX mappings for the elements carbon, phosphorus, sulfur, and iron of friction lining FP3 in the states new condition, after run-in, and after failure.

Figure 5.17 presents BSE images of the surface of steel plates from step tests ($p = 4.0\,\mathrm{N/mm^2}$, $n = 140\,\mathrm{min^{-1}}$) with FP3 friction plates in the states new condition, after run-in, and after failure at 150x and 1 000x magnification. In the new condition state, coarse and fine scratches on the steel surface can be seen. After run-in, only coarse scratches remain. In the after failure state, the finer scratches are completely smoothed out, and only deeper ones remain. In addition, however, a basic roughening of the steel plate can be seen, and depressions occur in particular areas. EDX mappings are used to determine the local distribution of the elements. Only large-area noise can be seen for all elements in the new condition and after run-in states. In the after failure state, localized deposits of sulfur and carbon are detected. The sulfur deposits are located in the depressions of the steel surface visible in the BSE image. The mapping of phosphorus shows no differences between the states of the steel plate. The X-ray spectra shown in the appendix (see Figure A.16 – Figure A.18) of the EDX analyses confirm these results.

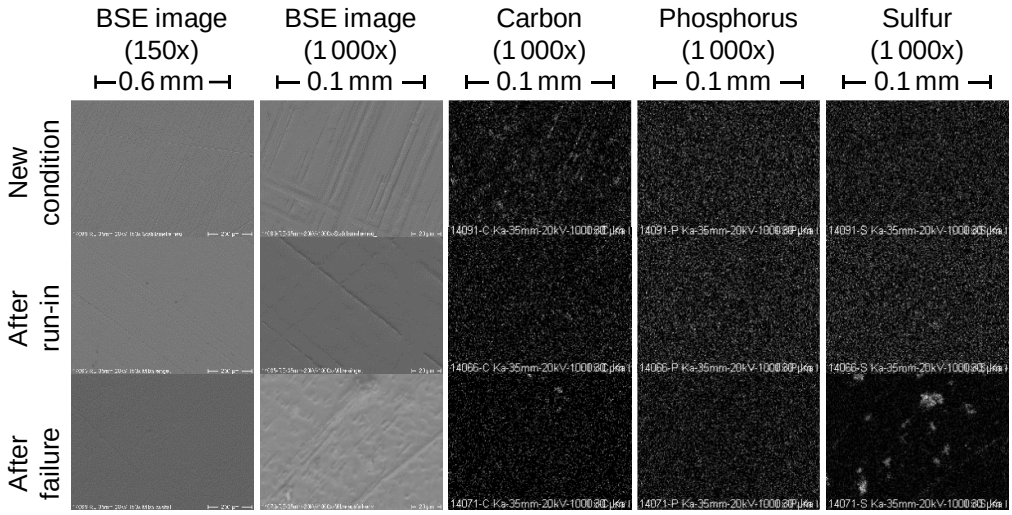

Figure 5.17: BSE images and EDX mappings for the elements carbon, phosphorus, and sulfur of steel plates for the friction system FS3 in the states new condition, after run-in, and after failure.

5.2.4 Modification of the Microstructure

Metallographic microstructural investigations of steel plates in different states are conducted to describe the structural condition of the steel plates before and after the damaging step tests in more detail. Investigations are performed in the new condition, after run-in, after the appearance of the first local discoloration, and after the failure of the clutch. The etching time is 30 s. The procedure is described in more detail in Section 4.1.3. Figure 5.18 compares the micrographs of the steel plates from step tests of the friction systems FS1, FS2, and FS3 for the different conditions. In each case, the steel plate "C" of the clutch under investigation is used for the microstructure examinations, and the analyses are carried out on the inner, mean, and outer friction diameters. For the investigations, samples are cut from the plates, precluding the analysis of a single plate under all conditions during the tests. Instead, a separate clutch assembly is required for each condition.

In the new condition of the steel plates, a martensitic microstructure is present in all sections. After the run-in, fewer martensite needles appear for all three clutch variants (FS1, FS2, FS3), indicating a clear heat contribution. As the first local discolorations appear, the granular structure becomes more prevalent, and the martensite needles diminish for all three friction systems. Differences are noted in the radial direction. Measurements on the outer friction diameter show a more pronounced decrease of martensite needles and an increase of granular microstructure in the material depth than on the inner friction diameter. In the case of the FS1 and FS2 friction systems, heat zones can also be seen as black discoloration at the edges of the mean and outer friction diameters. These heat zones occur more intensely on the outer diameter than on the mean diameter. No heat zones are observed for the FS3 friction system after the appearance of the first local

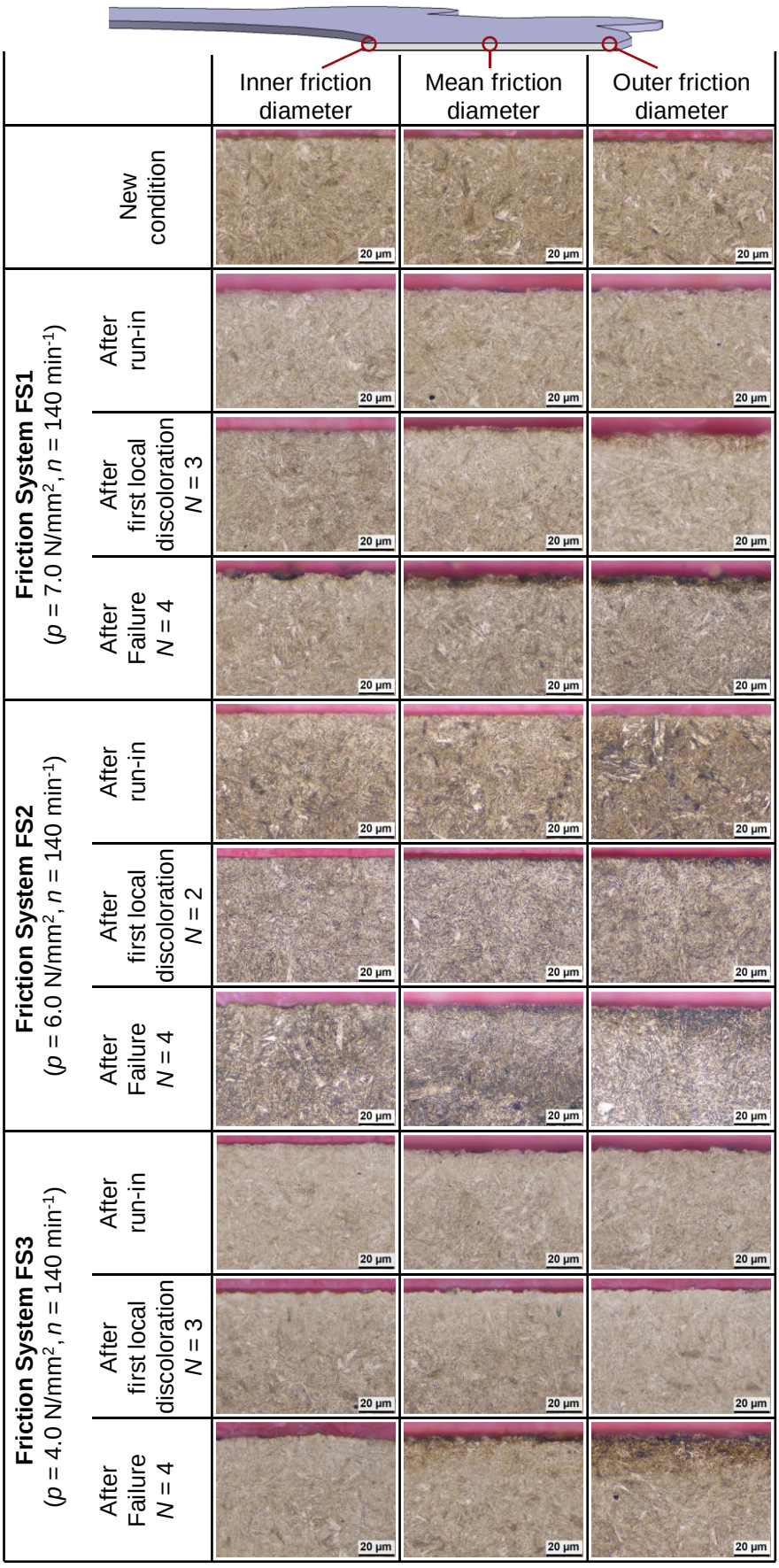

Figure 5.18: Micrographs of the friction systems FS1, FS2 and FS3 for the states new condition, after run-in, after local discoloration and after failure.

discolorations. After the failure, heat zones can be seen at the edge zone for all three friction systems. These are more intense at the outer friction diameter than at the inner friction diameter. The core exhibits a granular structure. Along with microstructural investigations, hardness tests are carried out at the inner, mean, and outer friction diameters of the steel plates. Ten measurements are taken per measuring point, and the results for the friction systems FS1, FS2, and FS3 are shown in Figure 5.19 for the states new condition, after run-in, after first local discoloration, and after failure.

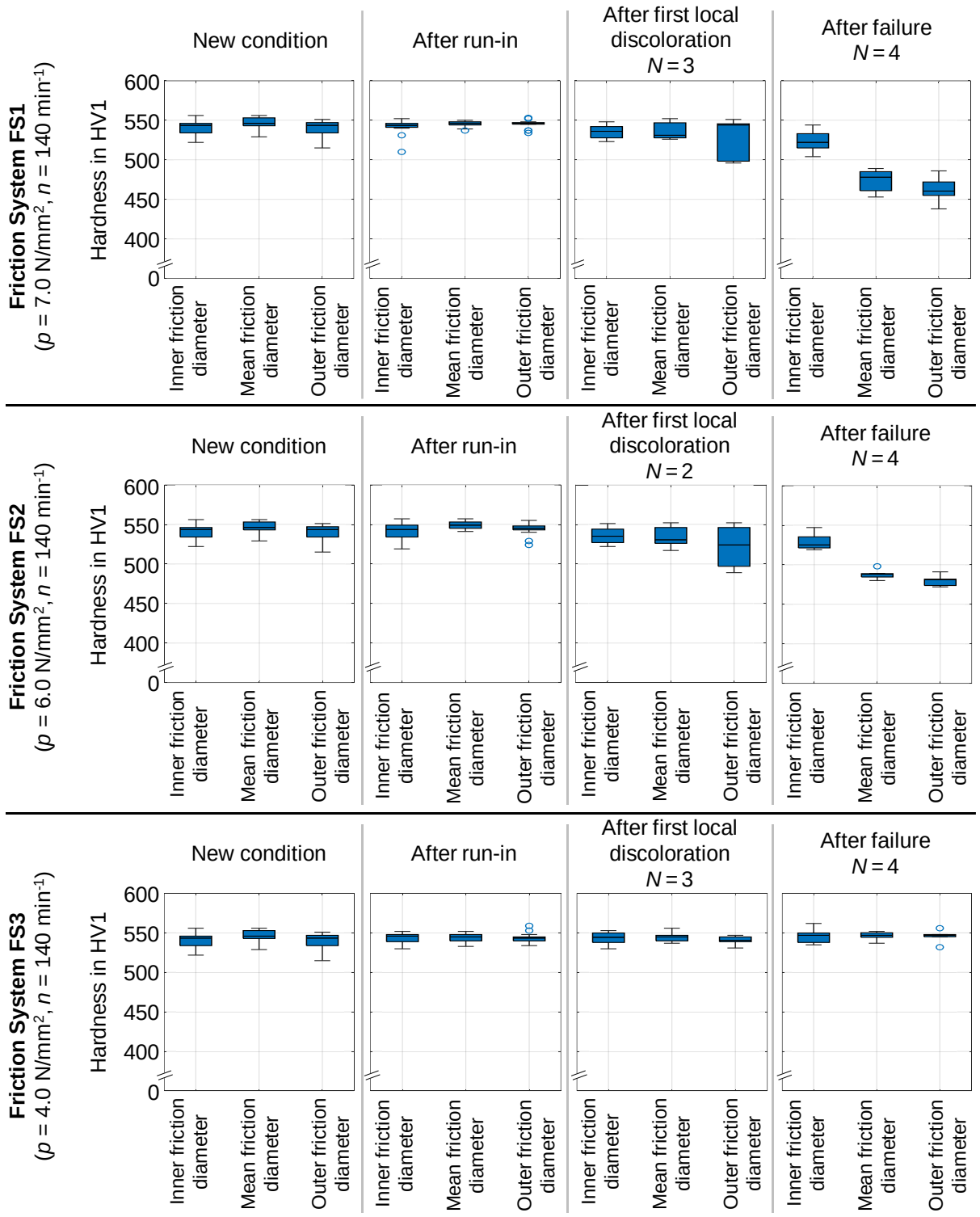

Figure 5.19: Hardness measurements using the Vickers method for the steel plates of friction systems FS1, FS2, and FS3 for the states new condition, after run-in, after first local discoloarion, and after failure.

For all three friction systems, there are almost no differences in the hardness values of the steel plates at the inner, mean, and outer friction diameters in the new condition and after the run-in. The median values range between HV1 = 540 and HV1 = 550. For the friction system FS3, no changes in the hardness measurements are observed even for the conditions after first local discoloration and after failure. There are also no apparent differences between inner, mean, and outer friction diameters. The median values are between HV1 = 540 and HV1 = 550. For friction systems FS1 and FS2, differences in the hardness measurements become evident when considering both the diameter and the condition (after first local discoloration, after failure). After the first local discoloration, a decrease in hardness measurements is noted, which becomes more pronounced with larger diameters. The median values range between HV1 = 520 and HV1 = 540. After the failure of the FS1 and FS2 friction systems, a further drop in hardness can be seen, more pronounced at the middle and outer diameters (median HV1 = 470 – 490) compared to the inner diameter (median HV1 = 520 – 530).

5.2.5 Modification of the Friction and the Temperature Behavior

Step tests are performed for all five friction systems (FS1 – FS5) to evaluate the change in friction as well as thermal behavior. The detailed procedure is provided in Section 4.3.2. Each load level consists of load engagements and subsequent reference engagements, enabling the investigation of the change in frictional behavior. In all tests, the steel plate temperature is measured by a thermocouple. The loads for each load level are based on the results of the basic investigation from Section 5.1.4.

A total of nine step tests with varying pressure and slip speed are carried out with the FS1 friction system. Figure 5.20 displays the characteristic coefficient of friction μ_{top} and the maximum measured steel plate temperature for four step tests. The data of the remaining five step tests are shown in the appendix in Figure A.19. The test results are presented in bar charts with standard deviations. The blue bars represent the results of the load engagements, and the gray bars are the results of the reference engagements. The step tests with friction system FS1 are carried out with pressures of 4.0 – 8.0 N/mm^2 and a maximum slip speed of 80 – 140 min^{-1}. The characteristic coefficient of friction μ_{top} decreases during the step tests in the load engagements (shown in blue). In the failure load level, there is an increase in the characteristic coefficient of friction μ_{top} in individual step tests. The standard deviation of the characteristic coefficient of friction μ_{top} shows a tendency to grow as the load level increases. The maximum measured temperature in the steel plate and its standard deviation also increase in the load levels during the course of the step test. In the reference engagements (shown in gray), a constant temperature level with a small standard deviation can be seen over all load levels. The characteristic coefficient of friction μ_{top} in the reference engagements initially decreases in the first load levels. In the experiments with several load levels, the characteristic coefficient of friction μ_{top} stabilizes around 0.09. No further systematic decline in the characteristic value is seen in subsequent load levels.

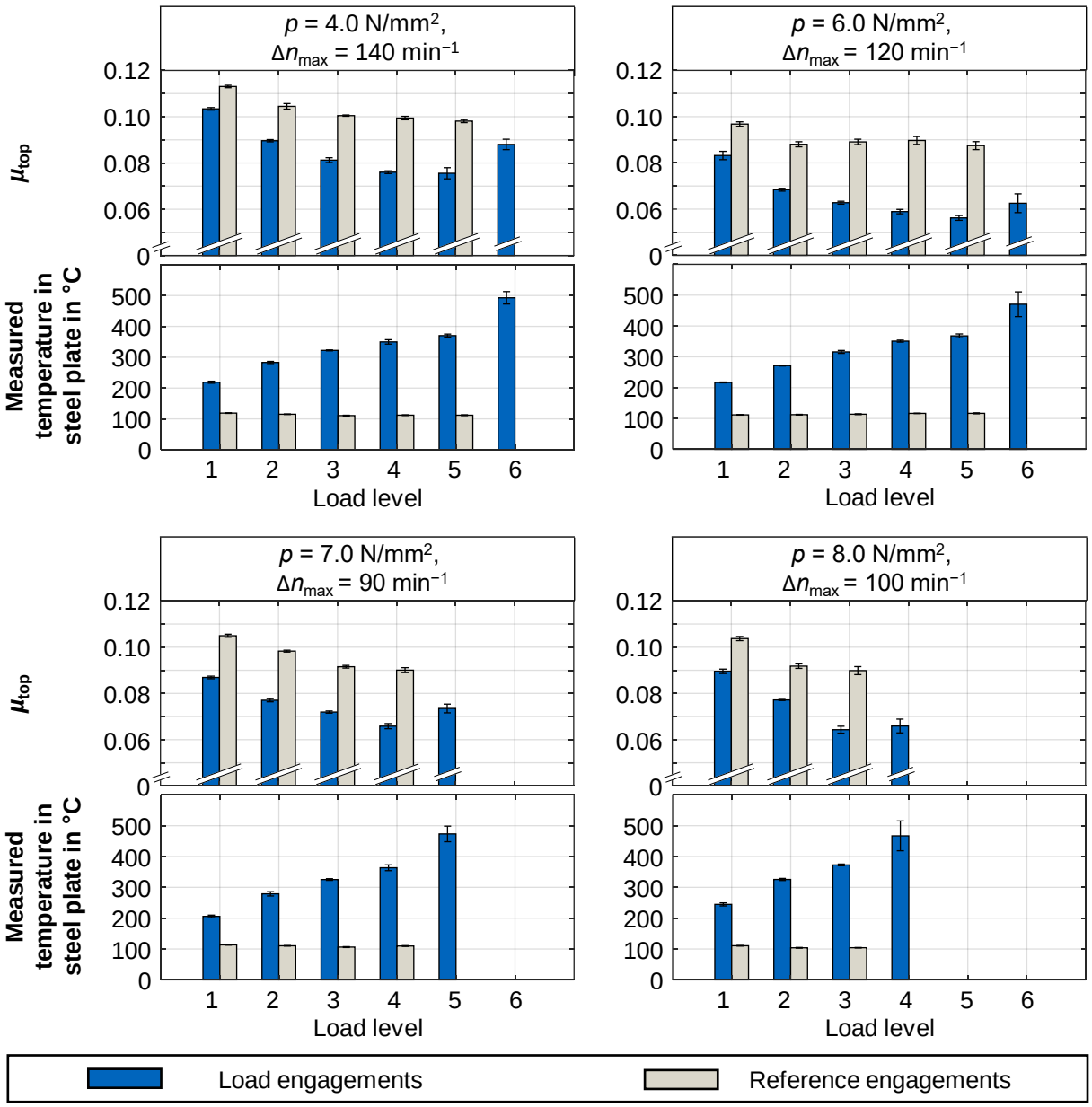

Figure 5.20: Characteristic coefficient of friction μ_{top} and measured maximum temperature in the steel plate for step tests with friction system FS1.

Figure 5.21 displays the measured maximum temperatures in the steel plate and the characteristic coefficient of friction μ_{top} for four step tests with the FS2 friction system. The data of the remaining step tests are shown in the appendix in Figure A.20. The results of the step tests are presented with blue bars, while the reference engagements are depicted with gray bars. In the step tests, the pressures range from 4.0 – 8.0 N/mm², and the maximum slip speeds vary between 60 – 140 min⁻¹. The characteristic coefficient of friction μ_{top} decreases from load level to load level in the load engagements. The maximum measured temperature in the steel plate and its standard deviation also increase during the step test. In the reference engagements (shown in gray), a constant temperature level with a small standard deviation can be seen over all load levels. The characteristic coefficient of friction μ_{top} in the reference engagements is lower at higher load levels than at the beginning of the step test and decreases from load level to load level.

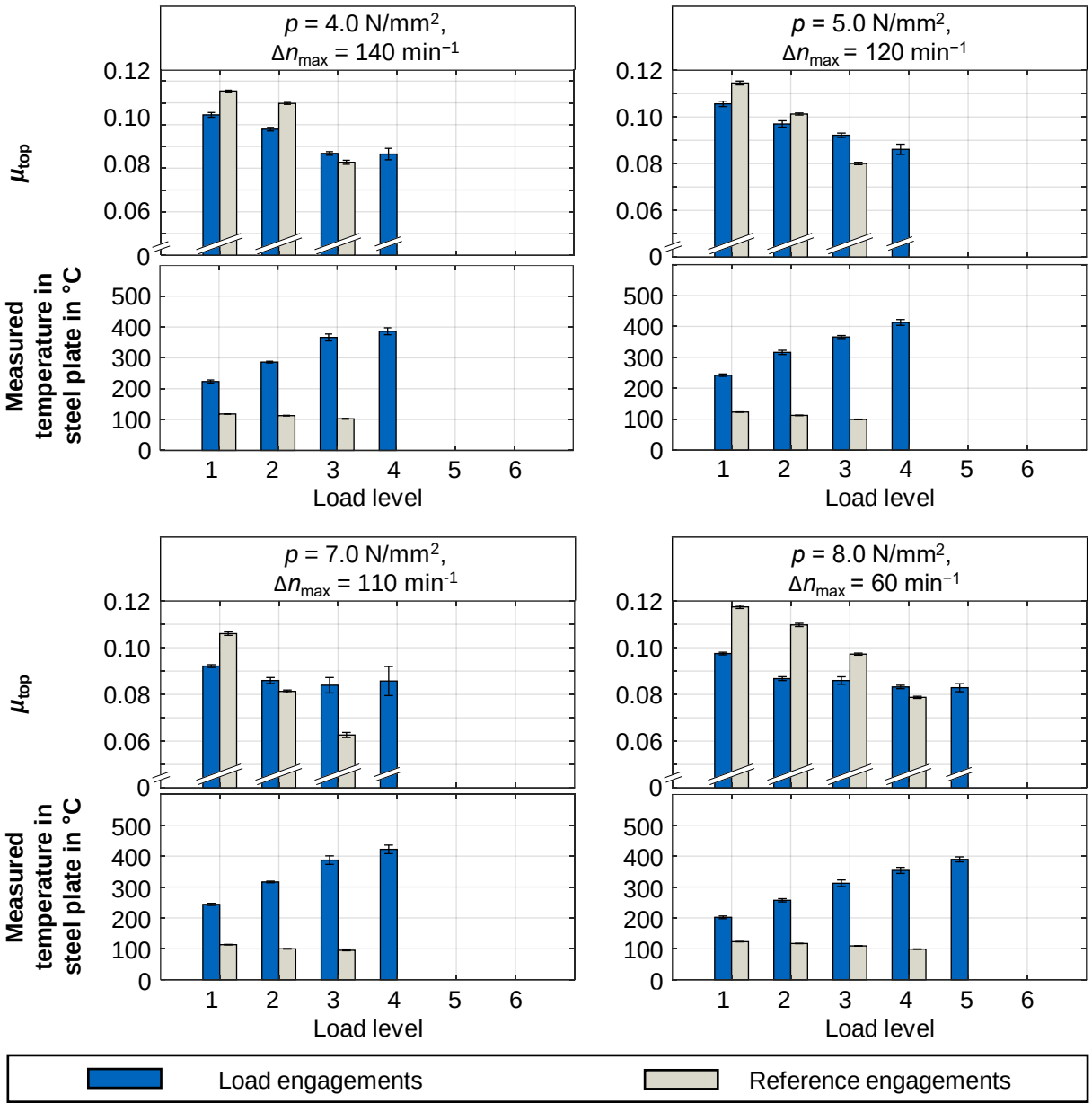

Figure 5.21: Characteristic coefficient of friction μ_{top} and measured maximum temperature in the steel plate for step tests with friction system FS2.

Figure 5.22 illustrates the measured maximum temperatures in the steel plate and the characteristic coefficient of friction μ_{top} for four step tests using the friction system FS3. The data from the remaining step tests are presented in the appendix in Figure A.21. The pressures in the step tests range from 4.0 – 8.0 N/mm², and the maximum slip speeds vary between 50 – 140 min⁻¹. The characteristic coefficient of friction μ_{top} decreases with consecutive load levels in the step tests in the load engagements. The maximum measured temperature in the steel plate and its standard deviation increase continuously during the step test. Temperatures above 300 °C are measured in the failure load levels. In the reference engagements, a constant temperature level can be seen, which is at the same level across all tests for FS3. The characteristic coefficient of friction μ_{top} in the reference engagements stays consistently high throughout the step test.

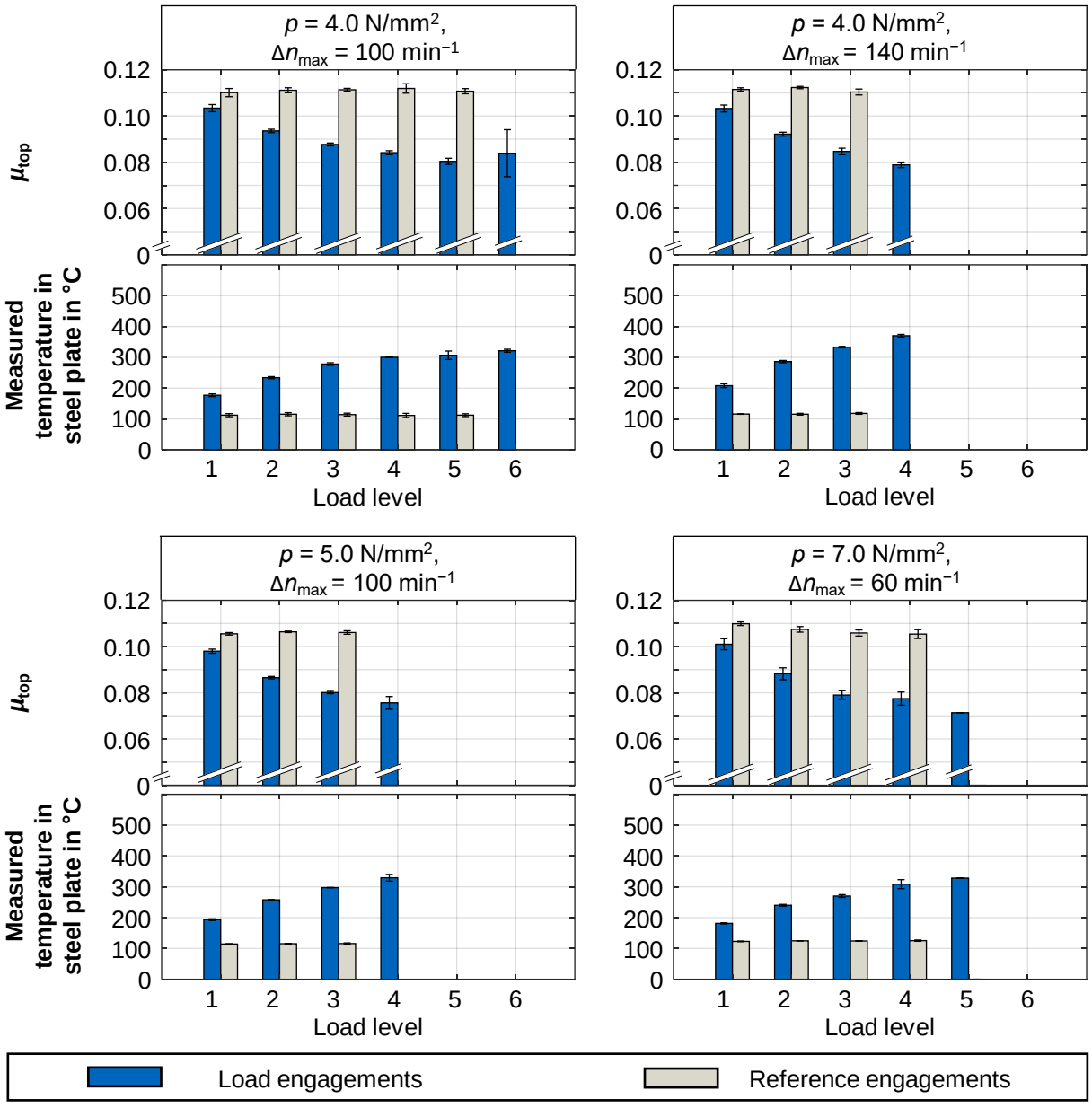

Figure 5.22: Characteristic coefficient of friction μ_{top} and measured maximum temperature in the steel plate for step tests with friction system FS3.

A total of three step tests with pressures of 5.0 – 8.0 N/mm² and a maximum sliding speed of 80 – 130 min⁻¹ are conducted with the FS4 friction system (steel plate thickness 1.2 mm). Figure 5.23 shows the course of the characteristic coefficient of friction μ_{top} and the maximum measured steel plate temperature in the step tests. The characteristic coefficient of friction μ_{top} declines initially in the early load levels of the step tests and then stabilizes at a consistent value in the following load levels (shown in blue). In the failure load level, there is an increase of μ_{top} in the individual step tests. The standard deviation of μ_{top} shows a tendency to grow as the load level rises. The maximum measured temperature in the steel plate and its standard deviation also increase during the step test in the load levels. Temperatures above 500 °C are measured in the failure load levels. In the reference engagements (shown in gray), a constant temperature measurement with a small standard deviation can be seen. The characteristic coefficient of friction μ_{top} in the reference engagements tends to decrease in the course of the step test.

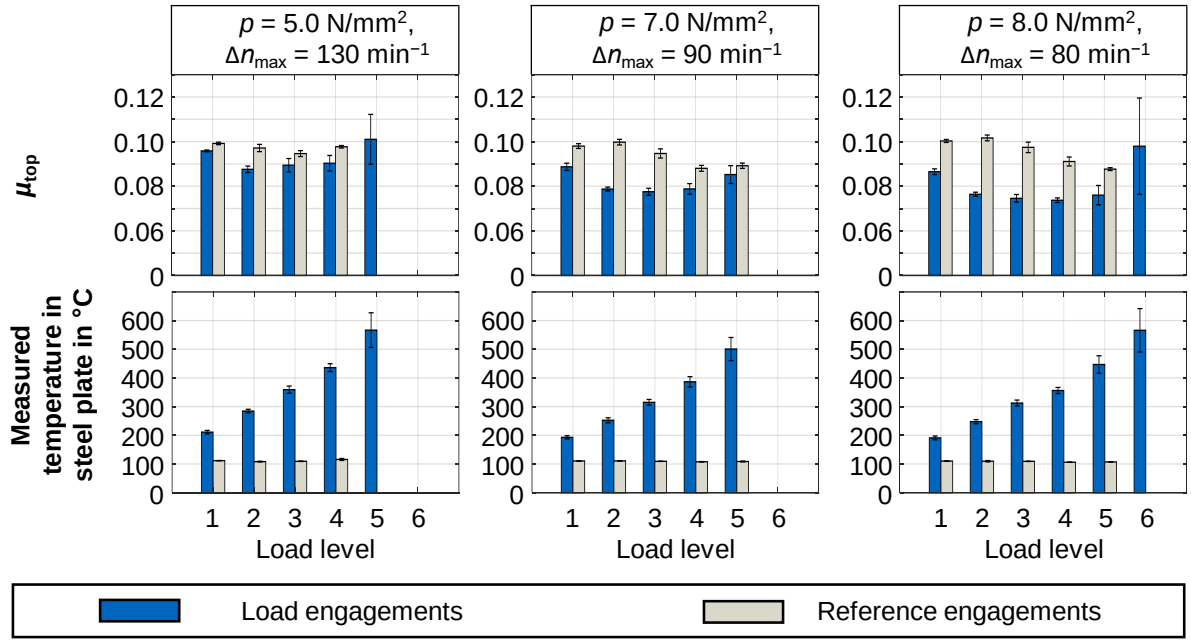

Figure 5.23: Characteristic coefficient of friction μ_{top} and measured maximum temperature in the steel plate for step tests with friction system FS4.

Figure 5.24 shows the measured maximum temperatures in the steel plate and the characteristic coefficient of friction μ_{top} for three step tests with the FS5 friction system (steel plate thickness 1.6 mm). In these tests, pressures range from 4.0 – 8.0 N/mm², and the maximum sliding speeds lie between 60 – 140 min⁻¹. The characteristic coefficient of friction μ_{top} initially decreases in the step tests during load engagements and then increases again as the step test progresses. The maximum measured temperature in the steel plate and its standard deviation increase during the step test. Temperatures above 500 °C are measured in the failure load levels. A constant temperature level with a small standard deviation can be observed at the reference engagements. The characteristic coefficient of friction μ_{top} in the reference engagements is lower at higher load levels than at the beginning of the step test and decreases from load level to load level. In the failure load level, there is a repeated increase of μ_{top}.

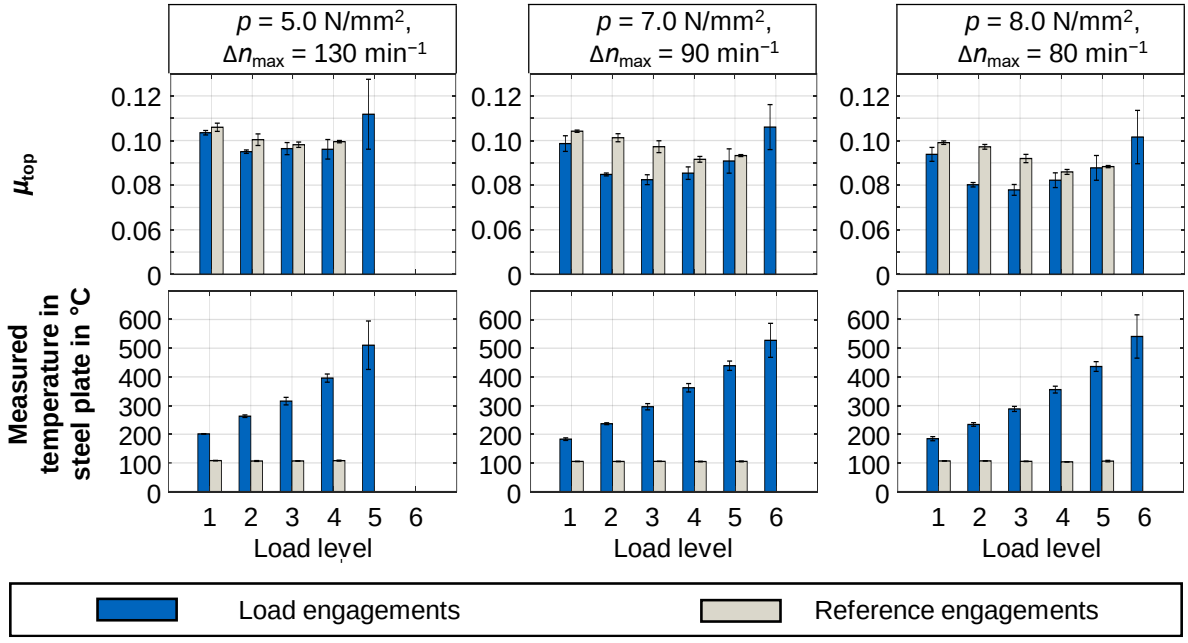

Figure 5.24: Characteristic coefficient of friction μ_{top} and measured maximum temperature in the steel plate for step tests with friction system FS5.

5.2.6 Modification of the Frictional Behavior Due to Pre-Damage

Three different clutch conditions are investigated to describe the friction behavior in endurance operation after previous damage. Here, run-in clutches are compared with pre-damaged clutches in endurance tests. The loads for the run-in (200 collective runs) and the endurance test (1 000 collective runs) correspond to those of the run-in and are listed in Table 4.7. In each case, the damage to the pre-damaged clutches takes place after the run-in and before the endurance test.

Friction system FS1:

Figure 5.25 shows the steel and friction plates of the reference clutch and the pre-damaged clutch for the friction system FS1 before and after endurance tests. A step test ($p = 6.0\,\mathrm{N/mm^2}$, $n = 140\,\mathrm{min^{-1}}$, $N = 7$) to load level 7 is conducted for the pre-damage after the run-in. As a result of the damage, the steel plate shows a noticeable black discoloration, and the friction plate is also discolored black. The plates presented in the figure indicate that the discoloration diminishes during endurance testing, and the visual signs of damage decrease throughout the testing. In contrast, the reference clutch does not show any significant optical changes.

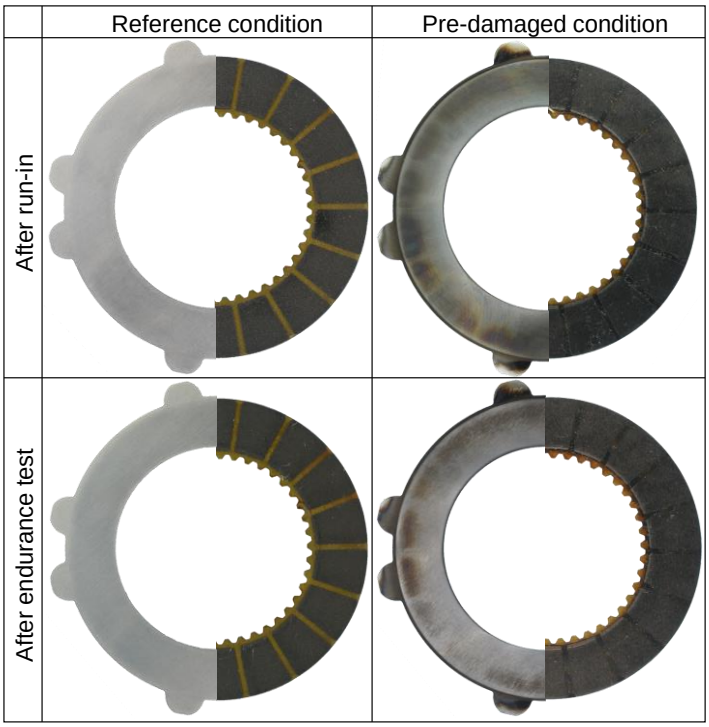

Figure 5.25: Photos of the reference and pre-damaged steel and friction plates of the friction system FS1 before and after the endurance test.

Based on the visual inspection, however, limited conclusions can be drawn about the friction behavior during and after the end of continuous operation. For this reason, the characteristic value μ_{top} during the run-in (collective run 0 – 200) and endurance test (collective run 201 – 1 000) are displayed in Figure 5.26, with each load level represented individually based on the collective passes. A 95 % confidence interval is provided for the run-in, which can be derived from the run-ins of all FS1 friction systems examined. The confidence interval aims to facilitate the evaluation of the differences between the reference clutch and the pre-damaged clutch. The rise in the characteristic value μ_{top} from the end of the run-in period to the start of the endurance test can be attributed to reconditioning effects resulting from the disassembly of the clutch and its subsequent documentation, as also discussed by Voelkel [Voe20a]. Depending on the load level, the characteristic value μ_{top} for the pre-damaged clutch is either lower or higher than for the reference clutch. For load levels S1, S4, and S5, the characteristic value μ_{top} of the reference clutch remains consistently higher in the continuous shifting test, and the difference grows with an increasing number of collectives. The differences between the curves of μ_{top} at load levels S2, S3, and S6 are minimal. The increase in the μ_{top} value at the transition from the run-in to the endurance test can be explained by reconditioning effects. The parts are removed and photographed after the run-in. Overall, all curves show a slight increase in the coefficient of friction within the continuous operation. A

pronounced influence of the damage on the friction behavior during continuous operation is observed only at load level S4 and the end of load level S1. Additionally, it becomes evident that the differences between the two variants are rather subtle at higher pressures.

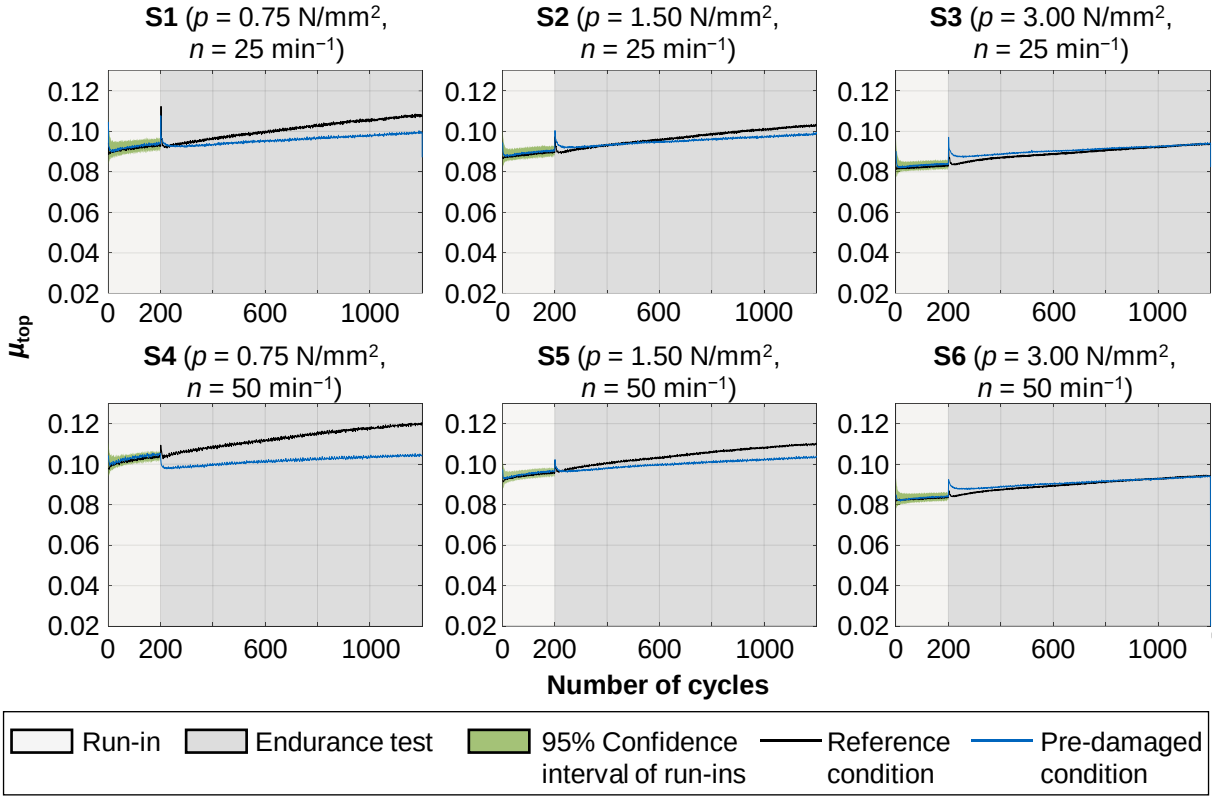

Figure 5.26: Characteristic value μ_{top} during run-in and endurance test with the reference and pre-damaged clutches with friction system FS1 for load levels S1 – S6.

Friction system FS2:

Figure 5.27 shows the steel and friction plates of the reference clutch and the pre-damaged clutch for the FS2 friction system, both before and after the endurance test. A step test ($p = 6.0\ \mathrm{N/mm^2}$, $n = 140\ \mathrm{min^{-1}}$, $N = 7$) up to load level 7 is performed for the pre-damage after the run-in. The pre-damage of the clutch becomes visually evident through the dark discoloration of the steel and friction plate. The discoloration appears to weaken, especially in the area of the friction interface, after the endurance test. The reference clutch shows no significant visual changes.

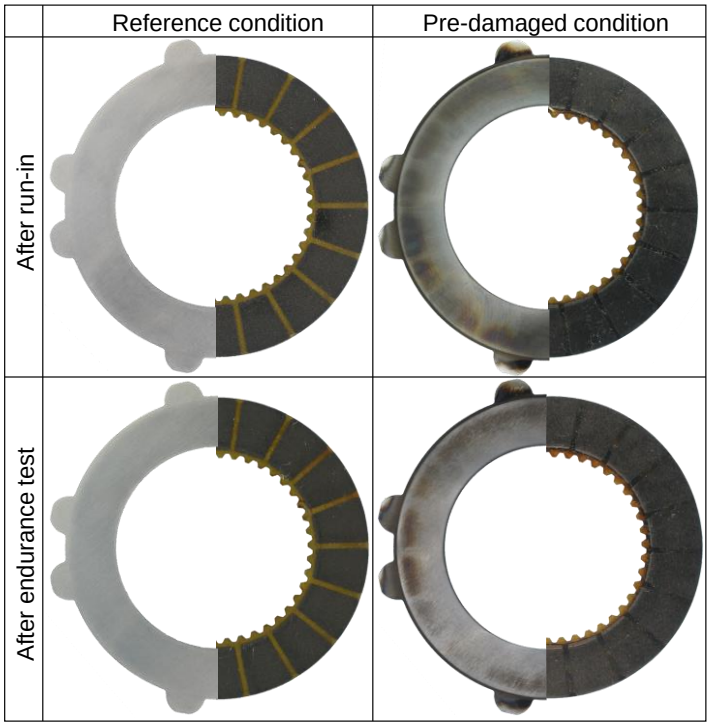

Figure 5.27: Photos of the reference and pre-damaged steel and friction plates of the friction system FS2 before and after the endurance test.

To illustrate how the friction behavior evolves during the endurance test operation, the characteristic value

μ_{top} is represented as a function of the collective runs (see Figure 5.28). As in the run-in, the individual load levels are considered separately. The characteristic value μ_{top} of the reference clutch maintains a consistent level throughout the endurance test, with a slight upward trend. It can be seen that it is as much as 50 % lower in some instances than for the as-new clutch across all load levels. The characteristic value μ_{top} of the pre-damaged clutch stays relatively stable between the collective runs from 201 to 1 000, with a minor dip afterward. Meanwhile, the characteristic value μ_{top} of the clutch rises as the endurance test progresses. In general, the differences between the reference clutch and the pre-damaged clutch decrease as the surface pressure increases and as the differential speed decreases.

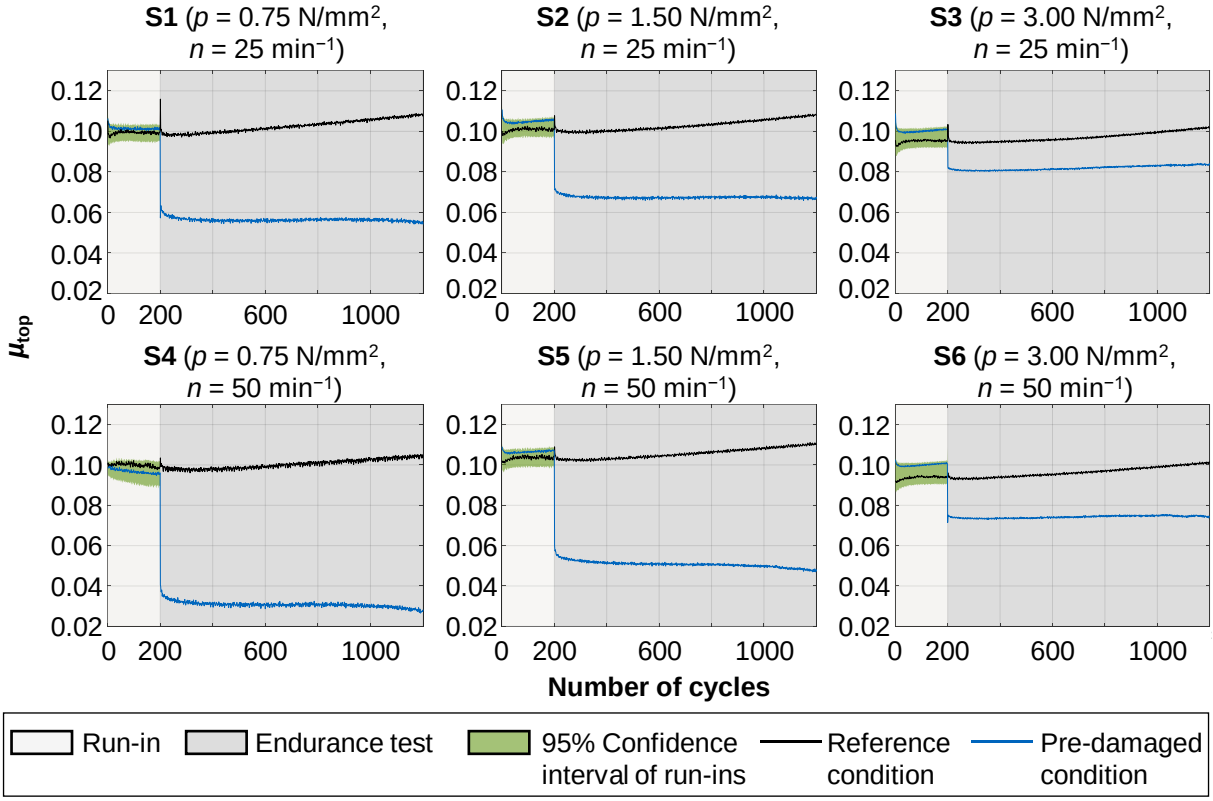

Figure 5.28: Characteristic value μ_{top} during run-in and endurance test with the reference and pre-damaged clutches with friction system FS2 for load levels S1 – S6.

Friction system FS3:

Figure 5.29 illustrates the steel and friction plates of the reference clutch and the pre-damaged clutch for the friction system FS3 before and after endurance testing. The pre-damage results from a step test ($p = 5.0\ \mathrm{N/mm^2}$, $n = 140\ \mathrm{min^{-1}}$, $N = 3$), manifesting as slight black discoloration on the steel plate and between the friction lining pads on the friction plate. As the endurance tests progress, the discoloration diminishes. The visual signs of damage diminish over the course of the endurance tests. No significant visual changes can be seen in the reference clutch. Figure 5.30 presents the friction behavior during run-in (collective run 0 – 200) and endurance test (collective run 201 – 1 000) by representing μ_{top} for all load levels as a function of the collective runs. A 95 % confidence interval is given for the run-in, calculated using the run-ins of all the clutches examined with the FS3 friction system, to obtain comparable values between the reference clutch and the pre-damaged clutch. For load levels S1, S4, and S5, the reference clutch exhibits a consistently higher μ_{top}, value, with the difference amplifying as the number of collectives rises.

Differences between the μ_{top} curves at load levels S2, S3, and S6 are minor. The increase in the characteristic value μ_{top} at the transition from the run-in to the endurance test can be explained by reconditioning effects. The parts are inspected after the run-in. In total, all curves show a slight increase in the characteristic value μ_{top} during continuous operation. The damage has a more decisive influence on μ_{top} during continuous operation only at load level S4 and at the end of load level S1. At higher pressures, the differences between the two variants are less pronounced.

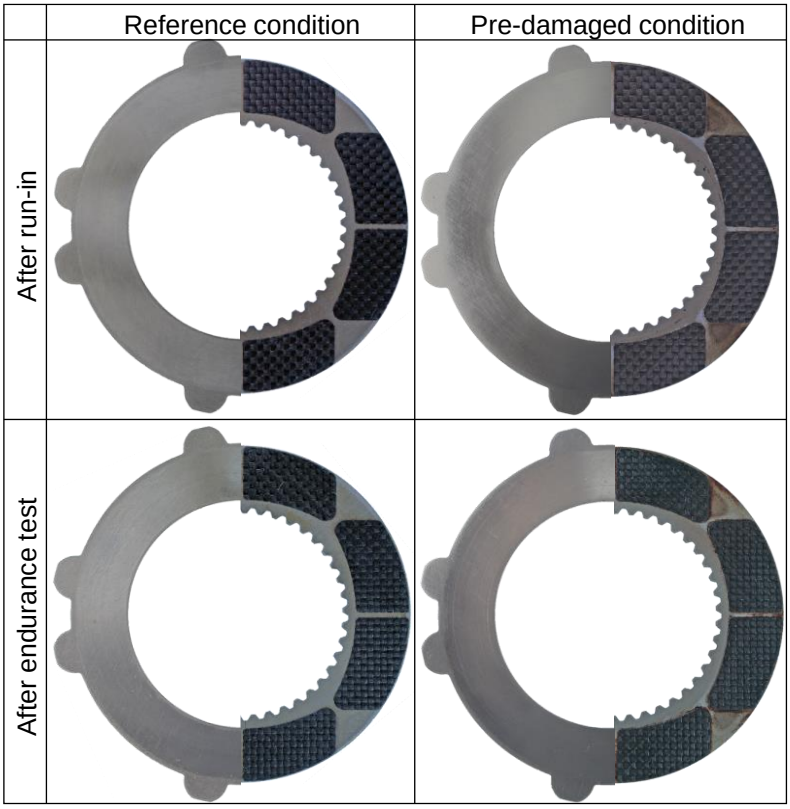

Figure 5.29: Photos of the reference and pre-damaged steel and friction plates of the friction system FS3 before and after the endurance test.

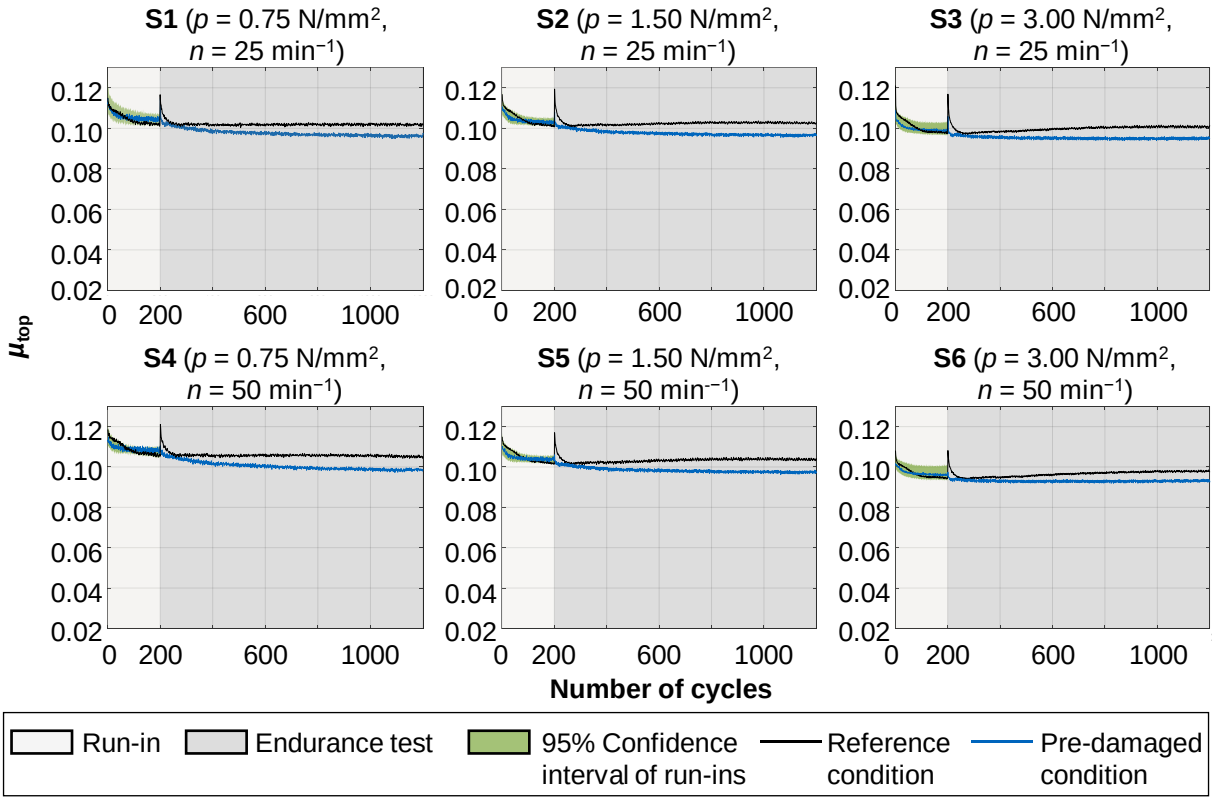

Figure 5.30: Characteristic value μ_{top} during run-in and endurance test with reference and pre-damaged clutches with friction system FS3 for load levels S1 – S6.

6 Development of Simulation Models of Multi-Plate Clutches

The results of the experimental investigations, as well as the state of the art, indicate that thermal behavior has a significant influence on the spontaneous damage behavior of multi-plate clutches. In this section, two-dimensional and three-dimensional thermomechanical finite element model for a multi-plate clutch are developed based on work from the literature [Acu16a, Cui15, Mil23, Neu08, Sto23, Wan21]. A two-dimensional model offers the advantage of time-efficient execution of extensive parameter studies regarding material parameters and geometry sizes. Detailed considerations are conducted with a three-dimensional model, especially in the circumferential direction. Mesh and time-step analyses ensure that the quality of the results of the simulation models is independent of the numerical settings. The models are also validated with experimental data from test rig runs. The results presented below are published by Schneider et al. [Sch22c].

6.1 Mathematical Model

The study of the thermomechanical behavior of a clutch is a broad and multi-disciplinary field of expertise. The fields of heat transfer, thermal expansion, contact mechanics, and rigid body mechanics need to be coupled. In the following, all the required physical relationships are described.

6.1.1 Thermal Principles

In the energy conversion process from mechanical to thermal energy, under conditions of heat flow coupling, no energy losses are assumed. The following equation calculates the local heat flux density $\dot{q}$ between two contacting surfaces of a clutch:

$$\dot{q} = \mu \cdot \omega_{\mathrm{rel}} \cdot r \cdot p \tag{6.1}$$

$$v_{\mathrm{rel}} = \omega_{\mathrm{rel}} \cdot r. \tag{6.2}$$

Symbol	Unit	Description	Symbol	Unit	Description
$\dot{q}$	W/m²	Heat flux density	μ	–	Coefficient of friction
ω_{rel}	rad/s	Relative angular velocity	p	N/mm²	Surface pressure
v_{rel}	m/s	Sliding speed			

Most of the frictional heat generated at the contact surfaces is absorbed by the lining and steel plates. A minor part of the thermal energy is absorbed by the lubricating film and particles. Therefore, this ratio is described by the proportionality coefficient δ:

$$\dot{q} \cdot \delta = \lambda_{\mathrm{sp}} \cdot \frac{\partial T_{\mathrm{sp,fl}}}{\partial z} - \lambda_{\mathrm{fl}} \cdot \frac{\partial T_{\mathrm{fl,sp}}}{\partial z}. \tag{6.3}$$

Symbol	Unit	Description	Symbol	Unit	Description
$\dot{q}$	W/m²	Heat flux density	δ	–	Proportionality coefficient
λ_{sp}	W/m·K	Thermal conductivity steel plate	λ_{fl}	W/m·K	Thermal conductivity friction lining
$T_{\mathrm{sp,fl}}$	K	Temperature field steel plate in contact with the friction lining	$T_{\mathrm{fl,sp}}$	K	Temperature field friction lining in contact with the steel plate
z	m	Axial coordinate			

The boundary condition at the contact surface requires continuous temperature at the contact point on the friction pair. This means that for frictional contact, the temperature of the steel plate surface is equal to the temperature of the friction plate surface, where $T_{\mathrm{sp,fl}}$ and $T_{\mathrm{fl,sp}}$ represent the contact point temperatures of the steel and friction plates, respectively:

$$T_{\mathrm{sp,fl}} = T_{\mathrm{fl,sp}}. \tag{6.4}$$

Symbol	Unit	Description	Symbol	Unit	Description
$T_{\mathrm{sp,fl}}$	K	Temperature field steel plate in contact with the friction lining	$T_{\mathrm{fl,sp}}$	K	Temperature field friction lining in contact with the steel plate

The temperature distribution in the steel and friction plate is calculated using the parabolic heat conduction Equation (6.5) in cylindrical coordinates, which is suitable for axisymmetric modeling and assumes a uniform heat flow in the circumferential direction. Since the heat flux remains independent of the θ-direction, Equation (6.5) can be simplified:

$$\frac{\rho_i \cdot c_i}{\lambda_i} \cdot \frac{\partial T_i}{\partial t} = \frac{\partial^2 T_i}{\partial r^2} + \frac{1}{r} \cdot \frac{\partial T_i}{\partial r} + \frac{1}{r^2} \cdot \frac{\partial^2 T_i}{\partial \theta^2} + \frac{\partial^2 T_i}{\partial z^2}, \tag{6.5}$$

$$\frac{\rho_i \cdot c_i}{\lambda_i} \cdot \frac{\partial T_i}{\partial t} = \frac{\partial^2 T_i}{\partial r^2} + \frac{1}{r} \cdot \frac{\partial T_i}{\partial r} + \frac{\partial^2 T_i}{\partial z^2}. \tag{6.6}$$

Symbol	Unit	Description	Symbol	Unit	Description
ρ_i	kg/m3	Density of solid i	c_i	J/kg·K	Specific heat capacity of solid i
λ_i	W/m·K	Thermal conductivity of solid i	T_i	K	Temperature field of solid body i
r	m	Radius	θ	°	Angular coordinate
z	m	Axial coordinate	t	s	Time

Heat conduction also takes place between the lining carrier and the friction lining, whereby the temperatures at the contact surface between the friction lining and the lining carrier are assumed to be the same:

$$-\lambda_{\mathrm{fl}} \frac{\partial T_{\mathrm{fl,cp}}}{\partial z} + \lambda_{\mathrm{sp}} \frac{\partial T_{\mathrm{cp,ff}}}{\partial z} = 0, \tag{6.7}$$

$$\mathrm{T}_{\mathrm{fl,cp}} = T_{\mathrm{cp,fl}}. \tag{6.8}$$

Symbol	Unit	Description	Symbol	Unit	Description
λ_{fl}	W/m· K	Thermal conductivity friction lining	T_{fl}	K	Temperature field friction lining
δ	–	Proportional coefficient	z	m	Axial coordinate
$T_{\mathrm{fl,cp}}$	*K*	Temperature field friction lining in contact with the carrier	$T_{\mathrm{cp,fl}}$	K	Temperature field carrier plate in contact with the friction lining

The clutch components transfer thermal energy to the inner and outer carriers and axial mounting parts. Between these components, there exists a steel–steel contact. However, effective contact between these surfaces occurs only at a few points separated by large distances, reducing the contact area to 1 – 2 % of the nominal area [Mad96]. Therefore, the heat flow lines are narrowed to pass only through the actual contact points, creating resistance to heat flow, which results in a sharp drop in temperature at the interface. This additional resistance to the heat flow, caused by the reduction of the contact area at the interface, is termed the thermal contact conductance h_c, and its reciprocal is defined as the thermal contact resistance [Dou16]. As early as 1969, Cooper et al. [Coo69] publish a paper on the model-based description of thermal conductivity in the contact between two bodies. This work is subsequently extended fundamentally by Mikic [Mik74]. Recent publications, such as those by Asif [Asi16], Tariq [Tar16], and Dou [Dou16], build on these equations and demonstrate that the heat flow rate in a steel-steel contact is calculated as follows:

$$\dot{Q} = h_c \cdot A \cdot \Delta T. \tag{6.9}$$

Symbol	Unit	Description	Symbol	Unit	Description
$\dot{Q}$	W	Heat flow rate	h_c	W/m² · K	Thermal contact conductance
A	m²	Apparent contact area	ΔT	K	Temperature difference at the interface

6.1.2 Mechanical Principles

In addition to the thermal equations, mechanical equations are required to calculate the clutch's thermomechanical behavior. The contact pressure distribution, which according to Equation (6.1), strongly influences the local heat input, depends on the expansions of the materials. The total strain is divided into thermal strain and mechanical strain:

$$\varepsilon = \varepsilon_E + \varepsilon_T. \tag{6.10}$$

Symbol	Unit	Description	Symbol	Unit	Description
ε	%	Total strain	ε_E	%	Mechanical strain
ε_T	%	Thermal strain			

The mechanical strain of the material derives from the quotient of the length change ΔL and the initial length L_0. Thermal strain is a change in the geometric dimension of a body caused by temperature changes and, according to Equation (6.12), depends on the temperature difference ΔT and the material-specific coefficient of thermal expansion α:

$$\varepsilon_E = \frac{L - L_0}{L_0} = \frac{\Delta L}{L_0}, \tag{6.11}$$

$$\varepsilon_T = \alpha \cdot (T - T_0) = \alpha \cdot \Delta T. \tag{6.12}$$

Symbol	Unit	Description	Symbol	Unit	Description
ε_E	%	Mechanical strain	L	m	Stretched length
L_0	m	Initial length	ΔL	m	Length change
ε_T	%	Thermal strain	α	K⁻¹	Linear thermal expansion
T	K	Temperature rise	T_0	K	Initial temperature
ΔT	K	Temperature change			

The stresses in the individual parts of the clutch are calculated based on the total strain ϵ according to Equation (6.10) and the elastic matrix of the materials D:

$$\sigma = D \cdot (\varepsilon_E + \varepsilon_T). \tag{6.13}$$

Symbol	Unit	Description	Symbol	Unit	Description
σ	N/m²	Stress	D	N/m²	Elastic matrix
ε_E	%	Mechanical strain	ε_T	%	Thermal strain

The equations introduced are used to calculate the temperature behavior as well as the stresses and pressure distribution as a function of temperature for clutches.

6.2 Material Properties

In addition to the physical relations, it is also necessary to specify the material properties for the simulation. The mounting parts, the outer plates, and the lining carrier plates consist of steel. The friction linings are made of organic blended fabric and are paper-based. Table 6.1

enumerates the material properties used for the simulation model. With exception of the Young's modulus of the friction material, the values are derived from the literature [Woh09].

	Unit	Steel	Friction lining
Young's modulus	N/m^2	$2.1 \cdot 10^{11}$	Regression function (6.14)
Poisson's ratio	–	0.3	0.2
Coefficient of thermal expansion	1/K	$13.3 \cdot 10^{-6}$	$70 \cdot 10^{-6}$
Density	kg/m^3	7850	900
Specific heat capacity	J/kg · K	520	2890
Thermal conductivity	W/m · K	52	0.25

Table 6.1: Material parameters according to Wohlleber [Woh09].

The Young's modulus of the friction lining of the friction plate FP1 is measured. To this end, ten compression tests are performed on a set of plates (six steel plates, five friction plates). The measured data are shown in Figure 6.1 on the left. The material behavior exhibits nonlinearity. The measured data are characterized by a compensation curve to determine the Young's modulus:

$$\sigma = \left(\frac{x - c}{a}\right)^{\frac{1}{b}}. \tag{6.14}$$

Symbol	Unit	Description	Symbol	Unit	Description
σ	N/m^2	Stress	x	%	Strain
a	–	Regression coefficient = 0.04345	b	–	Regression coefficient = 0.5312
c	–	Regression coefficient = – 0.004454			

The Young's modulus represents the slope of the curve in the stress–strain diagram or, in mathematical terms, constitutes the first derivative of stress with respect to strain. The first derivative of Equation (6.14) is as follows:

$$E(\sigma) = \sigma'(\sigma) = \sigma^{1-b}\frac{1}{a \cdot b}. \tag{6.15}$$

Symbol	Unit	Description	Symbol	Unit	Description
E	N/m^2	Young's modulus	σ	N/m^2	Stress
a	–	Regression coefficient = 0.04345	b	–	Regression coefficient = 0.5312

Thus, the Young's modulus of the friction lining is described as a function of stress. The curve is shown on the right in Figure 6.1.

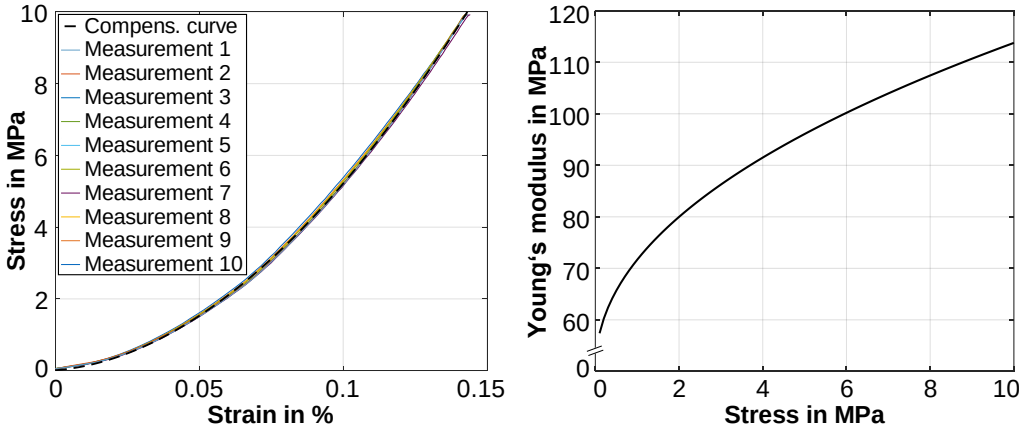

Figure 6.1: Results of compression tests for friction lining of friction plate FP1 (left); Young's modulus as a function of stress for friction lining (right).

6.3 Formulation of a Two-Dimensional Simulation Model

The two-dimensional thermomechanical simulation of the clutch is set up and performed in ANSYS Mechanical 2022 R1 using the internal scripting language APDL. The simulation setup follows the basic principle of published research [Acu16a, Mil18], where static-mechanical calculations are coupled with transient-thermal calculations in a sequential process. In the static-mechanical simulation, the deformation of the plates and the pressure distribution on the friction interfaces are determined, which serve as input parameters for the transient-thermal simulation. The local heat flux density $\dot{q}(r,\theta,t)$ is calculated for each element on the friction interfaces based on the local pressure $p(r,\theta,t)$ and the local sliding velocity $v_{rel}(t,r)$, as outlined in Equation (6.1). The computed temperature distribution is subsequently used as an input parameter for the mechanical simulation, in accordance with Equation (6.6). The total strains are determined based on the mechanical and thermal strains, and new pressure distribution is computed. A workstation with two Intel Xeon 6154 CPUs and 96GB of RAM and an NVIDIA Quadro P2000 GPU is used to perform the calculations. [Sch22c]

6.3.1 Geometry

The template for the two-dimensional model is based on the friction system FS1, with the steel plates serving as outer plates and the friction plates as inner plates. The geometry is reduced to two dimensions by utilizing rotational symmetry to minimize the complexity of the FEM simulation model. As a result, the grooves of the lining and the shape and number of teeth of the steel and friction plates are omitted from consideration. To maintain consistency, the diameters of steel or carrier plates are adjusted to ensure that the thermal mass of the simplified parts matches the thermal mass of the physical parts. The model setup, geometric dimensions, and mechanical boundary conditions are shown in Figure 6.2. The technical drawing of the parts to be analyzed is presented in Figure 4.5. [Sch22c]

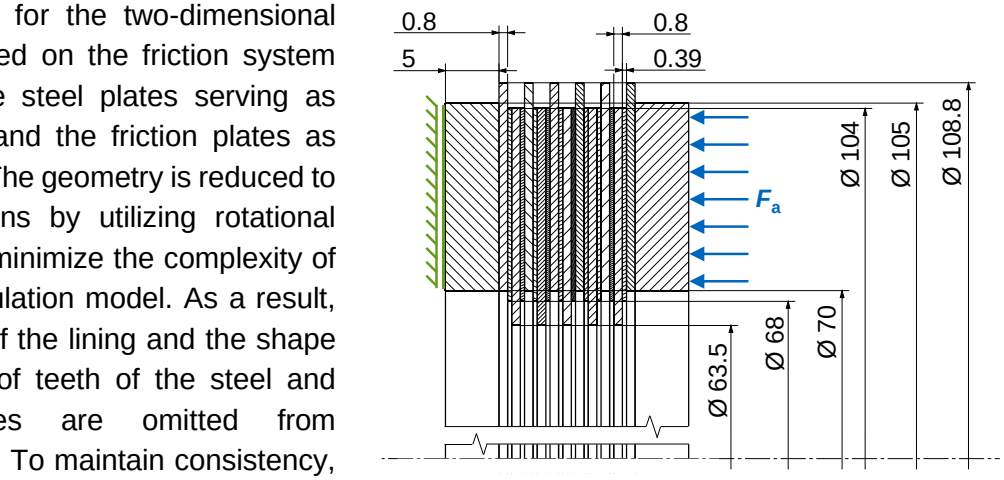

Figure 6.2: Model setup, geometrical dimensions in mm, and mechanical boundary conditions of the friction system FS1 [Sch22c].

6.3.2 Finite Element Method Settings

The basic principle of the two-dimensional model is based on preliminary work [Acu16a, Erd05, Mil18, Neu08, Sto23], and the results presented below have been published by Schneider et al. [Sch22c]. The area elements PLANE55 (thermal calculation) and PLANE182 (mechanical calculation), with four nodes each, are used for the geometric structure. Besides area elements, contact elements must also be evaluated and defined. A pair-based contact condition employing TARGE169 and CONTA172 elements is adopted. In the simulation model, the contact elements overlay the underlying surface elements. The Augmented Lagrangian method serves as the contact algorithm. Both Dirichlet and Neumann boundary conditions need definition for the mechanical and thermal calculations. For the mechanical calculations, two aspects govern the Dirichlet boundary conditions. Firstly, uniform axial displacement of the

right face of the pressure plate, where the axial force is applied, is assumed. Secondly, the left side of the reaction plate, as illustrated in Figure 6.2, is assumed to prohibit any axial displacement. For thermal calculations, the multi-plate clutch is assumed to start with a temperature of 80 °C. Additionally, passive cooling is implemented through the contact surfaces of the teeth in the circumferential direction and the axial mounting parts. The heat flow rate is calculated using Equation (6.9). In the two-dimensional model, the shape of the teeth of the steel plates and the lining carrier plate cannot be replicated due to rotational symmetry. Since the lateral surface area of the components in the finite element model is much larger than the contact surfaces of the teeth with the carriers, a dimensionless factor, A_{rat}, is introduced:

$$A_{\mathrm{rat}} = \frac{A_{\mathrm{Flank}}}{A_{\mathrm{FE-Model}}}. \tag{6.16}$$

Symbol	Unit	Description	Symbol	Unit	Description
A_{rat}	–	Area ratio of the model to the real part	A_{Flank}	m²	Tooth flank area
$A_{\mathrm{FE-Model}}$	m²	Contact area in the model			

Dietsch [Die21] indicates that the share of free convection and thermal radiation is approximately 0.15 % each. Consequently, both heat transport mechanisms are omitted in subsequent discussions.

The thermal Neumann boundary condition is defined by the heat flux rate in the contact elements, as calculated by Equation (6.1). The determination and application of $\dot{q}(r,\theta,t)$ must be done individually for each network element. The rationale for element-wise calculation lies in the relative velocity gradient, which increases with the radial coordinate, as shown in Figure 6.2. [Sch22c]

6.3.3 Operating Conditions

The load parameters of the clutch, which are derived from the experimental load parameters, are detailed below. These load parameters serve as the mechanical Neumann boundary conditions. The clutch operates under transient slip conditions. After the axial force is applied, the clutch undergoes repeated acceleration, and the differential speed is subsequently reduced to zero. The individual ramps for both the build-up and reduction of the differential speeds last for 2 s each. A pause of 0.5 s intervenes between the slip phases. Figure 6.3 shows the curve of the axial force and differential speed with exemplary values. [Sch22c]

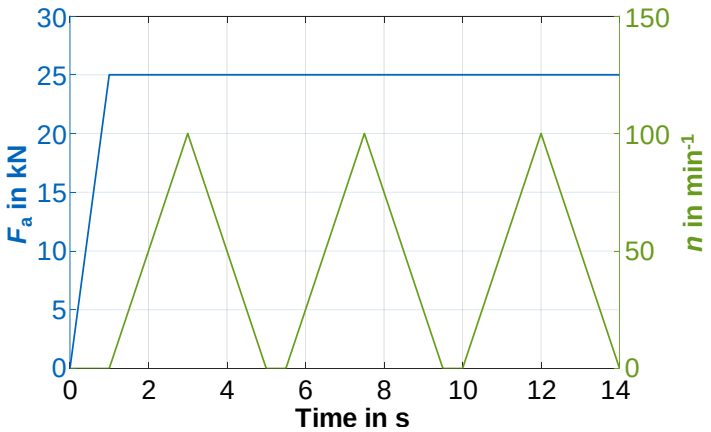

Figure 6.3: Curves of the load parameters axial force and differential speed with exemplary values [Sch22c].

6.3.4 Mesh and Time-Step Sensitivity Analysis

Figure 6.4 shows the model for the mesh and time-step sensitivity analysis. The maximum temperature T_{max} at the level of the mean friction diameter r_m of the third steel plate in the axial center, serves as the convergence criterion (see Figure 6.4). Consequently, temperatures at this specific location are compared across all simulations conducted. The load parameters of the simulations for the studies are detailed in Table 6.2. Figure 6.5 shows the simulated maximum temperature T_{max} as a function of different numbers of nodes and inverse time-step sizes. The lowest number of nodes for the mesh analysis is 1 190, which is successively increased.

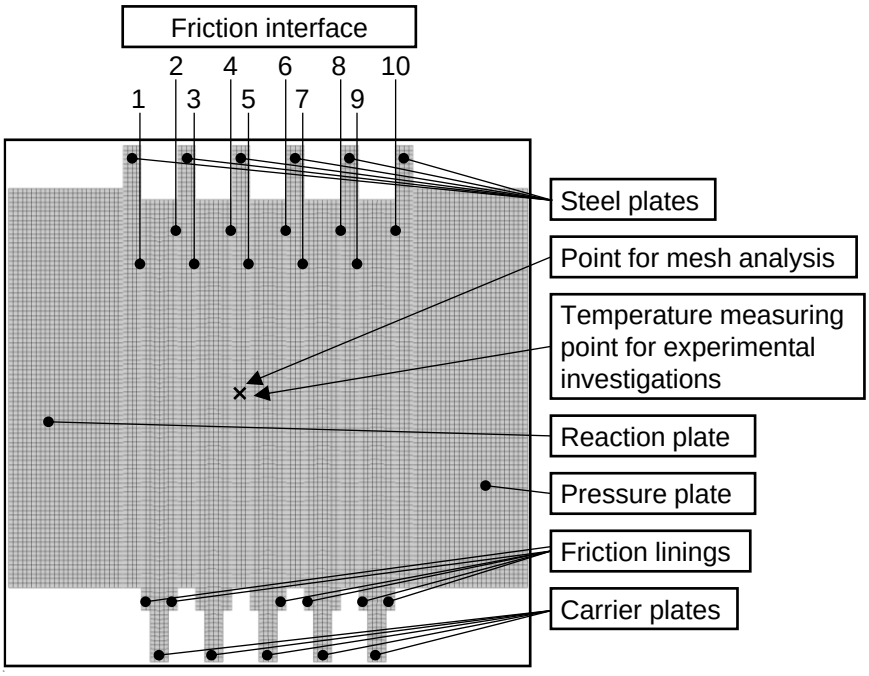

Figure 6.4: Model with meshing to simulate temperature and pressure distribution and as a reference model of the mesh and time-step sensitivity analysis [Sch22c].

	Unit	Value
Pressure p	N/mm²	5.0
Max. differential speed Δn_{max}	min⁻¹	110

Table 6.2: Load parameters for mesh and time-step analysis.

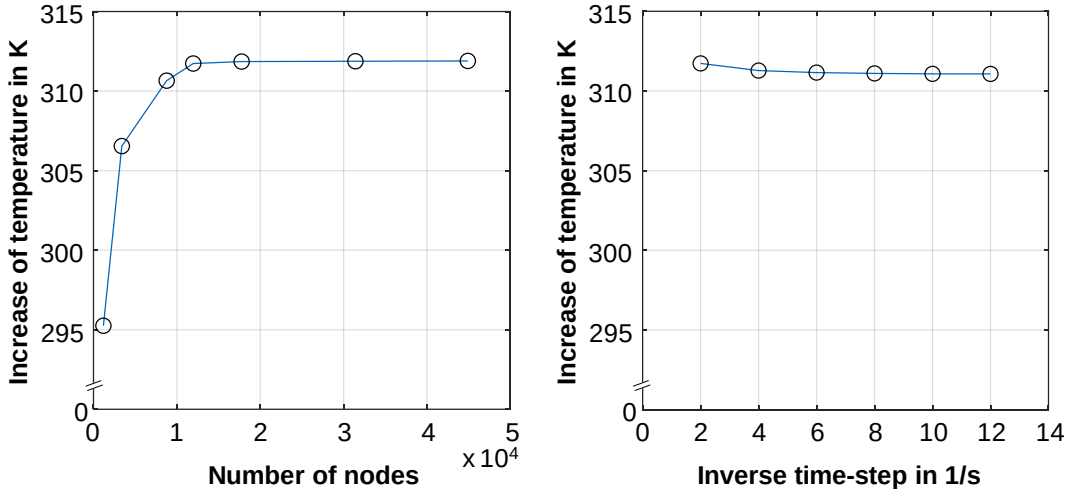

Figure 6.5: Calculated increase in temperature for different numbers of nodes (left) and time-step sizes (right) to evaluate the convergence behavior of the numerical solution [Sch22c].

The numerical solution of the temperature calculation is influenced by the computational mesh and converges as the number of nodes increases. A node count exceeding approximately 11 000 is deemed sufficient for subsequent analyses. This node count corresponds to an edge length of 0.2 mm per element. The smallest time-step size is given by the pause between two

slip phases and amounts to 0.5 s. (see Figure 6.3). The differences of the numerical solution of the temperature calculation, as a function of the time-step size, are very small, and the solution is thus only slightly influenced by the time-step size. Halving the time-step size roughly doubles the computational time, a trade-off that does not warrant the marginal increase in accuracy. Consequently, a time-step size of 0.5 s is employed in subsequent calculations. [Sch22c]

6.3.5 Validation with Experimental Data

Experimental tests are used to validate the simulation model to ensure that it computes correctly and accurately represents application-related conditions. For this purpose, temperature measurements are compared with the simulation results. First, a single test incorporating three slip phases is configured within the simulation framework. The coefficient of friction obtained from the experimental test is replicated in the simulation through the use of numerous reference nodes. Both differential speed and axial force are treated as linear variables, with absolute values sourced from the measurements. This data is detailed in Table 6.3.

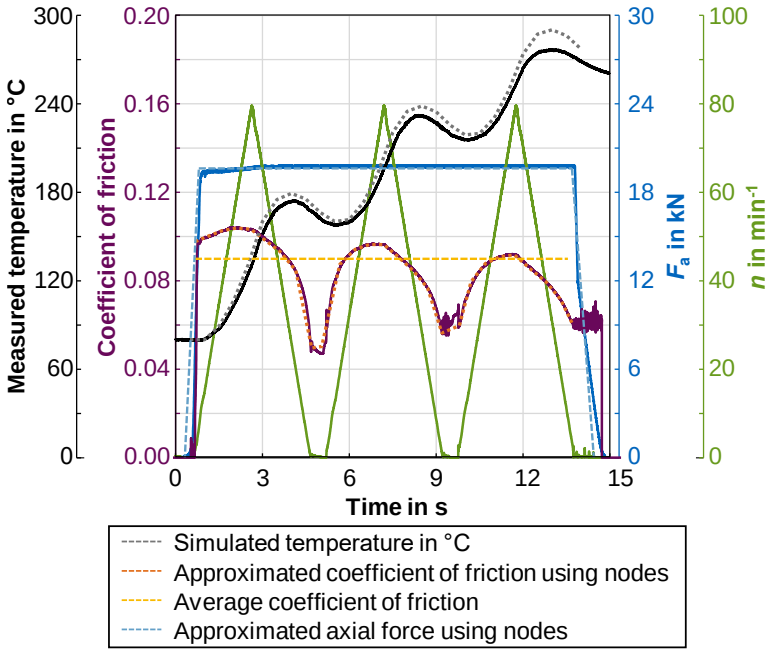

Figure 6.6: Measurement recording of a slip cycle and comparison of the simulated temperature with the measured temperature [Sch22c].

	Unit	Value
Pressure p	N/mm^2	4.0
Max. differential speed Δn_{max}	min^{-1}	80
Approximated coefficient of friction using reference nodes	–	0.098, 0.100, 0.103, 0.104, 0.103, 0.098, 0.093, 0.085, 0.059, 0.060, 0.087, 0.094, 0.096, 0.096, 0.090, 0.060, 0.079, 0.088, 0.091, 0.092, 0.084, 0.080, 0.071, 0.0607, 0.084, 0.077, 0.056
Average coefficient of friction	–	0.085

Table 6.3: Load parameters, coefficient of friction as reference nodes and averaged coefficient of friction for the comparison of the simulated temperature with the measured temperature [Sch22c].

The location for evaluating temperature in both the simulation and the experimental measurement aligns, as indicated in Figure 6.4. Data from the experimental test, approximated input parameters for the simulation, and the simulated temperature curve are shown in

Figure 6.6. The measured and simulated temperature curves agree very well over the entire slip cycle. The deviations between measurement and simulation are in the range of ± 10 K. Figure 6.6 shows that the simulated temperatures tend to be higher than the measured ones and that the measured temperature increases are flatter than the simulated increases.

For a more comprehensive validation of the simulation model, numerous individual tests are conducted on the test rig, and the measurement results are compared with those from the simulation. For each test, the average value of the measured coefficient of friction across the entire slip cycle is computed and integrated into the simulation model. The tests are performed with the following parameters:

- $p = 4.0 \ldots 8.0\,\mathrm{N/mm^2}$
- $\Delta n_{max} = 60 \ldots 140\,\mathrm{min^{-1}}$
- Number of slip phases $N = 1 \ldots 3$

Figure 6.7 shows a comparison between simulated and experimental results. Congruence between simulation and experimental data occurs when the data points are precisely positioned on the bi-sector of the angle. A correlation exists between the simulation results and the experimentally measured values across all load cycles. The deviations between test rig results and simulation results are larger at high temperatures. In total, the differences are small and do not exceed 10 % at any point. The maximum absolute difference is 24 K. [Sch22c]

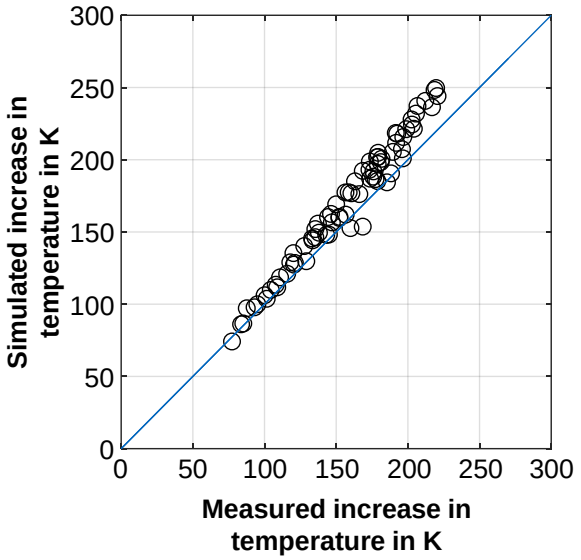

Figure 6.7: Comparison between simulated and measured temperature increase for different loads [Sch22c].

6.4 Formulation of a Three-Dimensional Simulation Model

The three-dimensional thermomechanical simulation of the clutch is configured and executed in ANSYS Mechanical, using Workbench 2022 R1 and the Coupled Field Transient Analysis System. Similar to the two-dimensional simulation model, mechanical calculations are coupled with thermal calculations to analyze the thermomechanical behavior of the clutch. The computations are performed on the SuperMUC-NG, utilizing Intel Skylake Xeon Platinum 8174 processors. Each node has 48 cores and 96 GBytes of memory per node.

6.4.1 Geometry

The geometry for the three-dimensional simulation model is derived from the dimensions of the FS1 friction system. Therefore, the same plates investigated in the two-dimensional simulation are used in the three-dimensional simulation. Figure 4.5 in Section 4.2 shows the technical drawings of the steel and friction plates, which are faithfully replicated in the simulation model. Similar to the two-dimensional simulations, the steel plates are modeled as outer plates, and the friction plates as inner plates. To compute the thermomechanical behavior of the clutch, a half-section of the steel plates and of the friction plate is modeled in the axial direction. This approach helps to manage the computational effort and allows for the study of the clutch's thermomechanical behavior in the circumferential direction without any restrictions.

6.4.2 Finite Element Method Settings

The three-dimensional model in ANSYS is designed based on the two-dimensional model described in Section 6.3.2, as well as the preliminary work by Wang and Zang [Wan21] and Sabri et al. [Sab21a]. The volume elements PLANE222, along with the contact elements CONTA174 and TARGE170, are employed. The steel plate flanks are unblocked in the axial direction and fixed in the circumferential direction, thereby serving as a mechanical Dirichlet boundary condition. A symmetry boundary condition is implemented on the rear side of the steel plate, under the assumption of no axial displacement. The thermal simulation commences with an initial temperature of 80 °C for the multi-plate clutch. Heat flow from the tooth flanks to the mounting parts is implemented in a similar manner as the two-dimensional simulation model for both the steel and friction plates. Due to the brief duration of the friction phases, the axial heat flow at the interfaces between the lining and the steel plates is negligible. The rotational velocity is applied to the flanks of the friction plate. In line with the two-dimensional model, the analysis does not consider free convection due to its minimal impact.

6.4.3 Operating Conditions

The load parameters (axial force, differential speed) for the three-dimensional model are obtained from experimental data. These load parameters define the mechanical Neumann boundary conditions. The clutch is operated under transient slip conditions. However, due to the high computational effort required for the three-dimensional model, a different approach is taken compared to the two-dimensional model. In the three-dimensional simulation, the differential speed is accelerated once and then returned to zero after applying the axial force. Each ramp, for both the increase and decrease of the differential speeds, lasts 2 s. In separate simulations, the axial force and differential speed are varied. Figure 6.8 illustrates the curve of the axial force and differential speed with exemplary values.

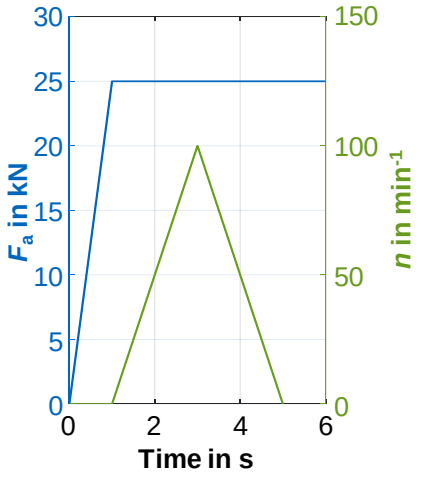

Figure 6.8: Exemplary load parameters for the three-dimensional simulation model.

6.4.4 Mesh and Time-Step Sensitivity Analysis

To ensure the quality and independence of the results from mesh parameters and time-step width, a sensitivity analysis for mesh and time-step is conducted. The convergence criterion is based on the maximum temperature (T_{max}) at the location of the temperature sensor used in the experiment (see Figure 4.17). This criterion allows for a direct comparison of temperature values at the same location across all simulations. Table 6.4 lists the load parameters used in the mesh and time-step sensitivity analysis simulations. Additionally, Figure 6.9 provides an example of the meshing of the steel plate, carrier plate, and friction lining. The simulated maximum temperature (T_{max}) as a function of different node numbers and inverse time-step sizes is presented in Figure 6.10.

	Unit	Value
Pressure p	N/mm^2	8.0
Max. differential speed Δn_{max}	min^{-1}	80

Table 6.4: Load parameters for mesh and time-step analysis.

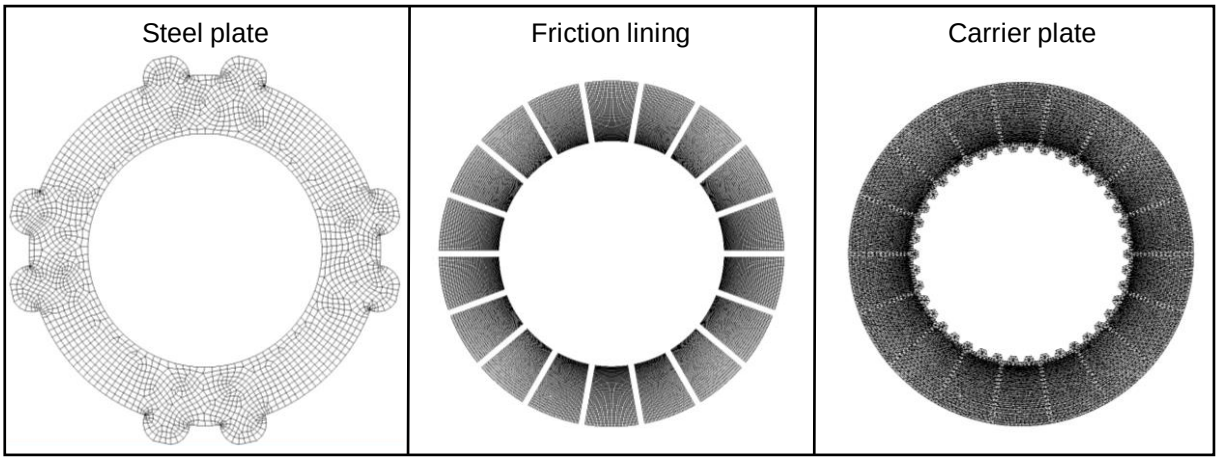

Figure 6.9: Models of the steel plate, friction lining and carrier plate with exemplary meshing.

The mesh analysis reveals a range of node numbers, from 30 175 to 145 828. The influence of node number on the temperature calculation is minimal, with the calculation converging as the number of nodes increases. A node number exceeding 100 000 is considered sufficient for subsequent analyses. For the time-step sizes, variations are applied between 0.00175 s and 0.015 s. As shown in Figure 6.10, the temperature calculation exhibits negligible differences with respect to the time-step size. The influence of the time-step size on the temperature calculation is minimal. Based on these findings, a fixed time-step size is not defined for the three-dimensional simulation model; instead, the Auto Time Stepper provided by ANSYS is utilized.

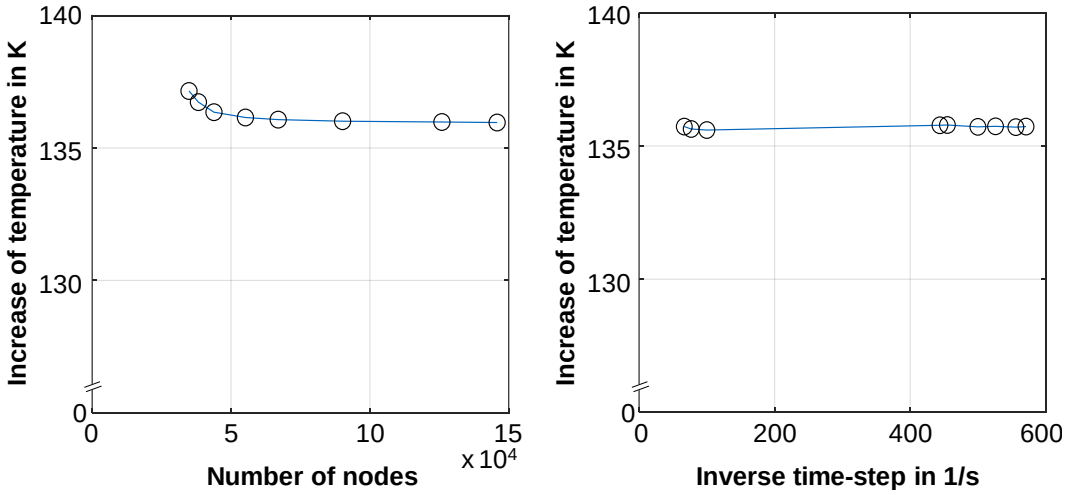

Figure 6.10: Calculated increase in temperature for different numbers of nodes (left) and time-step sizes (right) to evaluate the convergence behavior of the numerical solution of the three-dimensional model.

6.4.5 Validation with Experimental Data

The three-dimensional simulation model is validated in a manner similar to the two-dimensional model, using experimental tests to ensure the accuracy and real-world representation of the calculations. This involves comparing the temperature measurements with the simulation results. To start, a single test is conducted in which the coefficient of friction from the experimental test is accurately replicated in the simulation using multiple reference nodes. The axial force and differential velocity are assumed to have a linear relationship, and their absolute values are derived from the experiment. The corresponding data can be found in Table 6.5.

	Unit	Value
Pressure p	N/mm²	8.0
Max. differential speed Δn_{max}	min⁻¹	80
Approximated coefficient of friction using reference nodes	–	0.097, 0.097, 0.058, 0.043,
Average Coefficient of friction	–	0.079

Table 6.5: Load parameters, coefficient of friction as reference nodes and averaged coefficient of friction for the comparison of the simulated temperature with the measured temperature

Figure 6.11 presents the approximated data from the experimental test used as input parameters for the simulation, along with the simulated temperature curve and the measured data from the experiment. The comparison between the measured and simulated temperatures is conducted at the same location on the steel plate. The simulated and measured temperature curves agree very well over the slip phase. The deviations between the measurement and simulation fall within the range of ± 10 K. Notably, the simulated temperatures tend to be slightly higher than the measured temperatures, while the measured temperature gradients appear to be less steep compared to the simulated values.

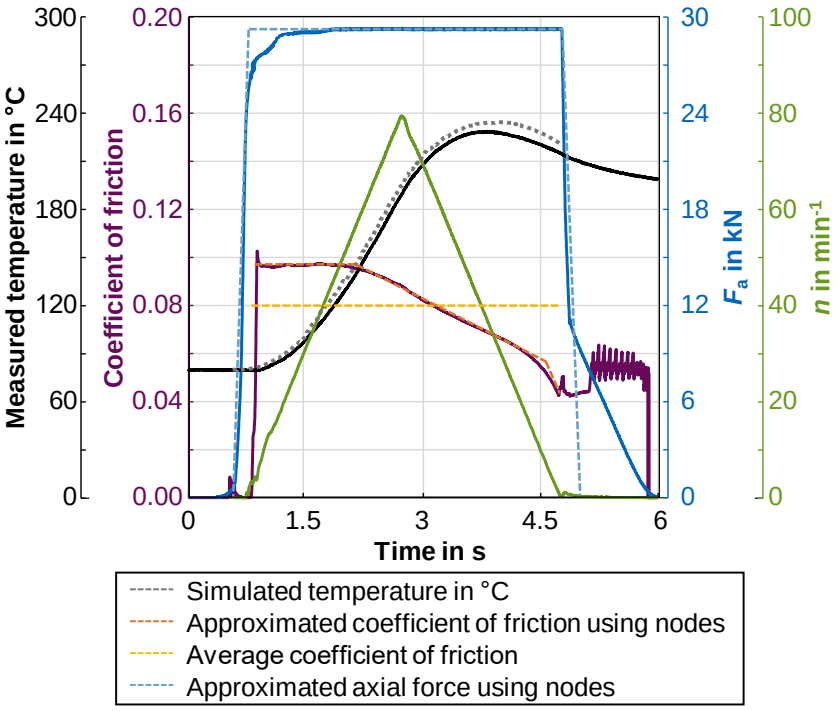

Figure 6.11: Measurement recording of a slip phase and comparison of the simulated temperature with the measured temperature.

In addition to comparing the temperature curves individually, the maximum temperatures from both the simulation and the experiment are compared in multiple tests to validate the simulation model. In each comparison, the average value of the measured coefficient of friction during the entire slip phase in the experiment is calculated and used in the simulation model. The tests are conducted with the following parameters:

- $p = 4.0 \ldots 8.0\,\mathrm{N/mm^2}$
- $\Delta n_{max} = 60 \ldots 140\,\mathrm{min^{-1}}$
- Number of slip phases $N = 1 \ldots 3$

Figure 6.12 ilustrates the comparison between the simulated and experimental temperature increases, demonstrating a correlation between the simulation results and the experimentally measured values for all load cycles. It is observed that the differences between the simulated and experimental results are more pronounced at high temperatures. However, overall, these differences remain small and do not exceed 10 % at any point. The maximum absolute difference is 12 K.

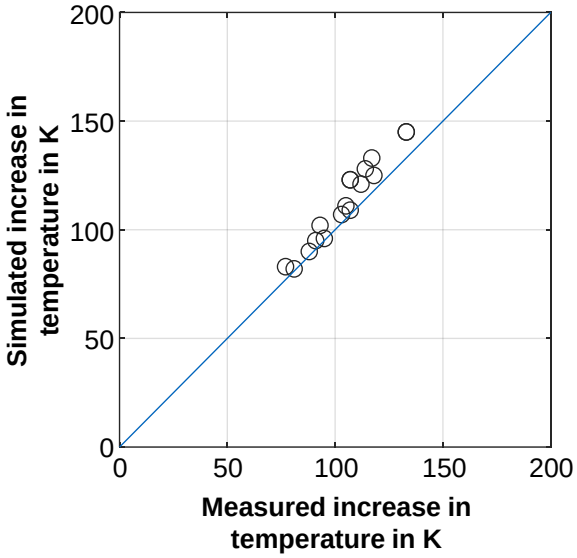

Figure 6.12: Comparison between simulated and measured temperature increase for different loads.

6.5 Simulation Process

In the previous sections, the mechanical and thermal principles, material parameters, geometries, simulation settings (element selection, Neumann boundary conditions, Dirichlet boundary conditions), and operating conditions for the two-dimensional and three-dimensional simulation models are presented. To enhance understanding, Figure 6.13 illustrates the simulation process for the two-dimensional model. Once all the necessary parameters are defined, the mechanical calculation begins. The calculated pressures are then used for the heat flow density calculation. In the thermal simulation, the heat flow is applied, and the temperature distribution of the clutch is determined. Once the sub-steps are completed, a comparison is made ($i = n$) with the number of time-steps. The results of the thermal analysis serve as input files for the subsequent mechanical calculations.

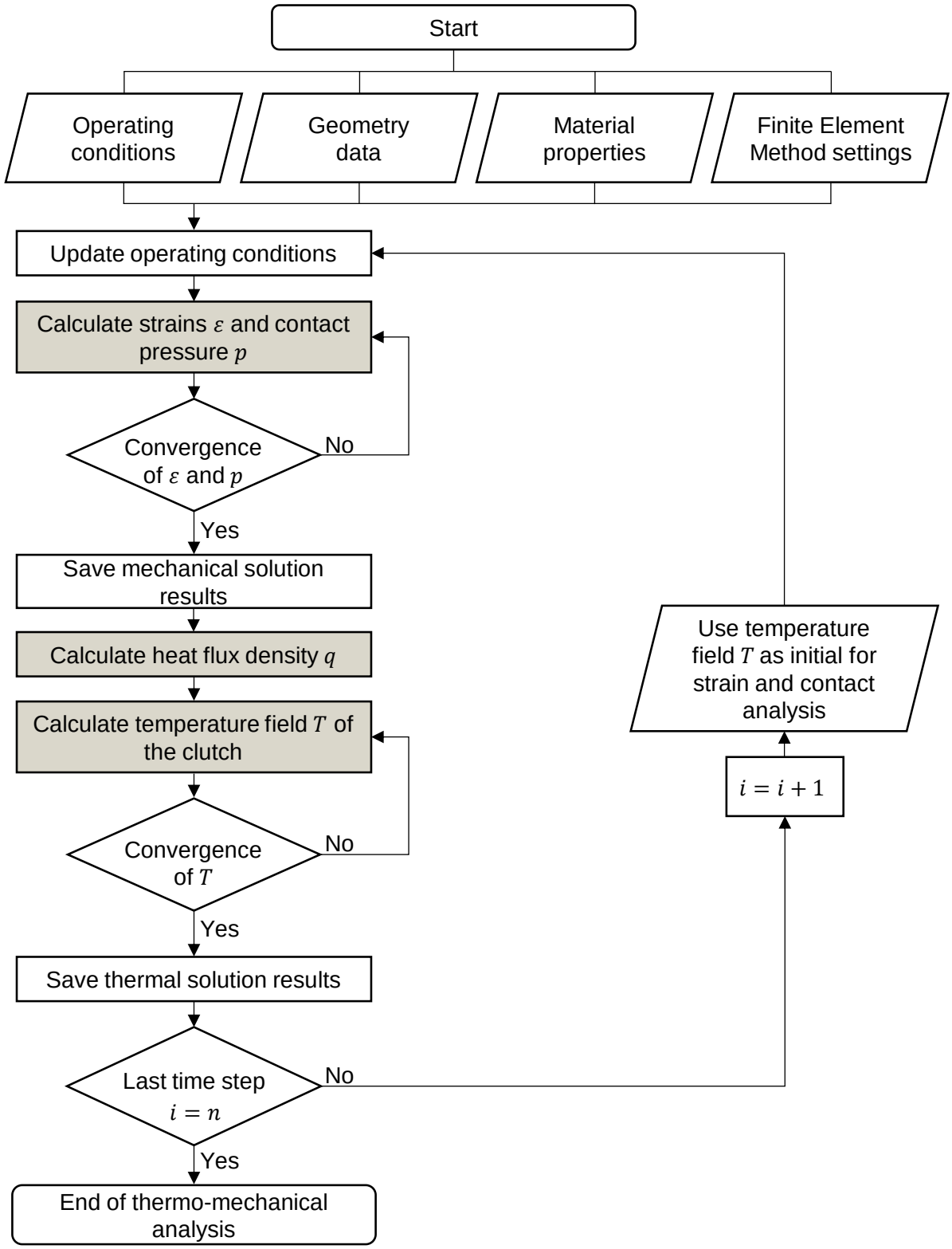

Figure 6.13: Flow chart for the simulation process [Sch22c].

7 Simulation of the Thermomechanical Behavior of Multi-Plate Clutches

In this section, the simulation results of the two-dimensional as well as the three-dimensional model are presented. On the one hand, the temperature and pressure behavior are evaluated. On the other hand, different geometrical and material parameters are varied, and their effect on the thermal behavior of the clutch is investigated. In addition, the simulation data are used to develop a temperature prediction model for different load parameters and lining thicknesses.

7.1 Two-Dimensional Analysis of the Thermomechanical Behavior

In the following subsections, the simulation results of the two-dimensional model are presented. First, the temperature and pressure distribution during the slip cycle are explained. Subsequently, a sensitivity analysis is performed with respect to the material as well as geometric parameters regarding the temperature behavior. Finally, a metamodel of the thermal behavior of the clutch is developed using machine learning algorithms. The results presented below are published by Schneider et al. [Sch22c].

7.1.1 Temperature and Pressure Distribution

After validating the simulation model with respect to numerical parameters (number of nodes, time-step size) and comparison with experimental data (see Section 6.3), the temperature and pressure distribution during a slip cycle are examined in more detail below. The temperature distribution of the clutch at different times during the slip cycle is shown in Figure 7.1. The load parameters correspond to the slip cycle shown in Figure 6.6 and are listed in Table 6.3. The clutch assembly is heated by the individual slip phases, with the most intense heating occurring within the steel plates. The heat dissipation at the inner and outer carriers and the lack of frictional contact at the inner and outer diameters of the plates create a temperature gradient in the radial direction across the individual plates. This radial gradient is more noticeable at the maximum speed difference than at the end of a slip phase. The outer regions of the multi-plate clutch in the axial direction experience less heating due to the heat dissipation

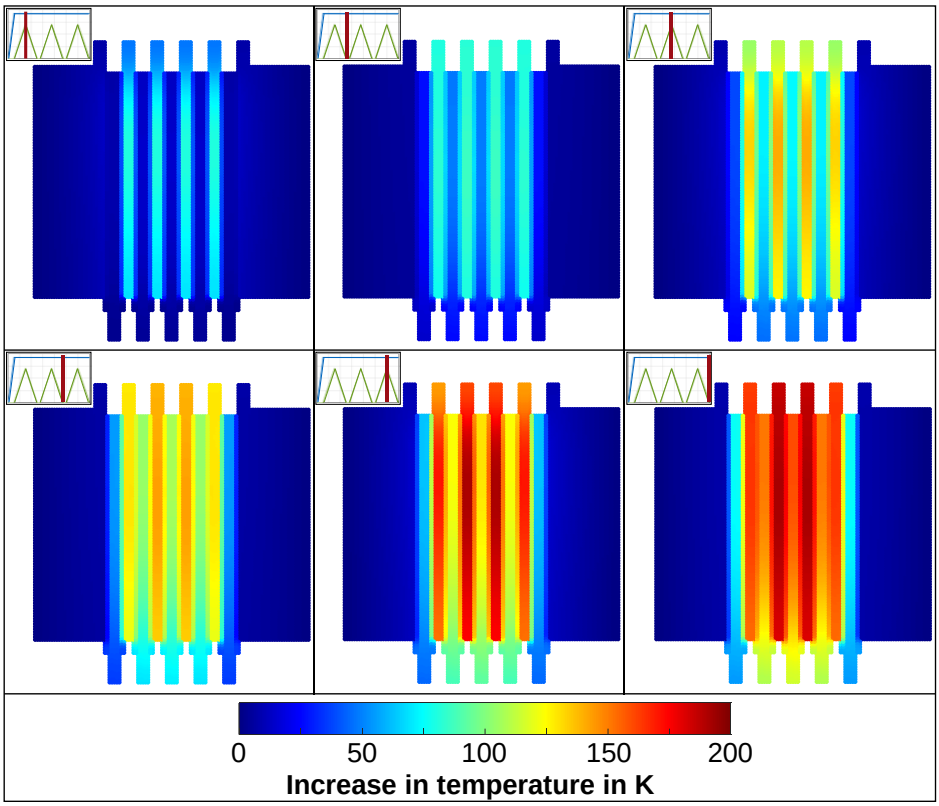

Figure 7.1: Temperature distribution in the clutch at selected times during a slip cycle [Sch22c].

at the reaction and pressure plates, along with their thermal masses. The temperature maximum is at the two steel plates in the clutch center. [Sch22c]

Figure 7.2 shows the temperature and pressure distribution of friction interfaces 1 – 5 (see Figure 6.4) as a function of time. The results for friction interfaces 6 – 10 (see Figure 6.4), which are equivalent to those of friction interfaces 1 – 5 due to the symmetrical structure of the model, can be found in Figure A.22 in the Appendix. Figure 7.2 shows that the friction interfaces in the center of the clutch (friction interfaces 4 and 5) heat up more than the outer friction interfaces. The temperature distribution over time shows that the heating occurs with the individual slip phases. The temperature maximum for each slip phase is reached after the corresponding speed maximum. The temperature at the friction interfaces decreases between the individual slip phases. In the radial direction, the highest temperatures are observed at approximately 46 mm, indicating that the highest temperatures occur near the outer diameter (mean friction radius r_m = 43.5 mm). The inner diameter heats up due to delayed heat transfer as soon as frictional contact is established (see Figure 6.4). These areas are exclusively heated by heat conduction. The absolute temperature increase declines from slip phase to slip phase, which can also be seen in Figure 6.6. The pressure distribution is very homogeneous after the axial force is built up. A

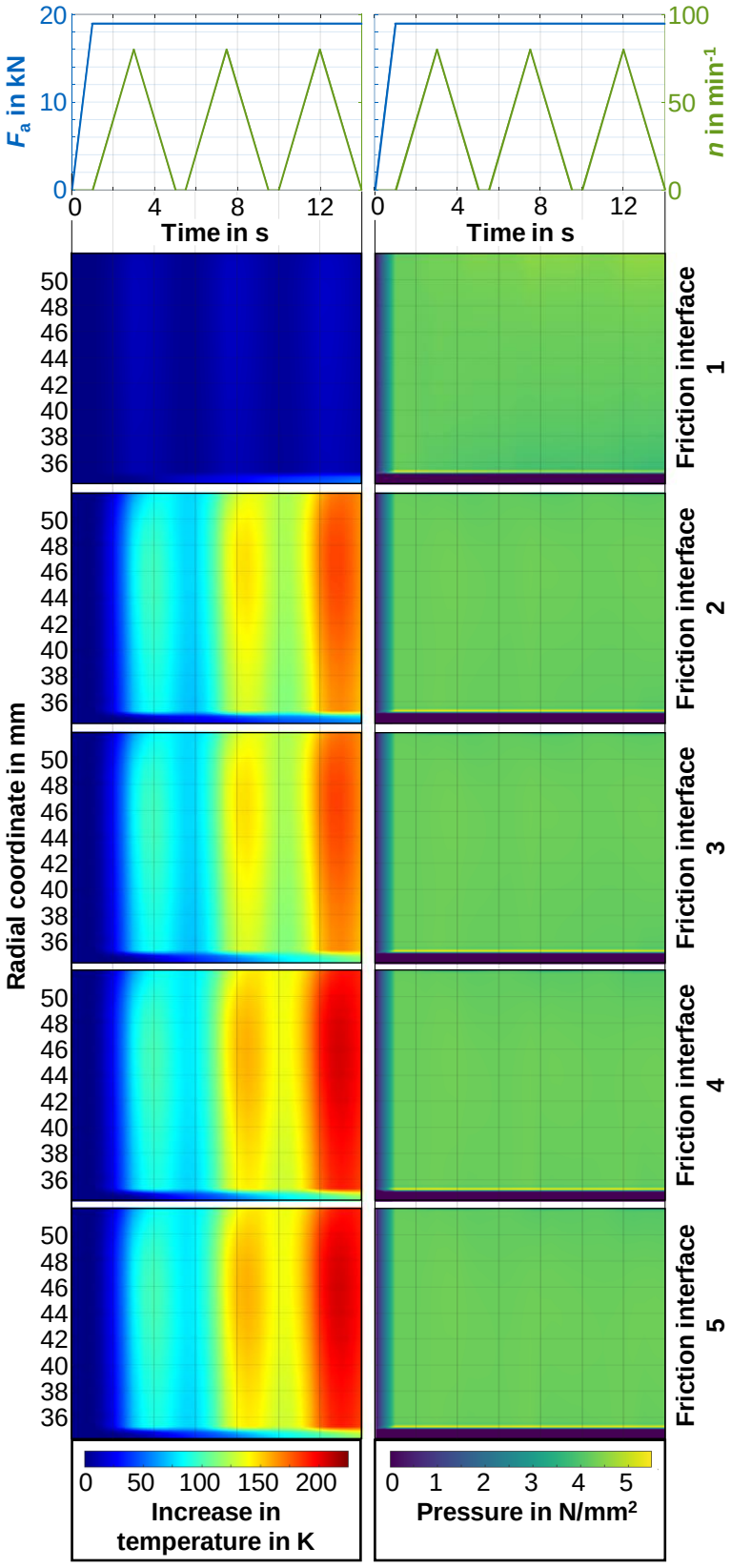

Figure 7.2: Temperature and pressure distribution of friction interfaces 1 – 5 as a function of time [Sch22c].

slight increase in pressure can be observed on the inner diameter of the friction interfaces at the contact edge. In radial direction < 35 mm, no contact takes place, so that no pressure is present. No differences in pressure level can be seen over the entire slip cycle. There are also no differences in the pressure distribution in radial direction except for the contact edge on the inner diameter. There is also no significant difference in pressure across the respective friction interfaces. [Sch22c]

7.1.2 Influence of the Material Parameters and the Geometric Parameters

For the parameter study on the influence of material and geometry parameters on the thermomechanical behavior of a clutch, a one-at-a-time (OAT) experimental design is employed. In the OAT method, each parameter is varied individually while keeping the values of other parameters constant. This approach allows a clear tracking of the individual contributions of each parameter and isolates their effects on the maximum temperature in the clutch. The OAT approach is chosen for its ability to conveniently examine the impacts of each parameter and its straightforward implementation.

Table 7.1 presents all thirteen parameters examined in this study, along with their respective upper and lower bounds. Both geometric parameters and material properties are varied. The upper and lower bounds are chosen to fall within acceptable and practical ranges. The variation range is defined for each parameter to ensure that a useful range of data is captured without rendering the simulation infeasible. The variation of the parameters is performed under a mechanical load at a pressure of 2 N/mm^2 and a rotational speed of 80 min^{-1}. To examine the effects of individual parameters on the maximum temperature in the clutch, a total of 1 000 simulations are conducted. The maximum temperature T_{max} in the clutch is used to compare the different parameter variations.

Component	Parameter	Symbol	Unit	Lower bound	Upper bound	Step size
Steel plate	Thickness	d_{sp}	mm	0.4	2	0.032
	Density	ρ_{sp}	kg/m^3	7 200	7 800	80
	Heat conductivity	λ_{sp}	W/mK	10	80	0.875
	Specific heat capacity	c_{sp}	J/kgK	340	700	18
Carrier plate	Thickness	d_{cp}	mm	0.4	2	0.032
	Density	$\rho_{cp} = \rho_{sp}$	kg/m^3	7 200	7 800	80
	Heat conductivity	$\lambda_{cp} = \lambda_{sp}$	W/mK	10	80	0.875
	Specific heat capacity	$c_{cp} = c_{sp}$	J/kgK	340	700	18
Friction lining	Thickness	d_{fl}	mm	0.2	0.8	0.015
	Density	ρ_{fl}	kg/m^3	400	1300	0.03
	Heat conductivity	λ_{fl}	W/mK	0.1	0.4	0.0075
	Specific heat capacity	c_{fl}	J/kgK	1 000	4 000	75
	Young's modulus	E_{fl}	N/m^2	40	220	3

Table 7.1: Upper and lower bounds of varied parameters.

Additionally, simulations are conducted to investigate the influence of the number of friction interfaces. Various simulation models are created with 6, 10, and 14 friction interfaces. For

each simulation model, four different loads are simulated. The inner and outer diameters are adjusted to ensure that the same pressure and specified friction work are applied in all three variants, enabling appropriate comparisons between them. The maximum temperature reached during the simulation is used for the analysis below.

Thickness of the Steel Plate and the Friction Lining:

In Figure 7.3, the simulated maximum temperature in the clutch is shown as a function of the steel and carrier plate thickness (left-hand plot) and the friction lining thickness (right-hand plot). The simulated maximum temperature decreases in each case as the thickness of the steel and carrier plates increases. This influence is stronger for the steel plate compared to the carrier plate. Doubling the thickness of the steel plate from 0.8 mm to 1.6 mm results in a temperature decrease of over 100 K. At the same time, the temperature decrease gradient diminishes as the thickness of the steel plate and carrier plate increases. Regarding the thickness of the friction lining, only a weak dependence on the maximum temperature in the clutch is observed. Increasing the thickness to 0.4 mm results in a slight increase in the peak temperature. However, from 0.4 mm to 0.8 mm, no further increase in the maximum temperature is observed with further thickening of the friction lining.

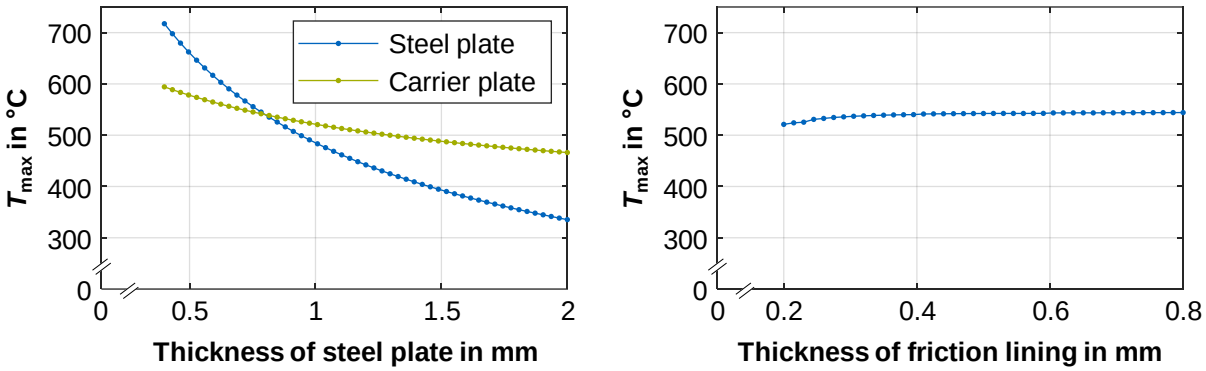

Figure 7.3: Dependence of the maximum temperature in the clutch on the thickness of the steel plate and carrier plate (left) and on the friction lining (right).

Heat Conductivity of the Steel and the Friction Lining:

Figure 7.4 shows the relationship between the simulated maximum temperature in the clutch and the thermal conductivity of the materials. The maximum temperature decreases with increasing thermal conductivity, both for steel (left-hand plot) and friction lining material (right-hand plot). For the friction lining, there is partial evidence indicating that the maximum temperature approaches asymptotic behavior. This implies that subsequent enhancements in thermal conductivity do not lead to additional reductions in the maximum temperature.

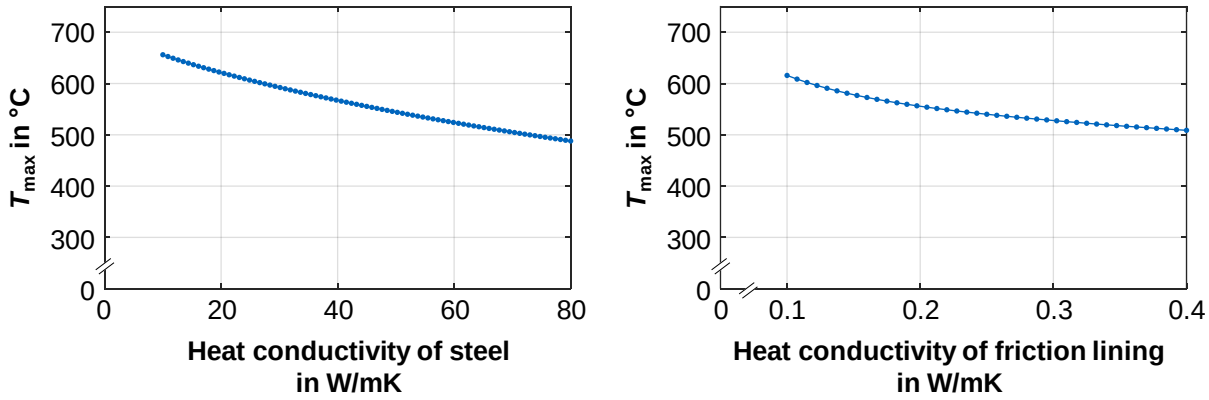

Figure 7.4: Dependence of the maximum temperature in the clutch on the heat conductivity of the steel (left) and on the friction lining (right) material.

Heat Capacity of the Steel Plate and the Friction Lining:

Figure 7.5 illustrates the variation in the simulated maximum temperature in the clutch as the specific heat capacities of the steel and friction lining are changed. For both materials, the maximum temperature in the clutch system decreases as the specific heat capacity increases. This decrease is more dominant for steel compared to the lining material. For instance, doubling the specific heat capacity of the steel from 350 J/kg to 700 J/kg results in a temperature reduction from approximately 625 °C to approximately 475 °C. In contrast, doubling the specific heat capacity of the friction lining from 2000 J/kg to 4000 J/kg only leads to a reduction from 560 °C to 520 °C.

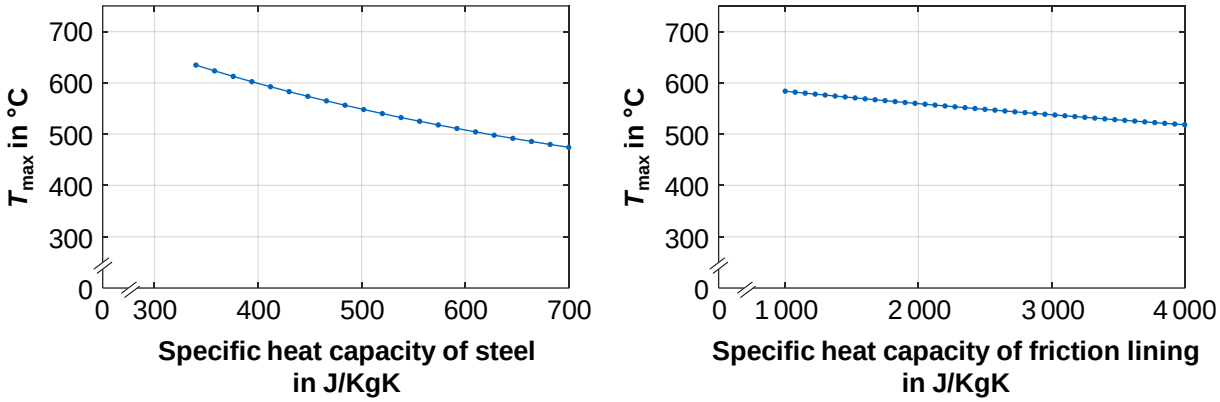

Figure 7.5: Dependence of the maximum temperature in the clutch on the heat capacity of the steel (left) and on the friction lining (right) material.

Steel and Friction Lining Density:

As shown in Figure 7.6, the relationship between the simulated maximum temperature of the clutch and the density follows a similar pattern as the dependence on specific heat capacity. Increasing the density of the materials leads to a decrease in the maximum temperature attained during the shifting process. This behavior is observed for both the density of the steel and the density of the lining. When increasing the density of the steel from 7200 kg/mm^3 to 8000 kg/mm^3, the maximum temperature decreases by approximately 25 K. Similarly, increasing the density of the lining material by 800 kg/mm^3, from 400 kg/mm^3 to 1200 kg/mm^3, results in a reduction in the maximum temperature by about 55 K.

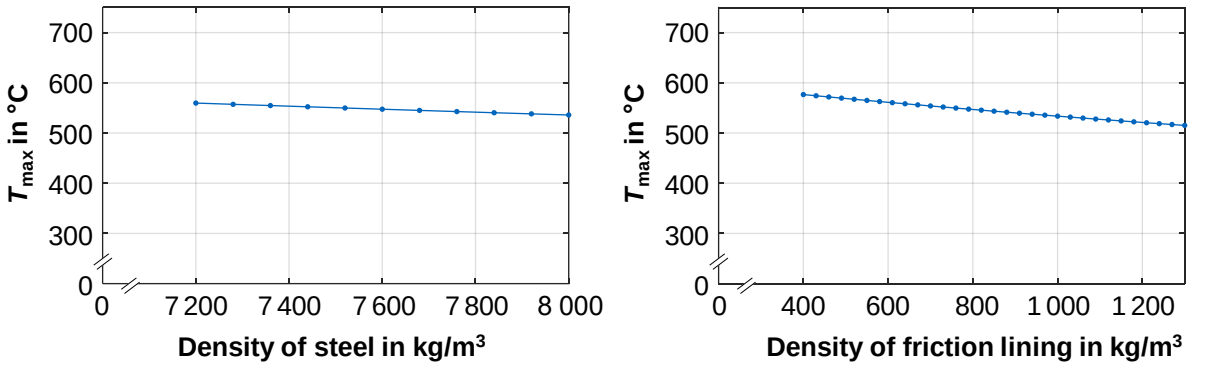

Figure 7.6: Dependence of the maximum temperature in the clutch on the density of the steel (left) and on the friction lining (right) material.

Young's modulus of the friction lining:

The relationship between the simulated maximum temperature in the clutch and the Young's modulus of the lining is shown in Figure 7.7. It is observed that the temperature exhibits minimal changes as the Young's modulus increases. When the value increases by more than five times, from $0.4 \cdot 10^8$ N/mm^2 to $2.2 \cdot 10^8$ N/mm^2, there is only a slight increase in the maximum temperature in the clutch, from 537 °C to 543 °C.

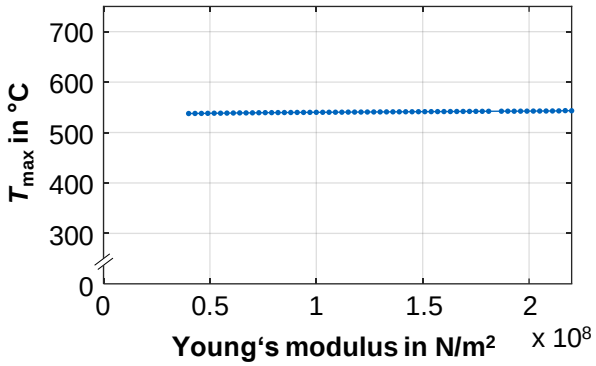

Figure 7.7: Dependence of the maximum temperature in the clutch on the Young's modulus of the friction lining.

Number of friction interfaces:

Figure 7.8 shows the maximum temperature of the clutch system as a function of the friction work for different numbers of friction interfaces. All three variants exhibit a linear trend. The variant with 6 friction interfaces yields the lowest maximum temperatures for all loads investigated. This is followed by the variant with 10 friction interfaces. The variant with 14 friction interfaces consistently exhibits the highest maximum temperature among the three variants investigated. Thus, it becomes evident that as the number of friction interfaces decreases, the maximum temperature reached is lower for the same friction work. Additionally, the temperature difference between the individual variants increases with higher friction work.

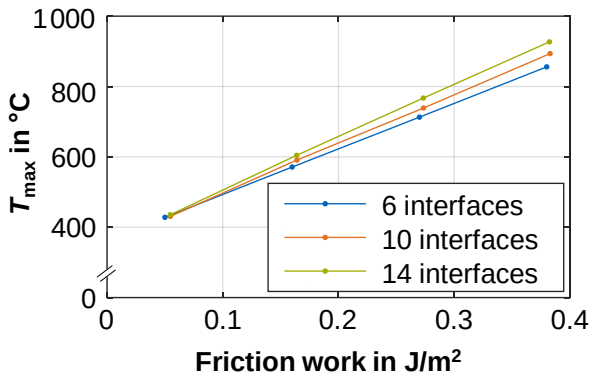

Figure 7.8: Dependence of maximum temperature on friction work with different number of friction interfaces.

7.1.3 Formulation of Surrogate Models

In addition to calculating temperature and pressure behavior with variations in material and geometry parameters, a surrogate model is being developed to predict the maximum temperature within a clutch system during operation. This model is based on two-dimensional thermo-mechanical finite element simulations of the clutch and the simulation process corresponds to the descriptions in Section 6. The results presented below are published by Schneider et al. [Sch22a]. Figure 7.9 illustrates the procedure for building surrogate models. The procedure can be roughly divided into four steps. The first two steps involve generating the required data from the finite element model. The parameters to be taken into account are defined, and then a large number of simulations are performed. These data are then processed to facilitate the creation of surrogate models and are tested using different algorithms. In the last step, the generated models undergo a parameter study to investigate the influence of the sample size on model performance and to evaluate the prediction.

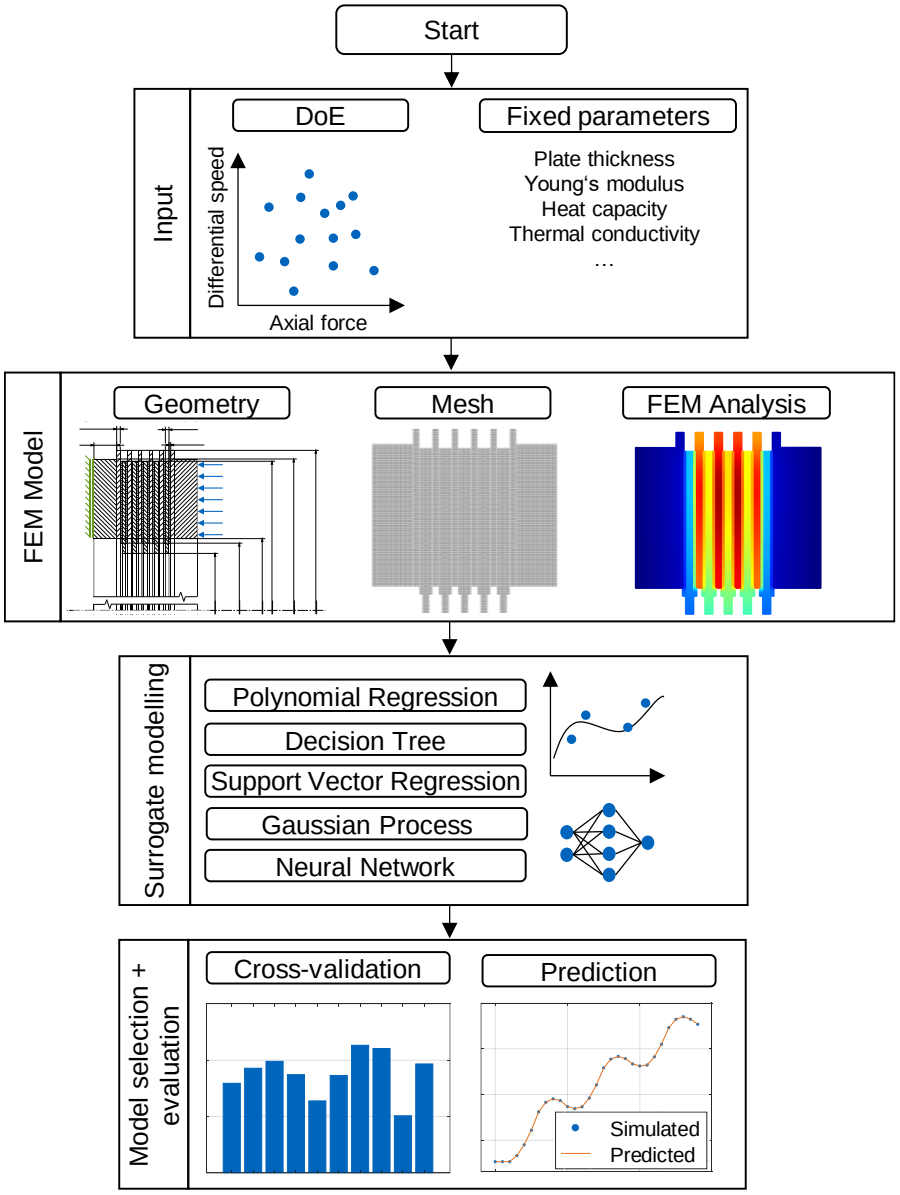

Figure 7.9: Graphical representation of the procedure for creating a surrogate model [Sch22a].

The data used to generate surrogate models comes from the finite element model described in Section 6.3. For each combination of input parameters, the simulation outputs the temperature

Parameter	Unit	Lower bound	Upper bound
Axial force F_a	N	9292	37168
Max. differential speed Δn_{max}	min^{-1}	80	140
Friction lining thickness d_f	mm	0.2	0.8

Table 7.2: Boundaries of the varied input parameters [Sch22a].

distribution of the clutch at each time step. Since the maximum temperature is of interest in relation to damage mechanisms, the maximum value from the temperature distribution at each time step is selected. To generate the data sets, 200 simulations with 29 time steps each are run per use case. Latin Hypercube sampling is employed to sample parameter combinations. The lower and upper bounds of individual parameters are shown in Table 7.2. Each simulation yields a tuple (p_i, T_i), where p_i represents a vector representing the varied parameters, and T_i is a vector with the maximum temperature T_{max} at each of the 29 time steps (see Table 7.3).

Input variables	Axial force F_a
	Max. differential speed Δn_{max}
	Fricition lining thickness d_f
	Time t
Output variables	Maximal temperature T_{max}

Table 7.3: Input and output variables for the models [Sch22a].

Due to the deterministic nature of FE simulation, no outliers are expected within the data. The entire dataset, consisting of 200 simulations (5900 data points), is divided into a training set and a test set. The test set includes data from 25 simulations, while the remaining data points are assigned to the training set. The goal of this split is to evaluate the quality of predictions made by trained models on unseen cases. Different subsets of the training set with varying sizes are created to investigate the influence of dataset size and the required number of simulations for adequate surrogate model generation. Training sets comprising 25, 50, 75, 100, 125, 150, and 175 simulations are examined. The dataset with 100 simulations serves as a baseline for this research. Five different machine learning methods, namely Polynomial Regression (PR), Decision Tree (DT), Support Vector Regression (SVR), Gaussian Process (GP), and Backpropagation Neural Networks (BPNN), are examined to construct surrogate models. These algorithms are explained in more detail in Schneider et al. [Sch22a] and by Murphy [Mur12]. Each algorithm undergoes hyperparameter optimization, and all the considered hyperparameters are listed in Table 7.4. All the models are implemented in Python. For the PR, DT, SVR, and GP algorithms, the implementations available in the scikit-learn package [Ped12] are used. The Tensorflow package [Aba16] with the Keras API is employed for the BPNN.

Model	Hyperparameter	Values
Polynomial Regression	Degree	$[1, 10]$
Decision Tree	Depth	{inf, 5, 10, 15, 20}
	Criterion	{'squared_error', 'friedman', 'poisson'}
Support Vector Regression	Kernel	Linear, poly, RBF
	C	$1, 10, 100, 1000$
	Epsilon	1×10^{-4}, 1×10^{-3}, 1×10^{-2}
Gaussian Process	Kernel	DotProduct, RationalQuadratic, RBF
	Alpha	$[1 \times 10^{-5}, 1 \times 10^{-2}]$
Backpropagation Neural Networks	Number of hidden layers	$[1, 10]$
	Number of neurons per layers	$[1, 50]$
	Learning rate	$[1 \times 10^{-5}, 1 \times 10^{-1}]$

Table 7.4: Parameters of hyperparameters optimization of the individual algorithms [Sch22a].

To investigate the generalizability of models and ensure independence of results from the randomly selected dataset, a nested cross-validation (CV) procedure is performed (see Figure 7.10). The process involves two nested loops. In the inner loop, optimal hyperparameters for a specific folding of data are determined. A grid search (PR, DT, SVR, GP) and a randomized search (BPNN) with 3-fold cross-validation are conducted for this purpose. The generalizability of the best model determined in the inner loop is examined in the outer loop. To further evaluate the performance of models, they are assessed using the test set. The Mean Squared Error (MSE), Root Mean Squared Error (RMSE), and Mean Absolute Percentage Error (MAPE) are used as metrics to measure the quality of models. More detailed descriptions of these error characteristics can be found in the study by Schneider et al. [Sch22a].

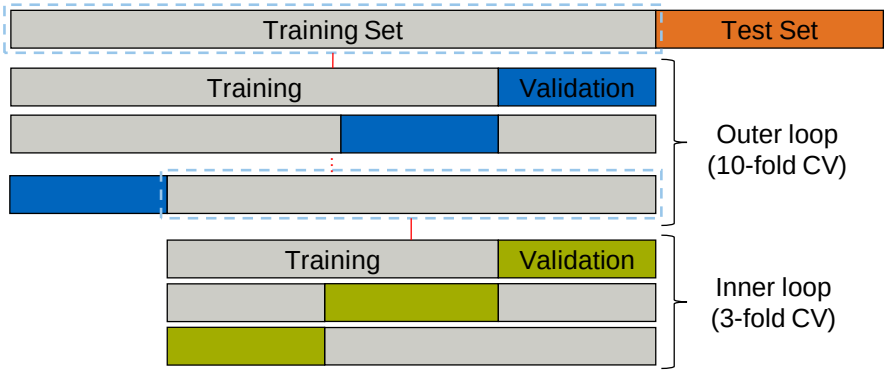

Figure 7.10: Graphical representation of the nested cross-validation (CV) procedure [Sch22a].

The results of the 10-fold cross-validation are shown in Figure 7.11. The Polynomial Regression (PR) and Support Vector Regression (SVR) models exhibit similar behavior and performance. The Root Mean Squared Error (RMSE) values of the individual folds for both models are similar, with average values of 26.7 K and 27.6 K, respectively. The Decision Tree (DT) model performs better, with an average RMSE score of 20.2 K. However, there is a significant variance among the values of the individual folds, ranging from 13.0 K to 27.0 K. This higher variance in RMSE values is also evident in the case of the Gaussian Process (GP), with values ranging from 11.1 K to 26.2 K. Among these four models, the GP achieves the best performance during cross-validation, with an average RMSE value of 18.0 K.

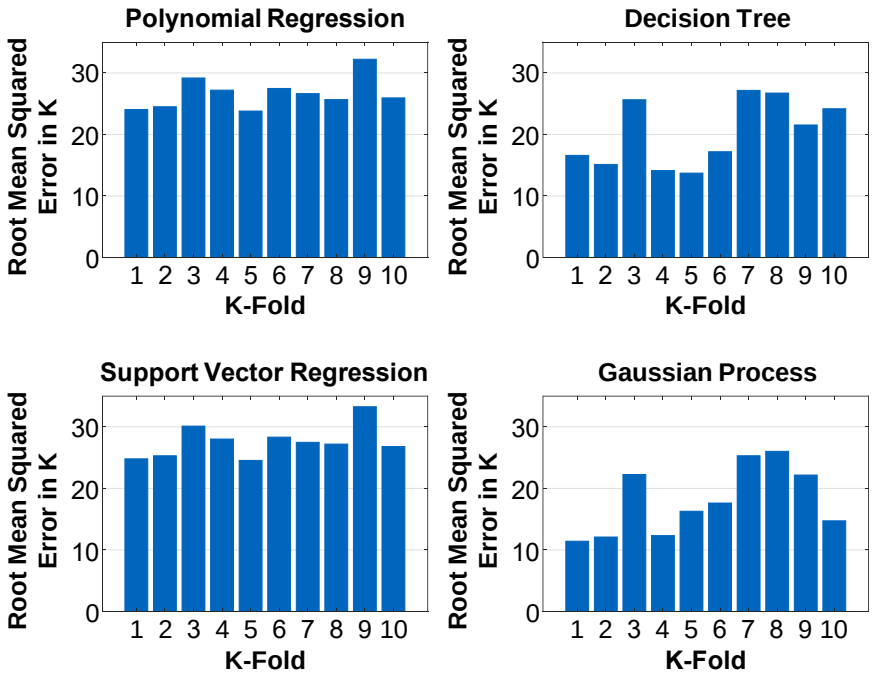

Figure 7.11: Root Mean Squared Error for 10-fold cross-validation of the Polynomial Regression, Decision Tree, Support Vector Regression, and Gaussian Process models [Sch22a].

Figure 7.12 displays the training history for the BPNN. The training is conducted for 10000 epochs, and early stopping is implemented when the validation loss does not improve for 100 epochs. The learning rate is adjusted during training by halving it when the validation loss reaches a plateau and does not improve for 50 epochs. The plotted curves demonstrate that the training process converges to an RMSE of 6.9 K after approximately 850 epochs. The RMSE for the validation set is 6.3 K, indicating the absence of overfitting.

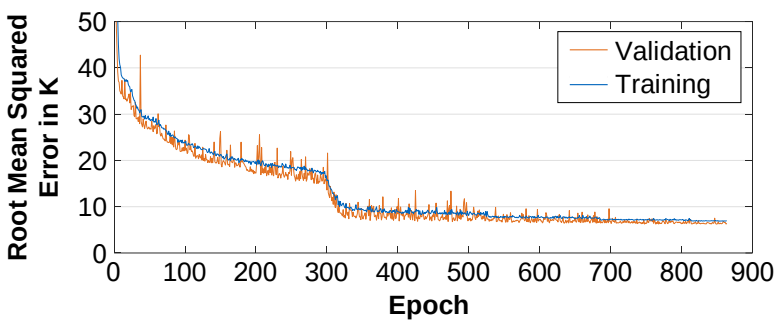

Figure 7.12: Training and validation loss of the BPNN during training [Sch22a].

To further verify the models' ability to generate accurate predictions using unseen data, predictions on the test dataset are performed. Table 7.5 presents the RMSE and MAPE values for each model on the test dataset. Additionally, the computation time required for inference and the computation time for the FE calculation are provided. Both the Polynomial Regression (PR) and Support Vector Regression (SVR) models yield the worst results, with RMSE values of approximately 24 K. The Decision Tree (DT) model performs slightly better, with an RMSE score of 19.71 K. The Gaussian Process (GP) and Backpropagation Neural Network (BPNN) exhibit the best performance, with RMSE values of 14.43 K and 6.31 K, respectively. Although SVR has the worst RMSE value, it achieves a better MAPE value compared to PR. While GP outperforms DT in terms of RMSE, both models have similar MAPE values of about 2.2 %. In terms of both RMSE and MAPE, BPNN achieves the best performance.

	PR	DT	SVR	GP	BPNN	FE Model
RMSE in K	24.6	19.7	24.8	14.4	6.3	–
MAPE in %	4.02	2.18	3.65	2.20	0.99	–
Training time in s	<1	<1	~15	~120	~400	–
Inference time in s	0.026	0.001	0.260	0.306	0.311	~ 1100

Table 7.5: Results of the models on the test set [Sch22a].

To illustrate the results and explore the application of the models, predictions for a selected slip cycle are presented in Figure 7.13. The Polynomial Regression (PR) and Support Vector Regression (SVR) models demonstrate the general temperature increase but fail to capture the temperature fluctuations. As a result, these models exhibit the poorest performance. The Gaussian Process (GP) model partially captures the temperature fluctuations but to a lesser extent. The Decision Tree (DT) model accurately models the fluctuating temperature increases but deviates in the range between 5 s and 10 s. The Backpropagation Neural Network (BPNN) model achieves the closest match between the predicted and actual temperatures, indicating the highest level of accuracy.

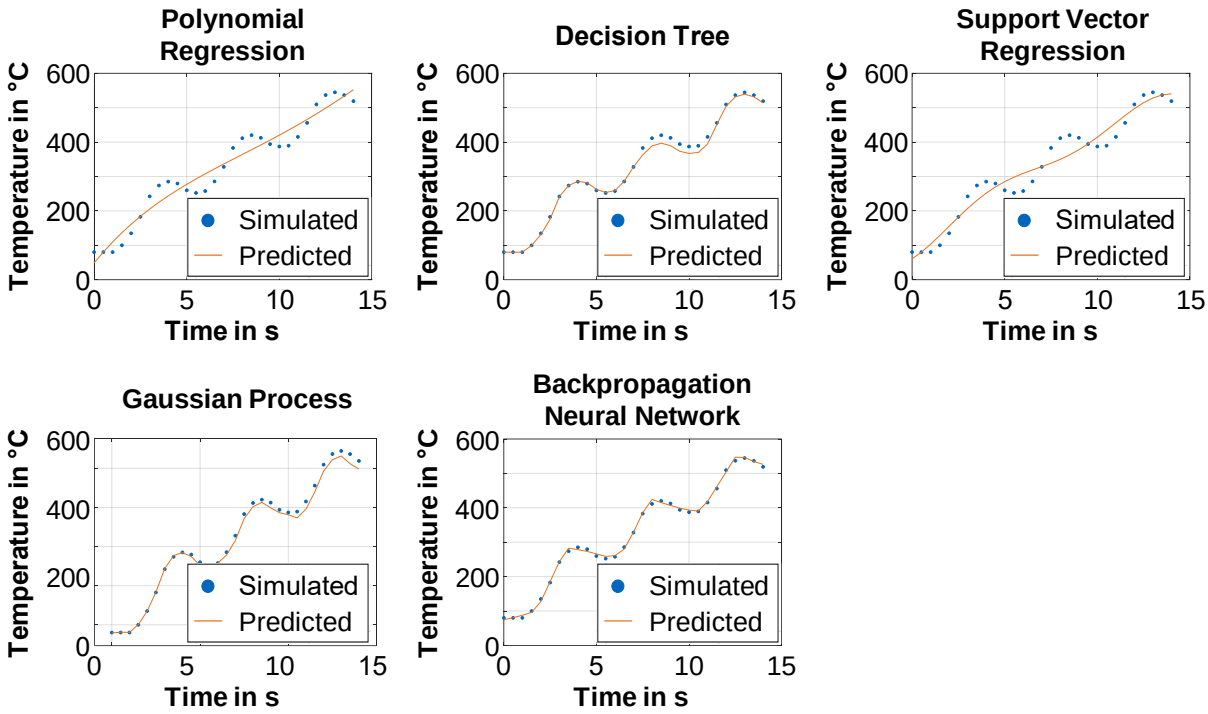

Figure 7.13: Exemplary predictions by the individual models for a slip cycle [Sch22a].

Figure 7.14 depicts the relationship between the model's performance using the RMSE and the amount of data. For the Polynomial Regression (PR) model, it becomes evident that there is almost zero correlation, with only small fluctuations in the range of RMSE scores between 25 K and 30 K. The Support Vector Regression (SVR) model initially performs worse than the PR model for up to 50 K simulations. However, beyond 50 K simulations, the performance of the two models becomes very similar. The Decision Tree (DT) model exhibits the poorest performance with a low number of simulations but improves continuously as the amount of data increases. With approximately 100 simulations, an RMSE score of about 20 K is achieved. Further increase in the amount of data does not lead to significant improvements. The Gaussian Process (GP) model demonstrates a high dependence on the amount of data, consistently showing improved results as the data volume increases. The Backpropagation Neural Network (BPNN) models consistently achieve the best performance across all data volumes. Even with only 10 simulations, they outperform the PR and SVR models. Notably, significant performance improvements occur from around 60 simulations onwards. Beyond 100 simulations, further improvements are marginal for all models.

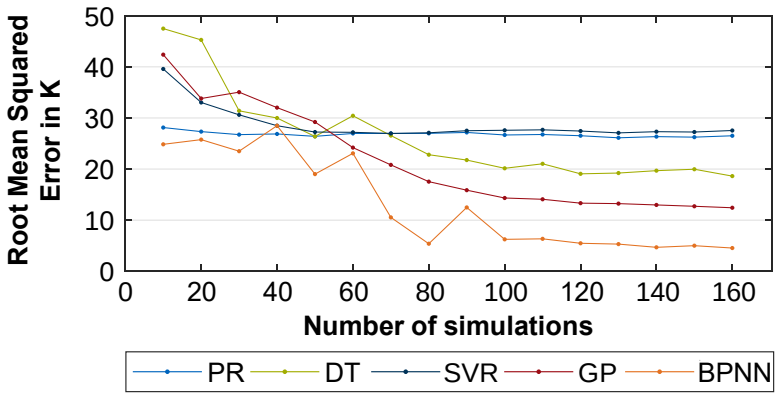

Figure 7.14: Root Mean Squared Error for the test sets as a function of the data volume [Sch22a].

7.2 Three-Dimensional Analysis of the Thermomechanical Behavior

In the following subsections, the simulation results of the three-dimensional model are presented. First, the temperature and pressure distribution during shifting are explained. Subsequently, geometry variations of the steel and friction plate are performed and compared with respect to their temperature behavior.

7.2.1 Temperature and Pressure Distribution

After validating the simulation model with regard to numerical parameters such as the number of nodes and time-step size, as well as comparing it to experimental data (see Section 6.4), the temperature and pressure distribution during a slip phase are investigated in more detail. Figure 7.15 presents the pressure distribution (nominal pressure 8.0 N/mm^2), while Figure 7.16 illustrates the temperature distribution of the steel and friction plates at various time points during the slip phase. The triangular differential speed curve in the slip phase lasts for 4 seconds, with a 2-second rise and a 2-second fall.

The representation of the pressure distribution during the slip phase (see Figure 7.15) does not show any significant differences over time. Once the pressure is applied, no changes can be observed at the indicated times. However, at the individual friction lining pads, there is a slight increase in pressure at the edges in the circumferential direction and at the inner diameter. In the circumferential direction across the individual lining pads, no discernible differences in pressure behavior are observed.

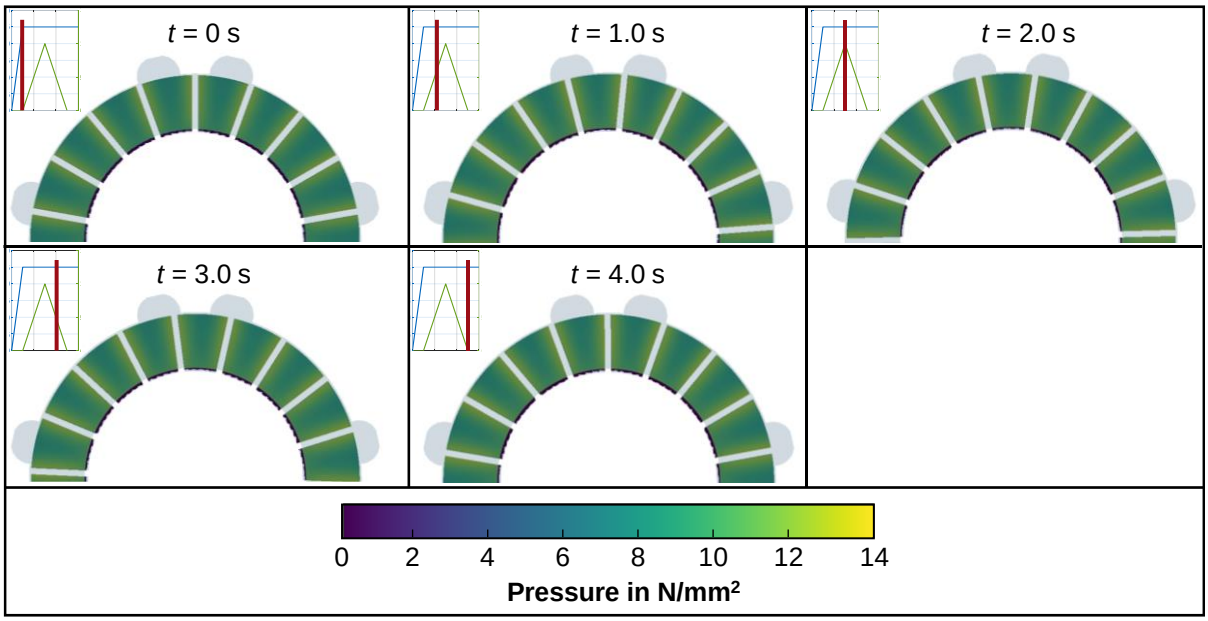

Figure 7.15: Pressure distribution at selected times during a slip phase

In addition to analyzing the pressure distribution during the slip phase, the temperature distribution at selected time steps is also examined (see Figure 7.16). The steel plate temperature increases by approximately 200 K during the slip phase, with the maximum temperature being observed in the second third of the slip phase. In the radial direction, the lowest temperature is found at the toothing. Heat conduction to the outer carrier occurs on the adjacent flank, resulting in a temperature gradient in the circumferential direction within the toothing area. The inner diameter of the steel plate experiences less heating compared to the outer diameter. The highest temperatures in the radial direction are located in the outer third of the friction interface. Temperature variations can be observed not only in the radial direction

but also in the circumferential direction of the steel plate surface. While temperature reductions are evident in the toothing area, temperatures between the double teeth increase. The friction plates also exhibit a temperature gradient in the circumferential direction, with lower temperatures being observed in the area of the steel plate's toothing. Heat dissipation through the toothing to the inner carrier creates a temperature gradient in the radial direction, noticeable at the end of the slip phase on the carrier plate. The direction of rotation of the friction plate also influences the temperature distribution, with the temperature peak occurring at the friction interface and being located ahead of the toothing in the direction of rotation.

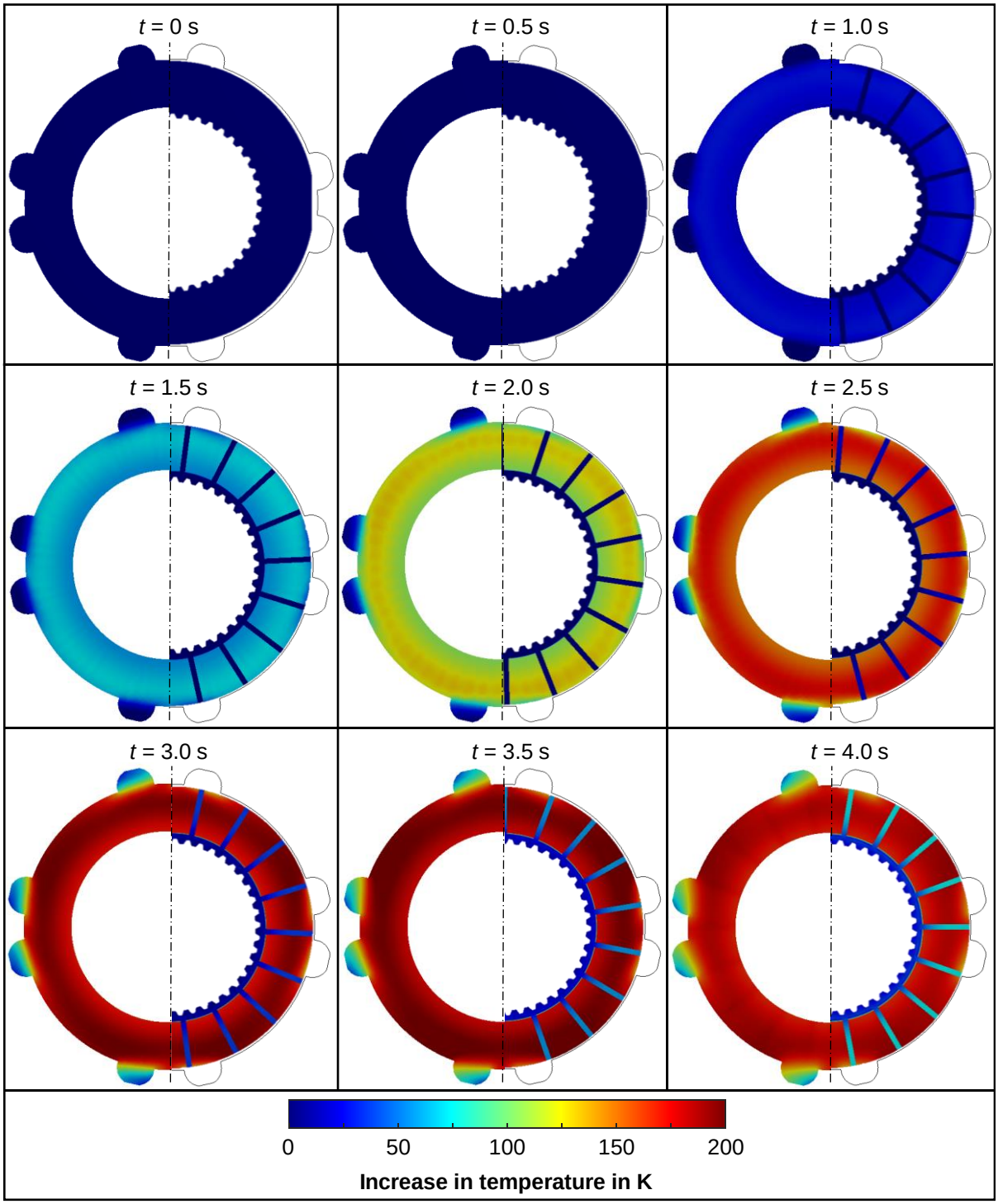

Figure 7.16: Temperature distribution of steel plate (left half of the friction surface) and friction plate (right half of the friction surface) at selected times during a slip phase.

7.2.2 Influence of the Geometry Parameters

In the following analysis, the influence of geometric variations in the circumferential direction of the steel and friction plate on the thermal behavior of the clutch is investigated. Therefore, two steel plate variants and two friction plate variants are compared to the reference model. Care is taken to maintain the same thermal mass for the steel plates, friction lining, and carrier plate in each variation. One variation involves steel plates with four teeth in a group, similar to the reference model commonly used in applications. Another variant features teeth evenly distributed around the circumference of the steel plate. For the friction plates, a plate with nine friction lining pads is used instead of the original 18. In this case, the grooves are widened to maintain the same friction interface area without altering its absolute value.

Figure 7.17 shows the thermal analyses at $t = 3.5$ s of a slip cycle, since the highest temperatures and temperature gradients occur at this time (see Figure 7.16). The variant with 9 friction lining pads instead of 18 demonstrates a temperature distribution very similar to the reference model. The maximum temperature on the friction interface differs by less than 1 °C. No significant differences are observed in the temperature distributions in the radial and circumferential directions between these two variants. The most notable changes are observed in the variant where the teeth of the steel plate are evenly distributed around the circumference. On one hand, the calculated maximum temperature on the friction interface is almost 9 °C lower compared to the reference model. On the other hand, the temperature distribution in the circumferential direction is more uniform in contrast to the reference model. In the radial direction, the temperature reaches its maximum at approximately the mean friction surface diameter, while the temperature decreases at both the inner and outer diameters of the friction interface. Lastly, the variant with 4 teeth in a group displays temperature distribution behavior very similar to the reference model. The maximum temperature differs by less than 1 °C. In the circumferential direction, th ere is a slightly more noticeable temperature decrease in the area of the external toothing compared to the reference model. In the radial direction, the temperature distribution remains the same as that of the reference model.

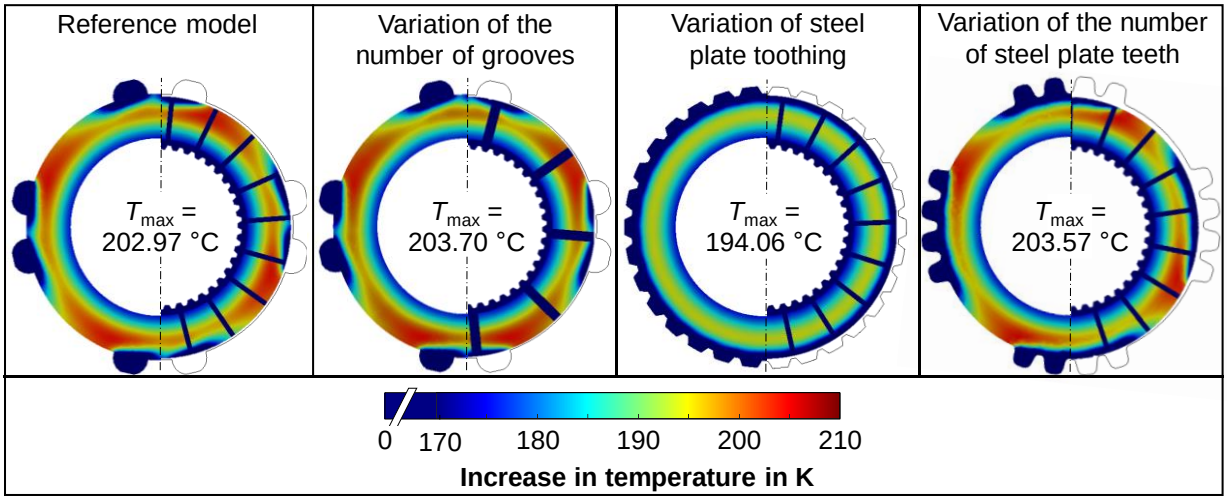

Figure 7.17: Temperature distribution at time $t = 3.5$ s of a slip phase for different geometry variations for steel plate (left half of the friction interface) and friction plate (right half of the friction interface).

8 Evaluation and Discussion

In the following, the experimental results from Section 5 and the simulation results from Section 7 are evaluated, discussed, and classified within the state of the art.

8.1 Derivation of a Limit of Damage and Damage Prevention

Critical damage limits are necessary to prevent spontaneous damage to wet multi-plate clutches during operation and can be determined using online calculations, data-based predictions, or condition monitoring systems. The current state of the art indicates that existing test methods often assess the susceptibility of wet clutches to spontaneous damage only at specific operating points and based on mechanical load variables [Str17]. However, several investigations for load shifting mode [And90, Sch20a, Sni06, Su06b, Yu19a] also demonstrate that the thermal behavior of multi-plate clutches significantly influences their susceptibility to spontaneous damage.

The experimental studies conducted in this thesis with the friction systems FS1 – FS5 also reveal the occurrence of spontaneous damage under high thermal loads. In addition to the temperature measurements of the steel plate, the presence of high thermal loads upon damage is confirmed by microstructure measurements. These measurements indicate changes in the microstructure (see Figure 5.18), as well as changes in the Vickers hardness (see Figure 5.19) of the steel plates. Figure 8.1 presents the measured steel plate temperatures at the penultimate load level, i.e., the load level preceding the failure load level, for the friction systems FS1 – FS3. The data correspond to those in Figure 5.20 – Figure 5.22 and Figure A.19 – Figure A.21. It can be observed that the temperatures of the individual step tests at the penultimate load level before failure are consistently high for each friction system, despite variations in factors such as pressure, maximum differential speed, and number of slip phases. While the temperature levels for friction

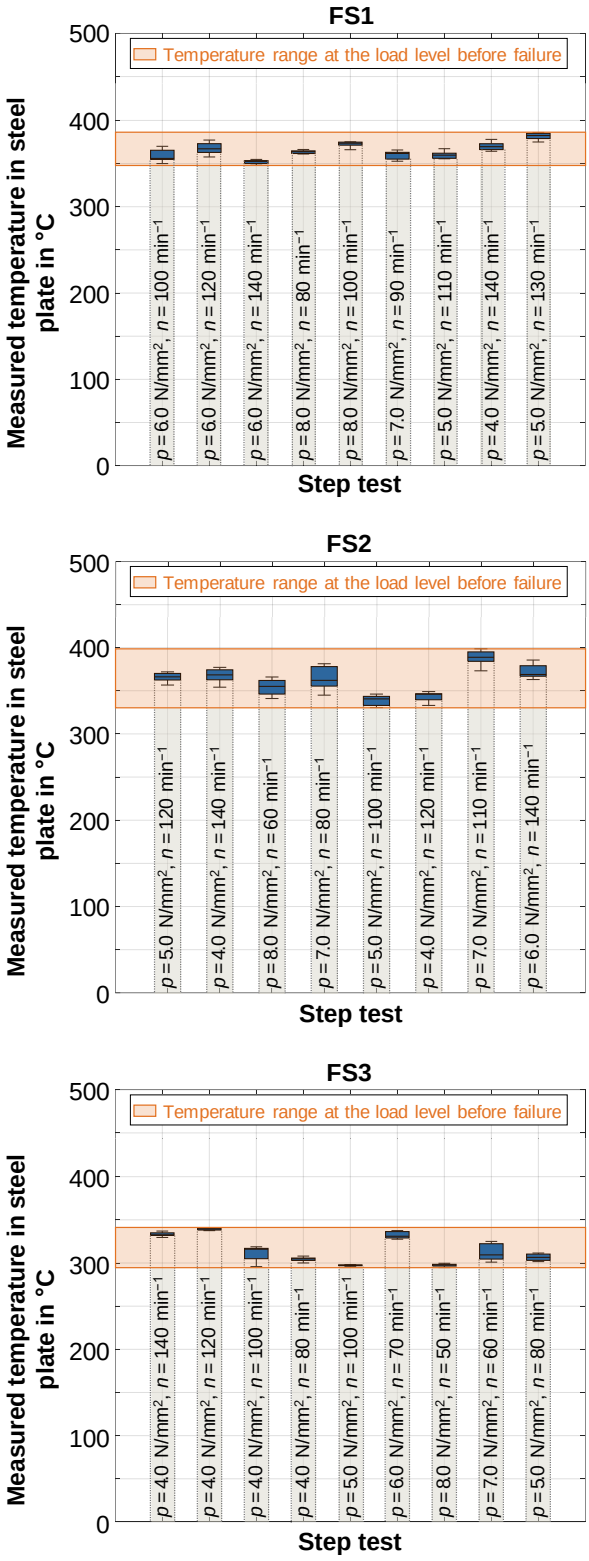

Figure 8.1: Measured steel plate temperatures at the load level before failure for friction systems FS1, FS2, and FS3.

systems FS1 and FS2 are similar, the temperatures for friction system FS3 are lower. Based on the experimental data, it can be concluded that critical temperature ranges for spontaneous damage can be determined for each individual friction system, even with different damage patterns such as buckling and lining detachment. These results enable the specification of a critical temperature range for each friction system, which should not be exceeded in order to prevent spontaneous damage:

- FS1: 348 °C – 386 °C
- FS2: 330 °C – 398 °C
- FS3: 294 °C – 340 °C

With the understanding that thermal damage limits can be identified despite different damage mechanisms, the next step is to explore methods for preventing such damage. One possible approach is to employ monitoring systems in the application to avoid entering the critical thermal range of the clutch. This involves continuous control of the clutch's temperature level. However, a challenge remains in not knowing, prior to a required shifting, whether the critical temperature range will be exceeded during the process. Surrogate models, as presented in Section 7.1.3, can be utilized to predict the expected maximum temperature. It is demonstrated that these models provide highly accurate temperature predictions. Particularly, the surrogate model based on Backpropagation Neural Network yields excellent results in terms of Mean Squared Error (MSE), Root Mean Squared Error (RMSE), and Mean Absolute Percentage Error (MAPE) during validation. Even with limited data sets or FEM simulations in this case, the models achieve precise temperature predictions. Models utilizing Polynomial Regression, Decision Tree, Support Vector Regression, and Gaussian Process approaches also demonstrate good predictive performance, but they are outperformed by the Backpropagation Neural Network Model in terms of accuracy and the number of data sets required for training. Including the time required for inferring the prediction of a temperature based on given load parameters, the model that uses a decision tree is highly recommended. With an inference time of just 0.001 s, this model predicts extraordinarily quickly compared to those using other investigated algorithms, which typically take longer than 0.2 s for a prediction. In addition to its efficiency, the decision tree-based model also boasts very high accuracy.

Furthermore, apart from preventing critical temperature occurrences, it is also possible to enhance the system fundamentally and reduce the temperature level under the same load in the clutch. Conversely, it is feasible to increase the critical temperature threshold at the onset of damage. These possibilities are discussed in detail in Section 8.2.

8.2 Parameters Influencing the Thermal Behavior

Both the state of the art and the experimental and simulative work of this thesis show that the thermal behavior of a clutch has a significant influence on the spontaneous damage behavior as well as on the long-term damage and friction behavior. In the following, the results of the investigations in this work on the influencing parameters of the thermal behavior of wet clutches will be discussed.

The thermal behavior of a clutch is strongly influenced by the load's friction work, friction power, and shift frequency. The results from Section 5.1.4 show that at very high friction work and friction power ($p = 6.0\ \mathrm{N/mm^2}$, $n = 100\ \mathrm{min^{-1}}$), a failure of the clutch system can be observed directly after two slip phases. At the same time, at low loads ($p = 3.0\ \mathrm{N/mm^2}$, $n = 100\ \mathrm{min^{-1}}$), no damage is observed even after 15 slip phases, and the measured steel plate temperature converges towards an approximate temperature of 300 °C. These results indicate that heat

dissipation via conduction, thermal convection, and thermal radiation corresponds to the amount of heat supplied by the shifting process. The findings from this work for transient slip are consistent with the research of Duminy [Dum79] and Strebel [Str17], who propose a friction work limit as a function of maximum friction power for load shifting mode.

Heat dissipation can be improved by increasing the contact area between the steel plates and friction plates with the carriers, as shown by the three-dimensional simulation results in Section 7.2.2. By the same token, both the experimental results from Section 5.1.3 and the simulative results from the parameter study in Section 7.1.2 indicate that robust axial heat conduction to the mating and pressure plates – e.g., through a short axial design and high thermal conductivity of the friction lining – lowers the temperature in the clutch. These findings are supported by simulative studies on the number of friction interfaces, which show that for the same specific load, fewer friction plates (6 interfaces) lead to lower maximum temperatures than with 14 friction interfaces. In the existing design, the role of the pressure and reaction plate as a heat sink becomes more pronounced with fewer friction interfaces and, thus, less friction material with low axial thermal conductivity.

Furthermore, the experimental results from Section 5.1.2 show that, especially at high temperatures, the cooling oil flow rate has a significant influence on the thermal behavior of the clutch. The higher the oil flow rate through the clutch, the lower the steel plate temperatures are measured at the same load. For load shifting, Schneider et al. [Sch21b] also demonstrate a statistically significant influence of the oil flow on the development of damage in paper-based friction systems. However, it must be considered that the design of the groove should allow for adequate cooling oil volume flow. Groetsch et al. [Gro21a] and Wimmer et al. [Wim05], in particular, highlight the limited absorption capacity of different groove shapes and clarify that the level of oil volume flow and groove design need to be coordinated.

In addition to passive cooling via heat conduction and heat convection through the mounting parts and a cooling oil volume flow, the investigations also reveal individual geometric and material-specific parameters that have a significant influence on the thermal behavior of the clutch. For example, a uniform and regular distribution of the teeth can significantly reduce the temperature gradients and the temperature level of the steel plate, as shown by the three-dimensional finite element model. The simulative results of the parameter study with the two-dimensional model demonstrate that the specific thermal conductivity of the steel plates and liner significantly affects the maximum temperature reached during operation. As indicated in Equation (6.5) for the frictional contact, the rate at which the generated heat flows into the steel plate or lining depends on the corresponding thermal conductivities of the materials. Since the thermal conductivity of the steel plate (52 W/mK) is more than 200 times greater compared to the lining (0.25 W/mK), the majority of the heat flow is conducted into the steel plates. Based on this physical law, Barber [Bar69] recommends a ratio of the thermal conductivities of the steel plates and the lining of 1, ensuring that the heat flow is evenly distributed between the friction lining and the steel plate. To investigate this influence further, additional simulations are performed in which

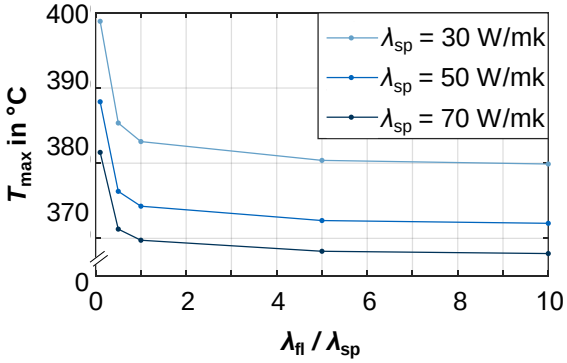

Figure 8.2: Maximum simulated temperature in the clutch as a function of the ratio of the thermal conductivities of the friction lining and the steel plate.

the maximum temperature reached is studied as a function of the ratio between the thermal conductivity of the friction lining and the one of the steel plate. This is done for three different values of the thermal conductivity of the steel plate. The results are shown in Figure 8.2. For all three values of the thermal conductivity of the steel plate, the dependence on the ratio of the thermal conductivities shows the same behavior. For ratios less than 1, i.e., when the thermal conductivity of the steel is greater than that of the friction lining, a sharp decrease in the maximum temperature in the clutch is seen with increasing ratios. For ratios greater than 1, i.e., when the thermal conductivity of the friction lining is greater than that of the steel, only very small reductions in the maximum temperature in the clutch are observed. For ratios greater than 1, i.e., when the thermal conductivity of the friction lining is greater than that of the steel, only very small reductions in the maximum temperature in the clutch are observed. These results confirm Barber's findings [Bar69], suggesting that materials should be selected to achieve a ratio of thermal conductivities close to 1.

The simulative results in Section 5 also show that the specific heat capacity and the density of the steel plates and the lining influence the maximum temperature reached during operation. An increase in the specific heat capacity of the materials leads to a decrease in the maximum temperature because more energy is required to raise the temperature of the materials. Similarly, an increase in the density of the materials leads to a decrease in the maximum temperature, as a higher density implies more mass available to absorb thermal energy. These results are consistent with previous studies on the thermal behavior of steel plates and their role as heat sinks [Bar93]. The experimental results with the FS4 friction systems also demonstrate that an increase in steel plate thickness from 0.8 mm (FS1) to 1.2 mm makes the temperatures at the load level before failure more tolerable by about 50 °C (see Figure 8.1 and Figure 8.3), and the same failure mode, namely buckling of the steel plate, occurs. Simultaneously, higher loads are required to reach this temperature level due to the greater thermal mass compared to the reference system FS1. Thus, it can be observed that increasing the steel plate thickness on one hand enhances the load-bearing capacity at the same temperature level and on the other hand, elevates the limit temperature for the damage case. The experimental results are confirmed by the FE simulations and demonstrate that the thickness of the steel plate has a significant influence on the maximum temperature in the clutch system. This affirms the role of the steel plates as heat sinks during the shifting process. As the thickness of the steel plate increases, the thermal mass acting as a heat sink also increases, allowing more heat to be absorbed and consequently reducing temperature maxima. The investigations with the friction system FS5, in which steel plates with a thickness of 1.6 mm are used, demonstrate that there are limits to the benefits of increasing the thickness of the steel plate. In the studied friction system,

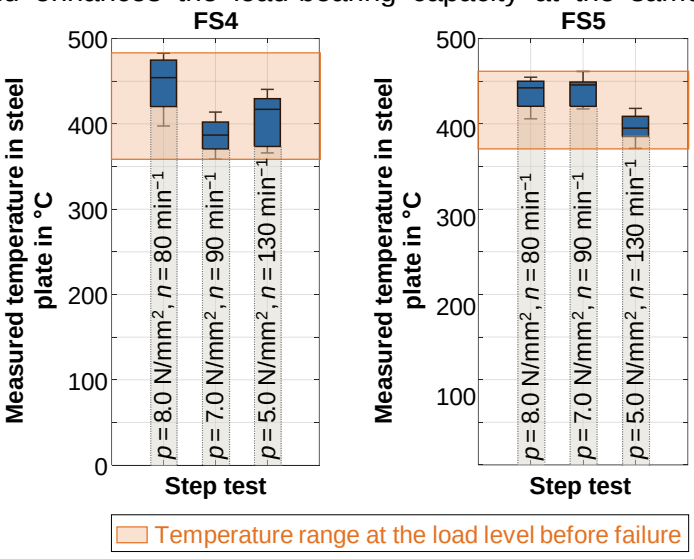

Figure 8.3: Measured steel plate temperatures at the load level before failure for friction systems FS4 and FS5.

the friction plate fails due to buckling. The temperature level at the load level before failure could not be further increased by augmenting the steel plate thickness compared to the FS4 friction system. The temperatures at the load level before failure are shown in Figure 8.3. Obviously, individual components (steel plate, friction lining, and carrier plate) must be very well matched to each other to optimize load-carrying capacity with respect to spontaneous damage.

The thickness of the carrier plate also influences the thermal behavior of the clutch (see Figure 7.3). However, since the carrier plate has no direct contact with the applied heat flux at the contact surface, it can only absorb heat transported by the lining. Due to the low thermal conductivity of the friction lining, it acts as a kind of insulation layer with respect to the carrier plate. An increase in the lining thickness (see Figure 7.3) thus also leads to an increase in the maximum temperature in the clutch since less heat from the frictional contact can be dissipated, and the steel plate consequently heats up. To investigate this insulating effect of the lining in more detail, the influence of the thickness of the steel plate and the carrier plate is considered for different thermal conductivities of the lining (see Figure 8.4). The higher the thermal conductivity, the weaker the insulating effect of the lining, and the more heat is transferred to the carrier plate. The thermal conductivity of the friction lining affects the steel plate and the carrier plate differently. The greater the thermal conductivity of the friction lining, the lower the temperature drop when the plate thickness is increased. However, for both higher and lower thermal conductivities, there is a decrease in temperature when the carrier plate thickness is increased. For the carrier plate, it can be observed that varying the thickness with the aim of lowering the maximum temperature is only beneficial when the thermal conductivity of the lining is high. Alternatively, the thickness of the friction lining can be reduced so that the carrier plate can also be used as an additional heat sink.

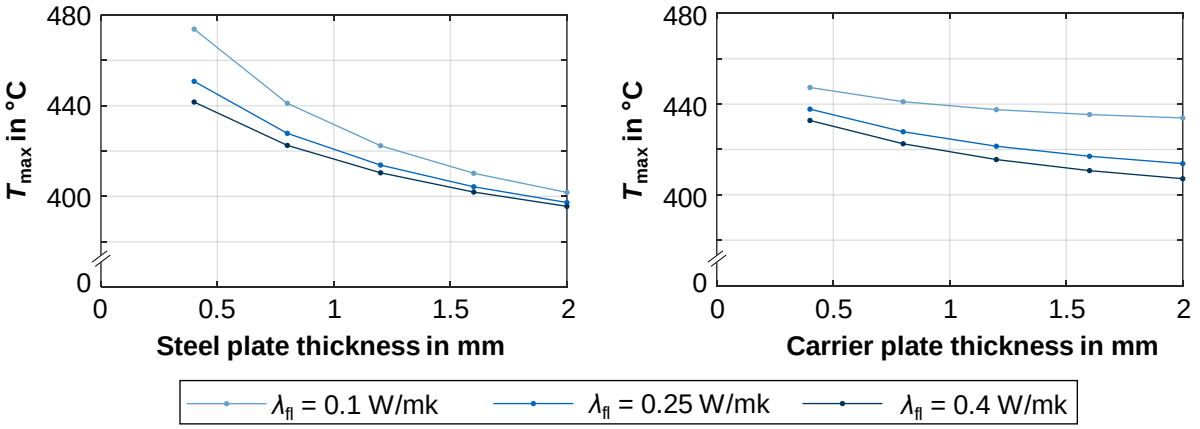

(a) Variation of steel plate thickness with carrier plate thickness 0.8 mm and lining thickness 0.39 mm.

(b) Variation of the carrier plate thickness with steel plate thickness 0.8 mm and lining thickness 0.39 mm.

Figure 8.4: Maximum simulated temperature in the clutch as a function of (a) steel and (b) carrier plate thickness.

Finally, as shown in Section 7.1.2, the Young's modulus of the lining has slight effect on the maximum temperature reached by the clutch system. While these results do not directly contradict previous findings, the effect and the recommendation of Sciezka and Zolnierz [Sci07a, Sci07b], Fieldhouse [Fie11], and Barber [Bar69] to use low Young's moduli are very weak. One possible reason for this difference is the area studied. In this study, Young's modulus varied between 40 and 220 MPa, while Fieldhouse [Fie11], for example, used Young's moduli in the range of about 86 000 MPa.

8.3 Parameters Influencing the Damage Patterns

In the state of the art, various forms of damage are reported, including sinter carryover with metallic friction material, as well as hot spots and hot bands with organic friction material. These forms of damage are mainly linked to the load shifting mode and have been extensively studied. However, there is a lack of comprehensive investigations of the damage patterns associated with spontaneous damage in the transient slip operating mode.

The experimental investigations conducted in this thesis on the transient slip mode of operation reveal that buckling of the steel plates is the failure mode for friction systems FS1, FS2, and FS4. In the case of friction system FS3, clutch failure occurs due to the detachment of the lining from the carrier plate. For friction system FS5, failure is caused by buckling of the friction plates. The initial form of damage observed in all friction systems is discoloration of the steel plates, which is a well-known phenomenon in the literature [And90, Hen14, Sch19] associated with load shifting. This discoloration occurs in both sintered and organic friction systems and is caused by deposits of oil cracking products.

During load shift mode with organic friction systems, failure damage such as hot spots or hot bands has been reported. The origin of these types of damages has been extensively discussed in the literature [Aff04, Bar67, Yu19a, Zha15], and can be attributed to thermoelastic instabilities. However, it should be noted that these types of damage are not observed in transient operation. The reason for this is that the frictional power during transient operation is significantly lower compared to load shifting. Consequently, the likelihood of thermoelastic instabilities occurring is much lower in transient operation. Moreover, the cooling-off periods between individual slip phases in transient operation contribute to reducing thermoelastic instabilities and high temperature gradients at specific points, thereby preventing the formation of hot spots. This reduction in high temperature gradients between slip phases is also evident in the thermal simulations (see Figure 7.1 and Figure 7.2).

Based on the findings from Sections 8.1 and 8.2, it becomes evident that all friction systems (FS1 – FS5) demonstrate a narrow temperature range in the load levels preceding failure, despite having different failure modes. This observation suggests that the thermal load plays a substantial role in the spontaneous damage behavior of wet multi-plate clutches during transient slip operation. In essence, the experimental investigations lead to the conclusion that a specific thermal level must be attained for spontaneous damage to take place.

Cenbo et al. [Cen15] provide an explanation in their experimental and theoretical investigations regarding the buckling of plates. According to their findings, plates buckle at a significant radial temperature difference and at an in-plane bending moment surpassing a critical threshold. The experimental investigations conducted in this thesis (see Figure 5.23) demonstrate that as the thickness of the steel plates increases, a higher temperature level is required for buckling to occur. Notably, in friction system FS4, where the steel plate has a thickness of 1.2 mm and the carrier plate of the friction plate is 0.8 mm thick, buckling of the steel plates is observed. However, results from friction system FS5 reveal that increasing the steel plate thickness to enhance the clutch's tolerance to temperature has limited effectiveness. Despite doubling the thickness of the steel plates from 0.8 mm to 1.6 mm compared to friction system FS1, the clutch fails at higher temperatures, but with a different type of damage – buckling of the friction plates with a carrier plate thickness of 0.8 mm. This indicates that not only the steel plates but also the friction plates can buckle if the bending moment exceeds a critical value. Therefore, when considering design improvements for the overall system, the interaction between the bending moments of the lining and the steel plates must be taken into account. As Cenbo et

al. [Cen15] suggest, the buckling is caused by radial temperature differences and the related thermal stresses. This implies that in the joint design of steel and lining thickness, the thermal properties of the lining must be considered to account for the thermal stresses on the carrier plate.

In addition to increasing the bending moment of the plates to prevent buckling, another factor to consider is the reduction of thermal stresses. One possibility is to lower the thermal level in the clutch system, which would result in reduced thermal stresses. Detailed discussion on various approaches to reduce the thermal level in the clutch system can be found in Section 8.2. Another approach involves implementing design solutions aimed at minimizing temperature differences and, consequently, mitigating thermal stresses. Specifically, simulation results from the three-dimensional model have shown that when using the same material input, a uniform and regular distribution of teeth around the circumference can significantly minimize the temperature level and temperature gradients within the clutch. At the same time, a uniform and regular distribution of the outer teeth on the steel plate can enhance its resistance to buckling [Yu19a]. Similarly, a symmetrical and uniform design in both the radial and circumferential directions is recommended for the friction plate to ensure a uniform temperature distribution. The more evenly the temperature is distributed among the individual components within the clutch, the lower the occurrence of thermal stresses. Additionally, as demonstrated by the two-dimensional simulation model, a high thermal conductivity of the friction lining helps to reduce temperature gradients in the axial direction [Sch22c]. Furthermore, the thermal mass of the carrier plates can be fully utilized in this manner.

The investigated friction system FS3 experiences failure due to the detachment of the friction lining. As shown in Section 8.1, a temperature limit can be established for the load level before system failure. This suggests that the adhesion and cohesion forces of the bond are highly temperature-dependent and decrease as the temperature rises. Furthermore, it can be inferred that the woven friction lining, which contains a high proportion of carbon fiber and a low proportion of matrix material, exhibits higher thermal conductivity compared to the paper-based friction lining of friction plate FP1 and the composite carbon friction lining of friction plate FP2 [Acu16a, Kea97, Ran04]. This offers the advantage of better utilizing the thermal heat capacity of the carrier plate to maintain a lower clutch temperature. Yang and Lam [Yan98] describe in their investigations that in traditional clutches, more than 90 % of the heat is absorbed by the steel plate, leading to a significant temperature gradient across the lining thickness during engagement. The temperature at the bonding interface between the carrier plate and friction material is much lower than the interface temperature, indicating the potential for improvements to enhance the overall thermal performance of the clutch. However, it is essential to design the bond layer to withstand the necessary shear forces even under high thermal loads.

8.4 Parameters Influencing the Friction Behavior

Torque transmission is one of the main tasks of a clutch. Accordingly, it is of major interest how the torque transmission capacity and, thus, the frictional behavior change under high to damaging loads. In Sections 5.2.5 and 5.2.6, the characteristic value μ_{top} for the friction systems FS1 – FS5 in the step tests and for the friction systems FS1 – FS3 in the endurance tests for non-pre-damaged reference clutches and pre-damaged clutches are presented.

The evaluations of the step tests in Section 5.2.5 (Figure 5.20 – Figure 5.22 and Figure A.19 – Figure A.21) clearly show that the characteristic value μ_{top} within the step tests

decreases with increasing mechanical load, and thus, also with increasing thermal load. Figure 8.5 presents the relationship between the friction behavior, represented by the characteristic value μ_{top}, and the measured steel plate temperature during the step tests for friction systems FS1, FS2, and FS3. The mean values of the measured steel plate temperature and the mean values of the characteristic value μ_{top} of the ten slip cycles of each load level are used. For friction systems FS1 and FS2, the measured steel plate temperatures are in the range of 200 °C – 400 °C, and for friction system FS3, in the range of 150 °C – 350 °C. For all three friction systems, it can be seen that the characteristic value μ_{top} decreases with an increasing thermal load. The values of coefficient of friction at measured steel plate temperatures below 250 °C are between 0.11 and 0.08. At higher temperatures, the values of coefficient of friction for all three friction systems drop sharply and, in some cases, fall below 0.06. There are no significant differences in the behavior of the coefficient of friction with an increase in the measured steel plate temperature between the three friction systems, which differ in the friction lining variant. The similar behavior of the three friction systems indicates an influence of temperature on the properties of the lubricant. The results are in agreement with the investigations of Marklund et al. [Mar07], who describe a significant influence of thermal effects on the transmissible torque of differentials under conditions with limited slip. Similarly, Voelkel et al. [Voe21] show the temperature dependence of the measured coefficient of friction at low sliding speeds.

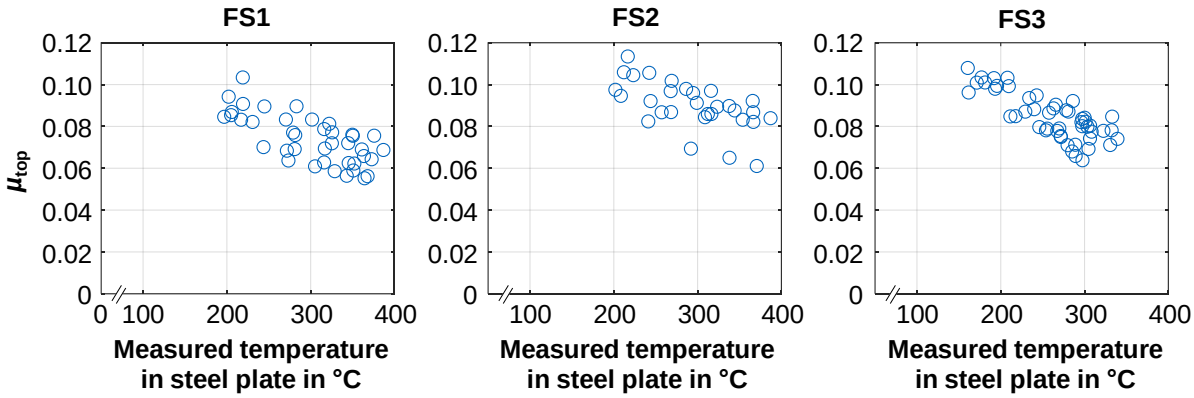

Figure 8.5: Characteristic value μ_{top} versus the measured temperatures of steel plates for friction systems FS1, FS2, and FS3 during step tests.

Figure 8.5 is used to analyze the friction behavior during shiftings with high mechanical and thermal loads. In addition to these results, the influence of shifts with high mechanical and thermal loads on subsequent shiftings with low loads will be considered in the following. Figure 8.6 compares the characteristic value μ_{top} in the reference engagements with the measured steel plate temperatures during the load engagements in a load level for the friction systems FS1, FS2, and FS3. The measured mean values of the steel plate temperature and mean values of the characteristic value μ_{top} of the ten slip cycles of each load level are used. The measured steel plate temperatures for friction systems FS1 and FS2 are in the range of 200 °C – 400 °C and for friction system FS3 in the range of 150 °C – 350 °C. A slight decrease of the characteristic value μ_{top} of approximately 0.01 in the reference engagements can be measured for friction system FS1 with increased thermal loads in the preceding shifts. For friction system FS2, the characteristic value μ_{top} drops significantly by approximately 0.06 with higher thermal loads in the previous engagements. In contrast, for friction system FS3, no correlation between changes in the characteristic value μ_{top} in the reference engagements and the thermal preload is evident.

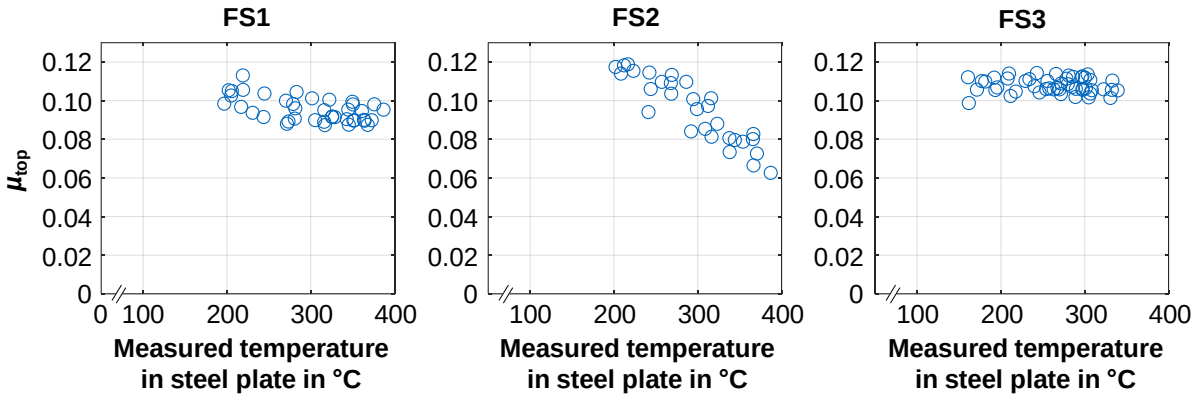

Figure 8.6: Characteristic value μ_{top} in the reference engagements versus the measured steel plate temperatures during the load engagements in a load level for FS1, FS2 and FS3 friction systems during step tests.

The differences between the three friction systems indicate that the friction lining type strongly influences future friction behavior in the case of thermal preloads. It is known from the literature [Acu16a, Acu14, Acu16b, Dev04, Iwa15, Mae03, Mat97b, Mor10, Neu01, Osa90, Sak93, Sto23] that the coefficient of friction of organic friction linings decreases at high loads due to clogging of the lining pores. The degree of wear and the intensity of clogging of the friction lining have an influence on the friction behavior and the level of the coefficient of friction. In this process, oil cracking products, which arise due to high friction surface temperatures, are deposited in the friction lining pores and reduce the core roughness depth of the lining. Due to the significantly lower thermal conductivity of organic friction linings (0.09 … 1.2 W/mK) [Awa05, Neu08] compared to metallic friction linings (5 … 138 W/mK) [Hae15, Kin99, Neu08], significantly higher peak friction interface temperatures occur with organic friction linings, which cause damage to the lubricant and friction lining [Sto23]. The SEM analyses of the friction linings for the systems FS1, FS2, and FS3 (Figure 5.12 – Figure 5.17, Figure A.1 – Figure A.18) clearly illustrate that the friction lining porosity changes strongly during the step test. The friction lining of friction system FS1 shows a highly porous structure when new, which changes only slightly during run-in. After failure, clear smoothing becomes evident, resulting from oil cracking products and mechanical flattening. In the new state, the friction lining of FS2 has a less porous structure than the friction lining of FS1. The run-in causes deposits in the friction lining of FS2, which are very pronounced after failure. This results in large smooth surface areas on the friction lining. Due to the woven carbon structure, FS3 shows only minor changes in the surface structure between the states new condition, after run-in and after failure. Smoothing takes place only on the plateaus of the woven structure. As a result of the woven structure, the possibilities of displacing the lubricant are largely given. Recommendations for removing excess lubricant and, thus, hydrodynamic effects that would cause the friction linings to float on the oil film are also made by Merkel and Koehler [Mer01] in a patent specification. In addition to a first group of grooves that effectively circulates the lubricant, they recommend a second group of grooves that are preferably arranged in the form of a network or grid. The grooves should be very close-meshed so that hydrodynamic effects can be prevented. Skubacz and Poll [Sku11] also observed different intensities of lining clogging with oil degradation products depending on the friction lining. At a minimum oil throughput, they observed less pronounced clogging of the pores in carbon friction linings than in sintered metal friction linings and concluded that the chemical effect of the additives depends on the lining. The results of the SEM measurements can be compared very well with the results presented in Section 5.2.5, Figure 8.5 and Figure 8.6, and extend the state of the art. A drop in the coefficient of friction level can be observed due to clogging the friction lining pores. The

intensity of the clogging of the friction lining depends strongly on the friction lining. It is evident that as the friction lining becomes increasingly clogged and loses porosity, the characteristic value μ_{top} correspondingly decreases.The research results regarding the influence of the lining porosity and the friction behavior, as well as the SEM investigations also help to explain the influence of pre-damage on friction behavior in the endurance test (Figure 5.26, Figure 5.28, and Figure 5.30). The friction system FS1 shows differences in the frictional behavior in the endurance test with the non-pre-damaged reference clutches and the pre-damaged clutches. While the non-pre-damaged reference system shows higher values for the characteristic coefficient of friction μ_{top} than the pre-damaged system at low pressure (p = 0.75 N/mm^2) and differential speeds of n = 25 min^{-1} and n = 50 min^{-1}, slight differences prevail at higher pressure (p = 1.5 N/mm^2), which consecutively diminish at very high pressure (p = 3.0 N/mm^2). For friction system FS2, the differences between the non-pre-damaged reference and pre-damaged systems are clearly visible. The characteristic value μ_{top} of the reference system is many times higher than that of the pre-damaged system. With increasing pressure, the differences decrease but are still clearly recognizable. An influence of the sliding speed on the coefficient of friction level can be seen, especially for friction systems FS1 and FS2 at pressures of p = 0.75 N/mm^2 and p = 1.5 N/mm^2. For the same pressure, the differences between non-pre-damaged reference clutches and the pre-damaged clutches are higher at increasing differential speeds. A decrease in the coefficient of friction, especially at high sliding speeds, due to clogged friction linings is also described in the literature for paper-based friction linings [Dev04, Mae03, Mat97b, Osa90, Sak93].

The results of the investigations regarding the influence of high mechanical and thermal loads as well as pre-damage on the friction behavior can be integrated very well into the state of the science and extend it. On the one hand, the influence of the friction lining type on the wear behavior and the clogging of the lining with oil cracking products in transient slip operation can be seen. On the other hand, the influence of the friction lining, the degree of wear, and the intensity of the lining contamination on the friction behavior are shown. The friction behavior in transient operation is directly influenced after high loads. The endurance tests show that a one-time pre-damage still influences the friction behavior at a high number of shiftings. Furthermore, the step tests show a load and temperature dependence of the friction behavior. The influence of the temperature level on friction behavior, as well as changes in the friction lining (wear, clogging), can be improved, especially in the FS2 friction system, by an optimized design. Numerous options are available for lowering the temperature level, which are explained in more detail in Section 8.2. In addition to lowering the clutch's temperature level, clogging of the friction lining should be prevented or at least limited. One way of reducing clogging of the friction lining is to improve its porosity in the new condition, as observed in friction system FS1. In addition to improving the friction lining porosity, the use of additives to increase the thermal stability of the lubricant has been proposed in the literature [Sto23]. Acuner [Acu16a] demonstrates that the detergent additive (overbased calcium sulfonate) is largely responsible for the formation of deposits in the carbon friction lining during synchronization, using experiments with model fluids in a component test rig and subsequent SEM/EDX analyses. In contrast, the dispersant additive (sucinimide) tends to inhibit deposits. In addition, Maeda et al. [Mae03] confirm that high temperature resistance of the detergent-dispersant additives used can prevent clogging of the friction linings up to a limiting temperature. With lifetime tests on organic friction linings of a wet multi-plate clutch, Iwai et al. [Iwa15] also show that over-based calcium detergent lowers the dynamic coefficient of friction due to an intense smoothing of the friction lining in the lifetime test.

9 Design Recommendations to Prevent Spontaneous Damage

In this section, the results of the literature research, the experimental investigations, and the theoretical studies are translated into design recommendations. If possible, these should be implemented to avoid spontaneous damage in transient slip applications. However, it should be noted that these recommendations are in conflict with other development goals, such as package space optimization, cost, and sustainability, among others.

9.1 Steel Plate

The steel plate is utilized in the clutch to absorb the converted mechanical energy into thermal energy and to simultaneously endure the mechanical and thermal loads encountered during operation. The following design recommendations are made to prevent spontaneous damage:

- Achieving a high absolute heat capacity of the steel plate can be done through:
  - Using a material with high density
  - Selecting a material with a high specific heat capacity
  - Employing a thick steel plate
- Achieving a high resistance moment against deformations can be accomplished through:
  - Using a thick steel plate
  - Ensuring a uniform and regular distribution of teeth along the circumference
  - Maintaining a symmetrical structure for the steel plate
- Using a steel plate material with high thermal conductivity

9.2 Friction Lining

Besides lubrication, the friction lining in the clutch exerts a significant influence on the clutch's friction behavior. The following recommendations are proposed to prevent spontaneous damage and also to ensure functional operation after very high thermal and mechanical loads have occurred:

- Achieving a high absolute heat capacity of the friction lining can be done through:
  - Using a material with high density
  - Selecting a material with high specific heat capacity
- Ensuring the friction lining material has high thermal conductivity
- Using a friction lining material with thermal conductivity similar to that of the steel plate material
- Having a uniform and regular distribution of the grooves. For this:
  - The first group of grooves should be designed to effectively circulate the lubricant
  - The second group of grooves should preferably take the form of a closely-meshed net or grid to prevent hydrodynamic effects
- Ensuring high lining porosity
- Designing the groove to be adapted to the oil flow rate

9.3 Carrier Plate

The carrier plate serves as a support for the friction lining, while also enduring the mechanical and thermal loads during operation. The following design recommendations can be made for the carrier plate:

- Achieving a high resistance moment against deformations can be accomplished through:
  - Ensuring a uniform and regular distribution of teeth along the circumference
  - Designing a symmetrical structure for the carrier plate
  - Choosing a carrier plate of greater thickness
- Achieving a high absolute heat capacity of the steel plate can be done through:
  - Using a material with high density
  - Selecting a material with high specific heat capacity
  - Using a thick carrier plate

9.4 Cooling

The clutch can be cooled by the cooling oil and through heat conduction to the mounting parts:

- Maintaining a high oil flow rate
- Providing a large contact surface with the pressure and counter plate
- Ensuring a large contact surface with the carriers

9.5 Clutch Assembly

Due to the mutual dependencies in the design of the individual clutch components, recommendations for assembly are also necessary:

- Aim for a ratio of the thermal conductivities of the steel material and the lining material of 1
- Match the thickness of the steel plate and the thickness of the carrier plate to the thermal conductivity of the friction lining

10 Conclusion and Outlook

The primary objective of this work is the investigation of the spontaneous damage behavior of wet multi-plate clutches under transient slip conditions, as they are used today in modern automotive powertrains in differential locks, transfer cases, and torque vectoring systems.

10.1 Summary of Achievements

In the first step, the damage mechanisms of wet multi-plate clutches in transient slip operation are investigated. Three different friction linings (paper-based friction lining, carbon composite friction lining, and woven carbon friction lining) and three different steel plate thicknesses (0.8 mm, 1.2 mm, and 1.6 mm) are used. Based on the state of the art, a test and evaluation methodology using step tests is proposed. Preliminary tests are carried out to validate the methodology and determine the test conditions, examining the number of friction interfaces, the oil flow rate, and load parameters (pressure, max. differential speed).

Different failure mechanisms are revealed. The friction systems with paper-based and carbon composite friction linings show buckling of the steel plate as the cause of failure, while the friction system with woven carbon friction lining fails due to detachment of the friction lining. In tests with a very thick steel plate (1.6 mm) and paper-based friction lining, buckling leads to failure in the carrier plate instead of the steel plate. Non-contact topography measurements quantify the buckling of the steel plates, showing an axial deformation of up to 2.4 mm. Microstructural investigations confirm temperature measurements of the steel plates during experimental tests, indicating that very high temperatures (> 400 °C) can occur when the clutch fails. EDX measurements reveal that the carbon composite friction lining, in particular, is clogged with oil cracking products after high loads, explaining the deterioration of friction behavior.

After demonstrating the damage mechanisms, the focus turns to identifying when or at which loads the damage occurs. A multitude of tests under a wide variety of load parameters are carried out. Despite differing failure mechanisms and friction linings, a critical temperature range for the failure causes (buckling and lining detachment) is identified at the load level before failure in the step test.

Based on these findings, the study seeks ways to prevent damage in the application. Initially, the knowledge of a critical temperature range can be used to minimize the temperature level at the same mechanical load in a clutch by design adjustments, for which experimental tests are carried out with thicker steel plates (1.2 mm, 1.6 mm). Furthermore, to complement this approach, a two-dimensional and a three-dimensional finite element model are built to calculate the thermomechanical behavior of the clutch during actuation and are validated with experimental data. The results of the experiments and the simulative parameter studies show that especially the thickness of the steel plate and the carrier plate, the thermal conductivity as well as the heat capacity of the steel plate and the friction lining have a great influence on the thermal behavior of the clutch. From a geometrical perspective, evenly distributed teeth and grooves should be ensured. In general, a symmetrical design of the steel plates, friction lining, and carrier plate should be aimed at to increase resistance against deformations, such as buckling, and minimize thermal stresses.

Predictive models can also avoid damage. Simulation data (5 900 data points) are used to train machine learning algorithms (Polynomial Regression, Decision Tree, Support Vector Regression, Gaussian Process, and Backpropagation Neural Networks). The models predict

the expected temperature stroke in the clutch for given load parameters. In particular, the model based on the Backpropagation Neural Network provides very accurate prediction values and critical temperature ranges. Considering the time required to derive a temperature prediction based on given load parameters, the decision tree-based model is highly recommended for its speed, requiring only 0.001 s for a prediction, compared to more than 0.2 s for other studied algorithms. The accuracy of the decision tree-based model further distinguishes it.

Figure 10.1 visualizes the development process and the major achievements of this work. The damage mechanisms and failure causes are demonstrated. It is shown that critical temperature ranges can be identified despite different failure causes. With the help of experimental investigations and FE simulation, design recommendations are derived to prevent damage as far as possible during the design process. Finally, prediction models are presented to avoid damaging conditions in the application.

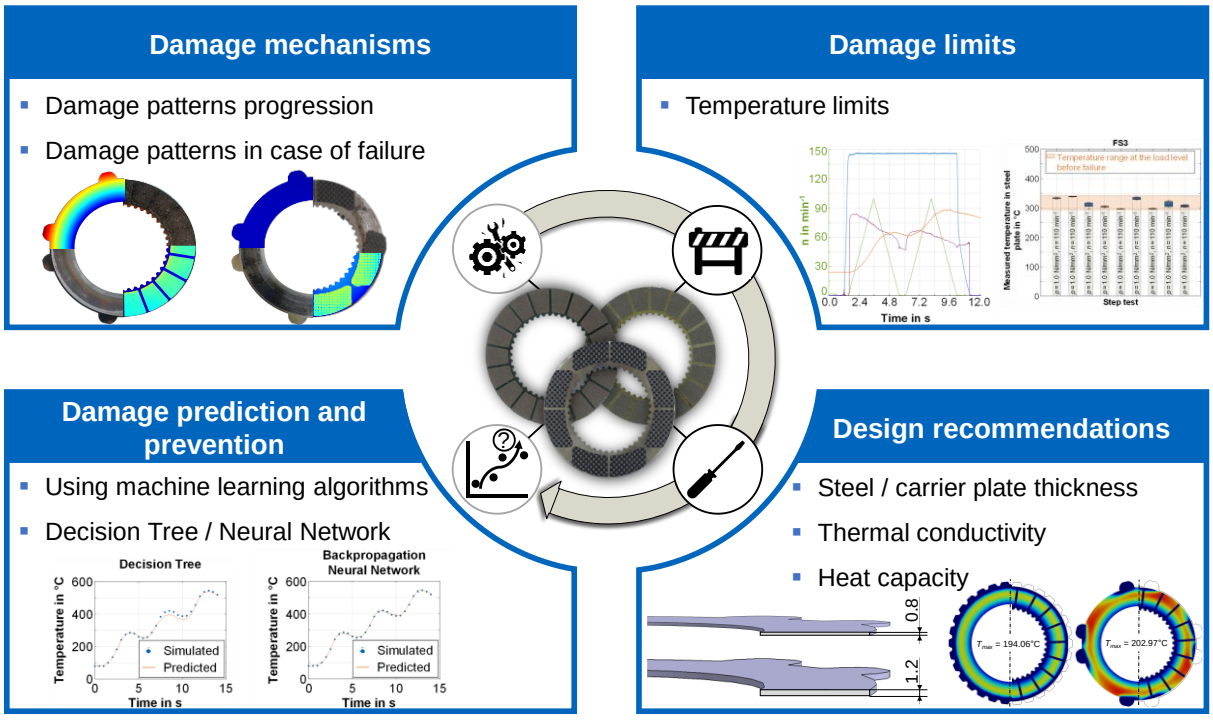

Figure 10.1: Visual representation of selected achievements of this thesis.

10.2 Future Work

When it comes to advancing the simulation-based calculation of the thermomechanical behavior of wet multi-plate clutches, it is crucial to prioritize the study of oil distribution and its cooling effects. The fundamental requirement for this development is to demonstrate the feasibility of determining heat transfer coefficients using Computational Fluid Dynamics (CFD) simulations. By establishing this foundation, a comprehensive model can be developed to encompass the domains of fluid dynamics, contact mechanics, and thermodynamics. Consequently, a wide range of groove geometries and oil supply configurations can be analyzed by considering the design of the clutch system. Based on the findings, recommendations for optimal designs can be proposed. However, a significant challenge lies in the current limitations of computational power necessary for executing such a complex multiphysics model.

Exciting advancements in the field of friction lining materials are observed with the increasing adoption of carbon fiber reinforced carbon (CFRC) friction linings. Although currently limited to niche applications, CFRC linings show great promise. The utilization of carbon as a matrix material, as opposed to plastic, offers significant improvements in both friction lining temperature and thermal conductivity. By incorporating carbon into the matrix, the friction lining can withstand higher temperatures without compromising its structural integrity. This enhanced thermal stability is crucial in applications that involve high heat generation, such as wet multi-plate clutches. Additionally, the improved thermal conductivity of CFRC linings allows for more efficient heat dissipation, resulting in better overall performance and reduced wear. However, the development of CFRC friction linings also presents certain challenges. One of the primary concerns is the need to establish a thermally stable adhesive layer that can effectively bond the CFRC material to the carrier plate. This layer must possess comparable thermal properties to ensure the integrity and durability of the overall system. While addressing this challenge is not without its difficulties, it is considered a viable objective within the realm of current possibilities.

11 References

11.1 Standards, Guidelines and Patents

[Aut12a] J286_201203: SAE No. 2 Clutch Friction Test Machine Guidelines (2012).

[Aut12b] J2490_201905: SAE No. 2 Friction Test Machine Durability Test (2012).

[Aut19a] J2490_201905: SAE No. 2 Friction Test Machine µPVT Test (2019).

[Aut19b] J2487_201905: SAE No. 2 Friction Test Machine 3600 rpm Stepped Power Test (2019).

[Aut19c] J2488_201907: SAE No. 2 Friction Test Machine 6000 rpm Stepped Power Test (2019).

[DIN86] DIN 50322:1986-03: Verschleiss - Kategorien der Verschleisspruefung [Wear, classification of categories in wear testing] (1986).

[DIN14] DIN EN 60584-1:2014-07: Thermoelemente - Teil 1: Thermospannungen und Grenzabweichungen [Thermocouples - Part 1: EMF specifications and tolerances] (2014).

[DIN18] DIN EN ISO 6507-1:2018-07: Metallische Werkstoffe - Haertepruefung nach Vickers - Teil 1: Pruefverfahren [Metallic materials - Vickers hardness test - Part 1: Test method] (2018).

[GFT02] GFT Gesellschaft fuer Tribologie: Arbeitsblatt 7 - Tribologie: Verschleiss, Reibung - Definitionen, Begriffe, Pruefung [Worksheet 7 - Tribology: Wear, Friction - Definitions, Terms, Testing]. GFT Gesellschaft fuer Tribologie e.V., Juelich (2002).

[Joi08] JCGM 100:2008: Evaluation of measurement data - Guide to the expression of uncertainty in measurement (2008).

[Mer01] Merkel, H.; Koehler, J.: Lamelle fuer ein Kraftuebertragungsaggregat, zum Beispiel fuer eine Schaltkupplung [Clutch Plate for a Power Transmission Unit, for Example for a Shifting Clutch], DE19957511A1 (2001).

[Sar04] Sarkar, R.; Calcut, B. D.; Linden, J. L.: Real time life models for automatic transmission fluids, US2005165583 (A1) (2004).

[VDI82] VDI 2241-1: Schaltbare fremdbetaetigte Reibkupplungen und -bremsen - Begriffe, Bauarten, Kennwerte, Berechnungen [Friction clutches and brakes; vocabulary, types, characteristic data, calculations] (1982).

[VDI84] VDI 2241-2: Schaltbare fremdbetaetigte Reibkupplungen und -bremsen - Systembezogene Eigenschaften, Auswahlkriterien, Berechnungsbeispiele [Friction clutches and brakes; typ related properties, criteria for selection, examples of calculations] (1984).

11.2 Books, Journal Articles, Dissertations, Student Theses

[Aba16] Abadi, M.; Barham, P.; Chen, J.; Chen, Z.; Davis, A.; Dean, J.; Devin, M.; Ghemawat, S.; Irving, G.; Isard, M.; Kudlur, M.; Levenberg, J.; Monga, R.; Moore, S.; Murray, D. G.; Steiner, B.; Tucker, P.; Vasudevan, V.; Warden, P.; Wicke, M.;

Yu, Y.; Zheng, X.: TensorFlow: A system for large-scale machine learning, CoRR (2016).

[Abb14] Abbasi, S.; Teimourimanesh, S.; Vernersson, T.; Sellgren, U.; Olofsson, U.; Lundén, R.: Temperature and thermoelastic instability at tread braking using cast iron friction material. Wear. Issue: 1-2, p. 171–180 (2014).

[Abd13a] Abdullah, O.: Stresses and Deformations Analysis of a Dry Friction Clutch System. Tribology in Industry, p. 155–162 (2013).

[Abd14a] Abdullah, O.: An Investigation of Heat Generation Due To Friction Using Finite Element Method. SAE 2014 World Congress & Exhibition (2014).

[Abd18a] Abdullah, O.; Rasham, A.; Jobair, H.: The influence of frictional facing thickness on the contact pressure distribution of multi-disc dry clutches. FME Transaction. Issue: 1, p. 33–38 (2018).

[Abd12a] Abdullah, O.; Schlattmann, J.: Finite Element Analysis of Temperature Field in Automotive Dry Friction Clutch. Tribology in Industry, p. 206–216 (2012).

[Abd13b] Abdullah, O.; Schlattmann, J.: Effect of Band Contact on the Temperature Distribution for Dry Friction Clutch. Tribology in Industry, p. 317–329 (2013).

[Abd14b] Abdullah, O.; Schlattmann, J.; Al-Shabibi, A.: Thermo-mechanical Analysis of the Dry Clutches under Different Boundary Conditions. Tribology in Industry, p. 172–180 (2014).

[Abd13c] Abdullah, O. I.; Schlattmann, J.: Contact Analysis of a Dry Friction Clutch System. ISRN Mechanical Engineering, p. 1–9 (2013).

[Abd14c] Abdullah, O. I.; Schlattmann, J.: An Investigation Into the Thermal Behavior of the Grooved Dry Friction Clutch. Journal of Tribology. Issue: 3 (2014).

[Abd18b] Abdullah, O. I.; Schlattmann, J.; Senatore, A.; Al-Shabibi, A. M.: Investigation of thermoelastic problem of multiple-disc friction clutches applying different thermal loads. Heat and Mass Transfer. Issue: 11, p. 3461–3471 (2018).

[Abd12b] Abdullah, O. I.; Schlattmann, J.: The Effect of Disc Radius on Heat Flux and Temperature Distribution in Friction Clutches. Advanced Materials Research, p. 154–164 (2012).

[Abd14d] Abdullaha, O. I.; Schlattmann, J.: Computation of surface temperatures and energy dissipation in dry friction clutches for varying torque with time. International Journal of Automotive Technology. Issue: 5, p. 733–740 (2014).

[Abu08] AbuBakar, A. R.; Ouyang, H.: Wear prediction of friction material and brake squeal using the finite element method. Wear. Issue: 11-12, p. 1069–1076 (2008).

[Acu16a] Acuner, R.: Synchronisierungen mit Carbon-Reibwerkstoffen unter hohen und extremen Beanspruchungen [Synchronizations with carbon friction materials under high and extreme stresses], Ph. D., Technical University of Munich (2016).

[Acu13] Acuner, R.; Pflaum, H.; Stahl, K.: Oeleinfluss Reibcharakteristik am Modell nasslaufende Lamellenkupplung; Entwicklung eines Reibungszahlkurztests [Oil influence on friction characteristics in a wet multi-plate clutch model;

Development of a friction coefficient short test.] - Research Project No. 490 IV, Issue: 1051. Forschungsvereinigung Antriebstechnik e.V., Frankfurt/Main (2013).

[Acu14] Acuner, R.; Pflaum, H.; Stahl, K.: Influence of Lubricant on Friction and Deterioration Behavior of Synchronizers with Carbon Friction Linings, Berlin. CTI (2014).

[Acu16b] Acuner, R.; Pflaum, H.; Stahl, K.: Tribologische Schaedigungsmechanismen von Synchronisierungen mit Carbon-Reibwerkstoffen [Tribological damage mechanisms of synchronizations with carbon friction materials]. GETLUB - Tribologie- und Schmierstoffkongress, Wuerzburg. FVA (2016).

[Aff04] Afferrante, L.; Decuzzi, P.: The effect of engagement laws on the thermomechanical damage of multidisk clutches and brakes. Wear. Issue: 1-2, p. 66–72 (2004).

[Ahm19] Ahmadijokani, F.; Shojaei, A.; Arjmand, M.; Alaei, Y.; Yan, N.: Effect of short carbon fiber on thermal, mechanical and tribological behavior of phenolic-based brake friction materials. Composites Part B: Engineering, p. 98–105 (2019).

[Ala17] Alam, A.; Wan, C.; McNally, T.: Surface amination of carbon nanoparticles for modification of epoxy resins: plasma-treatment vs. wet-chemistry approach. European Polymer Journal, p. 422–448 (2017).

[Al-02] Al-Shabibi, A. M.; Barber, J. R.: Transient solution of a thermoelastic instability problem using a reduced order model. International Journal of Mechanical Sciences. Issue: 3, p. 451–464 (2002).

[And90] Anderson, A. E.; Knapp, R. A.: Hot spotting in automotive friction systems. Wear. Issue: 2, p. 319–337 (1990).

[Ank21] Ankur; Bharti, A.; Prasad, D.; Kumar, N.; Saxena, K. K.: A Re-investigation: Effect of various parameter on mechanical properties of copper matrix composite fabricated by powder metallurgy. Materials Today: Proceedings, p. 4595–4600 (2021).

[Arc56] Archard, J. F.; Hirst, W.: The wear of metals under unlubricated conditions. Proceedings of the Royal Society of London. Series A: Mathematical, Physical and Engineering Sciences. Issue: 1206, p. 397–410 (1956).

[Asi16] Asif, M.; Tariq, A.: Correlations of Thermal Contact Conductance for Nominally Flat Metallic Contact in Vacuum. Experimental Heat Transfer. Issue: 4, p. 456–484 (2016).

[Aud98] Audebert, N.; Barber, J. R.; Zagrodzki, P.: Buckling of Automatic Transmission Clutch Plates Due to Thermoelastic/Plastic Residual Stresses. Journal of Thermal Stresses. Issue: 3, p. 309–326 (1998).

[Aug12] Augustin, S.; Spreckels, M.; Skipper, G.: Comfort and efficiency optimized synchronization - an innovative approach to solving the target conflict. Internationaler Kongress Getriebe in Fahrzeugen, VDI-Gesellschaft Produkt- und Prozessgestaltung et al. 2012 – Getriebe in Fahrzeugen 2012 (2012).

[Awa05] Awasthi, S.; Taccini, G.: Pyrolytic Carbon Wet Friction Materials. 2005 SAE Commercial Vehicle Engineering Conference (2005).

[Bac13] Back, O.: How synchronizers will support the further success of DCTs. EUROFORUM Deutschland SE (2013).

[Bac10] Back, O.; Echtler, P.; Bergheim, M.: Potential of Sintered Friction Linings in Synchronizers. VDI-Gesellschaft Produkt- und Prozessgestaltung, VDI-Tagung Getriebe in Fahrzeugen et al. 2010 – Getriebe in Fahrzeugen 2010 (2010).

[Bag17] Bagheri, H.; Kiani, Y.; Eslami, M. R.: Asymmetric thermo-inertial buckling of annular plates. Acta Mechanica. Issue: 4, p. 1493–1509 (2017).

[Bao16] Bao, K.; Zhang, Z.; Liao, R.-D.: Failure Physics Analysis of the Thermoelastic Instability in Automotive Wet Friction Disks Based on Pressure Distributions of Return Springs. Prognostics and System Health Management Conference (PHM-Chengdu) (2016).

[Bar67] Barber, J. R.: The influence of thermal expansion on the friction and wear process. Wear. Issue: 2, p. 155–159 (1967).

[Bar69] Barber, J. R.: Thermoelastic instabilities in the sliding of conforming solids. Proceedings of the Royal Society of London. Series A: Mathematical, Physical and Engineering Sciences. Issue: 1510, p. 381–394 (1969).

[Bar93] Barker, K.: The Effect of Separator Flatness on the Performance and Durability of Wet Friction Clutches. International Congress & Exposition (1993).

[Bar01] Bartel, D.: Berechnung von Festkoerper- und Mischreibung bei Metallpaarungen [Calculation of solid-state and mixed friction in metal pairings], Ph. D. Thesis, University of Magdeburg. Shaker, Aachen (2001).

[Bar10a] Bartel, D.: Simulation von Tribosystemen - Grundlagen und Anwendungen [Simulation of Tribosystems - Fundamentals and Applications], Habilitation treatise, University of Magdeburg. Vieweg + Teubner, Wiesbaden, 1st Edition (2010).

[Bar94] Bartz, W. J.: Additive fuer Schmierstoffe [Additives for Lubricants]. expert Verlag, Renningen-Malmsheim, 1st Edition (1994).

[Bar10b] Bartz, W. J.: Einfuehrung in die Tribologie und Schmierungstechnik [Introduction to Tribology and Lubrication Technology]. expert Verlag, Renningen (2010).

[Bau20] Baumgartner, A.: Reibungsverhalten nasslaufender Lamellenkupplungen – Messunsicherheiten und Auswertemethoden [Friction Behavior of Wet Multi-Plate Clutches – Measurement Uncertainties and Evaluation Methods], Master Thesis, Technical University of Munich (2020).

[Ber13] Bernhardt, J.; Albers, A.; Ott, S.: Advanced ceramics as friction material in lubricated clutch systems. Tribology International, p. 267–272 (2013).

[Bij15] Bijwe, J.; Gupta, M. K.; Parida, T.; Trivedi, P.: Design and development of advanced polymer composites as high performance tribo-materials based on blends of PEK and ABPBI. Wear, p. 65–76 (2015).

[Bla05] Blau, P. J.; Jolly, B. C.: Wear of truck brake lining materials using three different test methods. Wear. Issue: 7-12, p. 1022–1030 (2005).

[Bru91] Bruegel, E.; Christian, K.; Wunderlich, P.: Entwicklung einer Mehrfachkonus-Synchronisierung fuer Nutzfahrzeuggetriebe [Development of a Multi-Cone Synchronization for Commercial Vehicle Transmissions]. Gesellschaft Entwicklung, Konstruktion, Vertrieb, Tagung 1991 – Getriebe in Fahrzeugen heute, p. 311–327 (1991).

[Bue98] Buergel, R.: Handbuch Hochtemperatur-Werkstofftechnik [Handbook of High-Temperature Materials Science]. Vieweg+Teubner Verlag, Wiesbaden (1998).

[Bur73] Burton, R. A.; Nerlikar, V.; Kilaparti, S. R.: Thermoelastic instability in a seal-like configuration. Wear. Issue: 2, p. 177–188 (1973).

[Cal04] Calcut, B. D.; Sarkar, R.; Linden, J. L.: Estimating the Useful Life of an ATF Using an Integrated Bulk Oxidation and Friction Degradation Model. 2004 Powertrain & Fluid Systems Conference & Exhibition (2004).

[Cel12] Celebi Efe, G.; Ipek, M.; Zeytin, S.; Bindal, C.: An investigation of the effect of SiC particle size on Cu–SiC composites. Composites Part B: Engineering. Issue: 4, p. 1813–1822 (2012).

[Cen15] Cenbo, X.; Biao, M.; Heyan, L.; Fenglian, Z.; Da, W.: Experimental Study and Thermal Analysis on the Buckling of Friction Components in Multi-Disc Clutch. Journal of Thermal Stresses. Issue: 11, p. 1323–1343 (2015).

[Che19] Chen, Z.; Yi, Y.-B.; Bao, K.; Zhao, J.: Numerical analysis of the coupling between frictionally excited thermoelastic instability and thermal buckling in automotive clutches. Proceedings of the Institution of Mechanical Engineers, Part J: Journal of Engineering Tribology. Issue: 1, p. 178–187 (2019).

[Che16] Chen, Z.; Yi, Y.-B.; Zhao, J.: Fourier finite element model for prediction of thermal buckling in disc clutches and brakes. Journal of Thermal Stresses. Issue: 10, p. 1241–1251 (2016).

[Che20] Cheng, Y.-C.; Wu, C.-M.; Lin, P.-C.; Lai, W.-Y.; Chen, P.-H.; Way, T.-D.: Friction behaviors of staple carbon fiber composites. Modern Physics Letters B. Issue: 07n09, p. 2040002 (2020).

[Chi01] Chiba, N.: Mechanism of compression fatigue of wet friction materials. JSAE Review. Issue: 2, p. 169–174 (2001).

[Cho18] Cho, H.-R.; Je, Y.; Chung, K.-H.: Assessment of Wear Characteristics of Paper-Based Wet Friction Materials. International Journal of Precision Engineering and Manufacturing. Issue: 5, p. 705–711 (2018).

[Coo69] Cooper, M. G.; Mikic, B. B.; Yovanovich, M. M.: Thermal contact conductance. International Journal of Heat and Mass Transfer. Issue: 3, p. 279–300 (1969).

[Cro93] Crosa, G.; Baumvol, I. J.: Tribology of polymer composites used as frictional materials. Composite Materials Series (1993).

[Cui14] Cui, J.; Wang, C.; Xie, F.; Xuan, R.; Shen, G.: Numerical investigation on transient thermal behavior of multidisk friction pairs in hydro-viscous drive. Applied Thermal Engineering. Issue: 1-2, p. 409–422 (2014).

[Cui15] Cui, J.; Xie, F.; Wang, C.: Numerical investigation on thermal deformation of friction pair in hydro-viscous drive. Applied Thermal Engineering, p. 460–470 (2015).

[Czé09] Czél, B.; Váradi, K.; Albers, A.; Mitariu, M.: Fe thermal analysis of a ceramic clutch. Tribology International. Issue: 42, p. 714–723 (2009).

[Czi20] Czichos, H.; Habig, K.-H.: Tribologie-Handbuch - Tribometrie, Tribomaterialien, Tribotechnik [Tribology Handbook - Tribometry, Tribomaterials, Tribotechnology], Wiesbaden, Heidelberg (2020).

[Dec18] Decker, K.-H.; Alber-Laukant, B.; Weidermann, F.; Rieg, F.; Engelken, G.; Hackenschmidt, R.: Decker Maschinenelemente - Funktion, Gestaltung und Berechnung [Decker Machine Elements - Function, Design, and Calculation]. Hanser, Munich, Issue: 20 (2018).

[Dec01] Decuzzi, P.; Ciaverella, M.; Monno, G.: Frictionally Excited Thermoelastic Instability in Multi-Disk Clutches and Brakes. Journal of Tribology. Issue: 4, p. 865 (2001).

[Dev04] Devlin, M. T.; Tersigni, S. H.; Senn, J.; Turner, T. L.; Jao, T.-C.; Yatsunami, K.: Effect of Friction Material on the Relative Contribution of Thin-Film Friction to Overall Friction in Clutches. SAE Technical Paper Nr. 2004-01-3025 (2004).

[Die21] Dietsch, M.: Modellierung des thermomechanischen Verhaltens einer Lamellenkupplung unter Einsatz von FEM und kuenstlicher Intelligenz [Modeling of the Thermomechanical Behavior of a Multi-Plate Clutch Using FEM and Artificial Intelligence], Master Thesis, Technical University of Munich (2021).

[Dou16] Dou, R.; Ge, T.; Liu, X.; Wen, Z.: Effects of contact pressure, interface temperature, and surface roughness on thermal contact conductance between stainless steel surfaces under atmosphere condition. International Journal of Heat and Mass Transfer, p. 156–163 (2016).

[Dow78] Dow, T. A.: Preventing Hot Spots in Sliding Contact. Machine Design. Issue: 50, p. 94–102 (1978).

[Dow73] Dow, T. A.; Burton, R. A.: The Role of Wear in the Initiation of Thermoelastic Instabilities of Rubbing Contact. Journal of Lubrication Technology. Issue: 1, p. 71–75 (1973).

[Dow72] Dow, T. A.; Burton, R. A.: Thermoelastic instability of sliding contact in the absence of wear. Wear. Issue: 3, p. 315–328 (1972).

[Duf03] Dufrénoy, P.; Weichert, D.: A Thermomechanical Model for the Analysis of Disc Brake Fracture Mechanisms. Journal of Thermal Stresses. Issue: 8, p. 815–828 (2003).

[Dum77] Duminy, J.; Federn, K.: Ermittlung der Leistungsgrenzen der Reibpaarung Stahl/Sinterbronze, in oelgeschmierten Reibungskupplungen unter Beruecksichtigung des Einflusses der Kuehl- und Schmiermittel [Determination of the performance limits of the steel/sintered bronze friction pairing in oil-lubricated friction clutches, taking into account the influence of cooling and lubricants] -

Research Project No. 91. Forschungsvereinigung Antriebstechnik e.V., Frankfurt/Main (1977).

[Dum79] Duminy, J.: Beurteilung des Betriebsverhaltens schaltbarer Reibkupplungen [Assessment of the Operating Behavior of Shiftable Friction Clutches], Ph. D. Thesis, Technical University of Berlin (1979).

[Egu01] Eguchi, M.; Nakahara, T.: Friction-Velocity Characteristics of a Paper-Based Wet Friction Material in Low Sliding Velocity (Part 1): Boundary Film Model Supposing Eyring Viscosity. Japanese Journal of Tribology. Issue: 46, p. 162–170 (2001).

[Erd05] Erdemir, A.: Review of engineered tribological interfaces for improved boundary lubrication. Tribology International. Issue: 3, p. 249–256 (2005).

[Eva90] Evans, R. E., Trainor, J.A.: Acrylic fibres in non-asbestos friction materials. 8th Annual SAE brake colloquium (1990).

[Fai01] Fairbank, D.; Maruo, K.; Du, S.; Newcomb, T.: ATF Additive Effects on Hot Spot Formation in Wet Clutches. SAE Technical Paper Series (2001).

[Far15] Farfán-Cabrera, L. I.; Gallardo-Hernández, E. A.; Vite-Torres, M.; Laguna-Camacho, J. R.: Frictional Behavior of a Wet Clutch Using Blends of Automatic Transmission Fluid (ATF) and Biolubricant (Jatropha Oil) in a Pin-on-Disk Tester. Tribology Transactions. Issue: 5, p. 941–946 (2015).

[Fei12] Fei, J.; Li, H.-J.; Huang, J.-F.; Fu, Y.-W.: Study on the friction and wear performance of carbon fabric/phenolic composites under oil lubricated conditions. Tribology International, p. 30–37 (2012).

[Fei08] Fei, J.; Li, H.-J.; Qi, L.-H.; Fu, Y.-W.; Li, X.-T.: Carbon-fiber reinforced paper-based friction material: study on friction stability as a function of operating variables. Journal of Tribology. Issue: 4, p. 41605 (2008).

[Fei16] Fei, J.; Li, W.; Huang, J.; Cao, L.; Yao, C.; Wenbin, L.; Jianfeng, H.; Liyun, C.; Chunyan, Y.: Variation of the tribological properties of carbon fabric composites in their whole service life. Tribology International, p. 29–37 (2016).

[Fei15] Fei, J.; Luo, W.; Huang, J. F.; Ouyang, H.; Xu, Z.; Yao, C.: Effect of carbon fiber content on the friction and wear performance of paper-based friction materials. Tribology International, p. 91–97 (2015).

[Fie11] Fieldhouse, J. D.; Bryant, D.; Talbot, C. J.: Hot Judder - An Investigation of the Thermo-Elastic and Thermo-Plastic Effects during Braking. SAE International Journal of Passenger Cars - Mechanical Systems. Issue: 2, p. 1086–1101 (2011).

[Fis73] Fish, R. L.; Lloyd, F. A.: Surface finish requirements of spacer plates for paper friction applications. SAE Technical Paper Nr. 1973-02-01 (1973).

[Fle72] Fleischer, G.; Wamser, H.: Terminologie Reibung und Verschleiss [Terminology of Friction and Wear]. Schmierungstechnik. Issue: 7, p. 202–205 (1972).

[Foe15] Foege, V.; Eder, M.; Nickel, F.: Innovation von Fiber Composite Reibsystemen – Von der Faser bis zur Anwendung [Innovation of Fiber Composite Friction

Systems – From Fiber to Application]. Kupplungen und Kupplungssysteme in Antrieben 2015, Karlsruhe. VDI (2015).

[Gao07] Gao, C. H.; Huang, J. M.; Lin, X. Z.; Tang, X. S.: Stress Analysis of Thermal Fatigue Fracture of Brake Disks Based on Thermomechanical Coupling. Journal of Tribology. Issue: 3, p. 536–543 (2007).

[Gao02a] Gao, H.; Barber, G.; Chu, H.: Friction Characteristics of a Paperbased Ftiction Material. International Journal of Automotive Technology. Issue: No. 4 (2002).

[Gao02b] Gao, H.; Barber, G. C.: Microcontact Model for Paper-Based Wet Friction Materials. Journal of Tribology. Issue: 2, p. 414–419 (2002).

[Gei37] Geiger, J.: Die Erwaermung von Kupplungen und Bremsen [The Heating of Clutches and Brakes]. Automobiltechnische Zeitschrift. Issue: 7, p. 34–35 (1937).

[Gib89] Gibson, D. W.; Taccini, C. J.: Carbon/Carbon Friction Materials for Dry and Wet Brake and Clutch Applications. 40th Annual Earthmoving Industry Conference, Hitco Gardena, CA (1989).

[Gon15] Gong, T.; Yao, P.; Xiao, Y.; Fan, K.; Tan, H.; Zhang, Z.; Zhao, L.; Zhou, H.; Deng, M.: Wear map for a copper-based friction clutch material under oil lubrication. Wear, p. 270–276 (2015).

[Gon18] Gong, Y.; Ge, W.; Yi, Y. B.: Finite element analysis of thermal buckling characteristics of automotive 430 dry clutch pressure plate. International Journal of Vehicle Design. Issue: 1/2/3/4, p. 108 (2018).

[Gra14] Graf, M.; Ostermeyer, G.-P.: Efficient computation of thermoelastic instabilities in the presence of wear. Wear. Issue: 1-2, p. 11–20 (2014).

[Gra12] Graf, M.; Ostermeyer, G.-P.: Hot bands and hot spots: Some direct solutions of continuous thermoelastic systems with friction. Physical Mesomechanics. Issue: 5-6, p. 306–315 (2012).

[Gra07] Graswald, C.; Bruegel, E.; Klumpp, A.: Methodik der vergleichenden Untersuchung von Reibschichten am Beispiel von Synchronisierungen [Methodology for the Comparative Study of Friction Layers Using the Example of Synchronization]. Erprobung und Simulation in der Fahrzeugentwicklung, Wuerzburg, Duesseldorf (2007).

[Gri98] Grieve, D. G.; Barton, D. C.; Crolla, D. A.; Buckingham, J. T.: Design of a lightweight automotive brake disc using finite element and Taguchi techniques. Proceedings of the Institution of Mechanical Engineers, Part D: Journal of Automobile Engineering. Issue: 4, p. 245–254 (1998).

[Gro21a] Groetsch, D.; Pflaum, H.; Stahl, K.: Echtzeit-Temperaturberechnung und Temperaturpraediktion nasslaufender Lamellenkupplungen im Betrieb [Real-Time Temperature Calculation and Temperature Prediction of Wet-Running Multi-Plate Clutches in Operation] - Research Project No. 413 V, Issue 1427. Forschungsvereinigung Antriebstechnik e.V., Frankfurt/Main (2021).

[Gro21b] Groetsch, D.; Stockinger, U.; Schneider, T.; Reiner, F.; Voelkel, K.; Pflaum, H.; Stahl, K.: Experimental investigations of spontaneous damage to wet multi-plate

clutches with carbon friction linings. Forschung im Ingenieurwesen/Engineering Research. Issue: 117, p. 2480 (2021).

[Gro18] Grote, K.-H.; Bender, B.; Goehlich, D.: Dubbel - Handbook for Mechanical Engineering [Dubbel - Handbook for Mechanical Engineering]. Springer, Berlin, Heidelberg (2018).

[Guh21] Guha Keshav, M.; Hemchandran, C. G.; Dharsan, B.; Pradhin, K.; Vaira Vignesh, R.; Govindaraju, M.: Manufacturing of continuous fiber reinforced sintered brake pad and friction material. Materials Today: Proceedings, p. 4493–4496 (2021).

[Guo17] Guo, L.; Zhang, G.; Wang, D.; Zhao, F.; Wang, T.; Wang, Q.: Significance of combined functional nanoparticles for enhancing tribological performance of PEEK reinforced with carbon fibers. Composites Part A: Applied Science and Manufacturing, p. 400–413 (2017).

[Hae15] Haeggstroem, D.; Stenstroem, W.; Sellgren, U.; Bjoerklund, S.: Parameter study of the thermomechanical performance of heavy duty synchronizers. Getriebe in Fahrzeugen 2015 / Drievetrain for vehicles, Friedrichshafen. VDI (2015).

[Hae95] Haemmerl, B.: Lebensdauer-und Temperaturverhalten oelgekuehlter Lamellenkupplungen bei Lastkollektivbeanspruchung [Service Life and Temperature Behavior of Oil-Cooled Multi-Plate Clutches under Load Collective Stresses], Ph. D. Thesis, Technical University of Munich (1995).

[Has59] Hasselgruber, H.: Temperaturberechnungen fuer mechanische Reibkupplungen [Temperature Calculations for Mechanical Friction Clutches]. Vieweg, Braunschweig (1959).

[Hen10] Henley, M.; Basu, S.; Schiferl, E.; Whitticar, D.; Baker, M.; Bartley, S.; Huston, M. E.: Next Generation Torque Control Fluid Technology, Part III: Using an Improved Break-Away Friction Screen Test to Investigate Fundamental Friction Material-Lubricant Interactions. SAE 2010 Powertrains Fuels & Lubricants Meeting (2010).

[Hen14] Hensel, M.: Thermische Beanspruchbarkeit und Lebensdauerverhalten von nasslaufenden Lamellenkupplungen [Thermal Load Capacity and Service Life Behavior of Wet-Running Multi-Plate Clutches], Ph. D. Thesis, Technical University of Munich (2014).

[Hir07] Hirano, T.; Maruo, K.; Gu, X.; Fujii, T.: Development of Friction Material and Quantitative Analysis for Hot Spot Phenomenon in Wet Clutch System. SAE World Congress & Exhibition (2007).

[Ho05] Ho, S. C.; Chern Lin, J. H.; Ju, C. P.: Effect of fiber addition on mechanical and tribological properties of a copper/phenolic-based friction material. Wear. Issue: 5-6, p. 861–869 (2005).

[Hoe01] Hoerbiger Antriebstechnik GmbH: Lamellen fuer Lastschaltgetriebe, Bremsen und Achsen - Hoerbiger Lamellenhandbuch [Clutch Plates for Powershift Transmissions, Brakes, and Axles - Hoerbiger Clutch Plate Handbook], Schongau (2001).

[Hua19] Huang, S.; Bao, J.; Yin, Y.; Ge, S.; Liu, T.: A Review of Brake Friction Materials: Development, Tribological Performance and Failure Prediction. Science of Advanced Materials. Issue: 5, p. 613–628 (2019).

[Hua09] Huang, X.: Fabrication and Properties of Carbon Fibers. Materials. Issue: 4, p. 2369–2403 (2009).

[Hui15] Huizhou Yang: Finite Element Analysis of Thermal Buckling in Automotive Clutch and Brake Discs, Master Thesis, University of Denver (2015).

[Ina00] Inacker, O.; Beckmann, P.; Oster, P.: Triboschutzschichtcharakterisierung; Untersuchungen zur Bildung, Charakterisierung und Wirkungsweise von Triboschutzschichten [Triboprotective Layer Characterization; Studies on the Formation, Characterization, and Functionality of Triboprotective Layers] - Research Project No. 289/I+II, Issue: 595. Forschungsvereinigung Antriebstechnik e.V., Frankfurt/Main (2000).

[Ing10a] Ingram, M.; Noles, J.; Watts, R.; Harris, S.; Spikes, H. A.: Frictional Properties of Automatic Transmission Fluids: Part I - Measurement of Friction-Sliding Speed Behavior. Tribology Transactions. Issue: 54, p. 145–153 (2010).

[Ing10b] Ingram, M.; Noles, J.; Watts, R.; Harris, S.; Spikes, H. A.: Frictional Properties of Automatic Transmission Fluids: Part II - Origins of Friction-Sliding Speed Behavior. Tribology Transactions. Issue: 54, p. 154–167 (2010).

[Ing10c] Ingram, M.; Spikes, H.; Noles, J.; Watts, R.: Contact properties of a wet clutch friction material. Tribology International. Issue: 43, p. 815–821 (2010).

[Ito98] Ito, K.; Barker, K. A.; Kubota, M.; Yoshida, S.: Designing Paper Type Wet Friction Material for High Strength and Durability. SAE Technical Paper Nr. 982034 (1998).

[Iva09] Ivanović, V.; Herold, Z.; Deur, J.; Hancock, M.; Assadian, F.: Experimental characterization of wet clutch friction behaviors including thermal dynamics. SAE International Journal of Engines. Issue: 1, p. 1211–1220 (2009).

[Iwa15] Iwai, T.; Ichihashi, T.; Kudo, M.: Influence of Calcium Sulfonate on Wet Clutch Durability. STLE 70th Annual Meeting and Exhibition, Dallas, Texas (2015).

[Izi91] Iziyumova, V. V.; Nikonova, L. M.; Chumicev, B. M.: Asbestos free friction compositions to be used in automobile disc brake linings. Trenie I Iznos. Issue: 5, p. 915–919 (1991).

[Jab21] Jabbar, N. A.; Hussain, I. Y.; Abdullah, O. I.: Thermal and thermoelastic problems in dry friction clutch: A comprehensive review. Heat Transfer. Issue: 8, p. 7855–7878 (2021).

[Jan02] Jang, J. Y.; Khonsari, M. M.: On the Formation of Hot Spots in Wet Clutch Systems. Journal of Tribology. Issue: 2, p. 336–345 (2002).

[Jan03] Jang, J. Y.; Khonsari, M. M.: A generalized thermoelastic instability analysis. Proceedings of the Royal Society of London. Series A: Mathematical, Physical and Engineering Sciences. Issue: 2030, p. 309–329 (2003).

[Jen08] Jen, T.-C.; Nemecek, D. J.: Thermal analysis of a wet-disk clutch subjected to a constant energy engagement. International Journal of Heat and Mass Transfer. Issue: 7-8, p. 1757–1769 (2008).

[Jon13] Jonathan, N.: Woven Carbon Synchronizer Materials. EUROFORUM Deutschland SE (2013).

[Kal16] Kalare, R. S.; Brooks, P. C.; Barton, D. C.: Characterisation of a carbon/carbon multi-plate clutch for a high energy, race car application. International Journal of Vehicle Performance. Issue: 3, p. 275 (2016).

[Kea97] Kearsey, A.; Wagner, D.: Carbon Fiber for Wet Friction Applications. SAE Technical Paper Nr. 972754 (1997).

[Keh98] Kehrwald, B.: Einlauf tribologischer Systeme [Run-in of Tribological Systems], Ph. D. Thesis, Technical University of Karlsruhe (1998).

[Keh99] Kehrwald, B.; Kopnarski, M.: Tribomutation - Untersuchung der Vorgaenge in tribologischen Systemen waehrend des Einlaufs [Tribomutation - Investigation of Processes in Tribological Systems During the Run-in Phase] - Issue: 616. Forschungsvereinigung Verbrennungskraftmaschinen, Frankfurt/Main (1999).

[Kim05] Kimura, Y.; Otani, C.: Contact and wear of paper-based friction materials for oil-immersed clutches—wear model for composite materials. Tribology International. Issue: 11-12, p. 943–950 (2005).

[Kin99] Kinugasa, T.: Thermal analysis of the synchronizer friction surface and its application to the synchronizer durability improvement. JSAE Review. Issue: 2, p. 217–222 (1999).

[Kit94] Kitahara, S.; T. Matsumoto: Present and Future Trends in Wet Friction Materials. Japanese Journal of Tribology, p. 1451–1459 (1994).

[Koe02] Koetniyom, S.; Brooks, P. C.; Barton, D. C.: The development of a material model for cast iron that can be used for brake system analysis. Proceedings of the Institution of Mechanical Engineers, Part D: Journal of Automobile Engineering. Issue: 5, p. 349–362 (2002).

[Kub98] Kubota, M.; Suenaga, T.; Kazuhiro, D.: A Study of the Mechanism Causing High-Speed Brake Judder. International Congress & Exposition (1998).

[Kuk99] Kukureka, S.; Hooke, C.; Rao, M.; Liao, P.; Chen, Y.: The effect of fibre reinforcement on the friction and wear of polyamide 66 under dry rolling–sliding contact. Tribology International. Issue: 2, p. 107–116 (1999).

[Kum11] Kumar, M.; Boidin, X.; Desplanques, Y.; Bijwe, J.: Influence of various metallic fillers in friction materials on hot-spot appearance during stop braking. Wear. Issue: 5-6, p. 371–381 (2011).

[Kum22] Kumar, N.; Mehta, V.; Kumar, S.; Grewal, J. S.; Ali, S.: Bamboo natural fiber and PAN fiber used as a reinforced brake friction material: Developed asbestos-free brake pads. Polymer Composites (2022).

[Kum16] Kumar, S.; Panneerselvam, K.: Two-body Abrasive Wear Behavior of Nylon 6 and Glass Fiber Reinforced (GFR) Nylon 6 Composite. Procedia Technology, p. 1129–1136 (2016).

[Kwa14] Kwabena Gyimah, G.; Huang, P.; Chen, D.: Dry Sliding Wear Studies of Copper-Based Powder Metallurgy Brake Materials. Journal of Tribology. Issue: 4 (2014).

[Lam06] Lam, R. C.; Chavdar, B.; Newcomb, T.: New Generation Friction Materials and Technologies. SAE 2006 World Congress & Exhibition (2006).

[Lau73] Lauster E., S. U.: Waermetechnische Berechnungen bei Lamellenkupplungen [Thermal Calculations of Multi-Plate Clutches]. VDI-Zeitschrift 115. Issue: 2 (1973).

[Lay11] Layher, M.: Einfluss der Schmierstoffadditivierung auf das Reibungsverhalten nasslaufender Reibschaltelemente [Influence of Lubricant Additivation on the Friction Behavior of Wet-Running Frictional Shifting Elements], Ph. D. Thesis, Technical University of Munich (2011).

[Leb76] Lebeck, A. O.: Theory of Thermoelastic Instability of Rotating Rings in Sliding Contact With Wear. Journal of Lubrication Technology. Issue: 2, p. 277–284 (1976).

[Lee06] Lee, H. G.; Hwang, H. Y.; Lee, D. G.: Effect of wear debris on the tribological characteristics of carbon fiber epoxy composites. Wear. Issue: 3-4, p. 453–459 (2006).

[Lee01] Lee, J. H.; Xu, G. H.; Liang, H.: Experimental and numerical analysis of friction and wear behavior of polycarbonate. Wear. Issue: 1-12, p. 1541–1556 (2001).

[Lee93] Lee, K.; Barber, J. R.: Frictionally Excited Thermoelastic Instability in Automotive Disk Brakes. Journal of Tribology. Issue: 4, p. 607–614 (1993).

[Lef13] Lefevre, J.; Hayrynen, K. L.: Austempered Materials for Powertrain Applications. Journal of Materials Engineering and Performance. Issue: 7, p. 1914–1922 (2013).

[Leh18] Lehua, Q.; Pan, G.; Fu, Y.; Zhang, X.; Hou, X.; Li, H.: Effect of MoS 2 on the tribological properties of carbon fabric composites under wet conditions. Proceedings of the Institution of Mechanical Engineers, Part J: Journal of Engineering Tribology. Issue: 2, p. 126–135 (2018).

[Ler19] Lertwassana, W.; Parnklang, T.; Mora, P.; Jubsilp, C.; Rimdusit, S.: High performance aramid pulp/carbon fiber-reinforced polybenzoxazine composites as friction materials. Composites Part B: Engineering (2019).

[Li08] Li, J.; Barber, J. R.: Solution of transient thermoelastic contact problems by the fast speed expansion method. Wear. Issue: 3-4, p. 402–410 (2008).

[Li17a] Li, M.; Khonsari, M. M.; McCarthy, D. M.; Lundin, J.: Parametric analysis of wear factors of a wet clutch friction material with different groove patterns. Proceedings of the Institution of Mechanical Engineers, Part J: Journal of Engineering Tribology. Issue: 8, p. 1056–1067 (2017).

[Li17b] Li, M.; Ma, B.; Li, H.; Li, H.; Yu, L.: Analysis of the thermal buckling of annular disks in clutches under the condition of radial temperature gradient. Journal of Thermal Stresses. Issue: 10, p. 1275–1284 (2017).

[Lia18] Liang, L.; Liu, M.; Martin, C.; Sun, W.: A deep learning approach to estimate stress distribution: a fast and accurate surrogate of finite-element analysis. Journal of the Royal Society, Interface. Issue: 138 (2018).

[Lie93] Liew, K. M.; Wang, C. M.: pb-2 Rayleigh - Ritz method for general plate analysis. Engineering Structures. Issue: 1, p. 55–60 (1993).

[Lin18] Lin, L.; Schlarb, A. K.: The roles of rigid particles on the friction and wear behavior of short carbon fiber reinforced PBT hybrid materials in the absence of solid lubricants. Tribology International, p. 404–410 (2018).

[Lin12] Lingesten, N.: Wear behavior of wet clutches. Ph. D. Thesis, Lulea University of Technology (2012).

[Liu12] Liu, P.; Huang, T.; Lu, R.; Li, T.: Tribological properties of modified carbon fabric/polytetrafluoroethylene composites. Wear, p. 17–25 (2012).

[Liu21] Liu, Y.; Chen, M.; Yu, L.; Wang, L.; Feng, Y.: Influence of Material Parameters on the Contact Pressure Characteristics of a Multi-Disc Clutch. Materials (Basel, Switzerland). Issue: 21 (2021).

[Loh16] Lohner, T.: Berechnung von TEHD Kontakten und Einlaufverhalten von Verzahnungen [Calculation of TEHD Contacts and Run-in Behavior of Gears], Ph. D. Thesis, Technical University of Munich (2016).

[Luo16a] Luo, W.; Liu, Q.; Li, Y.; Zhou, S.; Zou, H.; Liang, M.: Enhanced mechanical and tribological properties in polyphenylene sulfide/polytetrafluoroethylene composites reinforced by short carbon fiber. Composites Part B: Engineering, p. 579–588 (2016).

[Luo16b] Luo, W.; Liu, Q.; Li, Y.; Zhou, S.; Zou, H.; Liang, M.: Enhanced mechanical and tribological properties in polyphenylene sulfide/polytetrafluoroethylene composites reinforced by short carbon fiber. Composites Part B: Engineering, p. 579–588 (2016).

[Ma04] Ma, C.: Thermal buckling of automotive brake discs, Ph. D. Thesis, University of Michigan (2004).

[Mac02] Mackin, T. J.; Noe, S. C.; Ball, K. J.; Bedell, B. C.; Bim-Merle, D. P.; Bingaman, M. C.; Bomleny, D. M.; Chemlir, G. J.; Clayton, D. B.; Evans, H. A.; Gau, R.; Hart, J. L.; Karney, J. S.; Kiple, B. P.; Kaluga, R. C.; Kung, P.; Law, A. K.; Lim, D.; Merema, R. C.; Miller, B. M.; Miller, T. R.; Nielson, T. J.; O'Shea, T. M.; Olson, M. T.; Padilla, H. A.; Penner, B. W.; Penny, C.; Peterson, R. P.; Polidoro, V. C.; Raghu, A.; Resor, B. R.; Robinson, B. J.; Schambach, D.; Snyder, B. D.; Tom, E.; Tschantz, R. R.; Walker, B. M.; Wasielewski, K. E.; Webb, T. R.; Wise, S. A.; Yang, R. S.; Zimmerman, R. S.: Thermal cracking in disc brakes. Engineering Failure Analysis. Issue: 1, p. 63–76 (2002).

[Mad19] Madani, A.; Bakhaty, A.; Kim, J.; Mubarak, Y.; Mofrad, M. R. K.: Bridging Finite Element and Machine Learning Modeling: Stress Prediction of Arterial Walls in Atherosclerosis. Journal of biomechanical engineering. Issue: 8 (2019).

[Mad96] Madhusudana, C. V.; Madhusudana, C. V.: Thermal contact conductance. Springer, Berlin, Heidelberg (1996).

[Mae03] Maeda, M.; Murakami, Y.: Testing Method and Effect of ATF Performance on Degradation of Wet Friction Materials. 2003 JSAE/SAE International Spring Fuels and Lubricants Meeting (2003).

[Mae05] Maeki, R.: Wet Clutch Tribology - Friction Characteristics in Limited Slip Differentials, Ph. D. Thesis, Lulea University of Technology (2005).

[Mar07] Marklund, P.; Maeki, R.; Larsson, R.; Hoeglund, E.; Khonsari, M. M.; Jang, J.: Thermal influence on torque transfer of wet clutches in limited slip differential applications. Tribology International. Issue: 5, p. 876–884 (2007).

[Mar09] Marklund, P.; Sahlin, F.; Larsson, R.: Modelling and simulation of thermal effects in wet clutches operating under boundary lubrication conditions. Journal of Engineering Tribology. Issue: 223, p. 1129–1141 (2009).

[Mat93] Matsumoto, T.: A Study of the Influence of Porosity and Resiliency of a Paper-Based Friction Material on the Friction Characteristics and Heat Resistance of the Material. SAE Technical Paper Nr. 932924 (1993).

[Mat95] Matsumoto, T.: A Study of the Durability of a Paper-Based Friction Material influenced by Porosity. Journal of Tribology. Issue: 117, p. 272–278 (1995).

[Mat97a] Matsumoto, T.: Influence of Paper-Based Friction Material Visco-Elasticity on the Performance of a Wet Clutch. SAE International Congress and Exposition (1997).

[Mat97b] Matsuo, K.; Saeki, S.: Study on the Change of Friction Characteristics with Use in the Wet Clutch of Automatic Transmission. International Fuels & Lubricants Meeting & Exposition (1997).

[Mei16] Meingassner, G. J.; Pflaum, H.; Stahl, K.: Drehmomentuebertragungsverhalten nasslaufender Lamellenkupplungen bei geringen Differenzdrehzahlen [Torque Transmission Behavior of Wet-Running Multi-Plate Clutches at Low Differential Speeds]. 4. Tribologie- und Schmierstoffkongress GETLUB, p. 71–83 (2016).

[Mei15] Meingassner, G. J.; Pflaum, H.; Stahl, K.: Test-Rig Based Evaluation of Performance Data of Wet Disk Clutches. 14th International CTI Symposium (2015).

[Mer05] Mergler, Y. J.; van Kampen, R. J.; Nauta, W. J.; Schaake, R. P.; Raas, B.; van Griensven, J.; Meesters, C.: Influence of yield strength and toughness on friction and wear of polycarbonate. Wear. Issue: 5-6, p. 915–923 (2005).

[Mey84] Meyer, K.: Schichtbildungsprozesse und Wirkungsmechanismus schichtbildender Additive fuer Schmierstoffe [Layer Formation Processes and Mechanism of Action of Layer-Forming Additives for Lubricants]. Zeitschrift fuer Chemie. Issue: 12 (1984).

[Mik74] Mikić, B. B.: Thermal contact conductance; theoretical considerations. International Journal of Heat and Mass Transfer. Issue: 2, p. 205–214 (1974).

[Mil23] Mileti, M.: Performance Optimisation of a Coupled Cone and Dog Clutch for Automotive Application, Ph. D., Technical University of Munich (2023).

[Mil18] Mileti, M.; Pflaum, H.; Stahl, K.: TorqueLINE Cone Clutch: Thermo-Mechanical Stability of Cone Clutches for ATs. Dritev. International VDI Congress Dritev - Drivetrain for Vehicles, EDrive, Transmissions in Mobile Machines: June 27 and 28, 2018, Bonn, Duesseldorf (2018).

[Mor10] Mortier, R. M.; Fox, M. F.; Orszulik, S. T.: Chemistry and Technology of Lubricants. Springer Netherlands, Dordrecht (2010).

[Mur12] Murphy, K. P.: Machine learning - A probabilistic perspective. MIT Press, Cambridge, Mass. (2012).

[Nag14] Nagaraj, S.; Zhao, S.; Dharani, L. R.; Hilmas, G. E.; Wei, J.: Effect of Oxidation on Wear in C/C Aircraft Disk Brakes. International Review of Aerospace Engineering (IREASE). Issue: 1, p. 34 (2014).

[Nak97] Nakagawa, H.: The Influence of Fillers on Paper-Based Friction Materials Relative to Wet Clutch Slip Characteristics. SAE International Congress and Exposition (1997).

[Nak17] Nakamura, K.; Kanno, H.; Ishii, S.: Wear properties of carbon composite reinforced by vapor-grown carbon fibers treated with nitric acid and aqueous hydrogen peroxide. Materials Letters, p. 228–230 (2017).

[Nar93] Narisaw, I.: High-Speed Tribology of Polymer Composites. Advances in Composite Tribology (1993).

[Nau19] Naunheimer, H.; Bertsche, B.; Ryborz, J.: Fahrzeuggetriebe - Grundlagen, Auswahl, Auslegung und Konstruktion [Vehicle Transmissions - Fundamentals, Selection, Design and Construction], Issue: 3 (2019).

[Neu08] Neudoerfer, S.: Thermomechanische Einfluesse auf die Tribologie von Synchronisierungen [Thermomechanical Influences on the Tribology of Synchronizers], Ph. D. Thesis, Leibniz University of Hannover (2008).

[Neu01] Neumueller, M.: Einfluss der Oelalterung auf Reibungs- und Verschleissverhalten von Synchronisierungen [Influence of Oil Aging on the Friction and Wear Behavior of Synchronizers], Ph. D. Thesis, Technical University of Munich (2001).

[New06] Newcomb, T.; Sparrow, M.; Ciupak, B.: Glaze Analysis of Friction Plates. Powertrain & Fluid Systems Conference and Exhibition (2006).

[Nic95] Nicholson, G.: Facts about friction: a friction material manual almost all you need to know about manufacturing; 100 years of brake linings & clutch facings. P & W Price Enterprises, Incorporated (1995).

[Nie83] Niemann, G.: Maschinenelemente - Band 3: Schraubrad-, Kegelrad-, Schnecken-Ketten-, Riemen-, Reibradgetriebe, Kupplungen, Bremsen, Freilaeufe [Machine Elements - Volume 3: Helical, bevel, worm, chain, belt, friction gears, clutches, brakes, freewheels]. Springer, Berlin, Heidelberg, Issue: 2 (1983).

[Nie19] Niemann, G.; Winter, H.; Hoehn, B.-R.; Stahl, K.: Maschinenelemente 1 - Konstruktion und Berechnung von Verbindungen, Lagern, Wellen [Machine Elements 1 - Design and Calculation of Joints, Bearings, Shafts]. Springer, Berlin, Heidelberg (2019).

[Nym06] Nyman, P.; Maeki, R.; Olsson, R.; Ganemi, B.: Influence of surface topography on friction characteristics in wet clutch applications. Wear. Issue: 1, p. 46–52 (2006).

[Old06] Oldfield, R. C.; Watts, R. F.: Impact of lubricant formulation on the friction properties of carbon fiber clutch plates. Lubrication Science. Issue: 18, p. 37–48 (2006).

[Omp10] Ompusunggu, A.; Janssens, T.; Al-Bender, F.; Sas, P.; Brussel, H.; Vandenplas, S.: Contact Stiffness Characteristics of a Paper-Based Wet Clutch at Different Degradation Levels. 17th International Colloquium Tribology 2010 - Solving Friction and Wear Problems (2010).

[Omp13] Ompusunggu, A. P.; Papy, J.-M.; Vandenplas, S.; Sas, P.; van Brussel, H.: A novel monitoring method of wet friction clutches based on the post-lockup torsional vibration signal. Mechanical Systems and Signal Processing. Issue: 1-2, p. 345–368 (2013).

[Omp15] Ompusunggu, A. P.; Sas, P.; van Brussel, H.: Distinguishing the effects of adhesive wear and thermal degradation on the tribological characteristics of paper-based friction materials under dry environment: A theoretical study. Tribology International. Issue: 84, p. 9–21 (2015).

[Omr15] Omrani, E.; Barari, B.; Dorri Moghadam, A.; Rohatgi, P. K.; Pillai, K. M.: Mechanical and tribological properties of self-lubricating bio-based carbon-fabric epoxy composites made using liquid composite molding. Tribology International, p. 222–232 (2015).

[Ort04] Ortlinghaus-Werke GmbH: Technische Grundlagen [Technical Fundamentals] (2004).

[Osa90] Osanai, H.; Ikeda, K.; Kato, K.: Relations Between Temperature in Friction Surface and Degradation of Friction Materials During Engaging of Wet Friction Paper. International Congress & Exposition (1990).

[Ost01] Ost, W.; Baets, P. de; Degrieck, J.: The tribological behaviour of paper friction plates for wet clutch application investigated on SAE#II and pin-on-disk test rigs. Wear. Issue: 249, p. 361–371 (2001).

[Ost13] Ostermeyer, G.-P.; Graf, M.: Influence of wear on thermoelastic instabilities in automotive brakes. Wear. Issue: 1-2, p. 113–120 (2013).

[Pac90] Pacey, D. A.; Turnquist, R. O.: Modeling heat transfer in a wet clutch. SAE Technical Papers (1990).

[Pan04] Panier, S.; Dufrénoy, P.; Brunel, J. F.; Weichert, D.: Progressive Waviness Distortion: A New Approach of Hot Spotting in Disc Brakes. Journal of Thermal Stresses. Issue: 1, p. 47–62 (2004).

[Pay91] Payvar, P.: Laminar heat transfer in the oil groove of a wet clutch. International Journal of Heat and Mass Transfer. Issue: 7, p. 1791–1798 (1991).

[Ped12] Pedregosa, F.; Varoquaux, G.; Gramfort, A.; Michel, V.; Thirion, B.; Grisel, O.; Blondel, M.; Mueller, A.; Nothman, J.; Louppe, G.; Prettenhofer, P.; Weiss, R.; Dubourg, V.; Vanderplas, J.; Passos, A.; Cournapeau, D.; Brucher, M.; Perrot, M.; Duchesnay, É.: Scikit-learn: Machine Learning in Python (2012).

[Pfl88] Pflaum, H.: Das Reibungsverhalten oelgeschmierter Kegelreibkupplungen in Synchronisationseinrichtungen von Kraftfahrzeug-Schaltgetrieben [The Friction Behavior of Oil-Lubricated Cone Friction Clutches in Synchronization Devices of Automotive Manual Transmissions], Ph. D. Thesis, Technical University of Munich (1988).

[Pfl98] Pfleger, F.: Schalt- und Lebensdauerverhalten von Lamellenkupplungen [Shifting and Service Life Behavior of Multi-Plate Clutches], Ph. D. Thesis, Technical University of Munich (1998).

[Pit97] Pittman, C. U.; He, G.-R.; Wu, B.; Gardner, S. D.: Chemical modification of carbon fiber surfaces by nitric acid oxidation followed by reaction with tetraethylenepentamine. Carbon. Issue: 3, p. 317–331 (1997).

[Ran04] Rank, R.; Kearsey, A.: Carbon Based friction materials for automotive applications. 14th International Colloquium Tribology, Stuttgart/Ostfildern (2004).

[Rao11] Rao, G.: Modellierung und Simulation des Systemverhaltens nasslaufender Lamellenkupplungen [Modeling and Simulation of the System Behavior of Wet-Running Multi-Plate Clutches], Ph. D. Thesis, Technical University of Dresden (2011).

[Rao89] Rao, V. T. V. S. R.; Ramasubramanian, H.; Seetharamu, K. N.: Analysis of temperature field in brake disc for fade assessment. Waerme- und Stoffuebertragung. Issue: 1, p. 9–17 (1989).

[Rod60] Rodgers, J. J.; Haviland, M. L.: Friction of transmission clutch materials as affected by fluids, additives, and oxidation. SAE Technical Paper Series (1960).

[Sab19] Sabri, L. A.; Schlattmann, J.; Abdullah, O. I.; Beliardouh, N. E.; Assenova, E.: Three-dimensional simulation of the thermal problem in friction clutches using finite element technique. Proceedings on Engineering Sciences. Issue: 1, p. 309–315 (2019).

[Sab21a] Sabri, L. A.; Stojanović, N.; Senatore, A.; Jweeg, M. J.; Abed, A. M.; Abdullah, O. I.: Three-Dimensional Finite Element Analysis of Contact Problem in Dry Friction Clutches. Lubricants. Issue: 12, p. 115 (2021).

[Sab21b] Sabri, L. A.; Topczewska, K.; Jweeg, M. J.; Abdullah, O. I.; Abed, A. M.: Analytical and Numerical Solutions for the Thermal Problem in a Friction Clutch System. Computation. Issue: 11, p. 122 (2021).

[Sak93] Sakai, N.; Honda, F.; Nakajima, K.: Friction characteristics of wet paper clutch for automotive torque transmissions. Lubrication Engineering. Issue: 2, p. 97–101 (1993).

[Sat06] Satapathy, B. K.; Bijwe, J.: Composite friction materials based on organic fibres: Sensitivity of friction and wear to operating variables. Composites Part A: Applied Science and Manufacturing. Issue: 10, p. 1557–1567 (2006).

[Sch06] Schenkenberger, C.; Schiferl, E.; Garling, G.; Baker, M.; Huston, M. E.; Parham, D.; Prengaman, C.; Rhoads, G.; Vermilya, D.: Next Generation Torque Control Fluid Technology, Part II: Split-Mu Screening Test Development. Powertrain & Fluid Systems Conference and Exhibition (2006).

[Sch21a] Schmid, A.: Experimentelle Untersuchungen zum Spontanschaedigungsverhalten von nasslaufenden Lamellenkupplungen [Experimental studies on spontaneous damage behaviour of wet-running multiple disk clutches], Master Thesis, Technical University of Munich (2021).

[Sch21b] Schneider, T.; Bedrikow, A. B.; Voelkel, K.; Pflaum, H.; Stahl, K.: Comparison of Various Wet-Running Multi-Plate Clutches with Paper Friction Lining with Regard to Spontaneous Damage Behavior. Tribology in Industry. Issue: 1, p. 40–56 (2021).

[Sch20a] Schneider, T.; Pflaum, H.; Stahl, K.: Anwendungsorientierte Erweiterung der Erkenntnisse zu Spontanschaedigung nasslaufender Lamellenkupplungen und Erweiterung der Rechenmethodik [Application-Oriented Extension of Findings on Spontaneous Damage in Wet-Running Clutch Plates and Expansion of Computational Methodology] - Research Project No. 515 V. Forschungsvereinigung Antriebstechnik e.V., Frankfurt/Main, Issue: 1361 (2020).

[Sch19] Schneider, T.; Strebel, M.; Pflaum, H.; Stahl, K.: Spontaneous damage to wet-running multi-plate clutches with organic and metallic friction linings [Spontanschaedigungsverhalten von nasslaufenden Lamellenkupplungen mit organischen und metallischen Reibbelaegen]. Forschung im Ingenieurwesen/Engineering Research. Issue: 2, p. 199–207 (2019).

[Sch22a] Schneider, T.; Bedrikow, A. B.; Dietsch, M.; Voelkel, K.; Pflaum, H.; Stahl, K.: Machine Learning Based Surrogate Models for the Thermal Behavior of Multi-Plate Clutches. Applied System Innovation. Issue: 5, p. 97 (2022).

[Sch22b] Schneider, T.; Bedrikow, A. B.; Voelkel, K.; Pflaum, H.; Stahl, K.: Load Capacity Comparison of Different Wet Multi-Plate Clutches with Sinter Friction Lining with Regard to Spontaneous Damage Behavior. Tribology in Industry. Issue: 3, p. 394–406 (2022).

[Sch22c] Schneider, T.; Dietsch, M.; Voelkel, K.; Pflaum, H.; Stahl, K.: Analysis of the Thermo-Mechanical Behavior of a Multi-Plate Clutch during Transient Operating Conditions Using the FE Method. Lubricants. Issue: 5, p. 76 (2022).

[Sch20b] Schneider, T.; Voelkel, K.; Pflaum, H.; Stahl, K.: Friction Behavior of Pre-Damaged Wet-Running Multi-Plate Clutches in an Endurance Test. Lubricants. Issue: 7, p. 68 (2020).

[Sch21c] Schneider, T.; Voelkel, K.; Pflaum, H.; Stahl, K.: Einfluss von Vorschaedigung auf das Reibungsverhalten nasslaufender Lamellenkupplungen im Dauerschaltbetrieb [Influence of Pre-damage on the Friction Behaviour of Wet-

running Multi-plate Clutches in an Endurance Test]. Forschung im Ingenieurwesen/Engineering Research. Issue: 4, p. 859–870 (2021).

[Sch22d] Schneider, T.; Zilkens, A.; Voelkel, K.; Pflaum, H.; Stahl, K.: Failure Modes of Spontaneous Damage of Wet-Running Multi-Plate Clutches with Carbon Friction Linings. Tribology Transactions, p. 1–14 (2022).

[Sci07a] Scieszka, S.; Zolnierz, M.: The Effect of the Mine Winder Disc Brake's Design Feature on Its Thermoelastic Instability. Part I. Set-Up for Finite Element Modelling and Numerical Model Verification. Prob. Mach. Oper. Maintenance. Issue: vol. 42, p. 111–124 (2007).

[Sci07b] Scieszka, S.; Zolnierz, M.: The Effect of the Mine Winder Disc Brake's Design Feature on Its Thermoelastic Instability. Part II. Finite Element Simulation. Prob. Mach. Oper. Maintenance. Issue: vol. 42, p. 183–193 (2007).

[Sha11] Sharma, M.; Bijwe, J.; Mitschang, P.: Wear performance of PEEK–carbon fabric composites with strengthened fiber–matrix interface. Wear. Issue: 9-10, p. 2261–2268 (2011).

[Sit07] Sittig, K.: Tribologisch induzierte oberflaechennahe Veraenderungen der Stahl- und Belaglamellen einer nasslaufenden Lamellenkupplung [Tribologically Induced Near-Surface Changes in the Steel and Friction Plates of a Wet-Running Multi-Plate Clutch], Ph. D. Thesis, University of Karlsruhe (2007).

[Sku11] Skubacz, T.; Poll, G.: Entwicklung eines verallgemeinerbaren Modells zur Verschleißvorhersage von Synchronisierungen Teil III [Development of a Generalizable Model for Predicting Wear in Synchronizers Part III] - Research Project No. 403/III. Forschungsvereinigung Antriebstechnik e.V., Frankfurt/Main (2011).

[Sni06] Snima, K.: Kenngroessen und Belastungsgrenzen von nasslaufenden Lamellenkupplungen unter Dauerschlupfbeanspruchung [Characteristics and Load Limits of Wet-Running Multi-Plate Clutches under Continuous Slip Stress], Ph. D. Thesis, University of Karlsruhe (2006).

[Sow13] Sowjanya, K.; Suresh, S.: Structural Analysis of Disc Brake Rotor. International Journal of Computer Trends and Technology. Issue: 4 (2013).

[Ste62] Steinhilper, W.: Der zeitliche Temperaturverlauf in Reibungsbremsen und Reibungskupplungen beim Schaltvorgang [The Temperature Curve Over Time in Friction Brakes and Friction Clutches during the Shifting Process], University of Karlsruhe (1962).

[Sto21] Stockinger, U.; Groetsch, D.; Reiner, F.; Voelkel, K.; Pflaum, H.; Stahl, K.: Friction behavior of innovative carbon friction linings for wet multi-plate clutches. Forschung im Ingenieurwesen/Engineering Research, p. 471 (2021).

[Sto23] Stockinger, U.: Untersuchung der Leistungsfaehigkeit von Einfach- und Mehrfachkonus-Synchronisierungen [Investigation of the Performance of Single and Multiple Cone Synchronizers], Ph. D. Thesis, Technical University of Munich (2023).

[Sto17] Stockinger, U.; Pflaum, H.; Stahl, K.: Schmierstoffeinfluss auf das Reibungsverhalten mit Carbon- und Sinterreibbelaegen in Lamellenkupplungen; Entwicklung eines erweiterten Reibungszahl-Kurztests [Lubricant Influence on Friction Behavior with Carbon and Sintered Friction Linings in Multi-Plate Clutches; Development of an Extended Coefficient of Friction Short Test] - Research Project No. 490 VII. Forschungsvereinigung Antriebstechnik e.V., Frankfurt/Main, Issue: 1220 (2017).

[Str17] Strebel, M.: Spontanschaeden an nasslaufenden Lamellenkupplungen [Spontaneous Damage in Wet-Running Multi-Plate Clutches], Ph. D. Thesis, Technical University of Munich (2017).

[Str16] Strebel, M.; Pflaum, H.; Stahl, K.: Einfluesse auf die Spontanschaedigung von nasslaufenden Lamellenkupplungen mit organischen Reibbelaegen [Influences on Spontaneous Damage of Wet-Running Multi-Plate Clutches with Organic Friction Linings]. GETLUB - Tribologie- und Schmierstoffkongress, Wuerzburg. FVA (2016).

[Str02] Stribeck, B.: Die wesentlichen Eigenschaften der Gleit- und Rollenlager [Essential Characteristics of Sliding and Rolling Bearings]. Springer, Berlin (1902).

[Su06a] Su, F.; Zhang, Z.; Liu, W.: Mechanical and tribological properties of carbon fabric composites filled with several nano-particulates. Wear. Issue: 7-8, p. 861–868 (2006).

[Su06b] Su, F.; Zhang, Z.; Wang, K.; Jiang, W.; Men, X.; Liu, W.: Friction and wear properties of carbon fabric composites filled with nano-Al2O3 and nano-Si3N4. Composites Part A: Applied Science and Manufacturing. Issue: 9, p. 1351–1357 (2006).

[Sur10] Suresha, B.; Ramesh, B. N.; Subbaya, K. M.; Ravi Kumar, B. N.; Chandramohan, G.: Influence of graphite filler on two-body abrasive wear behaviour of carbon fabric reinforced epoxy composites. Materials & Design. Issue: 4, p. 1833–1841 (2010).

[Sza06] Szappanos, G.; Bartley, S.; Schiferl, E.; Huston, M. E.; Akucewich, E.; Baker, M.; Gentile, M.; Mount, J.; Rhoads, G.; Vermilya, D.; Whitticar, D.: Next Generation Torque Control Fluid Technology, Part I: Break-Away Friction Screening Test Development. Powertrain & Fluid Systems Conference and Exhibition (2006).

[Tar16] Tariq, A.; Asif, M.: Experimental investigation of thermal contact conductance for nominally flat metallic contact. Heat and Mass Transfer/Waerme- und Stoffuebertragung. Issue: 2, p. 291–307 (2016).

[Tat02] Tatara, R. A.; Payvar, P.: Multiple Engagement Wet Clutch Heat Transfer Model. Numerical Heat Transfer, Part A: Applications. Issue: 3, p. 215–231 (2002).

[Tim12] Timoshenko, S. P.; Gere, J. M.: Theory of elastic stability. Dover Publications, Newburyport, Second edition (2012).

[Tom09] Tomic, D.: Zum Verschleiss von Kegelreibkupplungen – Einfluesse von Belastung und Schmierstoff auf Reibschichteigenschaften [On the Wear of Cone

Friction Clutches – Influences of Load and Lubricant on Friction Layer Properties], Ph. D. Thesis, Technical University of Munich (2009).

[Ues16] Uestuen, T.; Ulus, H.; Karabulut, S. E.; Eskizeybek, V.; Şahin, O. S.; Avcı, A.; Demir, O.: Evaluating the effectiveness of nanofillers in filament wound carbon/epoxy multiscale composite pipes. Composites Part B: Engineering, p. 1–6 (2016).

[Ver12] Vernersson, T., Lundén, R., Abbasi, S., Olofsson, U.: Wear of railway brake block materials at elevated temperatures – pin-on-disc experiments. EuroBrake Conference Proceedings (2012).

[Voe20a] Voelkel, K.: Charakterisierung des Einlaufverhaltens nasslaufender Lamellenkupplungen [Characterization of the Running-in Behavior of Wet-running Multi-plate Clutches], Ph. D. Thesis, Technical University of Munich (2020).

[Voe21] Voelkel, K.; Meingassner, G. J.; Pflaum, H.; Stahl, K.: Reibungsverhalten nasslaufender Lamellenkupplungen am Uebergang Haftreibung – Gleitreibung [Friction behavior of wet multi-plate disk clutches at the transition from static to dynamic friction]. Forschung im Ingenieurwesen/Engineering Research (2021).

[Voe16] Voelkel, K.; Pflaum, H.; Stahl, K.: Erweiterung der Simulationsmethodik zur Berechnung des instationaeren Temperaturverhaltens nasslaufender Lamellenkupplungen [Extension of the Simulation Methodology for Calculating the Unsteady Temperature Behavior of Wet-running Multi-plate Clutches] - Research Project No. 150/VII. Forschungsvereinigung Antriebstechnik e.V., Frankfurt/Main, Issue: 1204 (2016).

[Voe20b] Voelkel, K.; Pflaum, H.; Stahl, K.: Einfluesse des Reibsystems auf das Einlaufverhalten von Lamellenkupplungen [Influences of the Friction System on the Running-In Behavior of Multi-plate Clutches] - Research Project No. 343 IV. Forschungsvereinigung Antriebstechnik e.V., Frankfurt/Main, Issue: 1390 (2020).

[Voe18] Voelkel, K.; Wohlleber, F.; Pflaum, H.; Stahl, K.: Kuehlverhalten nasslaufender Lamellenkupplungen in neuen Anwendungen [Cooling performance of wet multi-plate disk clutches in modern applications]. Forschung im Ingenieurwesen. Issue: 82, p. 197–203 (2018).

[Wag93] Wagner, D.: Neue Reibmaterialien und Konzepte fuer Einfach- und Mehrfachsynchronisierungen [New Friction Materials and Concepts for Single and Multiple Synchronizers]. ATZ Automobiltechnische Zeitschrift. Issue: 95, p. 380–387 (1993).

[Wan19a] Wang, B.; Fu, Q.; Li, H.; Qi, L.; Lu, Y.: Synergistic effect of surface modification of carbon fabrics and multiwall carbon nanotube incorporation for improving tribological properties of carbon fabrics/resin compositestribological properties of carbon fabrics/resin composites. Polymer Composites. Issue: 1, p. 102–111 (2019).

[Wan18] Wang, B.; Fu, Q.; Yin, T.; Li, H.; Qi, L.; Fu, Y.: Grafting CNTs on carbon fabrics with enhanced mechanical and thermal properties for tribological applications of carbon fabrics/phenolic composites. Carbon, p. 45–51 (2018).

[Wan10] Wang, Q.; Zhang, X.; Pei, X.; Wang, T.: Friction and wear properties of solid lubricants filled/carbon fabric reinforced phenolic composites. Journal of Applied Polymer Science. Issue: 4, p. 2480–2485 (2010).

[Wan19b] Wang, Q.; Cui, H.; Lian, Z.; Li, L.: Thermal behavior of double arc groove friction pairs in hydro-viscous drive under soft start-up condition. Thermal Science. Issue: 23, p. 835–847 (2019).

[Wan22] Wang, Q.; Wang, J.; Cui, H.; Wang, J.; Zhang, F.: Numerical investigation into thermal buckling of friction pairs in hydro-viscous drive under nonlinear radial temperature distribution. Proceedings of the Institution of Mechanical Engineers, Part J: Journal of Engineering Tribology. Issue: 6, p. 1081–1090 (2022).

[Wan15] Wang, W.; Huang, J.-F.; Li, W.; Jin, Y.; Wei, F.: The influence of added carbon nanotubes on the properties of the carbon-fiber-reinforced paper-based wet clutch friction materials. Lubrication Science. Issue: 7, p. 451–461 (2015).

[Wan21] Wang, Z.; Zhang, J.: Thermomechanical Coupling Simulation and Analysis of Wet Multi-Disc Brakes During Emergency Braking. Journal of Physics: Conference Series. Issue: 1, p. 12005 (2021).

[Web15] Weber, N.; Poll, G.: Analyse der Bauteilbewegungen und Verschleißuntersuchungen an Synchronisierungen im nicht geschalteten Zustand [Analysis of Component Movements and Wear Studies on Synchronizers in the Non-Engaged State] - Research Project No. 672/I. Forschungsvereinigung Antriebstechnik e.V., Frankfurt/Main, Issue: 1165 (2015).

[Wen15] Wenbin, L.; Jianfeng, H.; Jie, F.; Liyun, C.; Chunyan, Y.: Mechanical and wet tribological properties of carbon fabric/phenolic composites with different weave filaments counts. Applied Surface Science, p. 1223–1233 (2015).

[Wen16a] Wenbin, L.; Jianfeng, H.; Jie, F.; Liyun, C.; Chunyan, Y.: Simulation and application of temperature field of carbon fabric wet clutch during engagement based on finite element analysis. International Communications in Heat and Mass Transfer, p. 180–187 (2016).

[Wen16b] Wenbin, L.; Jianfeng, H.; Jie, F.; Zhenhai, L.; Liyun, C.; Chunyan, Y.: A novel preparation approach for improving the mechanical and wet tribological properties of carbon fabric/phenolic composites. Materials and Design, p. 356–364 (2016).

[Wen16c] Wenbin, L.; Jianfeng, H.; Jie, F.; Zhenhai, L.; Liyun, C.; Chunyan, Y.: Effect of aramid pulp on improving mechanical and wet tribological properties of carbon fabric/phenolic composites. Tribology International. Issue: 104, p. 237–246 (2016).

[Wes68] Weston, T. A.: On an Improved Friction Coupling and Break, and its Application to Hoists, Windlasses, and Shafting, &C. Proceedings of the Institution of Mechanical Engineers. Issue: 1, p. 214–237 (1868).

[Whi10] Whitticar, D.; Basu, S.; Greene, G.; Henley, M.; Parham, D.; Prengaman, C.; Schiferl, E.; Baker, M.; Bartley, S.; Huston, M. E.: Next Generation Torque Control Fluid Technology, Part IV: Using a New Split-μ Simulation Test for

Optimizing Friction Material-Lubricant Hardware Systems. SAE 2010 Powertrains Fuels & Lubricants Meeting (2010).

[Wil21] Willand, F.-G.: Experimentelle Untersuchungen zum Schaedigungsverhalten von nasslaufenen Lamellenkupplungen [Experimental investigations on den damage behaivour of wet running multi-plate clutches], Master Thesis, Technical University of Munich (2021).

[Wim05] Wimmer, T.; Pflaum, H.; Stahl, K.: Untersuchung der Einfluesse der Lastfolge auf das Betriebsverhalten von nasslaufenden Lamellenkupplungen [Investigation of the Influence of Load Sequence on the Operating Behavior of Wet-Running Multi-Plate Clutches] - Research Project No. 413 I. Forschungsvereinigung Antriebstechnik e.V., Frankfurt/Main, Issue: 754 (2005).

[Win85] Winkelmann, S.; Harmuth, H.: Schaltbare Reibkupplungen - Grundlagen, Eigenschaften, Konstruktionen [Shiftable Friction Clutches - Fundamentals, Properties, Designs]. Springer, Berlin (1985).

[Win08] Winkler, J.: Tribologischer Schichtaufbau bei Synchronisierungen und sein Einfluss auf Reibung und Verschleiß [Tribological Layer Formation in Synchronizers and its Impact on Friction and Wear], Ph. D. Thesis, Technical University of Munich (2008).

[Wit21] Wittel, H.; Spura, C.; Jannasch, D.: Roloff/Matek Maschinenelemente [Roloff/Matek Machine Elements]. Springer Vieweg, Wiesbaden, Issue: 25 (2021).

[Woh09] Wohlleber, F.; Pflaum, H.; Hoehn, B.-R.: Programmerweiterung zur thermischen Nachrechnung von Lamellenkupplungen und Integration des Programms in die FVA-Workbench [Program Extension for Thermal Post-Calculation of Multi-Plate Clutches and Integration of the Program into the FVA Workbench] - Research Project No.150 VI. Forschungsvereinigung Antriebstechnik e.V., Frankfurt/Main, Issue: 899 (2009).

[Wu20] Wu, C.-M.; Cheng, Y.-C.; Lai, W.-Y.; Chen, P.-H.; Way, T.-D.: Friction and Wear Performance of Staple Carbon Fabric-Reinforced Composites: Effects of Surface Topography. Polymers. Issue: 1 (2020).

[Wu16] Wu, S. C.; Zhang, S. Q.; Xu, Z. W.: Thermal crack growth-based fatigue life prediction due to braking for a high-speed railway brake disc. International Journal of Fatigue. Issue: 87, p. 359–369 (2016).

[Wu18] Wu, W.; Xiao, B.; Yuan, S.; Hu, C.: Temperature distributions of an open grooved disk system during engagement. Applied Thermal Engineering, p. 349–355 (2018).

[Xia20] Xiao, J.-K.; Xiao, S.-X.; Chen, J.; Zhang, C.: Wear mechanism of Cu-based brake pad for high-speed train braking at speed of 380 km/h. Tribology International (2020).

[Xio14] Xiong, C.; Li, H.; He, S.; Ma, B.; Yan, Q.; Li, H.; Xu, H.; Chen, J.: Simulation of hot spots generation process on separator disc in multi-disc clutch. 13th International Conference on Modeling and Applied Simulation, MAS 2014 (2014).

[Xio07] Xiong, X.; Chen, J.; Yao, P.; Li, S.; Huang, B.: Friction and wear behaviors and mechanisms of Fe and SiO2 in Cu-based P/M friction materials. Wear. Issue: 9-10, p. 1182–1186 (2007).

[Yag15] Yagi, S.; Katayama, N.; Hasegawa, H.; Matsushita, H.; Okihara, S.: Effects of Microscale Texture on the Tribological Behavior of Paper-Based Friction Materials for a Wet Clutch. Tribology Online. Issue: 5, p. 390–396 (2015).

[Yan22] Yang, K.; Zhang, F.; Chen, Y.; Zhang, H.; Xiong, B.; Chen, H.: Recent progress on carbon-based composites in multidimensional applications. Composites Part A: Applied Science and Manufacturing (2022).

[Yan98] Yang, Y.; Lam, R. C.: Theoretical and experimental studies on the interface phenomena during the engagement of automatic transmission clutch. Tribology Letters. Issue: 1, p. 57–67 (1998).

[Yan97] Yang, Y.; Twaddell, P. S.; Chen, Y.-F.; Lam, R. C.: Theoretical and Experimental Studies on the Thermal Degradation of Wet Friction Materials. SAE International Congress and Exposition (1997).

[Yao07] Yao, P.; Sheng, H.; Xiong, X.; Huang, B.: Worn surface characteristics of Cu-based powder metallurgy bake materials for aircraft. Transactions of Nonferrous Metals Society of China, p. 99–103 (2007).

[Yes92] Yesnik, M.; Lam, R. C.: Clutch Plate Surface Treatment for Improved Frictional Characteristics. SAE Technical Paper Nr. 922099 (1992).

[Yev10] Yevtushenko, A. A.; Grzes, P.: The FEM-Modeling of the Frictional Heating Phenomenon in the Pad/Disc Tribosystem (A Review). Numerical Heat Transfer, Part A: Applications. Issue: 3, p. 207–226 (2010).

[Yev22] Yevtushenko, A.; Grzes, P.; Ilyushenko, A.; Liashok, A.: An Effect of a Carbon-Containing Additive in the Structure of a Friction Material on Temperature of the Wet Clutch Disc. Materials. Issue: 2 (2022).

[Yi02] Yi, Y.-B.; Barber, J. R.; Hartsock, D. L.: Thermoelastic Instabilities in Automotive Disc Brakes — Finite Element Analysis and Experimental Verification. Gladwell, G. M. L.; Martins, J. A. C.; Marques, M. D. P. M. Contact Mechanics, Dordrecht (2002).

[Yi00] Yi, Y.-B.; Barber, J. R.; Zagrodzki, P.: Eigenvalue solution of thermoelastic instability problems using Fourier reduction. Proceedings of the Royal Society of London. Series A: Mathematical, Physical and Engineering Sciences. Issue: 2003, p. 2799–2821 (2000).

[Yu20] Yu, L.; Ma, B.; Chen, M.; Li, H.; Liu, J.: Investigation on the thermodynamic characteristics of the deformed separate plate in a multi-disc clutch. Engineering Failure Analysis, p. 104385 (2020).

[Yu19a] Yu, L.; Ma, B.; Chen, M.; Li, H.; Liu, J.; Li, M.: Investigation on the failure mechanism and safety mechanical-thermal boundary of a multi-disc clutch. Engineering Failure Analysis, p. 319–334 (2019).

[Yu19b] Yu, L.; Ma, B.; Chen, M.; Li, H.; Ma, C.; Liu, J.: Comparison of the Friction and Wear Characteristics between Copper and Paper Based Friction Materials. Materials. Issue: 18 (2019).

[Yu19c] Yu, L.; Ma, B.; Li, H.; Liu, J.; Li, M.: Numerical and Experimental Studies of a Wet Multidisc Clutch on Temperature and Stress Fields Excited by the Concentrated Load. Tribology Transactions. Issue: 1, p. 8–21 (2019).

[Zag85] Zagrodzki, P.: Numerical analysis of temperature fields and thermal stresses in the friction discs of a multidisc wet clutch. Wear. Issue: 3, p. 255–271 (1985).

[Zag90] Zagrodzki, P.: Analysis of thermomechanical phenomena in multidisc clutches and brakes. Wear. Issue: 2, p. 291–308 (1990).

[Zag09] Zagrodzki, P.: Thermoelastic instability in friction clutches and brakes – Transient modal analysis revealing mechanisms of excitation of unstable modes. International Journal of Solids and Structures. Issue: 11-12, p. 2463–2476 (2009).

[Zag03] Zagrodzki, P.; Truncone, S. A.: Generation of hot spots in a wet multidisk clutch during short-term engagement. Wear. Issue: 5-6, p. 474–491 (2003).

[Zha09a] Zhang, L.; Yang, Q.; Weichert, D.; Tan, N.: Simulation and Analysis of Thermal Fatigue Based on Imperfection Model of Brake Discs. PAMM. Issue: 1, p. 533–534 (2009).

[Zha09b] Zhang, X.; Pei, X.; Zhang, J.; Wang, Q.: Effects of carbon fiber surface treatment on the friction and wear behavior of 2D woven carbon fabric/phenolic composites. Colloids and Surfaces A: Physicochemical and Engineering Aspects. Issue: 1-3, p. 7–12 (2009).

[Zha05] Zhang, Z.; Su, F.; Wang, K.; Jiang, W.; Men, X.; Liu, W.: Study on the friction and wear properties of carbon fabric composites reinforced with micro- and nano-particles. Materials Science and Engineering: A. Issue: 1-2, p. 251–258 (2005).

[Zha18a] Zhao, E.; Ma, B.; Li, H.-Y.: The Tribological Characteristics of Cu-Based Friction Pairs in a Wet Multidisk Clutch Under Nonuniform Contact. Journal of Tribology. Issue: 1 (2018).

[Zha12] Zhao, H.; Neville, A.; Morina, A.; Vickerman, R.; Durham, J.: Improved anti-shudder performance of ATFs—Influence of a new friction modifier and surface chemistry. Tribology International. Issue: 1, p. 62–72 (2012).

[Zha16] Zhao, J.; Chen, Z.; Yang, H.; Yi, Y.-B.: Finite element analysis of thermal buckling in automotive clutch plates. Journal of Thermal Stresses. Issue: 1, p. 77–89 (2016).

[Zha13] Zhao, J.; Ma, B.; Li, H.; Yi, Y.: The effect of lubrication film thickness on thermoelastic instability under fluid lubricating condition. Wear. Issue: 1-2, p. 146–153 (2013).

[Zha08] Zhao, S.; Hilmas, G. E.; Dharani, L. R.: Behavior of a composite multidisk clutch subjected to mechanical and frictionally excited thermal load. Wear. Issue: 11-12, p. 1059–1068 (2008).

[Zha09c] Zhao, S.; Hilmas, G. E.; Dharani, L. R.: Numerical simulation of wear in a C/C composite multidisk clutch. Carbon. Issue: 9, p. 2219–2225 (2009).

[Zha01] Zhao, W.; Zagrodzki, P.: Study of Wet Friction Material Test Under Severe Thermal and Mechanical Loading (“Bump Test”). Wear. Issue: 1, p. 224 (2001).

[Zha18b] Zhao, Z.-K.; Du, S.-S.; Li, F.; Xiao, H.-M.; Li, Y.-Q.; Zhang, W.-G.; Hu, N.; Fu, S.-Y.: Mechanical and tribological properties of short glass fiber and short carbon fiber reinforced polyethersulfone composites: A comparative study. Composites Communications, p. 1–6 (2018).

[Zha15] Zhao, J. X., Ma, B., & Li, H. Y.: Thermoelastic stability of wet clutches during engaging process. Jilin Daxue Xuebao (Gongxueban). Issue: 45, p. 22–28 (2015).

[Zho19] Zhou, H.; Yao, P.; Xiao, Y.; Fan, K.; Zhang, Z.; Gong, T.; Zhao, L.; Deng, M.; Liu, C.; Ling, P.: Friction and wear maps of copper metal matrix composites with different iron volume content. Tribology International, p. 199–210 (2019).

[Zho09] Zhou, X. H.; Sun, Y. S.; Wang, W. S.: Influences of carbon fabric/epoxy composites fabrication process on its friction and wear properties. Journal of Materials Processing Technology. Issue: 9, p. 4553–4557 (2009).

11.3 Websites and User Manuals

[Ali22] Alicona Imaging GmbH: Alicona InfiniteFocus - Technical Specifications. URL: https://www.alicona.com/products/infinitefocus/. Last access:12.08.2022.

[Coo22] Coollaboratory: Data sheet thermal paste. URL: https://www.coollaboratory.com/product/coollaboratory-liquid-pro/. Last access:22.08.2022.

[Ifd22] Ifd Allensbach: Deutsche PKW-Fahrer nach Motorleistung des selbstgefahrenen Fahrzeugs von 2018 bis 2022 [German Car Drivers by Engine Power of the Vehicle Driven from 2018 to 2022]. URL: https://de-statista-com.eaccess.tum.edu/statistik/daten/studie/170972/umfrage/motorleistung-des-ueberwiegend-gefahrenen-pkw-in-ps/?locale=de. Last access:15.03.2023.

[Ins22] Institut fuer Fertigungstechnik (IFT): Alicona Infinite Focus G4. URL: http://www.ift.at/forschungsbereiche/fertigungsmesstechnik-und-adaptronische-systeme/form-welligkeit-rauheit/alicona-infinite-focus-g4. Last access:12.08.2022.

[Kor21] Kords, M.: Anzahl der Neuzulassungen von Personenkraftwagen im Segment SUVs in Deutschland von 2013 bis 2021 [Number of New Registrations of Passenger Cars in the SUV Segment in Germany from 2013 to 2021]. URL: https://de.statista.com/statistik/daten/studie/426828/umfrage/pkw-neuzulassungen-in-deutschland-im-segment-suvs/. Last access:04.12.2022.

[Kor22] Kords, M.: Anzahl der Elektroautos in Deutschland von 2012 bis 2022 [Number of Electric Cars in Germany from 2012 to 2022]. URL: https://de.statista.com/statistik/daten/studie/265995/umfrage/anzahl-der-elektroautos-in-deutschland/. Last access:04.12.2022.

[The22] Thermo Sensor Datenblatt: Data sheet type K thermocouple NiCr-Ni. URL: https://www.thermo-sensor.de/downloads-deutsch.html. Last access:22.08.2022.

Supervised Student Research Projects Relevant to This Thesis

The following student research projects were conducted at the Institute of Machine Elements, Gear Research Center (FZG). The processing, evaluation, interpretation, and presentation of results for these projects were completed under substantial scientific guidance from the author. Some of the results were incorporated into this work.

Tuerkarslan, U.: Thermo-Mechanische Finite-Elemente Simulation von nasslaufenden Lamellenkupplungen [Thermo-Mechanical Finite Element Simulation of Wet-Running Multi-Plate Clutches]. Semester Thesis, Gear Research Center, Technical University of Munich (2018).

Staerk, D.: Analyse des thermomechanischen Verhaltens von nasslaufenden Kupplungen mit der Finite Elemente Methode [Analysis of the thermomechanical behavior of wet clutch disks with the finite element method]. Bachelor Thesis, Gear Research Center, Technical University of Munich (2018).

Tapia, G.: Simulation des thermischen Haushalts nasslaufender Lamellenkupplungen mit der Finite Elemente Methode [Simulation of the thermal behavior of wet-running multiplate clutches using the finite element method]. Bachelor Thesis, Gear Research Center, Technical University of Munich (2019).

Wirkner, J.: Thermo-Mechanische Finite Elemente Simulation nasslaufender Lamellenkupplungen [Thermo-Mechanical Finite Element Simulation of Wet-Running Multi-Plate Clutches]. Semester Thesis, Gear Research Center, Technical University of Munich (2019).

Wirkner, J.: Abgleich einer thermo-mechanischen Finite Elemente Simulation trockenlaufender Lamellenkupplungen mit experimentellen Versuchsreihen am Komponentenpruefstand [Calibration of a Thermo-Mechanical Finite Element Simulation of Dry-Running Multi-Plate Clutches with Experimental Test Series on a Component Test Stand]. Master Thesis, Gear Research Center, Technical University of Munich (2020).

Felder, T.: Thermo-Mechanische Finite Elemente Simulation nasslaufender Kupplungen [Thermo-Mechanical Finite Element Simulation of wet running clutches]. Bachelor Thesis, Gear Research Center, Technical University of Munich (2020).

Schmid, A.: Experimentelle Untersuchungen zum Spontanschaedigungsverhalten von nasslaufenden Lamellenkupplungen [Experimental studies on spontaneous damage behaviour of wet-running multiple disk clutches]. Master Thesis, Gear Research Center, Technical University of Munich (2021).

Willand, F.: Experimentelle Untersuchungen zum Schaedigungsverhalten von nasslaufenen Lamellenkupplungen [Experimental investigations on den damage behaivour of wet running multi-plate cluthes]. Master Thesis, Gear Research Center, Technical University of Munich (2021).

Kamel, Y.: Experimentelle Untersuchungen zum Spontanschaedigungsverhalten von Lamellenkupplungen mit gewobenen Carbonreibbelag [Experimental investigations on

the spontaneous damage behavior of multi-plate clutches with woven carbon friction linings]. Bachelor Thesis, Gear Research Center, Technical University of Munich (2021).

Dietsch, M.: Modellierung des thermomechanischen Verhaltens einer Lamellenkupplung unter Einsatz von FEM und kuenstlicher Intelligenz [Modeling of the Thermomechanical Behavior of a Multi-Plate Clutch using FEM and Artificial Intelligence]. Master Thesis, Gear Research Center, Technical University of Munich (2021).

Vicente, F.: Simulation und Berechnung des thermomechanischen Verhaltens einer Kupplung mit ANSYS [Calculation and Simulation of the Thermo-Mechanical Behavior of a Clutch Using ANSYS]. Master Thesis, Gear Research Center, Technical University of Munich (2021).

Bedrikow, A.: Finite-Elemente-Ersatzmodell fuer nasslaufende Lamellenkupplungen [Finite-Element Surrogate Model for Wet-Running Multi-Plate Clutches]. Semester Thesis, Gear Research Center, Technical University of Munich (2023).

Other Unpublished Work

The following papers were written between 2017 and 2023 at the Institute of Machine Elements, Gear Research Center (FZG) and have been partially incorporated into this work:

Schneider, T.; Pflaum, H.; Stahl, K.: Anwendungsorientierte Erweiterung der Erkenntnisse zu Spontanschaedigung nasslaufender Lamellenkupplungen und Erweiterung der Rechenmethodik [Application-oriented extension of the knowledge on spontaneous damage of wet-running multi-plate clutches and extension of the calculation methodology] - Research Project No. 515 V. Forschungsvereinigung Antriebstechnik e.V., Frankfurt/Main, Issue: 1361 (2020).

Schneider, T.; Pflaum, H.; Stahl, K.: Spontanschaedigungsverhalten nasser Bremsen bei Tauchschmierung und Kupplungen in Differentialen [Spontaneous Damage Behavior of Wet Brakes with Immersion Lubrication and Clutches in Differentials] - Research Project No. 515 VI. Forschungsvereinigung Antriebstechnik e.V., Frankfurt/Main, Issue: 1499 (2022).

A Appendix

A.1 Oil Composition

Chemical name	Substance identity	Concentration
Hydrocarbons, low-viscosity	EC: 500-183-1	10.00 - < 20.00 Wt. %
Organic polysulfide	EINECS: 273-103-3	1.00 - < 5.00 Wt. %
Alcohol ethoxylate phosphate ester	Polymer	1.00 - < 5.00 Wt. %
Hydrocarbons, low-viscosity	EC: 500-228-5	1.00 - < 5.00 Wt. %
Amine salt of a phosphoric acid ester	EC: 942-466-6	1.00 - < 3.00 Wt. %
Alkylamine	EINECS: 263-189-0	1.00 - < 2.50 Wt. %
Imidazole derivative	EINECS: 244-501-4	0.10 - < 0.25 Wt. %

Table A.1: Composition of the test lubricant according to the manufacturer's specifications. All concentrations are given in percent by weight.

A.2 Statistical Analyses

Statistical test	Null hypothesis	p-Value	Conclusion
t-Test	Temperature difference between variants originate from a normal distribution with mean 0.	2.19e-16	Null hypothesis can be rejected.
ANOVA	Temperature difference between variants does not depend on temperature level ($\beta_1 = 0$).	3.81e-34	Null hypothesis can be rejected.

Table A.2: Statistical tests for the influence of the oil flow rate ($\dot{v}_{oil} = 0.50$ mm^3/mm^2/s, $\dot{v}_{oil} = 1.00$ mm^3/mm^2/s) on the temperature difference of the measured steel plate temperatures.

Statistical test	Null hypothesis	p-Value	Conclusion
t-Test	Temperature difference between variants originate from a normal distribution with mean 0.	1.29e-16	Null hypothesis can be rejected.
ANOVA	Temperature difference between variants does not depend on temperature level ($\beta_1 = 0$).	4.92e-39	Null hypothesis can be rejected.

Table A.3: Statistical tests for the influence of the oil flow rate ($\dot{v}_{oil} = 0.25$ mm^3/mm^2/s, $\dot{v}_{oil} = 0.50$ mm^3/mm^2/s) on the temperature difference of the measured steel plate temperatures.

Statistical test	Null hypothesis	p-Value	Conclusion
t-Test	Temperature difference between variants originate from a normal distribution with mean 0.	1.15e-26	Null hypothesis can be rejected.
ANOVA	Temperature difference between variants does not depend on temperature level ($\beta_1 = 0$).	3.26e-13	Null hypothesis can be rejected.

Table A.4: Statistical tests for the influence of the number of friction interfaces (6 and 10) on the temperature difference of the measured steel plate temperatures.

Statistical test	Null hypothesis	p-Value	Conclusion
t-Test	Temperature difference between variants originate from a normal distribution with mean 0.	0.2839	Null hypothesis cannot be rejected.

Table A.5: Statistical tests for the influence of the number of friction interfaces (10 and 14) on the temperature difference of the measured steel plate temperatures.

A.3 Elemental Analyses

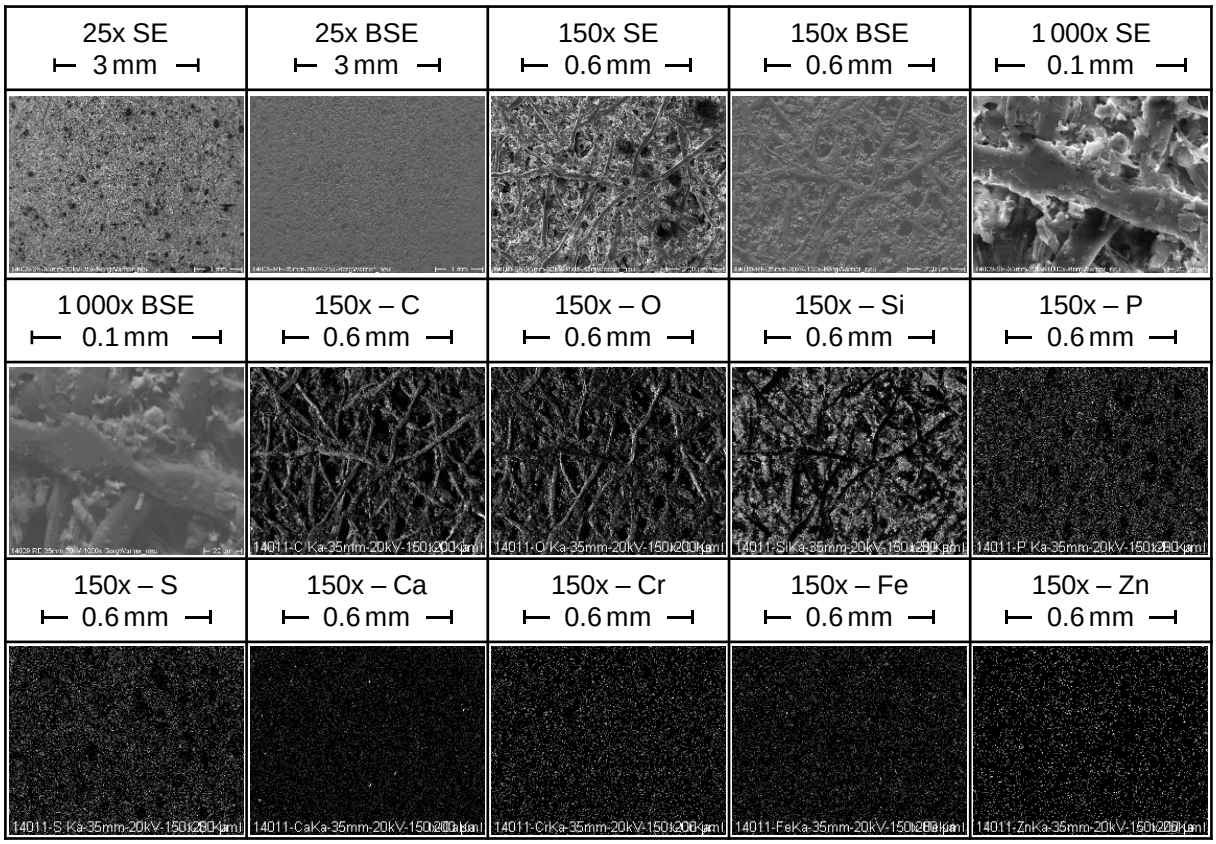

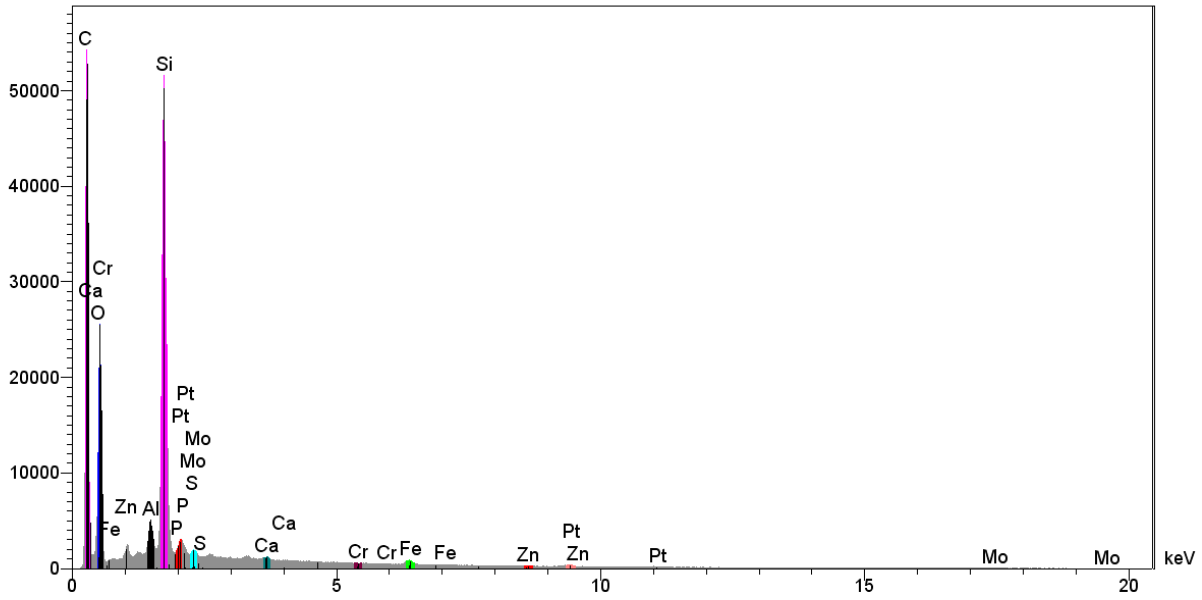

Figure A.1: SE images, BSE images, EDX mappings and X-ray spectra of friction linings for the friction system FS1 in the state new condition.

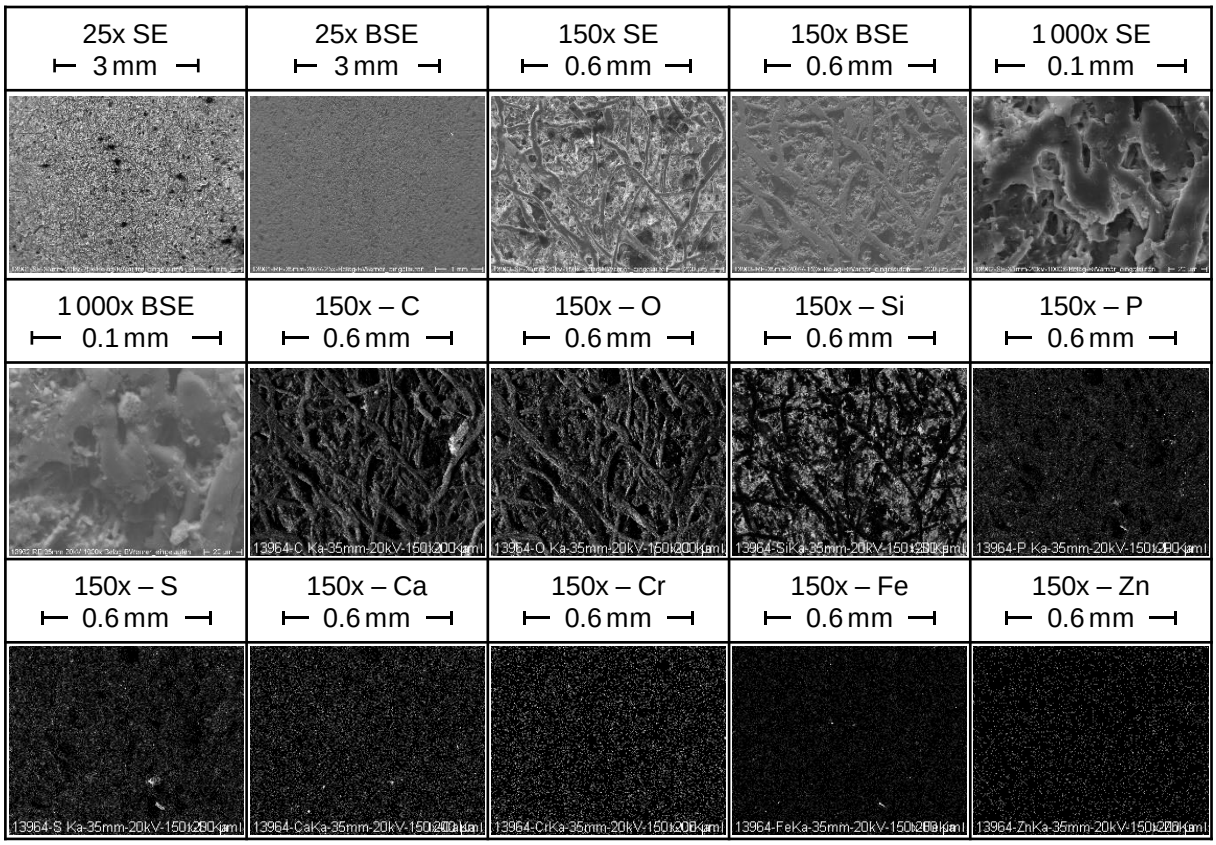

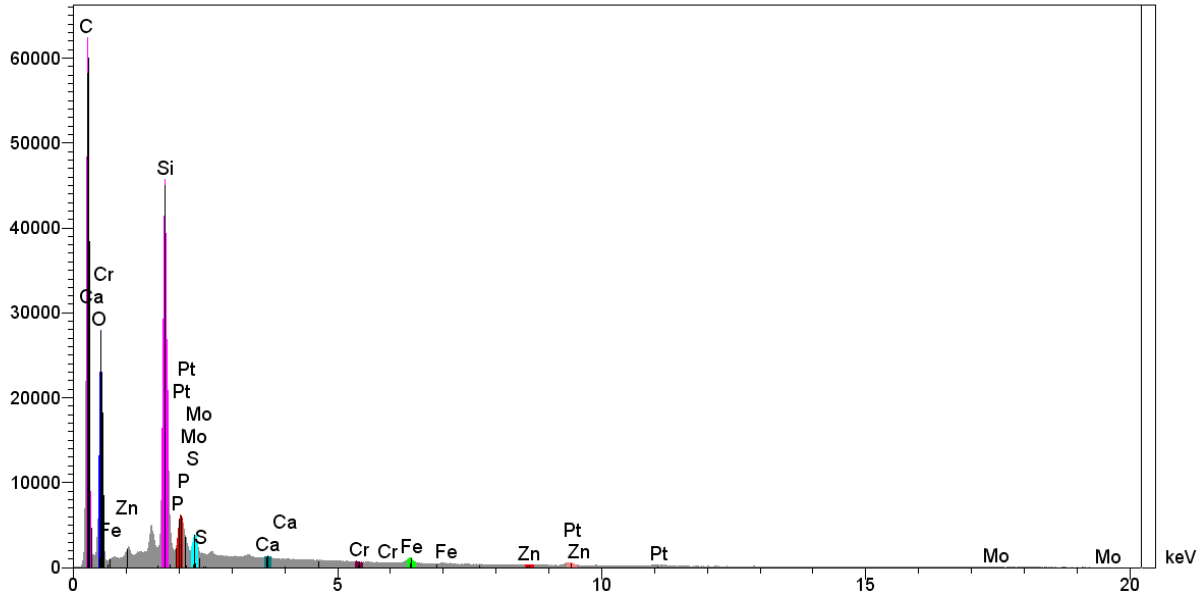

Figure A.2: SE images, BSE images, EDX mappings and X-ray spectra of friction linings for the friction system FS1 in the state after run-in.

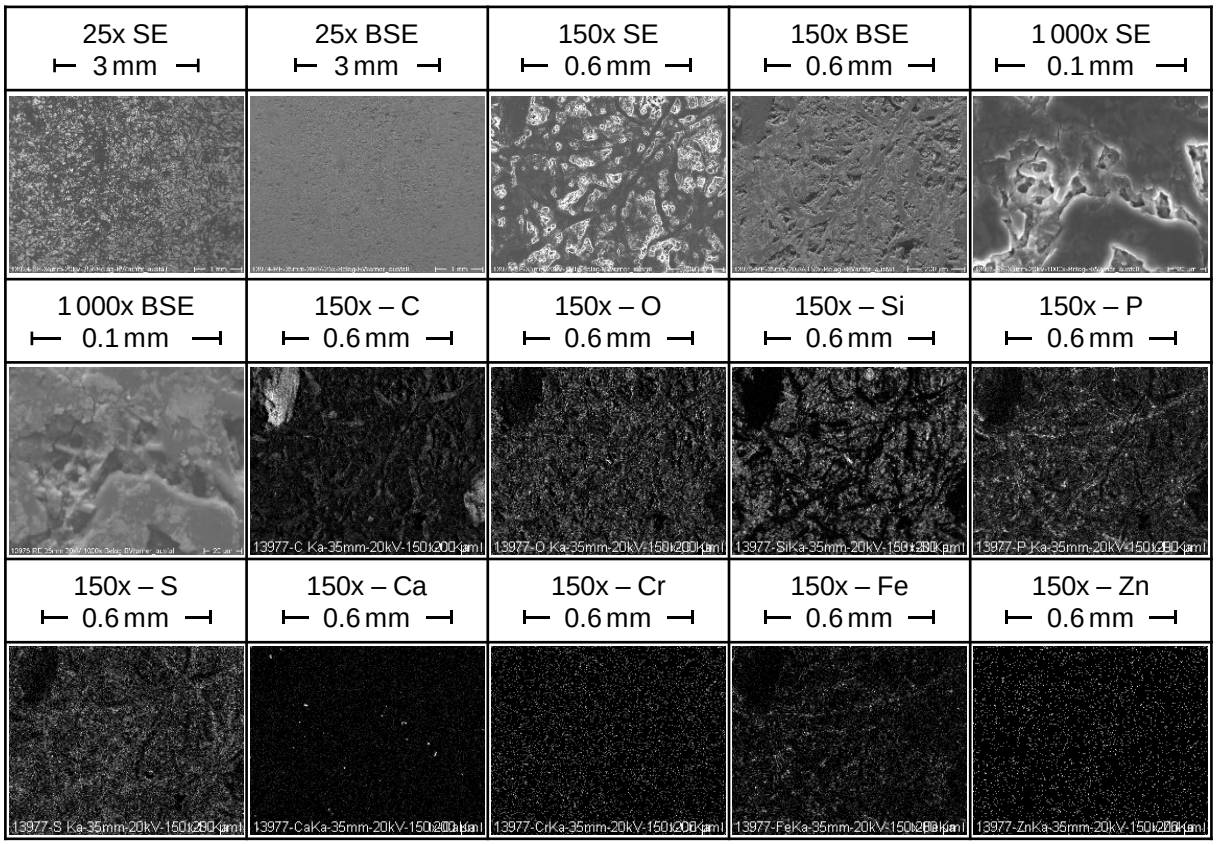

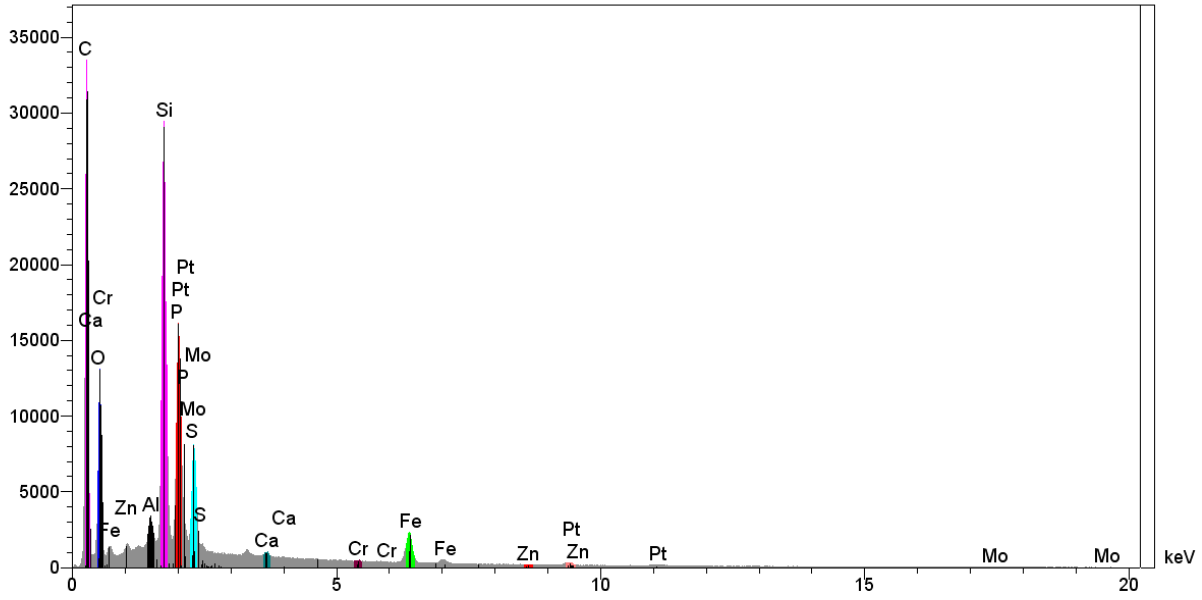

Figure A.3: SE images, BSE images, EDX mappings and X-ray spectra of friction linings for the friction system FS1 in the state after failure.

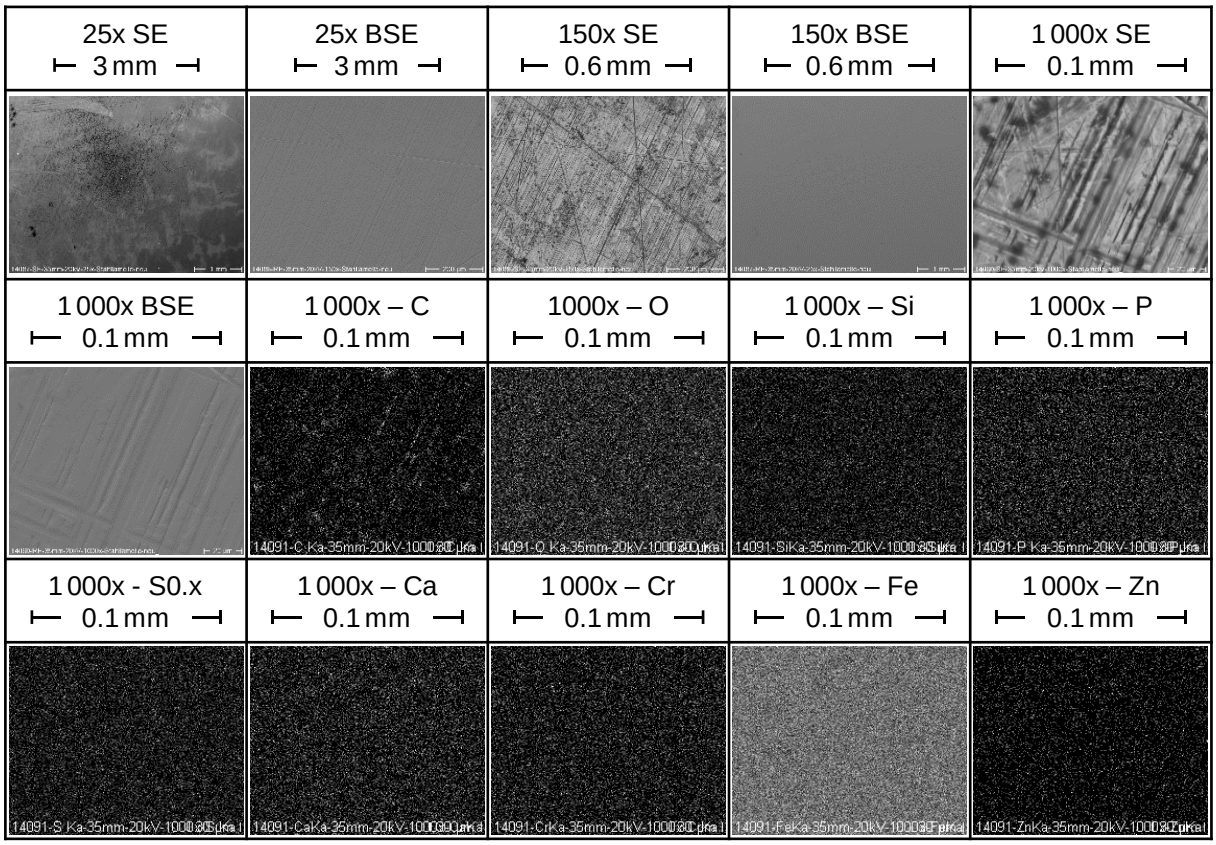

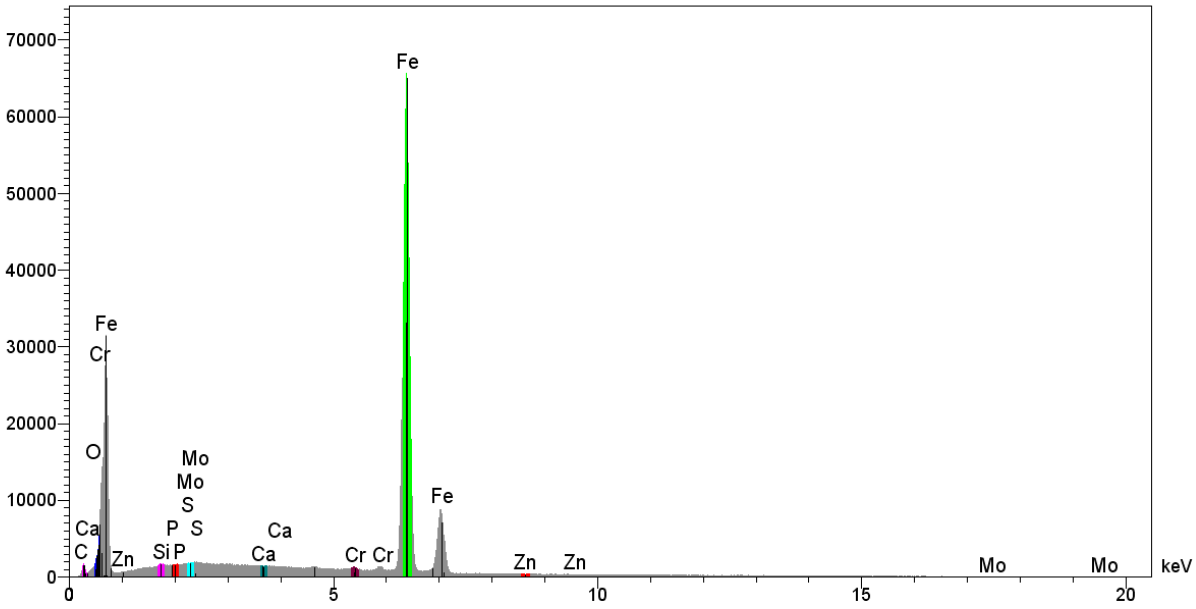

Figure A.4: SE images, BSE images, EDX mappings and X-ray spectra of steel plates for the friction system FS1 in the state new condition.

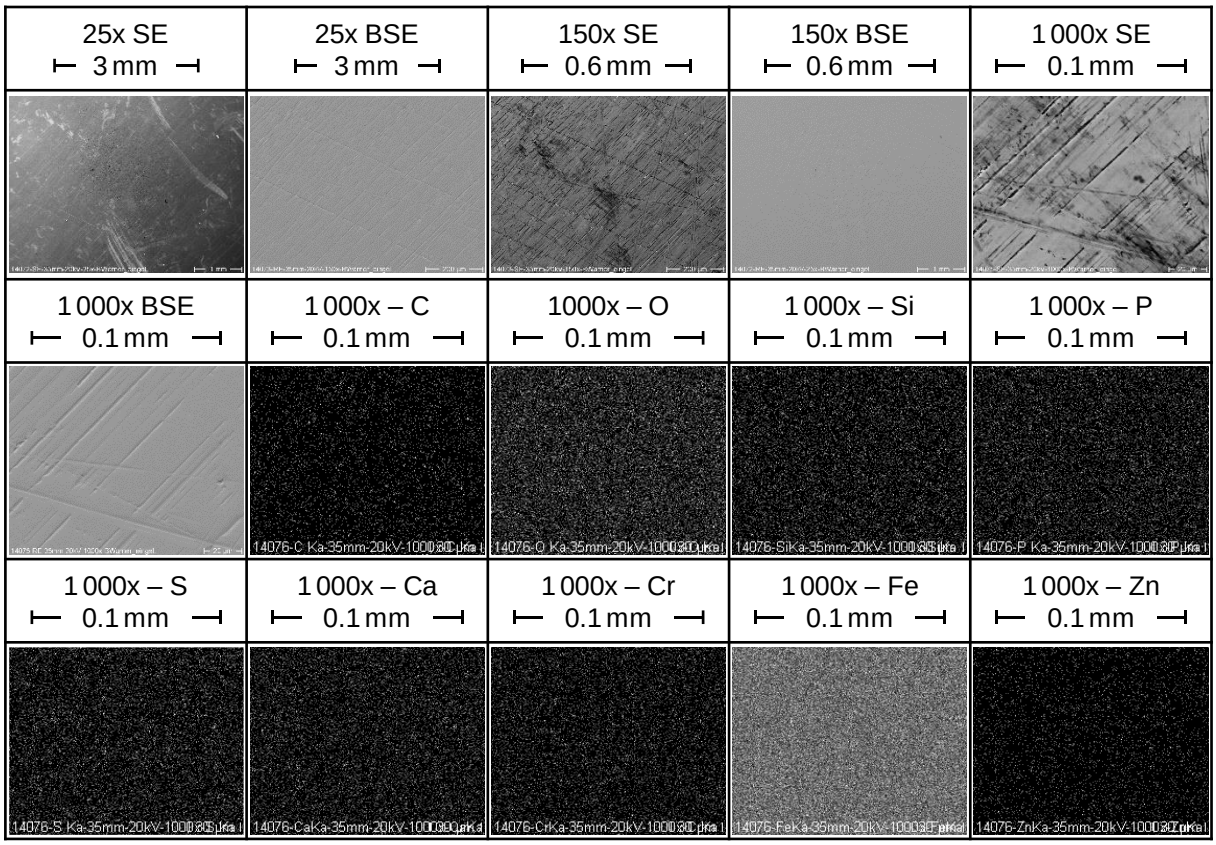

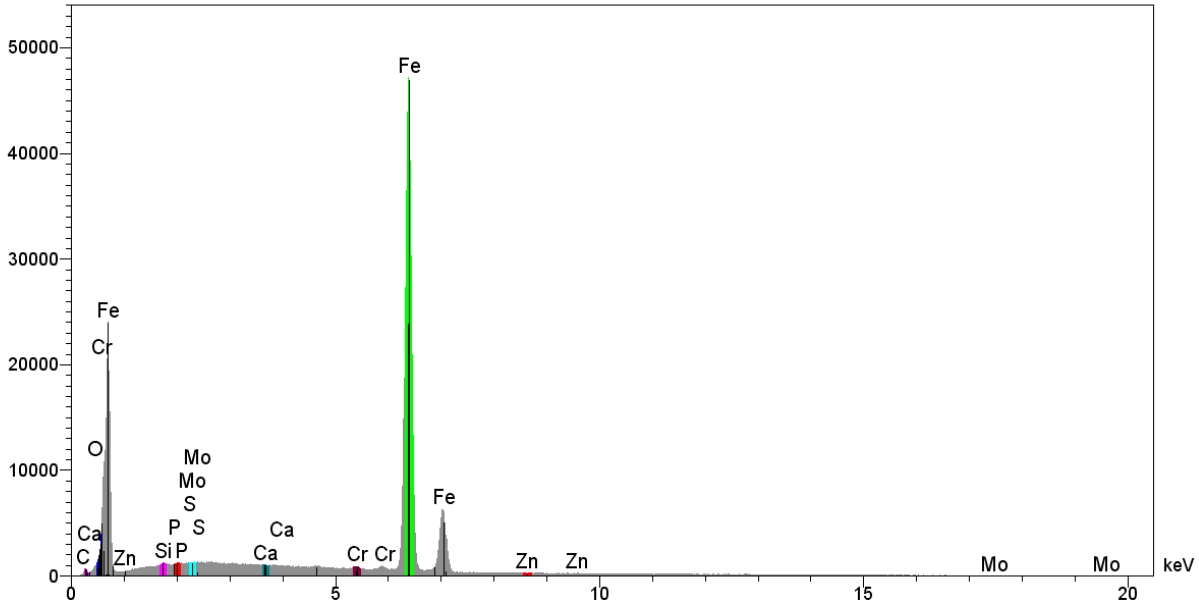

Figure A.5: SE images, BSE images, EDX mappings and X-ray spectra of steel plates for the friction system FS1 in the state after run-in.

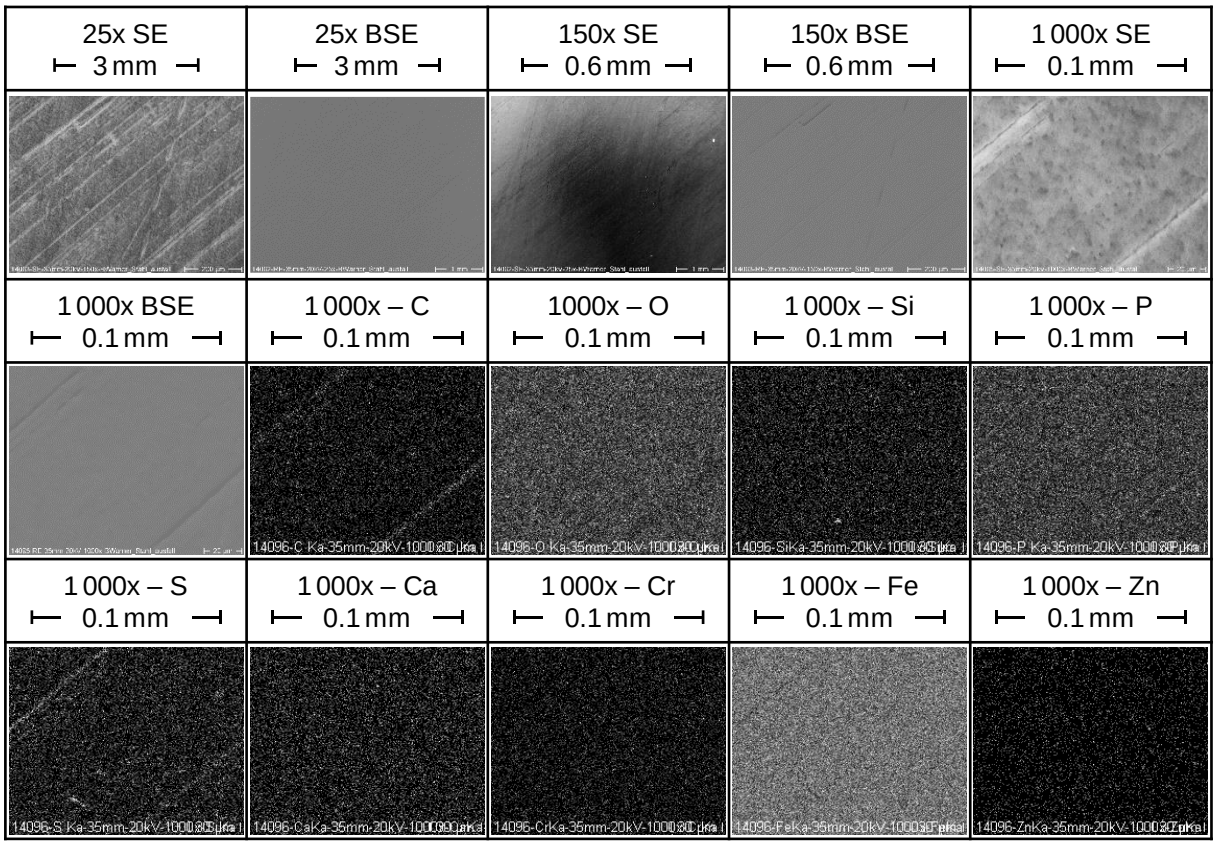

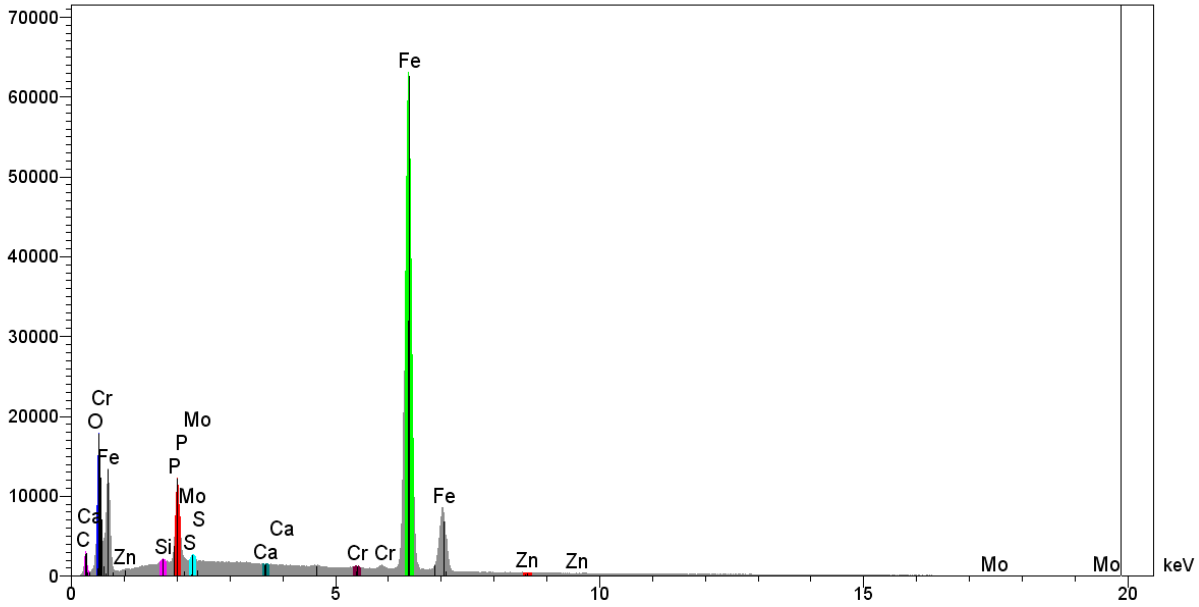

Figure A.6: SE images, BSE images, EDX mappings and X-ray spectra of steel plates for the friction system FS1 in the state after failure.

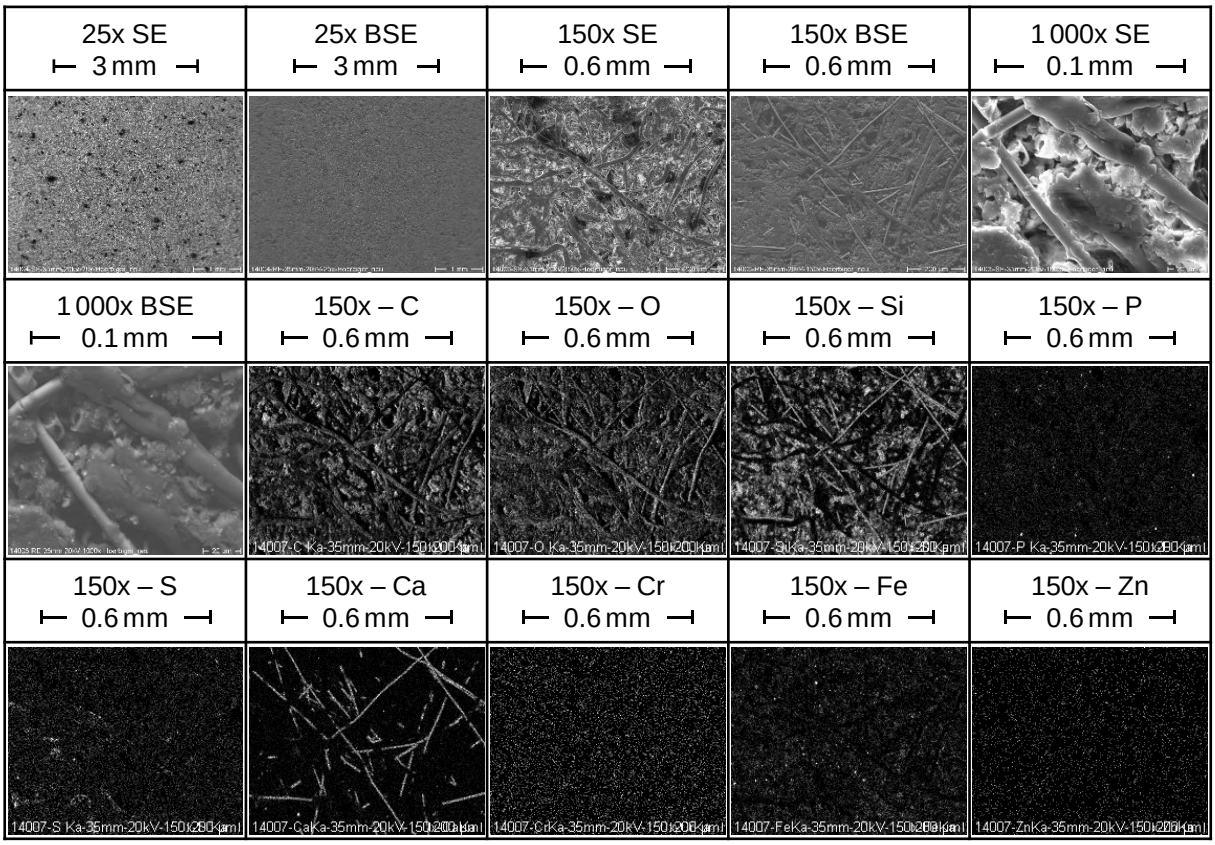

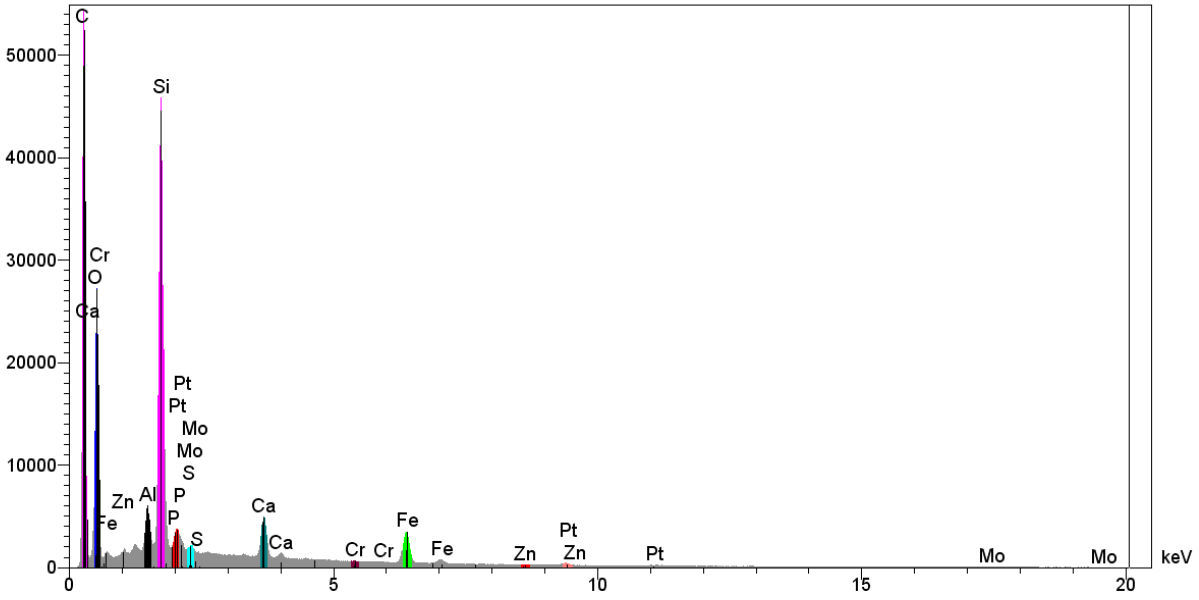

Figure A.7: SE images, BSE images, EDX mappings and X-ray spectra of friction linings for the friction system FS2 in the state new condition.

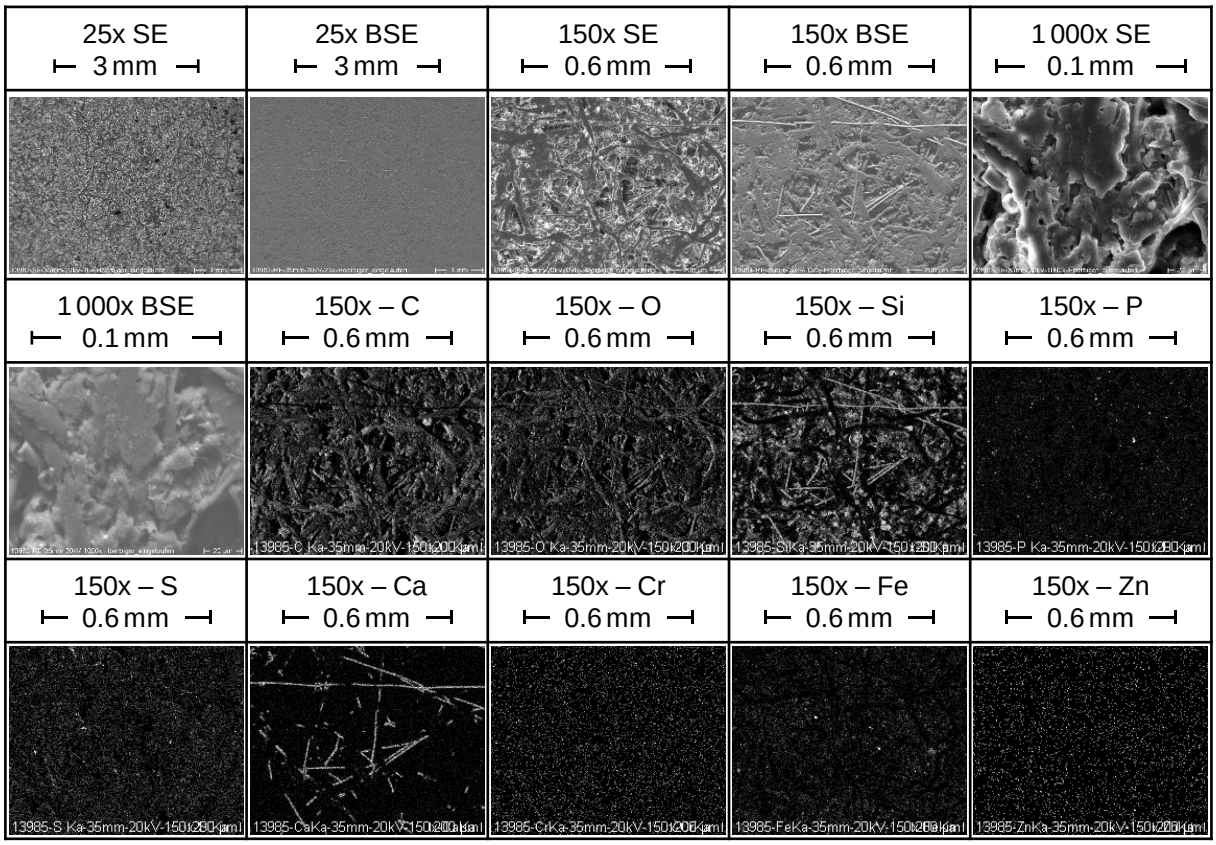

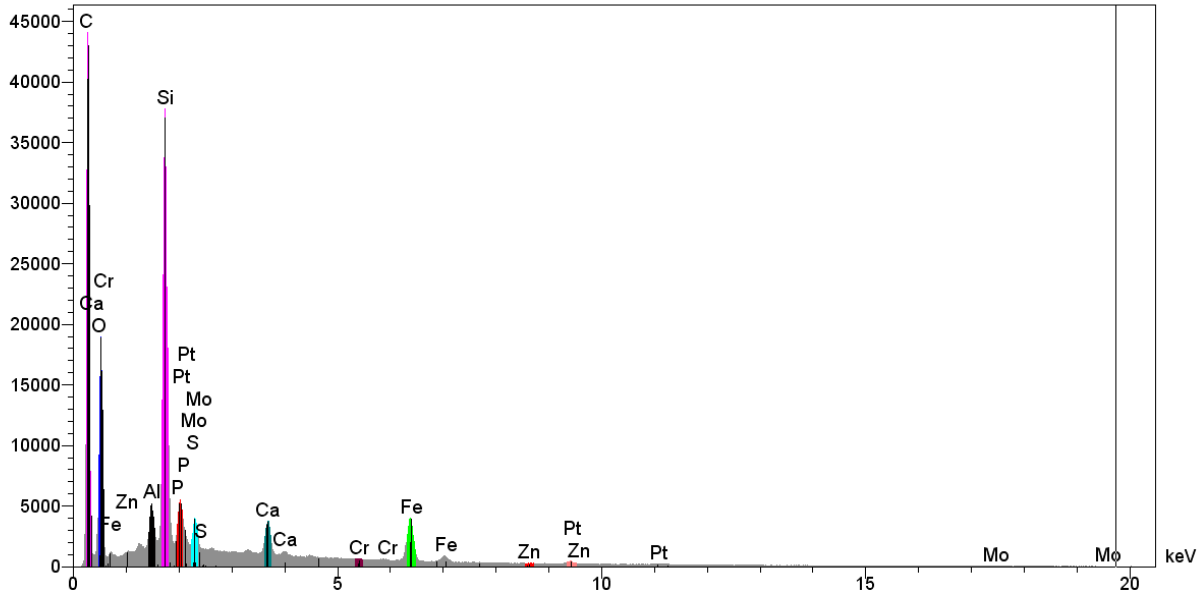

Figure A.8: SE images, BSE images, EDX mappings and X-ray spectra of friction linings for the friction system FS2 in the state after run-in.

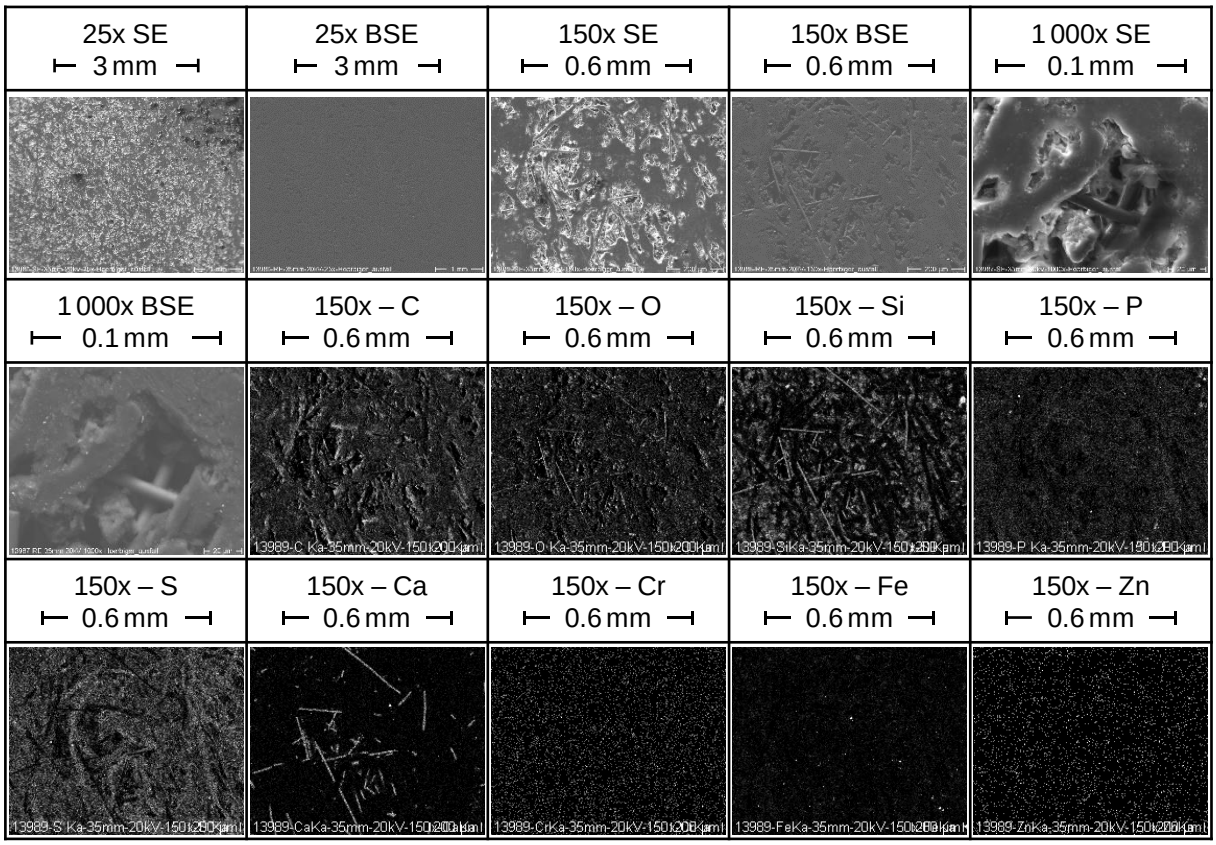

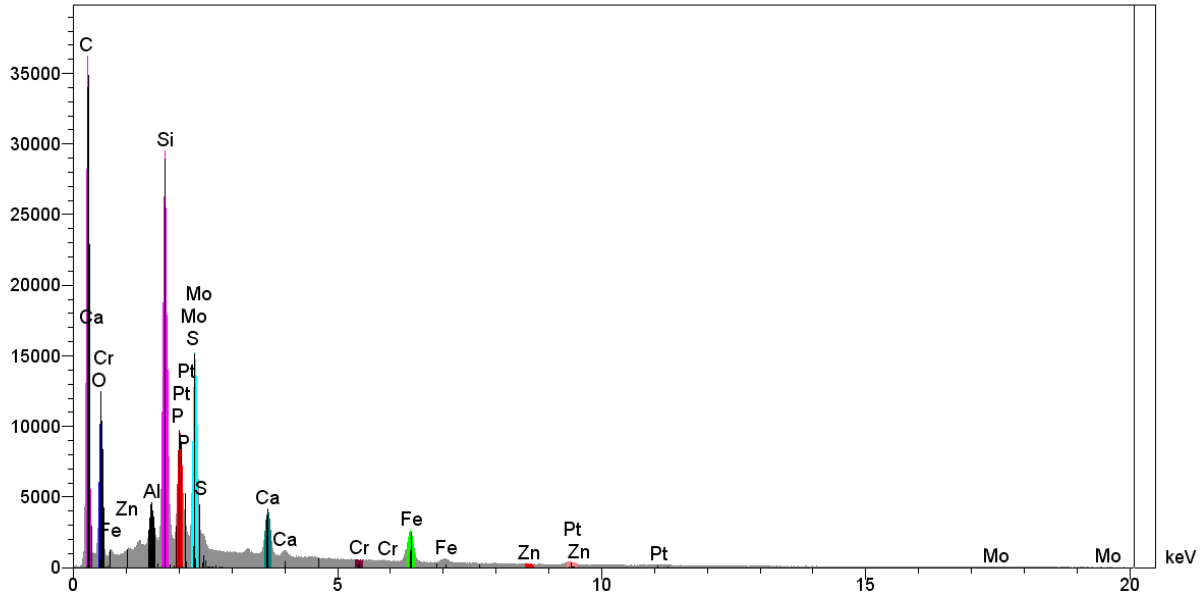

Figure A.9: SE images, BSE images, EDX mappings and X-ray spectra of friction linings for the friction system FS2 in the state after failure.

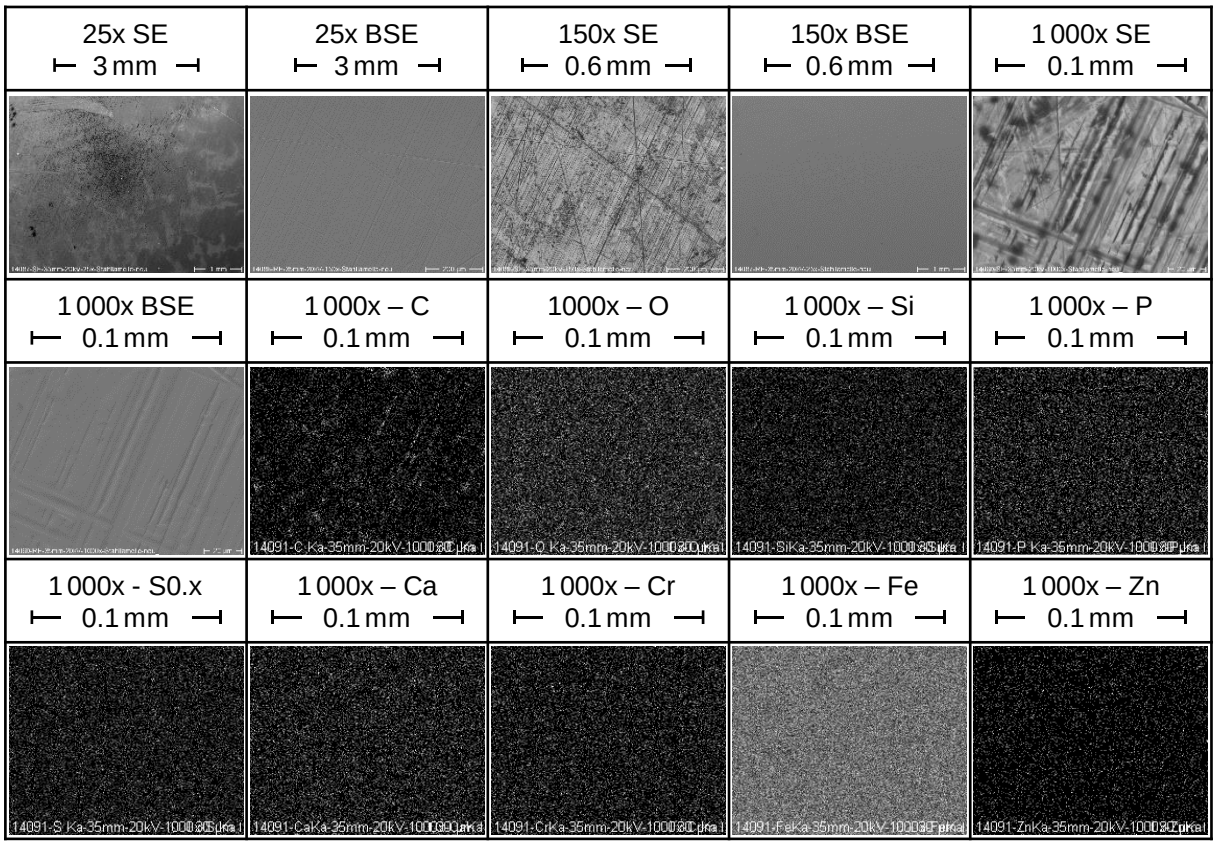

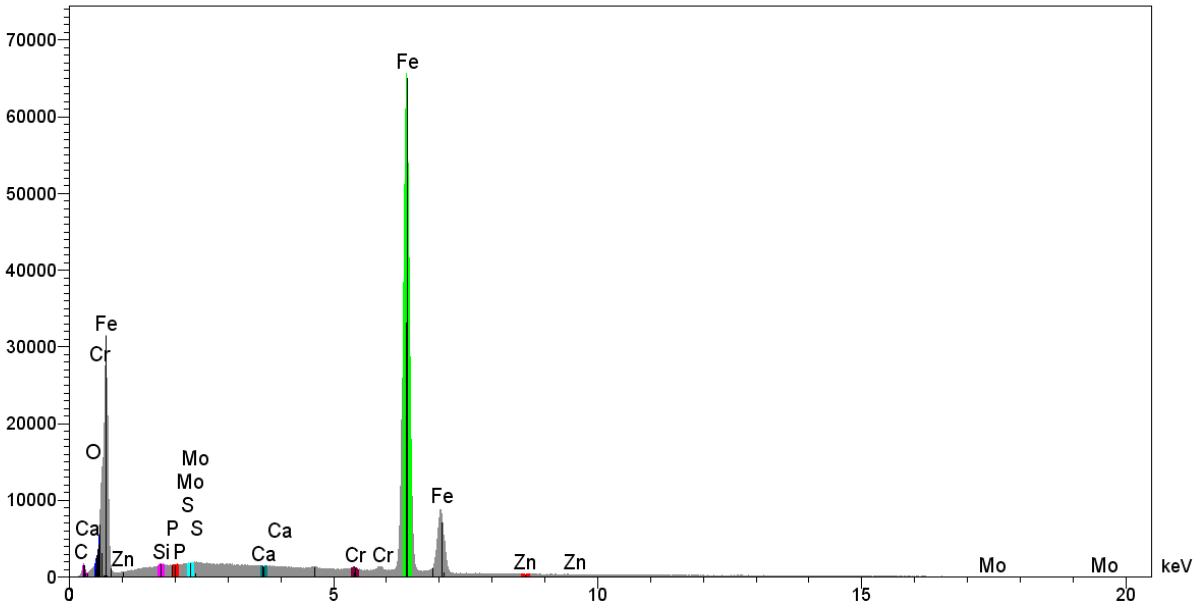

Figure A.10: SE images, BSE images, EDX mappings and X-ray spectra of steel plates for the friction system FS2 in the state new condition.

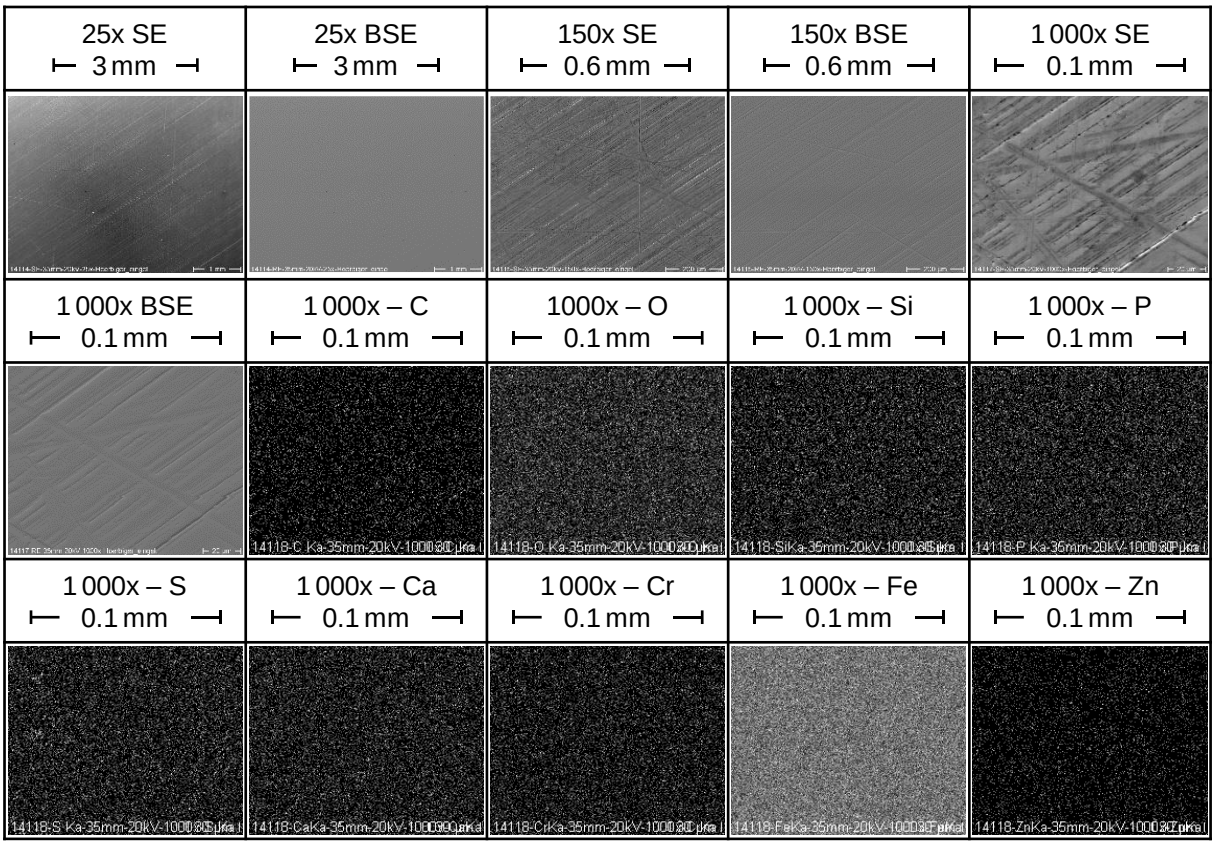

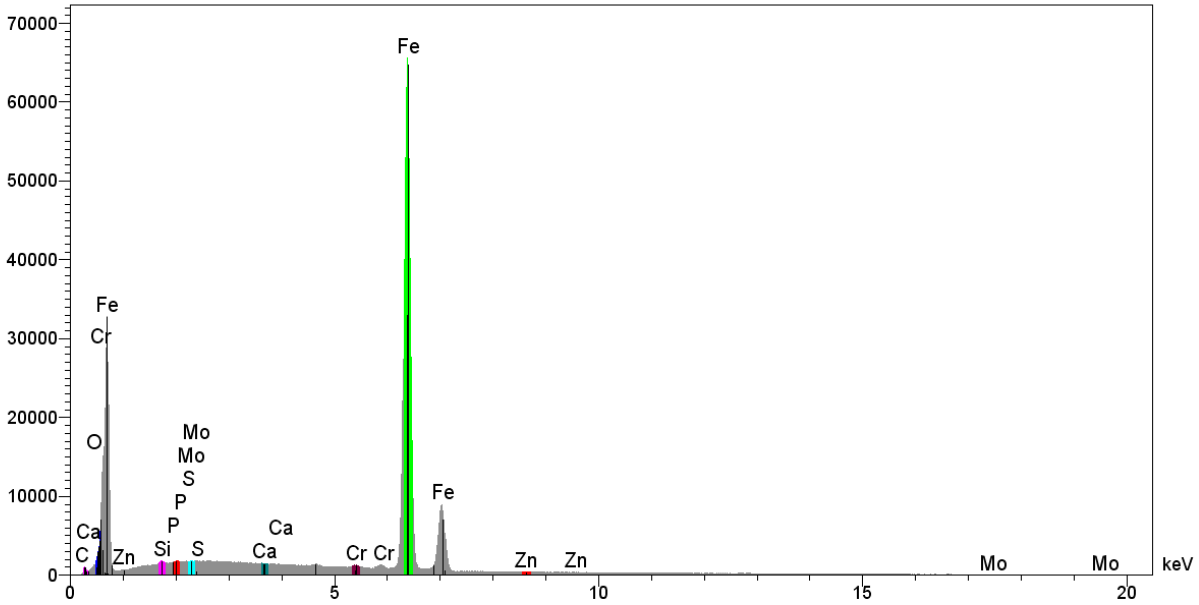

Figure A.11: SE images, BSE images, EDX mappings and X-ray spectra of steel plates for the friction system FS2 in the state after run-in.

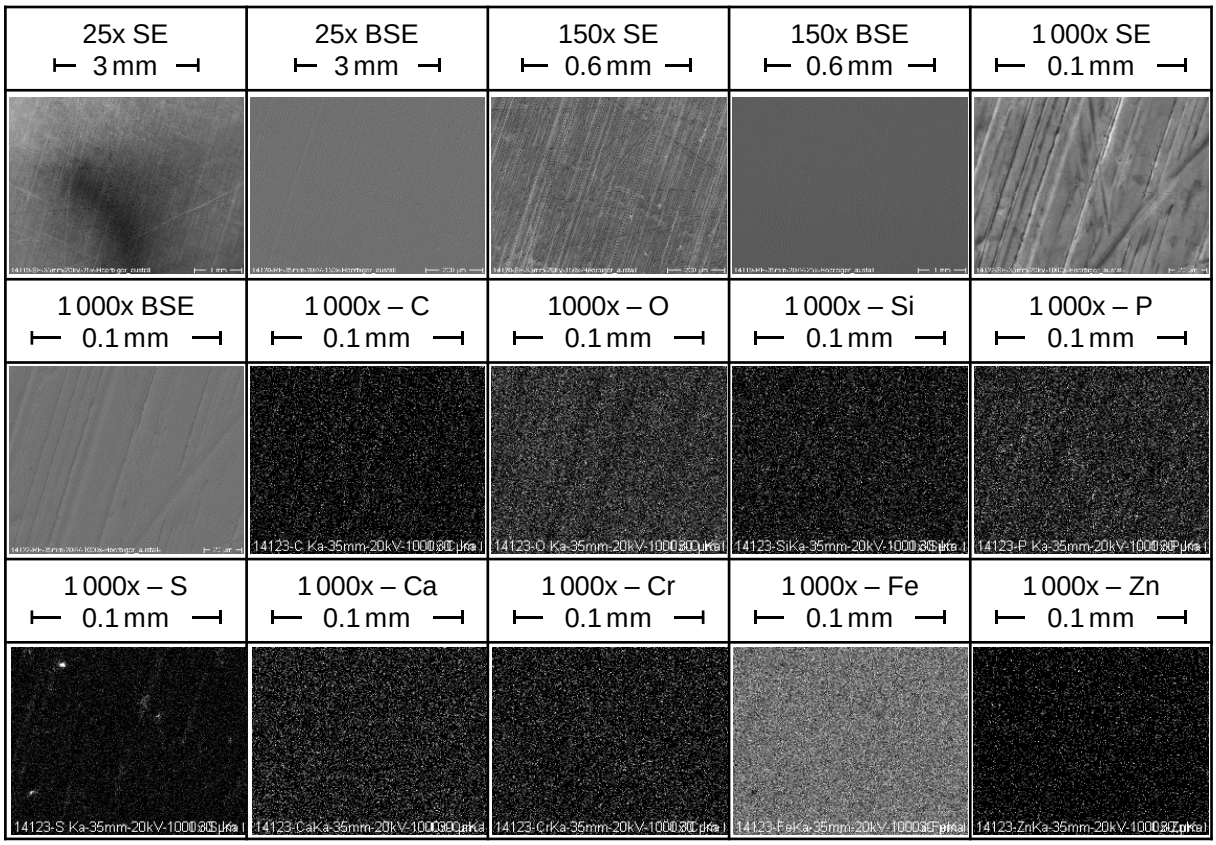

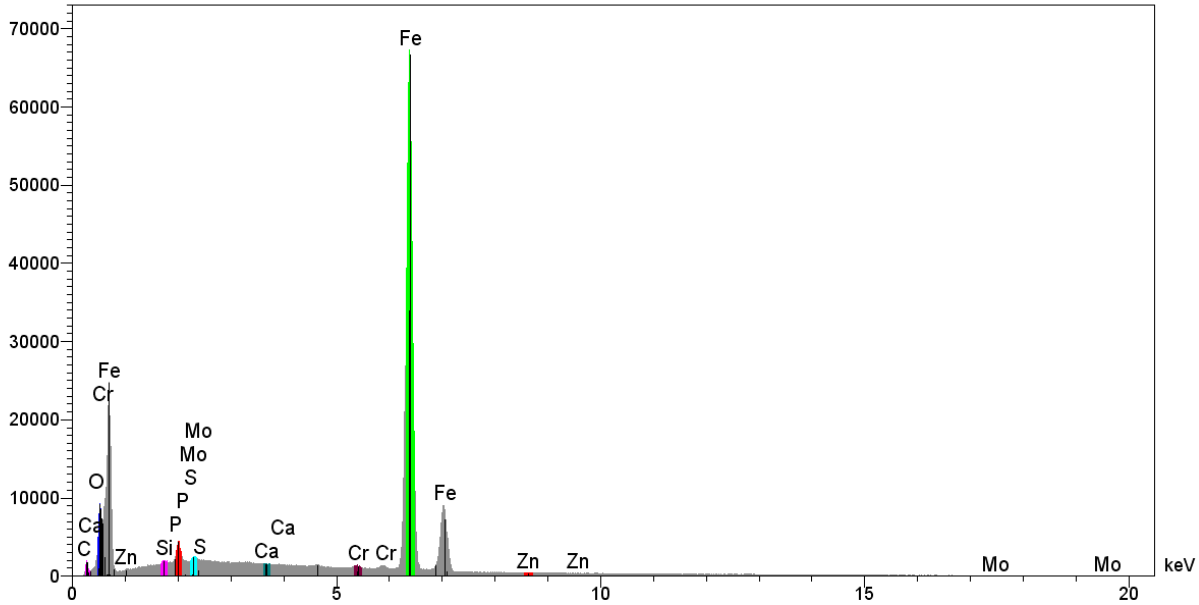

Figure A.12: SE images, BSE images, EDX mappings and X-ray spectra of steel plates for the friction system FS2 in the state after failure.

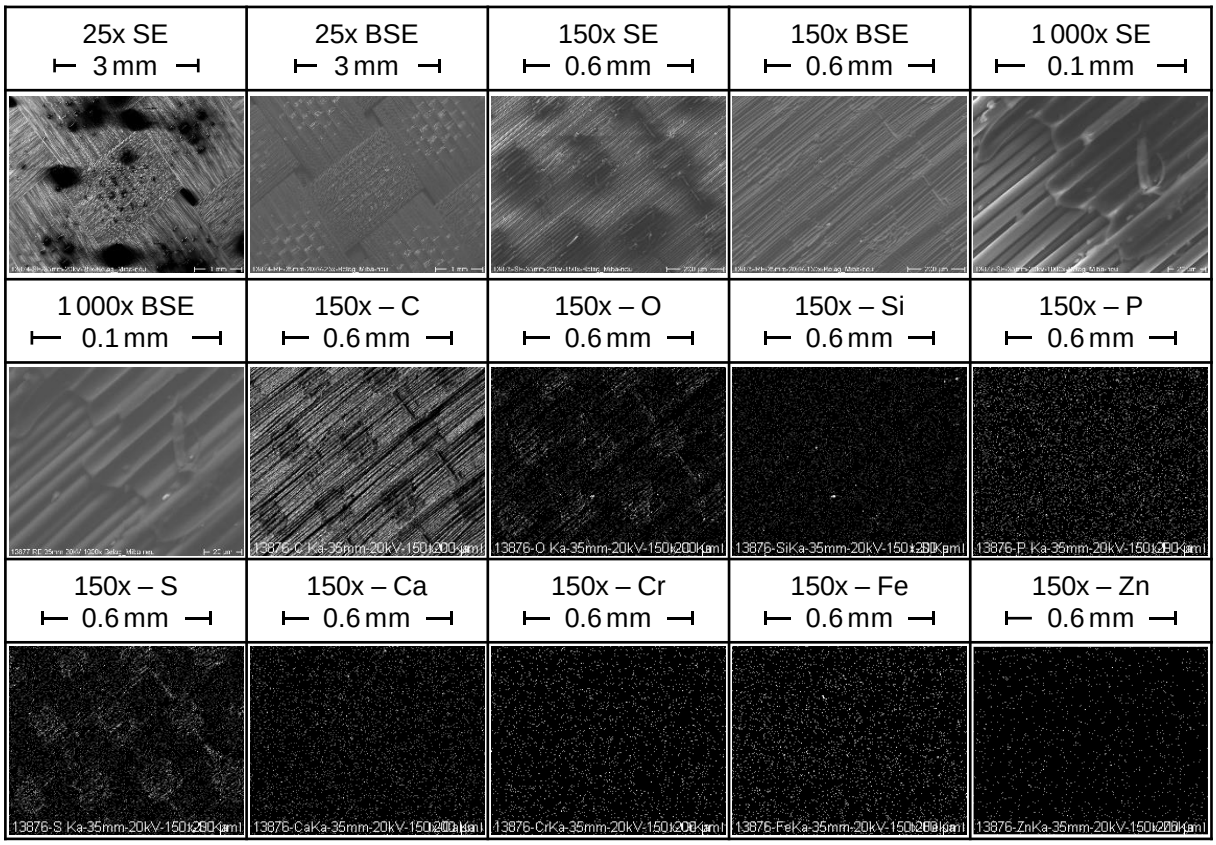

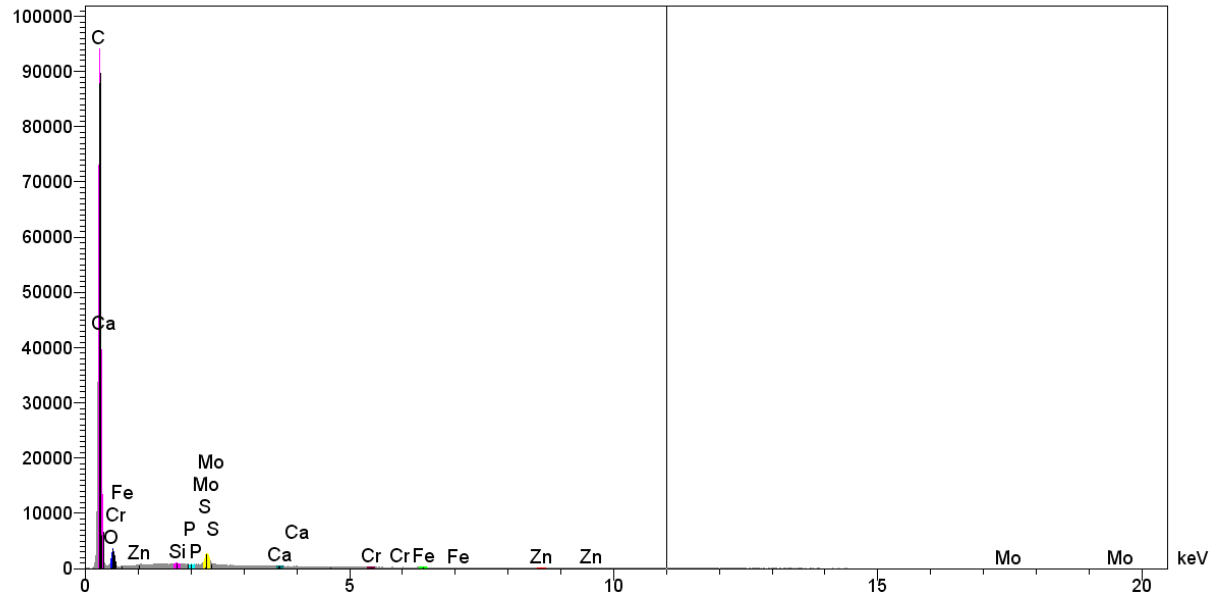

Figure A.13: SE images, BSE images, EDX mappings and X-ray spectra of the friction linings for the friction system FS3 in the state new condition.

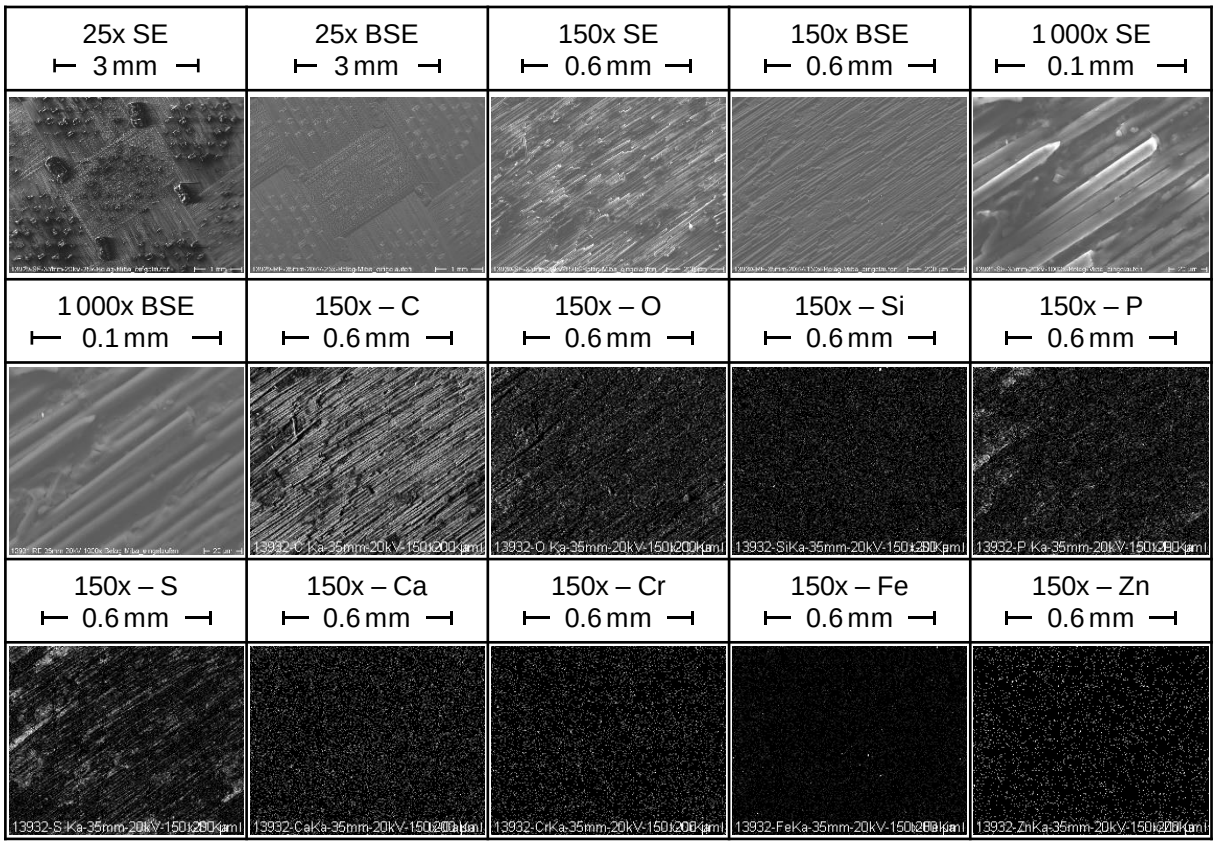

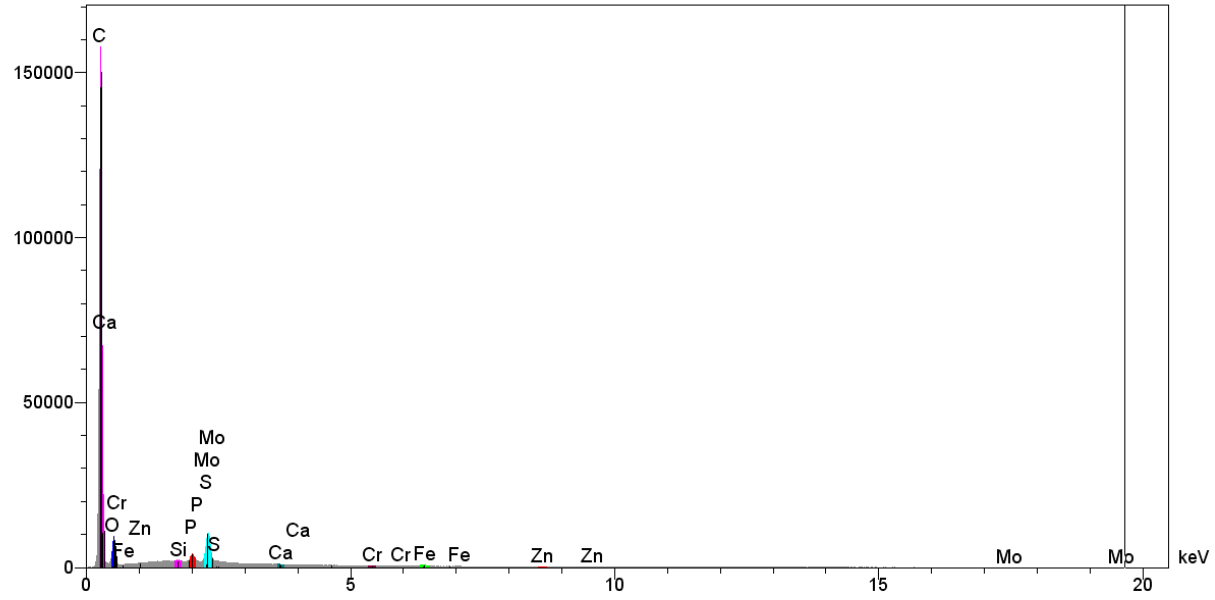

Figure A.14: SE images, BSE images, EDX mappings and X-ray spectra of friction linings for the friction system FS3 in the state after run-in.

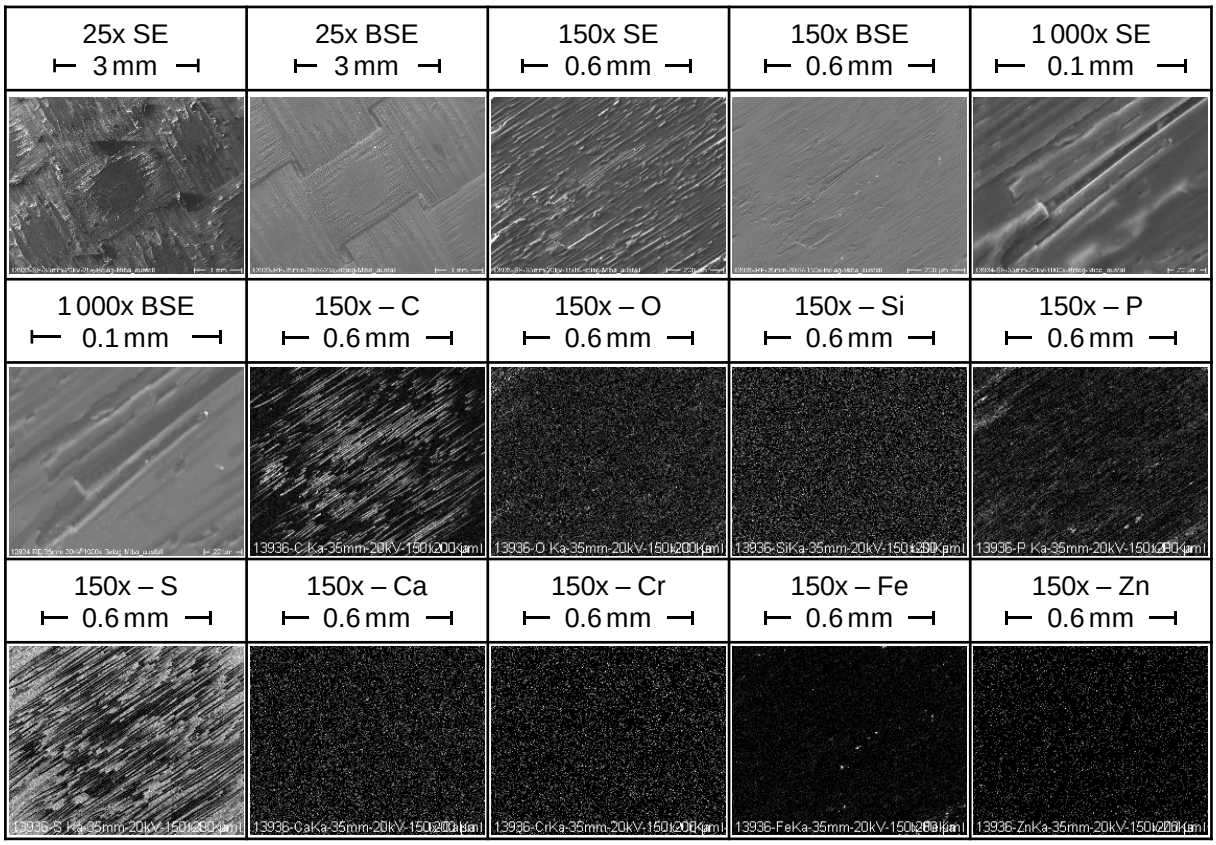

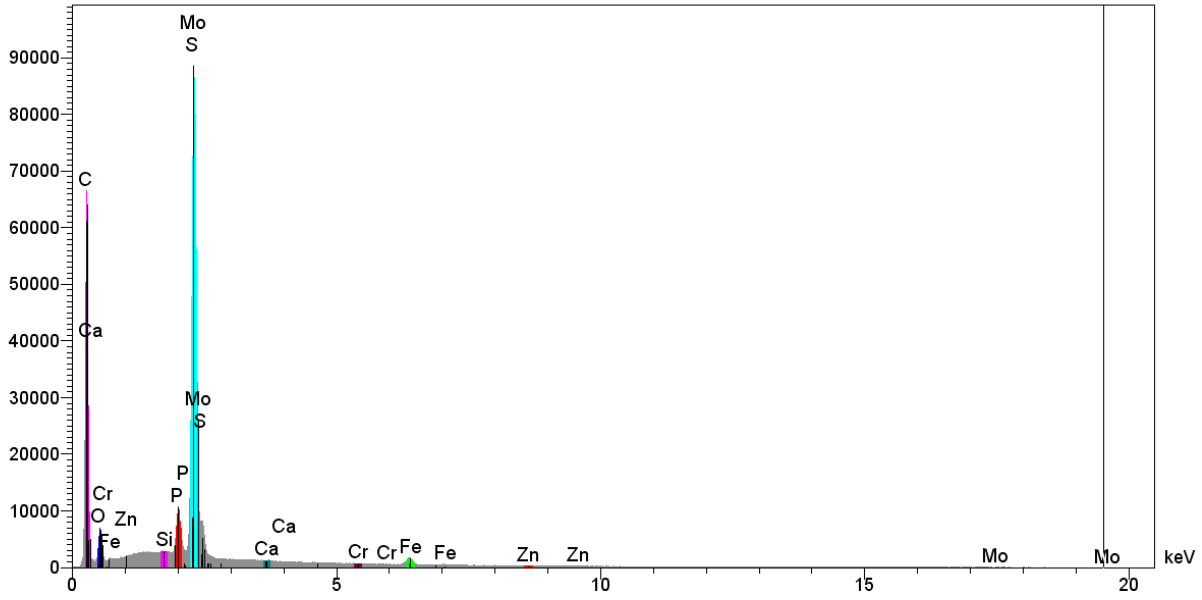

Figure A.15: SE images, BSE images, EDX mappings and X-ray spectra of friction linings for the friction system FS3 in the state after failure.

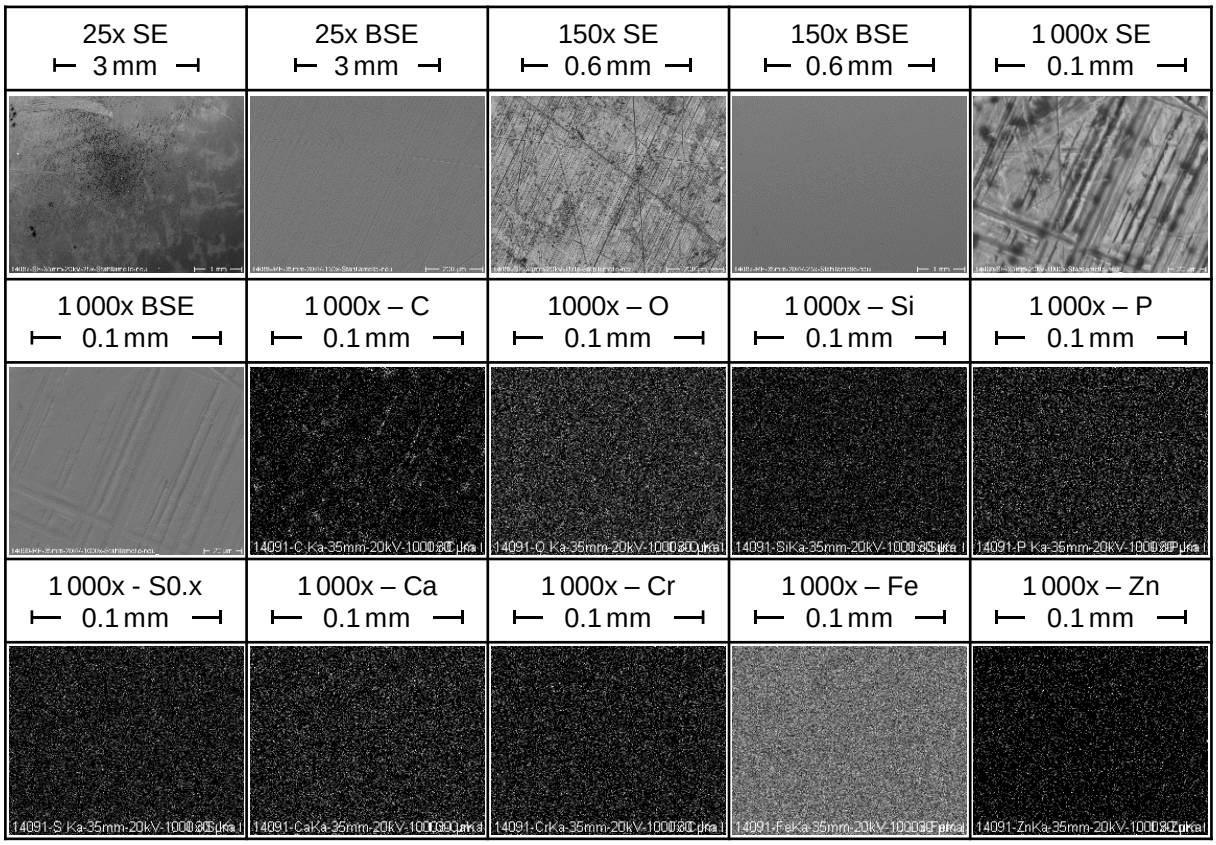

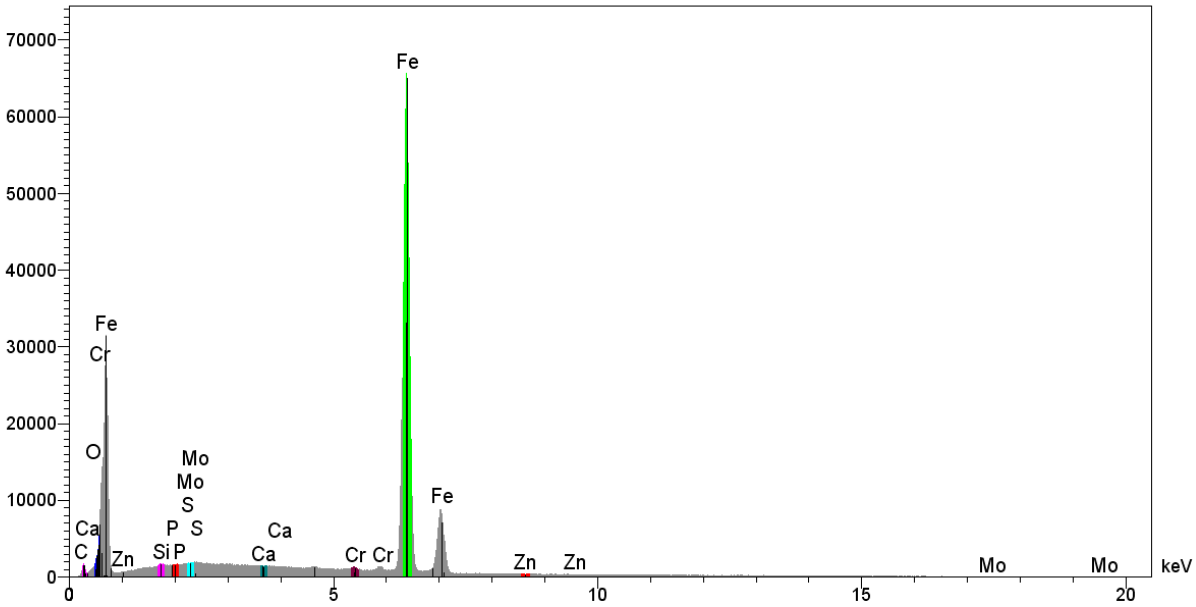

Figure A.16: SE images, BSE images, EDX mappings and X-ray spectra of steel plates for the friction system FS3 in the state new condition.

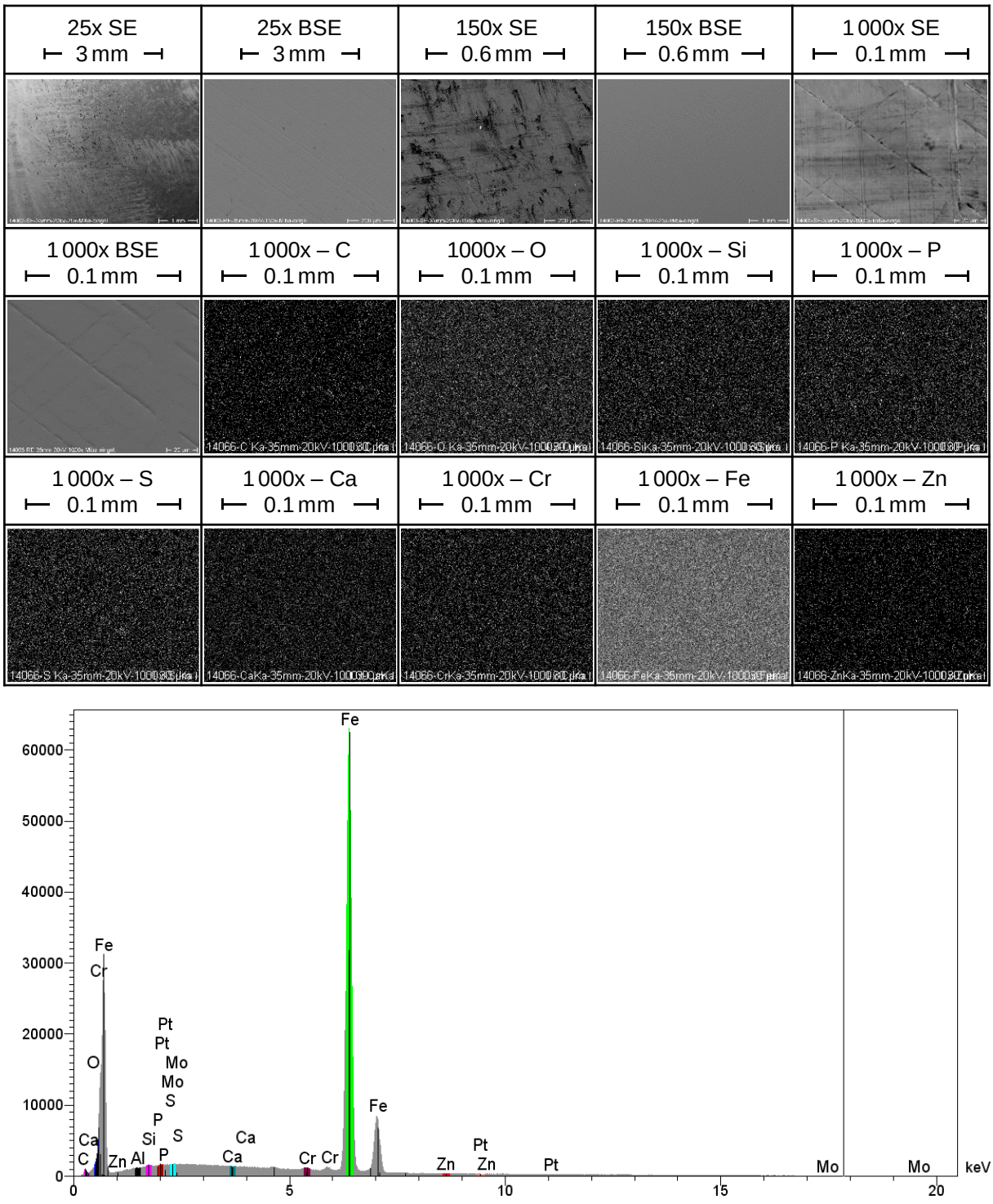

Figure A.17: SE images, BSE images, EDX mappings and X-ray spectra of steel plates for the friction system FS3 in the state after run-in.

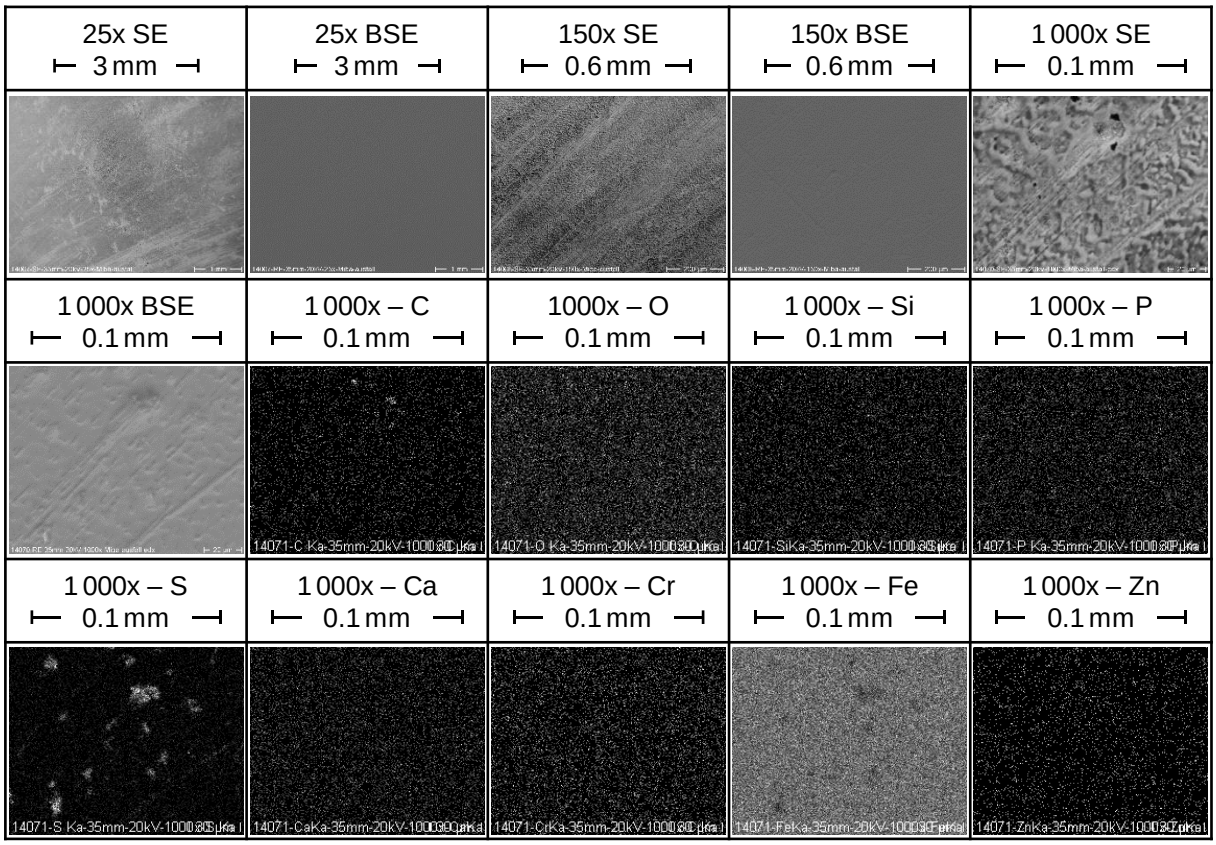

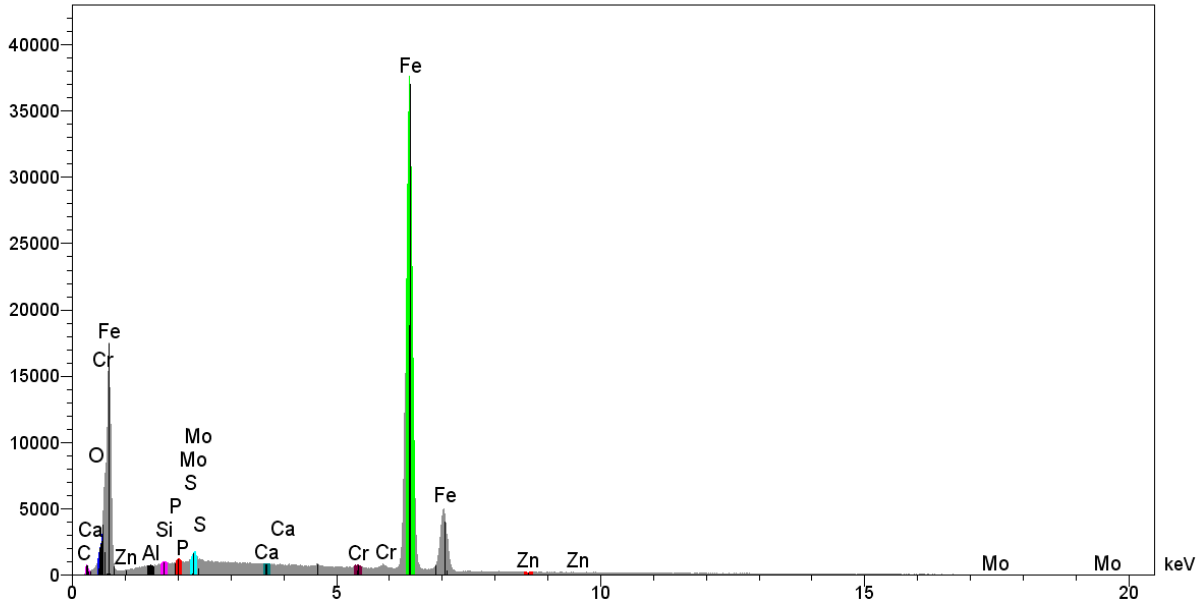

Figure A.18: SE images, BSE images, EDX mappings and X-ray spectra of steel plates for the friction system FS3 in the state after failure.

A.4 Modification of Friction and Temperature Behavior

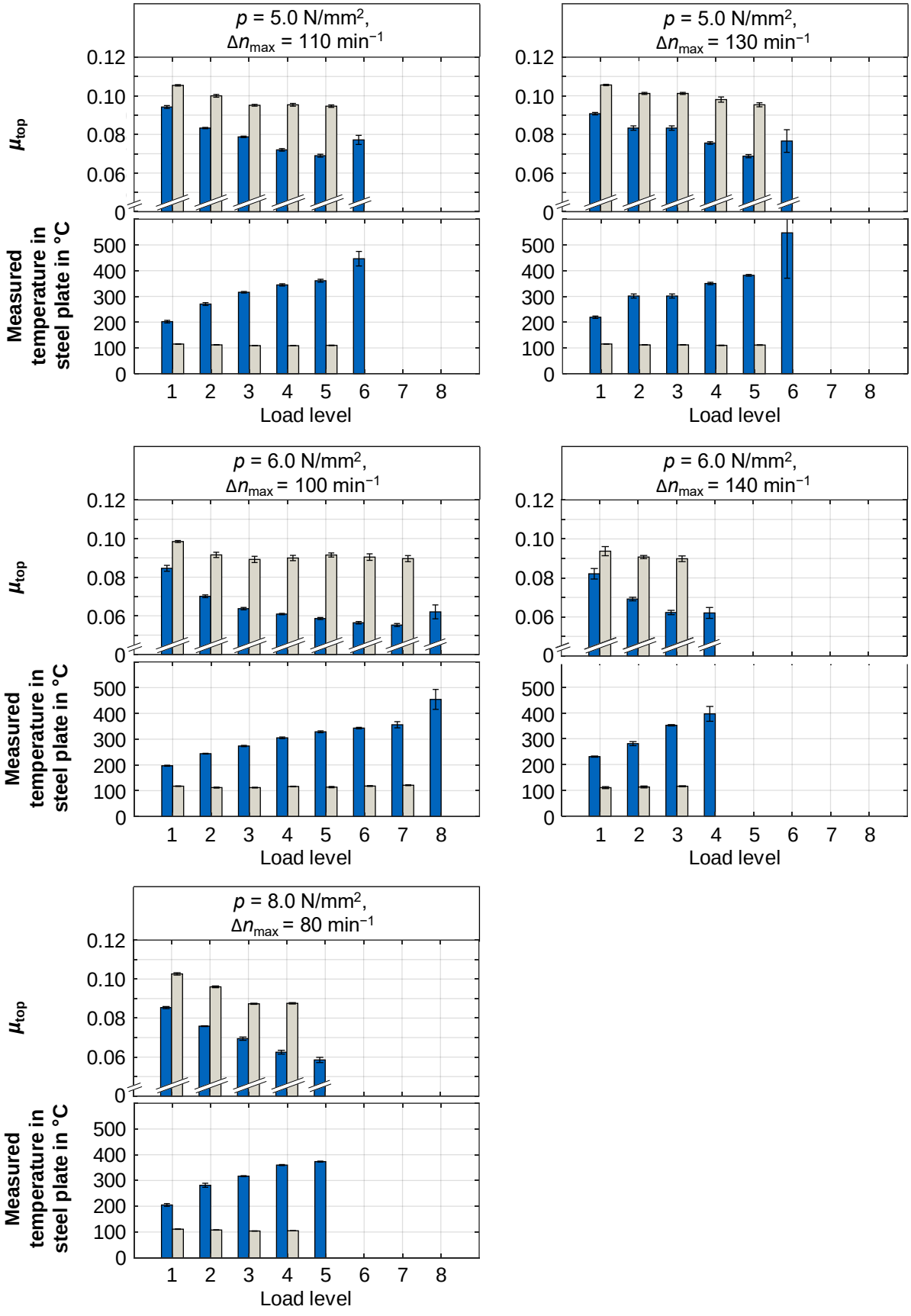

Figure A.19: Characteristic coefficient of friction μ_{top} and measured maximum temperature in the steel plate for step tests with friction system FS1.

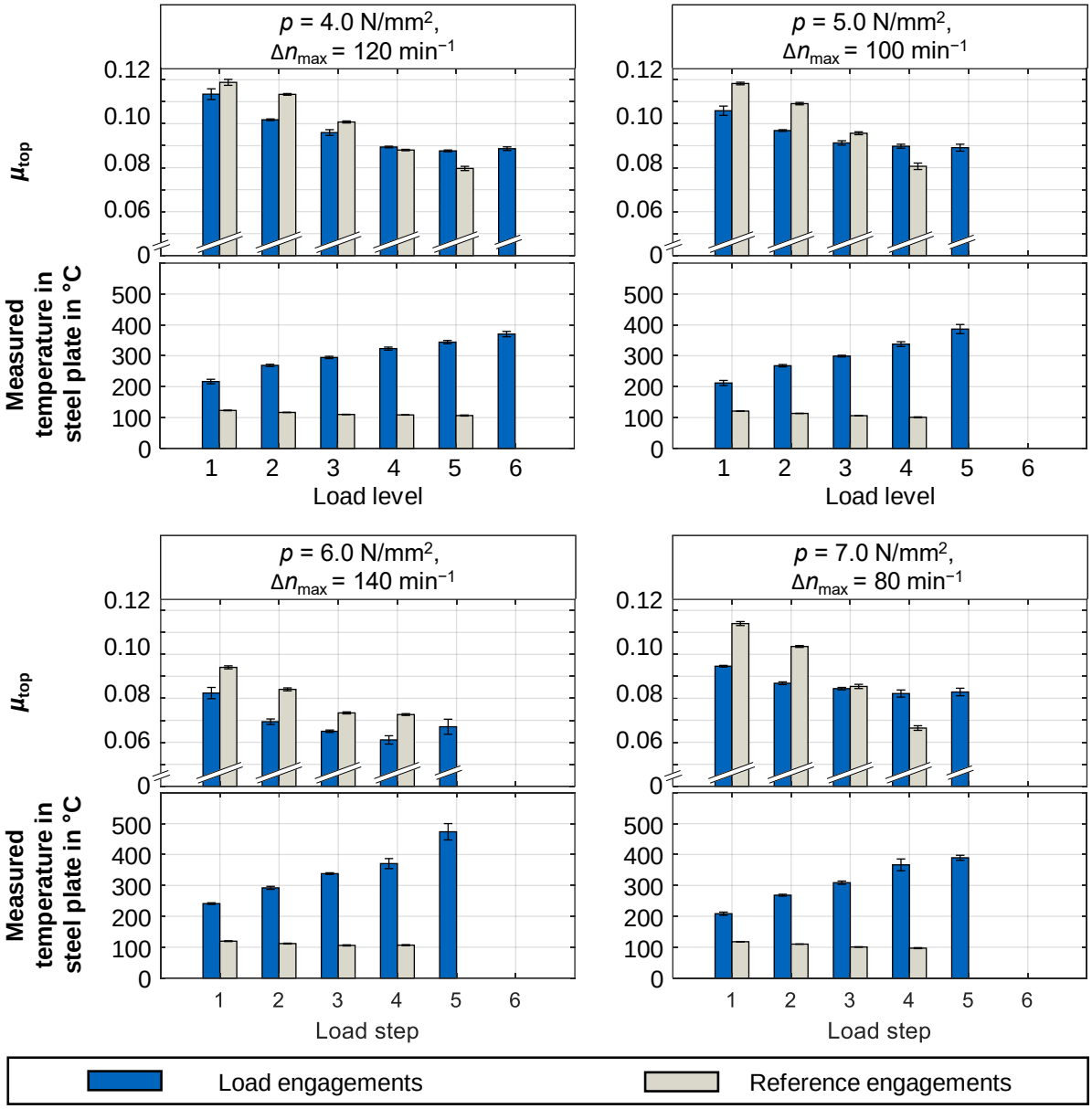

Figure A.20: Characteristic coefficient of friction μ_{top} and measured maximum temperature in the steel plate for step tests with friction system FS2.

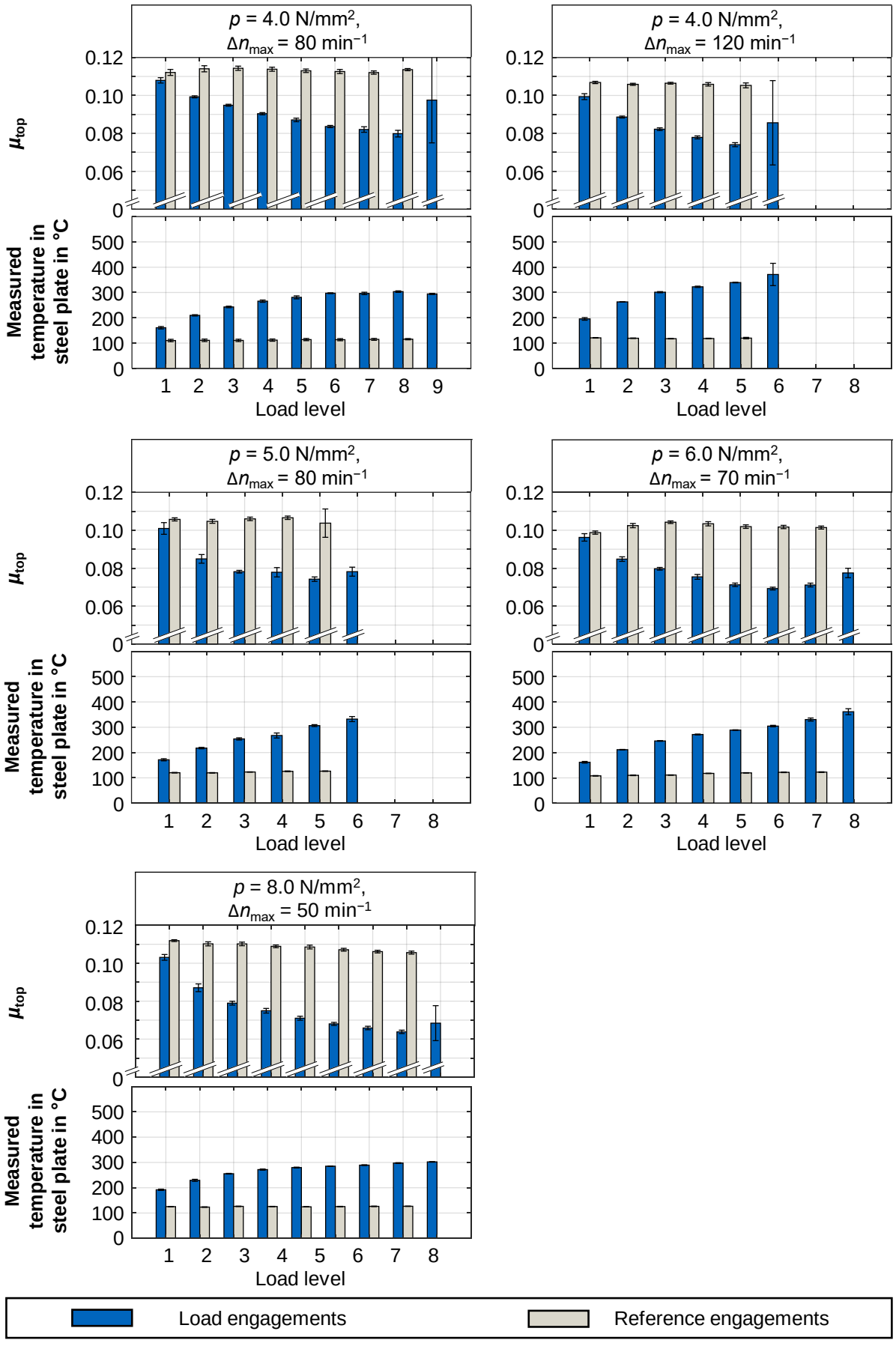

Figure A.21: Characteristic coefficient of friction μ_{top} and measured maximum temperature in the steel plate for step tests with friction system FS3.

A.5 Two-Dimensional Analysis of the Thermomechanical Behavior

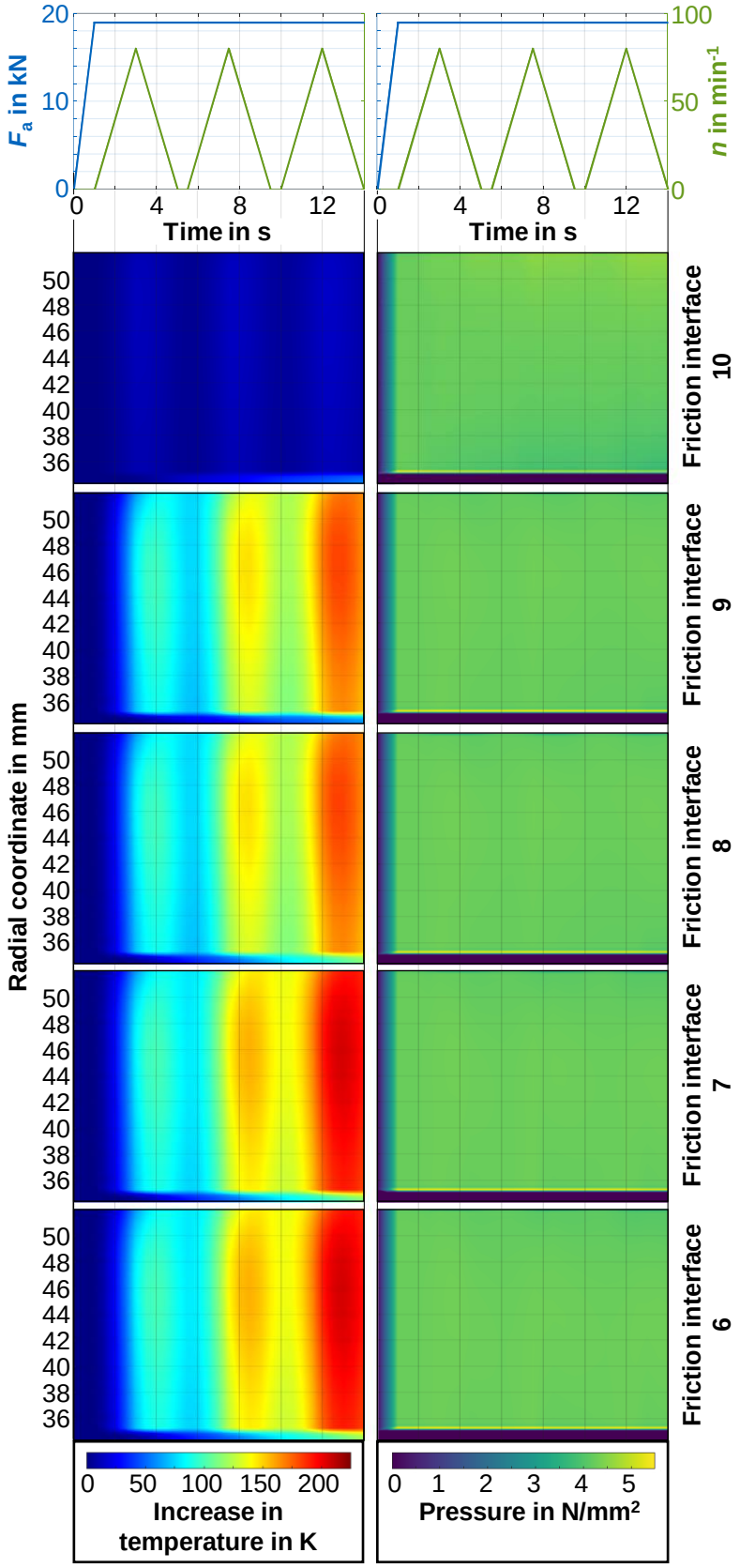

Figure A.22: Temperature and pressure distribution of friction interfaces 6 – 10 as a function of time [Sch22c].

B Dissertations at FZG

1	PERRET, H.	Übertragung konstanter Leistung durch stufenlos mechanische Regeltriebe. TH Braunschweig (1935).
2	BELLMANN, H.	Beiträge zur Prüfung von Bremsbelägen. TH Braunschweig (1939).
3	HIERSIG, H.M.	Der Zusammenhang von Gestaltung und Beanspruchung bei Schneckengetrieben mit Evolventenverzahnung. TH Braunschweig (1943).
4	HELBIG, F.	Walzenfestigkeit und Grübchenbildung von Zahnrad- und Wälzlagerwerkstoffen. TH Braunschweig (1943).
5	ARF, D.	Pendelrollenlager mit symmetrischen und unsymmetrischen Rollen. TH Braunschweig (1944).
6	OESMANN, W.	Entwicklung einer Stahlsand-Schalt- und Regelkupplung. TH Braunschweig (1945).
7	RUBO, E.	Ermittlung der Achsfehler-Empfindlichkeit verschiedener Zylinder-Schneckengetriebe mit Hilfe des Einlauf-Abschliffvolumens. TH Braunschweig (1948).
8	GLAUBITZ, H.	Drehmomentmessungen zum Wendevorgang bei Raupenfahrwerken. TH Braunschweig (1948).
9	TALKE, H.	Beiträge zur hydrodynamischen Schmiertheorie des ebenen Gleitschuhes auf ebener Fläche. TH Braunschweig (1948).
10	CRAMER, H.	Über die Reibung und Schmierung feinmechanischer Geräte. TH Braunschweig (1949).
11	THOMAS, W.	Reibscheiben-Regelgetriebe mit Linienberührung. TH Braunschweig (1949).
12	MAUSHAKE, W.	Theoretische Untersuchung von Schneckengetrieben mit Globoidschnecke und Stirnrad. TH Braunschweig (1950).
13	KRAUPNER, K.W.	Das plastische Verhalten umlaufender Stahlrollen bei Punktberührung. TH Braunschweig (1951).
14	BANASCHEK, K.	Die Gleitreibung geschmierter Flächen kleiner Schmiegung. Einfluß von Werkstoffpaarung, Krümmung, Oberfläche und Schmierstoff. TH Braunschweig (1951).
15	HEYER, E.	Versuche mit Zylinderschneckentrieben. Einfluß von Zahnform, Modul, Durchmesser und Schmierstoff auf Verlustleistung und Tragfähigkeit. TH München (1952).
16	HENTSCHEL, G.	Der Hochleistungswälztrieb. Entwicklungsstand und Entwicklungsmöglichkeiten. TH München (1952).
17	WINTER, H.	Tragfähigste Evolventengeradverzahnung. TH München (1954).

18	ROY, A.K.	Spannungsoptische Untersuchung eines schrägverzahnten Stirnrades. TH München (1957).
19	RETTIG, H.	Dynamische Zahnkraft. TH München (1957).
20	OHLENDORF, H.	Verlustleistung und Erwärmung von Stirnrädern. TH München (1958).
21	UNTERBERGER, M.	Geräuschuntersuchungen an geradverzahnten Zahnrädern. TH München (1958).
22	LOOMAN, J.	Das Abrichten von profilierten Schleifscheiben zum Schleifen von schrägverzahnten Stirnrädern. TH München (1959).
23	JARCHOW, F.	Versuche an Stirnrad-Globoidschneckentrieben. TH München (1960).
24	POPOVIC, L.	Einfluß von Zahnform und Bearbeitung auf die Zahnfußfestigkeit. TH München (1960).
25	EHRLENSPIEL, K.	Die Festkörperreibung von geschmierten und ungeschmierten Metallpaarungen mit Linienberührung. TH München (1962).
26	PITTROFF, H.	Riffelbildung infolge Stillstandserschütterungen bei Wälzlagern. TH München (1962).
27	SCHREIBER, H.	Zur Auswertung von Lebensdauerversuchen an Wälzlagern. TH München (1962).
28	ROTH, K.	Untersuchungen über die Eignung der Evolventenzahnform für eine allgemein verwendbare feinwerktechnische Normverzahnung. TH München (1963).
29	NARUSE, Ch.	Verschleiß, Tragfähigkeit und Verlustleistung bei Schraubenradgetrieben. TH München (1964).
30	GARTNER, F.	Die Mischreibung bei Linienberührung. TH München (1964).
31	ASSMANN, H.	Vergleichende Untersuchung von Getriebeölen im FZG-Stirnrad- und Esso-Hypoidprüfstand. TH München (1965).
32	REISTER, D.	Einseitiges Breitentragen bei Stirnrädern. TH München (1965).
33	KORRENN, H.	Gleitreibung in den Kontaktstellen zwischen den Wälzkörpern und den Laufbahnen der Ringe von Wälzlagern. TH München (1965).
34	HÖSEL, Th.	Geräuschuntersuchungen an schrägverzahnten Stirnrädern mit Evolventenverzahnung. TH München (1965).
35	LANGENBECK, K.	Die Verschleiß- und Freßgrenzlast der Hypoidgetriebe. TH München (1966).

36	MEMMEL, M.	Untersuchungen über die Tragfähigkeit und Gebrauchsdauer von Gelenklagern. TH München (1966).
37	BÖTSCH, H.	Der Einfluß der Oberflächenbearbeitung und -behandlung auf die Flankenfestigkeit von Stirnrädern aus Vergütungsstahl. TH München (1966).
38	LECHNER, G.	Die Freßlastgrenze bei Stirnrädern aus Stahl. TH München (1966).
39	LANGE, S.	Untersuchungen von Helicon- und Spiroidgetrieben mit abwickelbaren Schneckenflanken nach der hydrodynamischen und nach der Hertzschen Theorie. TH München (1967).
40	SCHWÄGERL, D.	Untersuchung von Helicon- und Spiroidgetrieben mit trapezförmigem Schneckenprofil nach der Hertzschen und nach der hydrodynamischen Theorie. TH München (1967).
41	MICHELS, K.	Schneckengetriebe mit Werkstoffpaarung Stahl/Grauguß. TH München (1968).
42	GACKSTETTER, G.	Verlustarme Verzahnung. TH München (1968).
43	GEUPEL, H.	Flüssigkeitsreibung bei Punktberührung. TH München (1969).
44	GREKOUSSIS, R.	Vergleichende Untersuchungen zur Freßtragfähigkeit von Hypoid- und Stirnrädern. TH München (1969).
45	BAETHGE, J.	Zahnfederhärte, Drehwegfehler und Geräusch bei Stirnrädern. TH München (1969).
46	SCHULZ, H.D.	Untersuchung über Tragfähigkeiten und Verlustleistung von Schneckengetrieben mit trapezförmigem Schneckenprofil und kegeliger Schnecke. TH München (1969).
47	STÖLZLE, K.	Leistungsübertragung in Planetengetrieben bei statischem und dynamischem Betrieb. Berechnung, Optimierung und Versuchsergebnisse. TH München (1970).
48	SEITZINGER, K.	Die Erwärmung einsatzgehärteter Zahnräder als Kennwert für ihre Freßtragfähigkeit. TU München (1971).
49	STÖSSEL, K.	Reibungszahlen unter elasto-hydrodynamischen Bedingungen. TU München (1971).
50	SCHMIDT, G.	Berechnung der Wälzpressung schrägverzahnter Stirnräder unter Berücksichtigung der Lastverteilung. TU München (1972).
51	HIRT, M.	Einfluß der Zahnfußausrundung auf Spannung und Festigkeit von Geradstirnrädern. TU München (1974).

52	WILKESMANN, H.	Berechnung von Schneckengetrieben mit unterschiedlichen Zahnprofilformen (Tragfähigkeits- und Verlustleistung für Hohlkreis-, Evolventen- und Geradlinienprofil). TU München (1974).
53	RICHTER, M.	Der Verzahnungswirkungsgrad und die Freßtragfähigkeit von Hypoid- und Schraubenradgetrieben - Versuchsergebnisse und Berechnungsmethoden. TU München (1976).
54	RÖSCH, H.	Untersuchungen zur Wälzfestigkeit von Rollen - Einfluß von Werkstoff, Wärmebehandlung und Schlupf. TU München (1976).
55	GAGGERMEIER, H.	Untersuchungen zur Reibkraftübertragung in Regel-Reibradgetrieben im Bereich elasto-hydrodynamischer Schmierung. TU München (1977).
56	KÄSER, W.	Beitrag zur Grübchenbildung an gehärteten Zahnrädern. Einfluß von Härtetiefe und Schmierstoff auf die Flankentragfähigkeit. TU München (1977).
57	KNABEL, W.	Geräusche und Schwingungen an Stirnradgetrieben. Untersuchungen geometrischer Einflüsse bei hohen Drehzahlen und Belastungen. TU München (1977).
58	WIRTH, X.	Über den Einfluß von Schleifkerben auf die Zahnfußtragfähigkeit und das Schädigungsverhalten oberflächengehärteter Zahnräder. TU München (1977).
59	HUBER, G.	Zylinderschneckengetriebe, ein Beitrag zur Berechnung von Grübchen- und Gleitverschleiß und Angaben zum Wirkungsgradverhalten aus Versuchen. TU München (1978).
60	BROSSMANN, U.	Über den Einfluß der Zahnfußausrundung und des Schrägungswinkels auf Beanspruchung und Festigkeit schrägverzahnter Stirnräder. TU München (1979).
61	PLEWE, H.-J.	Untersuchungen über den Abriebverschleiß von geschmierten, langsam laufenden Zahnrädern. TU München (1980).
62	FRESEN, G.	Untersuchungen über die Tragfähigkeit von Hypoid- und Kegelradgetrieben (Grübchen, Ridging, Rippling, Graufleckigkeit und Zahnbruch). TU München (1981).
63	OSTER, P.	Beanspruchung der Zahnflanken unter Bedingungen der Elastohydrodynamik. TU München (1982).
64	HORNUNG, K.	Zahnräder aus Bainitischem Gusseisen mit Kugelgraphit. TU München (1983).
65	WEISS, T.	Zum Festigkeits- und Verzugsverhalten von randschichtgehärteten Zahnrädern. TU München (1983).

66	VOJACEK, H.	Das Reibungsverhalten von Fluiden unter elastohydrodynamischen Bedingungen. Einfluß der chem. Struktur des Fluides, der Werkstoffe und der Makro- und Mikrogeometrie der Gleit/Wälzkörper. TU München (1984).
67	SCHÖNNENBECK, G.	Einfluß der Schmierstoffe auf die Zahnflankenermüdung (Graufleckigkeit und Grübchenbildung) hauptsächlich im Umfangsgeschwindigkeitsbereich 1...9 m/s. TU München (1984).
68	WIENER, H.	Untersuchung der Rollenkinematik im Axial-Pendelrollenlager. TU München (1984).
69	MATHIAK, D.	Untersuchungen über Flankentragfähigkeit, Zahnfußtragfähigkeit und Wirkungsgrad von Zylinderschneckengetrieben. TU München (1984).
70	STRASSER, H.	Einflüsse von Verzahnungsgeometrie, Werkstoff und Wärmebehandlung auf die Zahnfußtragfähigkeit. TU München (1984).
71	JOACHIM, F.-J.	Untersuchungen zur Grübchenbildung an vergüteten und normalisierten Zahnrädern (Einfluß von Werkstoffpaarung, Oberflächen- und Eigenspannungszustand). TU München 1984.
72	GERBER, H.	Innere dynamische Zusatzkräfte bei Stirnradgetrieben - Modellbildung, innere Anregung und Dämpfung. TU München (1984).
73	SIMON, M.	Messung von elasto-hydrodynamischen Parametern und ihre Auswirkung auf die Grübchentragfähigkeit vergüteter Scheiben und Zahnräder. TU München (1984).
74	SCHMIDT, W.	Untersuchungen zur Grübchen- und zur Zahnfußtragfähigkeit geradverzahnter evolventischer Innenstirnräder. TU München (1984).
75	FUNCK, G.	Wärmeabführung bei Getrieben unter quasistationären Betriebsbedingungen. TU München (1985).
76	PAUL, M.	Einfluß von Balligkeit und Lageabweichungen auf die Zahnfußbeanspruchung spiralverzahnter Kegelräder. TU München (1986).
77	HOPPE, F.	Das Abschalt- und Betriebsverhalten von mechanischen Sicherheitskupplungen. TU München (1986).
78	MICHAELIS, K.	Die Integraltemperatur zur Beurteilung der Freßtragfähigkeit von Stirnradgetrieben. TU München (1987).
79	WECH, L.	Untersuchungen zum Wirkungsgrad von Kegelrad- und Hypoidgetrieben. TU München (1987).

80	KNAUER, G.	Zur Grübchentragfähigkeit einsatzgehärteter Zahnräder - Einfluß von Werkstoff, Schmierstoff und Betriebstemperatur. TU München (1988).
81	PLACZEK, T.	Lastverteilung und Flankenkorrektur in gerad- und schrägverzahnten Stirnradstufen. TU München (1988).
82	PFLAUM, H.	Das Reibungsverhalten ölgeschmierter Kegelreibkupplungen in Synchronisationseinrichtungen von Kraftfahrzeug-Schaltgetrieben. TU München (1988).
83	BRINCK, P.	Zahnfußtragfähigkeit oberflächengehärteter Stirnräder bei Lastrichtungsumkehr. TU München (1989).
84		entfallen
85	NEUPERT, K.	Verschleißtragfähigkeit und Wirkungsgrad von Zylinder-Schneckengetrieben. TU München (1990).
86	PREXLER, F.	Einfluß der Wälzflächenrauheit auf die Grübchenbildung vergüteter Scheiben im EHD-Kontakt. TU München (1990).
87	SCHALLER, K.-V.	Betriebsfestigkeitsuntersuchungen zur Grübchenbildung an einsatzgehärteten Stirnradflanken. TU München (1990).
88	COLLENBERG, H.-F.	Untersuchungen zur Freßtragfähigkeit schnellaufender Stirnradgetriebe. TU München (1991).
89	MÜLLER, R.	Schwingungs- und Geräuschanregung bei Stirnradgetrieben. TU München (1991).
90	ANZINGER, M.	Werkstoff- und Fertigungseinflüsse auf die Zahnfußtragfähigkeit, insbesondere im hohen Zeitfestigkeitsgebiet. TU München (1991).
91	KAGERER, E.	Messung von elastohydrodynamischen Parametern im hochbelasteten Scheiben- und Zahnkontakt. TU München (1991).
92	HASLINGER, K.	Untersuchungen zur Grübchentragfähigkeit profilkorrigierter Zahnräder. TU München (1991).
93	VOLLHÜTER, F.	Einfluß der Achsversetzung auf die Grübchen- und Zahnfußtragfähigkeit von spiralverzahnten Kegelrädern. TU München (1992).
94	PINNEKAMP, B.	Das Schaltverhalten von PKW-Getriebesynchronisierungen. TU München (1992).
95	SCHUBERT, M.	Einfluß der Befestigungsart und Radkranzdicke auf die Zahntragfähigkeit von Innenstirnrädern. TU München (1993).
96	STEINGRÖVER, K.	Untersuchung zu Verschleiß, Verlustgrad und Fressen bei Zylinder-Schneckengetrieben. TU München (1993).

97	ELSTORPFF, M.-G.	Einflüsse auf die Grübchentragfähigkeit einsatzgehärteter Zahnräder bis in das höchste Zeitfestigkeitsgebiet. TU München (1993).
98	EMMERT, S.	Untersuchungen zur Zahnflankenermüdung (Graufleckigkeit, Grübchenbildung) schnellaufender Stirnradgetriebe. TU München (1994).
99	SUCHANDT, Th.	Betriebsfestigkeitsuntersuchungen zur Zahnfußtragfähigkeit einsatzgehärteter Zahnräder und zur Bruchfestigkeit vergüteter Laschenketten. TU München (1994).
100	HÄMMERL, B.	Lebensdauer- und Temperaturverhalten ölgekühlter Lamellenkupplungen bei Lastkollektivbeanspruchung. TU München (1994).
101	WEISS, R.	Einfluß der Ölalterung auf die Zahnflankentragfähigkeit. TU München (1994).
102	SCHLENK, L.	Untersuchungen zur Freßtragfähigkeit von Großzahnrädern. TU München (1995).
103	MANN, U.	Schmierfilmbildung in elastohydrodynamischen Kontakten, Einfluß verschiedener Grundöle und Viskositäts-Index-Verbesserer. TU München (1995).
104	RUDZEWSKI, S.	Systemtechnische Verknüpfung eingeführter Getriebeberechnungsprogramme. TU München (1995).
105	RANK, R.	Untersuchungen zur Lebensdauerprüfung von Synchronisierungen. TU München (1995).
106	EBERSPÄCHER, C.	Reihenfolgeeffekte bei der Grübchen-Betriebsfestigkeit einsatzgehärteter Zahnräder. TU München (1995).
107	RANK, B.	Untersuchungen zur Grübchenbildung bei Zylinder-Schneckengetrieben. TU München (1996).
108	SATTELBERGER, K.	Schwingungs- und Geräuschanregung bei ein- und mehrstufigen Stirnradgetrieben. TU München (1997).
109	HIRSCHMANN, V.	Tragfähigkeitsuntersuchungen an stufenlosen Umschlingungsgetrieben. TU München (1997).
110	THOMAS, J.	Flankentragfähigkeit und Laufverhalten von hartfeinbearbeiteten Kegelrädern. TU München (1998).
111	WIKIDAL, F.	Berechnung der Flankenpressung gerad- und schrägverzahnter Stirnräder für last- und fertigungsbedingte Abweichungen. TU München (1998).
112	PERPONCHER, V., CH.	Einflüsse von Reibflächentopographie und Beanspruchungen auf das Reibungs- und Verschleißverhalten von Synchronisierungen. TU München (1998).
113	SCHEDL, U.	Einfluß des Schmierstoffs auf die Grübchenlebensdauer einsatzgehärteter Zahnräder. TU München (1998).

114	VOLLMER, T.	Methodik zur Entwicklung einer Fahrstrategie für Fahrzeuge, ausgeführt am Beispiel des Autarken Hybrids. TU München (1998).
115	HEITMANN, A.	Entwicklung des i²-Getriebes für den Autarken Hybrid-Antriebsstrang. TU München (1998).
116	PFLEGER, F.	Schalt- und Lebensdauerverhalten von Lamellenkupplungen. TU München (1998).
117	KERSCHL, S.	Der Autarke Hybrid - Optimierung des Antriebsstrangs hinsichtlich Energieverbrauch und Bestimmung des Einsparpotentials. TU München (1998).
118	DÖBEREINER, R.	Tragfähigkeit von Hochverzahnungen geringer Schwingungsanregung. TU München (1998).
119	WEIGAND, U.	Werkstoff- und Wärmebehandlungseinflüsse auf die Zahnfußtragfähigkeit. TU München (1999).
120	SCHRADE, U.	Einfluß von Verzahnungsgeometrie und Betriebsbedingungen auf die Graufleckentragfähigkeit von Zahnradgetrieben. TU München (2000).
121	KÖLL, J.	Konstruktion des Getriebes für ein Pkw-Hybridantriebssystem. TU München (2000).
122	FÖRSTER, W.	Der Lastschaltvorgang beim stufenlosen i²-Getriebe des Autarken Hybrid-Antriebsstrangs. TU München (1999).
123	LANGE, N.	Hoch fresstragfähige Schneckengetriebe mit Rädern aus Sphaeroguß. TU München (2000).
124	LUTZ, M.	Methoden zur rechnerischen Ermittlung und Optimierung von Tragbildern an Schneckengetrieben. TU München (2000).
125	KOPATSCH, F.	Wirksamkeit von Viskositätsindex-Verbesserern im EHD-Zahnradkontakt. TU München (2000).
126	BAYERDÖRFER, I.	Einfluß von betriebsbedingten Schmierstoffveränderungen auf die Flankentragfähigkeit einsatzgehärteter Stirnräder. TU München (2000).
126e	DOMIAN, H.-J.	Systematische Synthese von Getriebestrukturen der Vorgelegebauart. TU München 2001.
127	TOBIE, T.	Zur Grübchen- und Zahnfußtragfähigkeit einsatzgehärteter Zahnräder. TU München (2001).
128	STAHL, K.	Grübchentragfähigkeit einsatzgehärteter Gerad- und Schrägverzahnungen unter besonderer Berücksichtigung der Pressungsverteilung. TU München (2001).
129	NEUMÜLLER, M.	Einfluß der Ölalterung auf Reibungs- und Verschleißverhalten von Synchronisierungen. TU München (2001).

130	MOSBACH, C.	Das Reibungs- und Reibschwing-Verhalten nasslaufender Lamellenkupplungen. TU München (2002).
131	DYLA, A.	Modell einer durchgängig rechnerbasierten Produktentwicklung. TU München (2002).
132	GRASWALD, C.	Reibung im elastohydrodynamischen Kontakt von Reibradgetrieben. TU München (2002).
133	GEISER, H.	Grundlagen zur Beurteilung des Schwingungsverhaltens von Stirnrädern. TU München (2002).
134	SCHINAGL, S.	Zahnfußtragfähigkeit schrägverzahnter Stirnräder unter Berücksichtigung der Lastverteilung. TU München (2002).
135	DOLESCHEL, A.	Wirkungsgradberechnung von Zahnradgetrieben in Abhängigkeit vom Schmierstoff. TU München (2003).
136	ANNAST, R.	Kegelrad-Flankenbruch. TU München (2003)
137	SÜSSMUTH, J.-F.	Eignungsbeurteilung von Schmierstoffen für stufenlose Umschlingungsgetriebe. TU München (2003).
138	MATTEN, D.	Methode zur Entwicklung ingenieurwissenschaftlicher Berechnungsprogramme. TU München (2003).
139	GEIER, N.	Untersuchung des Reibungs- und Verschleißverhaltens nasslaufender Kupplungen in Abhängigkeit ihrer Reibflächentopographie. TU München (2003).
140	HERTTER, T.	Rechnerischer Festigkeitsnachweis der Ermüdungstragfähigkeit vergüteter und einsatzgehärteter Stirnräder. TU München (2003).
141	KRIEGER, H.	Alterung von Schmierstoffen im Zahnradprüfstand und in Praxisgetrieben. TU München (2004).
142	STEUTZGER, M.	Einfluß der Baugröße auf die Zahnfußtragfähigkeit einsatzgehärteter Stirnräder. TU München (2004).
143	SCHMIDBAUER, T.	Aufbau und Erprobung des Autarken Hybrid-Antriebsstrangs im Versuchsfahrzeug. TU München (2004).
144	LIU, W.	Einfluss verschiedener Fertigungsverfahren auf die Graufleckentragfähigkeit von Zahnradgetrieben. TU München (2004).
145	FEHLING, R.	Höhere Tragfähigkeit bei Zahnradflanken durch eine nichtevolventische Profilmodifikation. TU München (2004).
146	GUTTENBERG, P.	Der autarke Hybrid am Prüfstand - Funktion, Kraftstoffverbrauch und energetische Analyse. TU München (2004).

147	WIMMER, T.	Einflüsse auf das Lastübernahmeverhalten von nasslaufenden Lamellenkupplungen. TU München (2004).
148	RADEV, T.	Einfluss des Schmierstoffes auf die Grübchentragfähigkeit einsatzgehärteter Zahnräder - Entwicklung des Praxisnahen Pittingtests. TU München (2005).
149	KRASTEV, I.	Optimierung des Lastschaltvorgangs im i²-Getriebe. TU München (2005).
150	HEILEMANN, J.	Tragfähigkeit und Wirkungsgrad bei unterschiedlichen Schnecken-Zahnflankenformen unter Berücksichtigung der Oberflächenhärte und Härtetiefe. TU München (2005).
151	HEIZENRÖTHER, M.	Das Stirnraddifferenzial mit Innenverzahnung im Vergleich zum Kegelraddifferenzial inklusive einer Sperrwertanalyse. TU München (2005).
152	WIMMER, A.	Lastverluste von Stirnradverzahnungen - Konstruktive Einflüsse, Wirkungsgradmaximierung, Tribologie. TU München (2006).
153	BRUCKMEIER, S.	Flankenbruch bei Stirnradgetrieben. TU München (2006).
154	HAUSER, C.	Einfluss der Ölalterung auf Reibcharakteristik und Reibschwingverhalten von Lamellenkupplungen. TU München (2007).
155	GROSSL, A.	Einfluss von PVD-Beschichtungen auf die Flanken- und Fußtragfähigkeit einsatzgehärteter Stirnräder. TU München (2007).
156	STEINBERGER, G.	Optimale Grübchentragfähigkeit von Schrägverzahnungen. TU München (2007).
157	JAROS, M.	Integration des STEP-Produktmodells in den Getriebeentwicklungsprozess. TU München (2007).
158	RADEV, S.	Einfluss von Flankenkorrekturen auf das Anregungsverhalten gerad- und schrägverzahnter Stirnradpaarungen. TU München (2007).
159	BRAYKOFF, C.	Tragfähigkeit kleinmoduliger Zahnräder. TU München (2007).
160	STANGL, M.	Methodik zur kinematischen und kinetischen Berechnung mehrwelliger Planeten-Koppelgetriebe. TU München (2007).
161	STENICO, A.	Werkstoffmechanische Untersuchungen zur Zahnfußtragfähigkeit einsatzgehärteter Zahnräder. TU München (2007).
162	SCHWIENBACHER, S.	Einfluss von Schleifbrand auf die Flankentragfähigkeit einsatzgehärteter Zahnräder. TU München (2008).

163	WINKLER, J.	Tribologischer Schichtaufbau bei Synchronisierungen und sein Einfluss auf Reibung und Verschleiß. TU München (2008).
164	WIRTH, C.	Zur Tragfähigkeit von Kegelrad- und Hypoidgetrieben. TU München (2008).
165	KREIL, O.	Einfluss der Oberflächenstruktur auf Druckverteilung und Schmierfilmdicke im EHD-Kontakt. TU München (2009).
166	OTTO, H.-P.	Flank load carrying capacity and power loss reduction by minimised lubrication. TU München (2009).
167	OTTO, M.	Lastverteilung und Zahnradtragfähigkeit von schrägverzahnten Stirnrädern. TU München (2009).
168	TOMIC, D.	Zum Verschleiß von Kegelreibkupplungen - Einflüsse von Belastung und Schmierstoff auf Reibschichteigenschaften. TU München (2009).
169	WEISEL, C.	Schneckengetriebe mit lokal begrenztem Tragbild. TU München (2009).
170	WEITL, R.	Zur Tragfähigkeitsberechnung von Wälzlagern und Stirnrädern. TU München (2010).
171	MULZER, F.	Systematik hochübersetzender koaxialer Getriebe. TU München (2010).
172	SCHUDY, J.	Untersuchungen zur Flankentragfähigkeit von Außen- und Innenverzahnungen. TU München (2010).
173	BRETL, N.	Einflüsse auf die Zahnfußtragfähigkeit einsatzgehärteter Zahnräder im Bereich hoher Lastspielzahlen. TU München (2010).
174	GRIGGEL, T.	Einfluss der Fertigungsqualität auf die Schwingungsanregung von Stirnrädern. TU München (2010).
175	LAYHER, M.	Einfluss der Schmierstoffadditivierung auf das Reibungsverhalten nasslaufender Reibschaltelemente. TU München (2011).
176	HOCHMANN, M.	Zahnradtragfähigkeit bei Schmierung mit Getriebefließfetten. TU München (2011).
177	DETZEL, J.	Tribologische Untersuchungen an Achsgetrieben zur Verbesserung des Wirkungsgrads. TU München (2011).
178	ZIEGLER, A.	Zur verkürzten Systemlebensdauerprüfung von Zahnradgetrieben. TU München (2011).
179	THOMA, F.	Lastübertragung im verformten System Lager-Welle-Zahnrad. TU München (2012).
180	FRÜHE, T.	Berechnung und Minimierung der Zahnfußspannung von Standard- und LowLoss-Verzahnungen. TU München (2012).

181	WITZIG, J.	Flankenbruch - Eine Grenze der Zahnradtragfähigkeit in der Werkstofftiefe. TU München (2012).
182	KLEIN, M.	Zur Fresstragfähigkeit von Kegelrad- und Hypoidgetrieben. TU München (2012).
183	KURTH, F.	Efficiency Determination and Synthesis of Complex-Compound Planetary Gear Transmissions. TU München (2012).
184	WOHLLEBER, F.	Thermischer Haushalt nasslaufender Lamellenkupplungen. TU München (2012).
185	HEIDER, M.	Schwingungsverhalten von Zahnradgetrieben. TU München (2012).
186	MONZ, A.	Tragfähigkeit und Wirkungsgrad von Schneckengetrieben bei Schmierung mit konsistenten Getriebefetten. TU München (2012).
187	WIRTH, M.	Schleppmomente in Synchronisierungen von Fahrzeuggetrieben. TU München (2012).
188	BANSEMIR, G.	Konstruktionsleitsystem für den durchgängig rechnerbasierten Zahnradgetriebeentwurf. TU München (2012).
189	HERGESELL, M.	Grauflecken- und Grübchenbildung an einsatzgehärteten Zahnrädern mittlerer und kleiner Baugröße. TU München (2013).
190	KOLLER, P.	Steigerung der Zahnflankentragfähigkeit durch Optimierung von Eigenspannungs- und Oberflächenzustand. TU München (2013).
191	SCHLEICH, T.	Temperatur- und Verlustleistungsverhalten von Wälzlagern in Getrieben. TU München (2013).
192	STEMPLINGER, J.-P.	Tragfähigkeit und Wirkungsgrad von Stirnradgetrieben bei Schmierung mit hochviskosen Fluiden und Fetten NLGI 0,1 und 2. TU München (2013).
193	FÜRSTENBERGER, M.	Betriebsverhalten verlustoptimierter Kunststoffzahnräder. TU München (2013).
194	HOMBAUER, M.	Grauflecken an Kegelrad- und Hypoidverzahnungen und deren Einfluss auf die Grübchentragfähigkeit. TU München (2013).
195	MAYER, J.	Einfluss der Oberfläche und des Schmierstoffs auf das Reibungsverhalten im EHD-Kontakt. TU München (2013).
196	BAUHOFFER, H.	Kontakt- und Laufverhalten von Kronenrädern unter Montageabweichungen. TU München (2014).
197	LECHNER, C.	Energiebilanzierung des CVT-Hybrid. TU München (2014).

198	HINTERSTOISSER, M.	Zur Optimierung des Wirkungsgrades von Stirnradgetrieben TU München (2014).
199	LOMBARDO, S.	Einfluss von verschiedenen Carbonitrierverfahren auf die Zahnfuß- sowie Zahnflankentragfähigkeit von Stirnrädern. TU München (2014).
200	IDLER, S.	Die Fresstragfähigkeit stufenloser Umschlingungsgetriebe. TU München (2014).
201	LANGHEINRICH, A.	Geometrie, Beanspruchung und Verformung asymmetrischer Stirnradverzahnungen. TU München (2014).
202	MATT, P.	Einfluss der Stirnkanten auf die Tragfähigkeit von Verzahnungen. TU München (2014).
203	HENSEL, M.	Thermische Beanspruchbarkeit und Lebensdauerverhalten von nasslaufenden Lamellenkupplungen. TU München (2014).
204	GEIGER, J.	Wirkungsgrad und Wärmehaushalt von Zahnradgetrieben bei instationären Betriebszuständen. TU München (2015).
205	SIGMUND, W.	Untersuchung und Simulation des Verschleißverhaltens von Schneckengetrieben mit unvollständigem Tragbild. TU München (2015).
206	PARLOW, J.	Erweiterter Verzahnungsentwurf im Anforderungs- und Gesamtsystemkontext. TU München (2016).
207	NEUBAUER, B.	Lastverteilung und Anregungsverhalten in Planetengetriebesystemen. TU München (2016).
208	NITSCH, C.	Dynamisches Betriebsverhalten von Werkstoffverbundzahnrädern. TU München (2016).
209	BIHR, J.	Untersuchung des Schwingungsverhaltens von mehrstufigen Stirnradgetrieben unter besonderer Berücksichtigung des Welle-Lager-Systems. TU München (2016).
210	SCHURER, S.	Einfluss nichtmetallischer Einschlüsse in hochreinen Werkstoffen auf die Zahnfußtragfähigkeit. TU München (2016).
211	KADACH, D.	Stillstandsmarkierungen an Zahnrädern und deren Auswirkungen auf die Flankentragfähigkeit. TU München (2016).
212	FELBERMAIER, M.	Untersuchungen zur Graufleckenbildung und deren Einfluss auf die Grübchentragfähigkeit einsatzgehärteter Stirnräder. TU München (2016).
213	ACUNER, R.	Synchronisierungen mit Carbon-Reibwerkstoffen unter hohen und extremen Beanspruchungen. TU München (2016).

214	LOHNER, T.	Berechnung von TEHD Kontakten und Einlaufverhalten von Verzahnungen. TU München (2016).
215	ZIMMER, M.	Berechnung und Optimierung von Geometrie und Eingriffsverhalten von Verzahnungen beliebiger Achslage. TU München (2017).
216	GWINNER, P.	Auslegung schwingungsarmer Stirnradverzahnungen für den automobilen Einsatz in hochdrehenden, elektrisch angetriebenen Achsgetrieben. TU München (2017).
217	SCHULTHEISS, H.	Zum Verschleißverhalten einsatzgehärteter Zahnradpaarungen in Abhängigkeit des Schmierungsmechanismus bei Fettschmierung. TU München (2017).
218	MOSER, K.	Methode zur Untersuchung des Betriebsverhaltens stufenloser Umschlingungsgetriebe. TU München (2017).
219	STREBEL, M.	Spontanschäden an nasslaufenden Lamellenkupplungen. TU München (2017).
220	BAAR, M.	Kennwerte zur Tragfäkigkeit kleinmoduliger Kronenradverzahnungen unterschiedlicher Werkstoffpaarung. TU München (2017).
221	WICKBORN, C.	Erweiterung der Flankentragfähigkeitsberechnung von Stirnrädern in der Werkstofftiefe. TU München (2017).
222	MEINGASSNER, G.	Methodik zur Untersuchung des Reibungsverhaltens nasslaufender Lamellenkupplungen bei Langsamlauf- und Mikroschlupf. TU München (2017).
223	ZORNEK, B.	Untersuchungen zur Flankentragfähigkeit vergüteter und nitrierter Innen- und Außenverzahnungen. TU München (2018).
224	DOBLER, F.	Einflüsse auf die Tragfähigkeit induktiv umlaufgehärteter Stirnräder. TU München (2018).
225	DAFFNER, M.	Validierung von Verformungsberechnungen im System Zahnrad-Welle-Lager-Gehäuse. TU München (2018).
226	HEIN, M.	Zur ganzheitlichen betriebsfesten Auslegung und Prüfung von Getriebezahnrädern. TU München (2018).
227	HASEL, C.	Zur Zahnfußtragfähigkeit von Kunststoffzahnrädern. TU München (2018).
228	KOHN, B.	Topologische Flankenkorrektur zur Anregungsoptimierung von Stirnradgetrieben. TU München (2019).
229	BOIADJIEV, I.	Schadensentwicklung und Tragfähigkeit carbonitrierter Kegelradverzahnungen. TU München (2019).
230	MAUTNER, E.	Grübchentragfähigkeit von Schneckengetrieben großer Baugröße mit unvollständigem Tragbild. TU München (2019).

231	ENGELHARDT, C.	Einfluss von Wasser in Getriebeölen auf die Zahnflankentragfähigkeit einsatzgehärteter Stirnräder. TU München (2019).
232	VÖLKEL, K.	Charakterisierung des Einlaufverhaltens nasslaufender Lamellenkupplungen. TU München (2020).
233	BANSEMIR, S.	Bewertung von Berechnungstiefe und Aussagegüte bei der Stirnradgetriebeberechnung. TU München (2020).
234	UTAKAPAN, T.	Schwingungsverhalten mehrstufiger Getriebe. TU München (2020).
235	KÖNIG, J.	Steigerung der Zahnflankentragfähigkeit durch optimierte Fertigung und Schmierung. TU München (2020).
236	JURKSCHART, T.	Erweiterte Bestimmung lastabhängiger Verluste von Stirnradgetrieben. TU München (2020).
237	EBNER, M.	Selbstschmierung hochbelasteter Zahnkontakte mit schmierstoffgetränkten porösen Eisenwerkstoffen. TU München (2021).
238	REIMANN, T.	Einfluss der Treibrichtung auf die Flankentragfähigkeit von Stirnrad-, Kegelrad-, und Hypoidgetrieben. TU München (2021).
239	DOBLER, A.	Verschleiß als Lebensdauergrenze für Zahnräder. TU München (2021).
240	DAI, R.	Change-Management-fokussierte Einführung eines "Ganzheitlichen Produktionssystems" in Klein- und Kleinstunternehmen. TU München (2021).
241	NORGAUER, P.	Verschleißverhalten von modernen Schneckenverzahnungen. TU München (2021).
242	GÜNTNER, C.	Zum Einfluss der Härtbarkeit auf die Zahnfußtragfähigkeit einsatzgehärteter Stirnräder größerer Baugröße. TU München (2021).
243	WEIGL, A.	Reibungsreduzierung durch DLC-Beschichtungen. TU München (2021).
244	ILLENBERGER, C.	Zahnflankentragfähigkeit ölgeschmierter Kunststoffverzahnungen. TU München (2021).
245	FROMBERGER, M.	Beschleunigung und Drehwegabweichung zur Erkennung von Grübchenschäden. TU München (2021).
246	PELLKOFER, J.	Zum Verzahnungswirkungsgrad von Kegelradgetrieben. TU München (2021).
247	SAGRALOFF, N.	Zuverlässige Beurteilung der Zahnrad-Graufleckentragfähigkeit von Getriebeölen. TU München (2022).
248	PAUCKER, T.	Berechnung der örtlichen Zahnfußtragfähigkeit von Stirnradverzahnungen. TU München (2022).

249	FUCHS, D.	Einfluss mikroskopischer Fehlstellen auf die Zahnfußtragfähigkeit. TU München (2023).
250	TRÜBSWETTER, M.	Geometrie des Wälzschälens. TU München (2023).
251	YILMAZ, M.	Getriebeschmierung mit wasserhaltigen Polyglykolen. TU München (2023).
252	KRATZER, D.	Zum Einfluss oberflächennaher Eigenschaften auf die Zahnradtragfähigkeit. TU München (2023).
253	GÖTZ, J.	Anregungs- und Schwingungsverhalten von Planetengetrieben. TU München (2023).
254	WEINBERGER, U.	Anregungsverhalten doppelschrägverzahnter Planetenradgetriebe – Einfluss des Apex-Punktes. TU München (2023).
255	MILETI, M.	Performance Optimisation of a Coupled Cone and Dog Clutch for Automotive Application. TU München (2023).
256	STOCKINGER, U.	Untersuchung der Leistungsfähigkeit von Einfach- und Mehrfachkonus-Synchronisierungen. TU München (2023).
257	SCHWARZ, A.	Thermal analysis of elastohydrodynamic contacts. TU München (2023).
258	GRÖTSCH, D.	Thermal Behavior of Wet Clutches in Industrial Applications. TU München (2023).
259	ROTH, P.	Methode zur Ermittlung der Fresstragfähigkeit von Schneckengetrieben. TU München (2024).